

School of Physics and Astronomy



Measuring the dynamics of suspended lipid bilayers and
their reaction to membrane proteins using label free
microscopy

Freya Turley

School of Physics and Astronomy
Cardiff University

30/11/24

Abstract

Cell membranes play crucial roles in biological processes, acting as a barrier and controlling exchange of molecules. This includes intercellular signalling via receptor mediated processes and budding of vesicles from the membrane. For these functions membrane dynamics are fundamental. The sorting of components on and within the membrane leads to a large portion of the complex organisation that exists at a cell surface. There is a reciprocal effect between these components and the membrane, exerting their effects predominantly by altering dynamics. Membranes are described using a fluid mosaic model with areas of differing fluidity, which have different properties due to the lipids they are made up of. Lipids can be in different phases such as gel, a solid state that confers stability, or liquid which can be ordered or disordered. Through this action they can influence the movement of structures such as proteins to sort them into areas with certain properties. This is a reciprocal effect with membrane components affecting the phase behaviour of the lipids and modulating membrane function. This interplay at a crucial structure makes the dynamics an interesting and important area of study. In this work we aimed to measure the dynamics of a membrane via thickness and height changes.

We demonstrate methods to probe these dynamics, generating suspended model membranes and measured with various techniques. Epifluorescence measurements allowed the visualisation of phase separation across the surface of a bilayer, to assess it's interaction with a pore forming toxin. We also show fitting and simulation methods developed using the label free method, quantitative Differential Interference Contrast microscopy (qDIC) to characterise vesicles and their internal volumes.

We introduce our novel label free technique interferometric Gated Off-axis Reflectometry (iGOR) to measure the thickness and axial position of the suspended membrane to sub nanometer resolution. This revealed the undamped dynamics occurring in these membranes at 327 Hz in a widefield conformation. These measurement conditions allowed fast acquisition of every pixel in the field of view simultaneously providing sufficient temporal resolution. Due to it's sensitivity and high resolution, iGOR is a step change in this field of imaging for these dynamics. We also employed iGOR to track nanoparticles in a 3D volume to ascertain their hydrodynamic radii and scattering cross-section. Combined these features of the iGOR technique make it a powerful tool for the investigation of model membrane dynamics and their interaction with proteins.

In this work we show how we made model membranes and how each measurement technique used is a step change in measuring membrane properties. We show measurement of lamellarity and internal refractive index of vesicles using qDIC and thickness and height changes with high temporal resolution using iGOR. Whilst we showed adequate sensitivity there is still outstanding optimisation to acquisition and analysis for full quantitative analysis.

Acknowledgements

First and foremost I would like to express my gratitude to Professor Wolfgang Langbein for his support and scientific guidance throughout my PhD. His strive for scientific rigour has made me a much better and more considered scientist and whose invaluable insights have helped shape my project. Together with Professor Paola Borri, they have guided my work to enable me to tackle a multidisciplinary project without ever feeling too out of my depth, taking time to explain concepts while stretching my understanding into a new field.

I would also like to extend a special thank you to Dr David Regan for all the time he put aside to help me learn and answer all of my questions throughout the years and keeping me entertained during long imaging sessions with seagull stories. His generosity with time and expertise is much appreciated.

I thank Dr Iestyn Pope and Dr Francesco Masia who both provided assistance with my project alongside help in the lab whenever I needed.

To friends in Cardiff who made me feel so welcome especially when starting in isolation and those that have joined along the way and made the office such a nice environment to work in. Special thanks to Emily, Adam, Nicole, Furqan, Martina, Emma and Tess who have kept me going throughout.

For the experiments that were undertaken as a collaboration I would like to thank Adam Cutts, Lainey Williamson and Colin Berry for the protein and Hannah Baird and Ollie Castell for DIBs.

I could not have done this without my friends spread far and wide who have supported me the whole time so to all of you thank you so much for always cheering me on.

A special thanks to Nicola and Emma who have ensured I have somewhere to stay on the occasions I had to do additional experiments in Cardiff I have never known such hospitality, better than any hotel.

And lastly to my family who have encouraged me throughout I truly could not have done it with out you so thank you.

Contents

1	Introduction and background	1
1.1	The importance of membranes and their dynamics	1
1.1.1	Membrane structure	1
1.1.2	Observable membrane dynamics	3
1.2	Membrane observation	5
1.2.1	Fluorescence	6
1.2.2	Label free observation techniques	7
1.2.3	Quantitative phase imaging	8
1.2.4	Interferometric gated off-axis reflectometry	11
1.3	Model membranes	11
1.4	Thesis outline	12
1.5	Project aims	13
2	Materials and methods	14
2.1	Lipid solutions	14
2.1.1	Lipid handling and storage	14
2.1.2	Preparation of lipid solutions	14
2.2	Lipid bilayer sample formation	16
2.2.1	Giant unilamellar vesicles (GUVs)	16
2.2.2	Filtration	18
2.2.3	Desiccator use	21
2.2.4	Spin coating	21
2.2.5	hs-GUV sample preparation	21
2.2.6	Droplet interface bilayers	22
2.2.7	Focal bead sample preparation	24
2.2.8	SUV preparation	24
2.3	Quantitative Differential Interference Contrast Microscopy	24
2.3.1	qDIC optical setup	25
2.3.2	qDIC data acquisition and processing workflow	25
2.4	Temperature control during microscopy	26
2.5	Calibration of numerical aperture	26
2.6	Protein insertion	27
2.6.1	GV sample preparation	27
2.7	Epifluorescence imaging	27
2.7.1	GV imaging during electroformation	28
2.7.2	GV imaging through protein addition	28
2.8	Droplet interface bilayer sample imaging	30
2.9	Interferometric gated off-axis reflectometry	30
2.9.1	Optical setup	30

2.9.2	Acquisition	31
2.9.3	GV sample imaging	35
2.9.4	Analysis pipeline	35
3	Suspended bilayer generation	38
3.1	GUV electroformation	39
3.1.1	Generating a lipid film	39
3.1.2	Electroformation	44
3.1.3	Internal solution	49
3.1.4	Filtration	52
3.1.5	Gel-phase lipid bilayers at room temperature	54
3.2	hs-GUV protocol development	56
3.2.1	ITO electroformation	56
3.2.2	PVA swelling	57
3.3	Droplet interface bilayers	69
3.3.1	Unmodified device	69
3.3.2	Device with deeper agarose layer	71
3.3.3	Device utilising a buffer supported monolayer	72
3.4	Discussion	72
4	Characterisation of giant vesicles using qDIC	75
4.1	Quantitative differential interference contrast microscopy	76
4.2	Refractive index of sucrose solution and lipid bilayers	76
4.3	Measuring refractive index and lamellarity	80
4.4	Measuring sucrose concentration and lamellarity using central column	80
4.5	Summary of initial qDIC analysis	84
4.6	qDIC GV simulations	84
4.6.1	Simulation methodology	85
4.6.2	Profile analysis	86
4.7	Identifying integrals for experimental comparison	90
4.7.1	Peak broadness	90
4.7.2	Evaluation of the effect of defocus	92
4.8	Comparing simulations to experimental data	96
4.8.1	Symmetrisation	96
4.8.2	Background fitting	97
4.8.3	Defocus correction	97
4.9	Further interpretation of phase profiles	100
4.9.1	Birefringence	102
4.9.2	NA dependence	102
4.9.3	Acquisition of numerical aperture data	102
4.9.4	Comparison of numerical aperture data	104
4.10	Discussion	104
5	Protein insertion into GUVs	108
5.1	POPC:POPE bilayer phase transition	110
5.1.1	Phase transition temperature in literature	110
5.1.2	GV morphology during phase transition	110
5.1.3	Determining 1:1 POPC:POPE phase transition temperature .	111
5.1.4	Phase transition temperature upon App6Aa1 insertion	112
5.1.5	Summary	112

5.2	Pore formation probed by leakage	112
5.2.1	Fluorophore choice	114
5.2.2	Imaging protocol	115
5.2.3	Maintaining fluorophore concentration in GUVs	116
5.2.4	Loss of fluorophore upon pore formation	116
5.2.5	Drawbacks and limitations	119
5.2.6	Preliminary study	119
5.3	Use of imaging funnels	121
5.4	Discussion	124
6	Interferometric gated off-axis reflectometry	125
6.1	Data acquisition	127
6.2	Expected geometries	129
6.3	Resolution	129
6.4	Data filtering processes	131
6.4.1	Power correction	131
6.4.2	Offset	131
6.4.3	Phase unwrapping	134
6.4.4	Amplitude correction	137
6.4.5	Excitation beam expansion	138
6.5	Refocussing	138
6.5.1	Interference issues	138
6.6	Spatio-temporal fluctuation frequency analysis	140
6.7	Original data	140
6.7.1	POPC:POPE (1:1)	140
6.7.2	DC ₁₅ PC membranes	142
6.8	POPC:POPE membrane properties	144
6.8.1	Unilamellar membrane fluctuations	144
6.8.2	Bilamellar GV dynamics	146
6.9	POPC:POPE loss of internal pressure	152
6.9.1	Initial characterisation	152
6.9.2	Time trace analysis	156
6.9.3	Power spectral analysis	161
6.10	DC ₁₅ PC phase transition	161
6.11	Discussion	162
7	Particle tracking	165
7.1	Particle tracking analysis	166
7.1.1	Background Correction	166
7.1.2	Coarse intensity tracking	167
7.1.3	X, Y axis fine particle tracking	167
7.2	Expected results	173
7.3	Controls	174
7.3.1	Polystyrene	174
7.4	Small unilamellar vesicle analysis	174
7.5	Discussion	180
8	Conclusion and outlook	181
	Bibliography	185

A	3D printed components	208
A.1	Tantalum wire holder	208
A.2	Wire clip	208
A.3	Imaging funnels	208
A.4	ITO mount	208
A.5	Modified DIB device design	208
B	Imaging supplementary	217
B.1	qDIC analysis software	217
B.2	Detailed iGOR optical set up	217
C	qDIC supplementary	220
C.1	Robust Fitting	220
D	Particle tracking software	223
D.1	Glycerol calculations	223

List of Figures

1.1	Lipid membranes and their components	3
2.1	Fluorophore spectra	15
2.2	Lipid handling	16
2.3	Pictures supporting the electroformation protocol	17
2.4	Filtration	19
2.5	Pictures of heated filtration setup	20
2.6	Sample slide for ready imaging	20
2.7	Pictures of the ITO mount	23
2.8	Spin coater and desiccator use	24
2.9	Slide heater	27
2.10	Open samples	28
2.11	Epifluorescence filter specifications	29
2.12	Simplified sketch of the iGOR setup	32
2.13	Linear approximation of bilayer reflectance	36
3.1	GUV development images	40
3.2	Volume of lipid applied to electrodes	41
3.3	The addition of pre-hydration	42
3.4	Wash steps prior to electroformation	43
3.5	Results of the sinusoidal and square waveforms	46
3.6	Effect of the square waveform	47
3.7	Differing responses of vesicles to high voltages	48
3.8	hs-GUVs combining on wire surface	48
3.9	Expulsion of hs-GUVs from wires using square waveform	50
3.10	Filtration results	53
3.11	Compatibility with DC ₁₅ PC	55
3.12	Diameter distribution of GVs	55
3.13	ITO electroformation development	58
3.14	Loss of lipid from ITO surface	59
3.15	Establishing a PVA layer	60
3.16	PVA sample heterogeneity	61
3.17	Establishing a lipid bilayer ontop of PVA	63
3.18	Partitioning of fluorophore into areas of differing curvature	64
3.19	Introducing pre-hydration to PVA swelling	65
3.20	Results of longer incubation time	66
3.21	PVA hs-GUV production	67
3.22	Washing method for PVA supported lipid bilayer	68
3.23	Droplet interface bilayer samples	70

3.24	DIC images of agarose Layer	71
3.25	DIB using a buffer supported monolayer	72
4.1	Example of qDIC analysis of a GV	77
4.2	Relationship between sucrose concentration and refractive index	78
4.3	Phase images as function of Wiener filter SNR κ	79
4.4	Refractive index analysis of POPC:POPE bilayers	81
4.5	Sucrose concentrations of measured vesicles	82
4.6	The dependency of lamellarity on sucrose concentration	83
4.7	3D overview of the illumination light cone and GV volume	87
4.8	Simulated GV phase profiles	88
4.9	Evaluating simulation accuracy	89
4.10	Integral determination from profiles	91
4.11	Effect of defocus on peak broadness	93
4.12	Integral Ratios	94
4.13	Defocussed GUV Phase Profiles	95
4.14	Dependencies of profile measurements on defocus	95
4.15	Example data pre-processing	96
4.16	Normalised profiles	97
4.17	Scaling the defocus response	98
4.18	Sample defocus	99
4.19	Radii dependency of integrals	100
4.20	Measured lamellarity and sucrose concentration	101
4.21	Birefringence effect on normalisation	102
4.22	Measured birefringence	103
4.23	Comparison of simulated and experimental NA variation	105
5.1	App6Aa1 protein structure	109
5.2	Partial phase diagram for POPC/POPE	111
5.3	Phase transition Fluorescent images	113
5.4	Deformation with high protein concentration	114
5.5	Fluorescence and DIC images of dye filled GVs	115
5.6	Schematic of hypothesised mechanism forming internal vesicles containing no fluorescence	117
5.7	Summary of Cry6Aa1 insertion experiments	118
5.8	5(6)-Carboxyfluorescein loss from GV after App6Aa1 addition	120
5.9	GV morphology from GV after App6Aa1 addition	121
5.10	Epifluorescence images of phase separation after App6Aa1	122
5.11	3D printed funnel used for GV imaging	123
6.1	Sketch of GV excitation	125
6.2	Simplified iGOR workflow	128
6.3	Amplitude and phase relating to membrane height and thickness	130
6.4	Fitting iGOR data	131
6.5	Reflectivity and phase measurements of a glass water interface	132
6.6	Effect of power correction correction on iGOR traces	133
6.7	Offset frame dependant on axial position	135
6.8	Efficacy of phase unwrapping	136
6.9	Temporal median amplitude average	137
6.10	Signal beam attenuation	139

6.11	iGOR refocusing data	141
6.12	Original POPC:POPE iGOR analysis	142
6.13	Vesicles imaged using iGOR	143
6.14	Unilamellar POPC:POPE vesicle as imaged in iGOR	144
6.15	Correlation of radius with thickness and height	145
6.16	Time trace analysis of unilamellar POPC:POPE surface fluctuations	147
6.17	Power spectral analysis of unilamellar POPC:POPE surface fluctuations	148
6.18	Bilamellar POPC:POPE vesicle as imaged in iGOR	149
6.19	Correlation of radius with thickness and height	150
6.20	Radius comparison between unilamellar and bilamellar vesicles	151
6.21	Time trace analysis of bilamellar POPC:POPE surface fluctuations	153
6.22	Power spectral analysis of bilamellar POPC:POPE surface fluctuations	154
6.23	Initial unilamellar POPC:POPE vesicle as imaged in iGOR	155
6.24	Comparison of the power spectra after fringe removal	155
6.25	Initial unilamellar POPC:POPE vesicle time traces	157
6.26	Unilamellar POPC:POPE ratio and thickness changes	158
6.27	Time traces after the loss of internal pressure	159
6.28	Comparison of radii fluctuations after loss of internal pressure	160
6.29	Power spectrums across the loss of internal pressure	161
6.30	Power spectra across a liquid disordered to gel phase transition	162
7.1	Coarse particle tracking	168
7.2	Steps used to improve particle tracking	169
7.3	Comparing α factors for particle tracking z correction	171
7.4	Effect of position in laser beam on scattering intensity	175
7.5	Properties of glycerol solutions	176
7.6	Mean square displacement analysis example	177
7.7	Measured hydrodynamic radii of controls	178
7.8	Measured hydrodynamic radii of SUVs	179
A.1	Tantalum wire holder print design	209
A.2	Wire clip print design	210
A.3	Funnel design 1	211
A.4	Funnel design 2	212
A.5	Funnel design 3	213
A.6	ITO base design	214
A.7	ITO screw design	215
A.8	ITO screw design	216
B.1	qDIC software	218
B.2	iGOR optical diagram	219
C.1	Robust fitting code 1	221
C.2	Robust fitting code 2	222
D.1	Glycerol viscosity code	224
D.2	Glycerol refractive index code	225

List of Tables

4.1	Summary of the membrane thickness literature values	81
4.2	Summary of the refractive index literature values	81

Abbreviations

AFM	Atomic force microscopy
ATP	Adenosine triphosphate
CARS	Coherent anti-Stokes Raman spectroscopy
CLWD	Close working distance
CMOS	Complementary Metal-Oxide-Semiconductor
DC₁₅PC	1,2-dipentadecyl-sn-glycero-3-phosphocholine
DHM	Digital holographic microscopy
DIB	Droplet interface bilayers
DIC	Differential interference contrast microscopy
DOPC	1,2-dioleoyl-sn-glycero-3-phosphocholine
DOPE	1,2-dioleoyl-sn-glycero-3-phosphoethanolamine
DPhPC	1,2-diphytanoyl-sn-glycero-3-phosphocholine
EDTA	Ethylenediaminetetraacetic acid
eH-CARS	Epi-detected heterodyne coherent anti-Stokes Raman spectroscopy
FCS	Fluorescence correlation spectroscopy
FRAP	Fluorescence recovery after photobleaching
FRET	Fluorescence resonance energy transfer
GFP	Green fluorescent protein
GPMV	Giant plasma membrane vesicle
GPU	Graphics Processing Unit
GUI	Graphical user interface
GUV	Giant unilamellar vesicle
GV	Giant vesicle
HEPES	4-(2-hydroxyethyl)-1-piperazineethanesulfonic acid

hs-GUV Half-sphere giant unilamellar vesicle

HTL Hydrothermal liquefaction

HWP Half-wave plate

iGOR Interferometric gated off-axis reflectometry

iSCAT Interferometric scattering microscopy

ITO Indium Tin Oxide

MSD Mean square displacement

NA Numerical aperture

NAD(P)H Nicotinamide adenine dinucleotide phosphate

OCT Optical coherence tomography

OPO Optical parametric oscillator

PC Phosphatidylcholine

PE Phosphatidylethanolamine

PLA Polylactic acid

POPC 1-palmitoyl-2-oleoyl-sn-glycero-3-phosphocholine

POPE 1-palmitoyl-2-oleoyl-sn-glycero-3-phosphoethanolamine

POPS 1-palmitoyl-2-oleoyl-sn-glycero-3-phospho-L-serine

PSF Point spread function

PTFE Polytetrafluoroethylene

PVA Polyvinyl alcohol

qDIC Quantitative differential interference contrast microscopy

QPI Quantitative phase imaging

SLB Supported lipid bilayer

SM Sphingomyelin

SMLM Single molecule localisation microscopy

STED Stimulated emission depletion

SUV Small unilamellar vesicle

TIRF Total internal reflection fluorescence

Chapter 1

Introduction and background

1.1 The importance of membranes and their dynamics

Membranes are key biological structures that form cells and their cellular components. Membranes are composed of phospholipids which are essential macromolecules for the function and organisation of cells. Owing to their amphipathic nature they spontaneously organise into bilayers where hydrophobic tails orient together to exclude water leaving hydrophilic head groups exposed. This is the most energetically favourable conformation and the basis for the existence of cells and transport vesicles.[1, 2, 3] Main functions of lipid membranes include segregation and control of transport allowing compartmentalisation of cells from both external and internal environments. Compartmentalisation provides protection for the cell from external toxins and helps to maintain its homeostasis.[4, 5] To fulfil this function membranes are highly complex and contain many components including proteins for which they can exist either embedded into the membrane with functions such as transport, receptors and enzymes, or peripheral to the membrane acting in signalling pathways, structural support and cell recognition.[6, 7] Membranes also contain steroids among various lipid compositions as sketched in Fig. 1.1a and b.[8, 9] These additional components control passage of any atoms or molecules that cannot otherwise cross such as positive ions (K^+ , Na^+ , Ca^{2+}).[6] Membranes are only permeable to hydrophobic molecules and small uncharged polar molecules, as the extracellular and cytosolic environment is polar the barrier needs to be non-polar.[1, 10] Communication with other cells is another key function of cells and therefore, as the outermost structure, the membrane must contain both excretion mechanisms and receptors.[11, 12] However, it's due to this complexity and fluid nature that has made them difficult to observe both *in vitro* and *in vivo*. This extends to membrane components as the hydrophobic environment is often challenging to maintain to stabilise membrane components.[13, 14]

1.1.1 Membrane structure

1.1.1.1 Phospholipid structure

Phospholipids are defined by a general structure of one or two fatty acid chains attached to a glycerol which is in turn attached to a phosphate group esterified onto an organic group, Fig. 1.1b. They can be grouped into either glycerophospholipids or sphingophospholipids depending on the nature of the alcohol backbone and the number of fatty acid chains, with sphingophospholipids containing one fatty acid

and glycerophospholipids containing two.[15, 16] The extensive variability observed in natural phospholipids is brought about by the wide-range of organic molecules that can be attached to the phosphate group and the nature of the fatty acid "tails". Tails introduce versatility as they can either be saturated, or unsaturated to varying degrees determining their shape by providing kinks in the chain and of varying length given by the numbers of carbon molecules.[17, 18] Alongside interactions with the surrounding medium, headgroups impact the stability of the membrane as a whole. Smaller headgroups such as ethanolamine give the phospholipid an overall conical shape as the diameter of the headgroup is smaller than that of the tails, this introduces a negative curvature on the leaflet and often destabilises it.[18, 19] In contrast, larger molecules such as inositol induce a positive curvature on the membrane, as shown in Fig. 1.1c.[20, 21] These contrasting inflections, as well as combinations of other headgroups, influence and facilitate varying membrane curvature leading to essential processes such as membrane budding and fusion.[20, 21, 22] Tails also impact membrane morphology via altering packing of phospholipids within the membrane with increased levels of unsaturation and chain length leading to looser packing and therefore increased fluidity.[17, 18] This is characteristic of the liquid disordered phase which contrasts the gel phase tendency of sphingolipids due to their saturated chains.[23, 24] The importance of lipids is underpinned by the devotion of some 5% of genes to the synthesis of lipids.[22] The major structural lipids found in eukaryotic cells are glycerophospholipids, phosphatidylcholine, phosphatidylethanolamine, phosphatidylserine, phosphatidylinositol and phosphatidic acid, with phosphatidylcholine accounting for more than half of most eukaryotic membranes. This is most likely due to its near cylindrical shape and therefore stability.[20, 21]

1.1.1.2 Other membrane components

The complexity of the membrane is further compounded by the other components found. Many of these span the membrane or are intercalated within the phospholipid tails, whilst others are anchored to the surfaces.[13, 25, 26] These components modulate membrane function via interaction with the surrounding environment and by directly affecting membrane fluidity.[27] Components anchored onto the cell surface are often involved in signalling.[11] Lipid interactions within the bilayer aid membrane protein insertion and the modulation of their activities.[20, 21] Sterols are a class of non-polar lipids that intercalate into the membrane and confer the correct fluidity as they interdigitate within the tails and ensure the correct packing of the phospholipids.[9] In eukaryotes cholesterol is the most predominant sterol with ergosterol most common in prokaryotes. These sterols preferentially mix with sphingolipids as the headgroup shields the non-polar sterol, known as the umbrella model.[28, 29, 30, 30] A major component of membranes are proteins which hold many functionalities including transport, signalling and synthesis of macromolecules associated with the membrane.[14, 31, 32] Proteins make up about half of the dry mass of the membrane and as their activities can modulate the function of the membrane, they are an essential area of research, further compounded by their pharmaceutical relevance as 60% of pharmaceuticals target membrane proteins.[22, 33, 34] The orientation of proteins within the membrane mainly depends on their primary structure, as proteins with a polar surface are more likely to be peripheral whereas a non-polar surface promotes insertion into the membrane.[31, 35, 36, 37] However due to the reciprocal effect of the membrane and protein behaviour they are notoriously difficult to observe due to the usual requirement of extraction from their

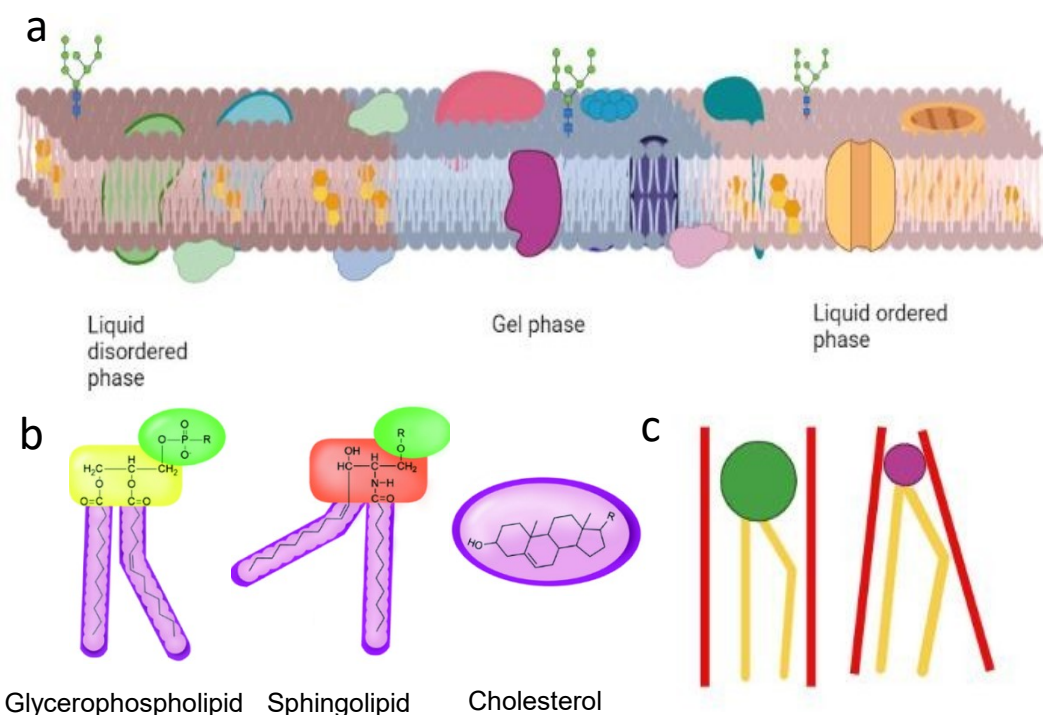


Figure 1.1: Lipid membranes and their components a) Schematic representing a lipid membrane in gel phase (magenta), Liquid-ordered(blue) and Liquid disordered(lilac). Key elements shown are cholesterol in the liquid disordered and ordered phases, and the variability of the components contained within. The regions at the intersection of the phases are known as phase boundaries where some proteins preferentially localise. b) Structure of a glycerophospholipid, sphingolipid and cholesterol to represent the variety of shapes these components confer in the membrane. Image adapted from Hilton *et. al.*[39]. c) Schematic demonstrating the effect of the differentially sized organic headgroups. The smaller headgroup generates a negative curvature whilst the green larger headgroup confers a cylindrical shape.

natural environment.[4, 14] An exception to this are nanodiscs where the immediate lipid environment is also removed and maintained during study.[38] This underlies the importance of being able to directly observe proteins in a lipid environment.

1.1.2 Observable membrane dynamics

1.1.2.1 Phase separation and spatial membrane organisation

Lipid bilayers can exist in multiple phase states; either a liquid disordered, ordered or a gel phase. These phases are determined by the van der Waals forces acting between the lipid tails, looser packing of the tails reduces the van der Waals forces and the lipids can move across the surface of the bilayer easily leading to a more disordered physiology.[40, 41] The liquid ordered and gel phase differ due to the presence of sterols in the liquid ordered phase. The presence of sterols confers an ordered physiology whilst maintaining lateral movement of components. Membranes in the gel phase are more ordered with restricted lateral movement leading to tight packing of the molecules; often unsaturated tails that would otherwise prevent tight packing go through trans isomerisation to lengthen the tails and al-

low tighter packing.[1, 42, 43, 44] Phase separation plays a vital role in biomolecular assemblies such as stress granules, nucleoli and signalling clusters, as well as membranes.[45, 46, 47] However, a main effect of phase separation is the regulation of protein phase behaviour by providing scaffolding platforms and influencing the curvature, fluidity and lateral organisation of the membrane.[31] Proteins can nucleate or partition into phase-separated domains in membranes, they can also drive lipid demixing especially via curvature-sensitive domains or clustering of lipid-binding motifs.[48, 49, 50, 51, 52, 53, 54] These processes act in a feedback loop where the lipids modulate the availability, curvature preference and anchoring of proteins and proteins alter lipid order, raft formation and lipid phase behaviour to control trafficking and signalling[26, 31]. An essential part of this is fusion events which mix lipid and protein compositions, and endocytosis which often involves localised phase separation of adaptor proteins and lipids acting as nucleation sites.[55, 56, 57] These processes are driven by the dynamics within the membrane largely domain reshaping. Lipid flip-flop and asymmetry also has an influence via modulation of membrane tension and leaflet coupling, this lipid redistribution alters phase behaviour alongside the cytoskeleton and the extracellular matrix.[58, 59, 60] The actin cortex and microtubule network can also confine, stabilise and dissolve condensates and organise receptor clustering which may underlie processes essential in signalling. Also exerting a similar effect is the extracellular matrix which also drives clustering or exclude proteins promoting compartmentalisation.[61, 62, 63] These effects combined provide dynamic control of the membrane providing functions to organise processes essential for cell signalling and organisation components across the surface. The tendency of certain membrane compositions to exist in either a gel or fluid phase can lead to phase separation and the subsequent emergence of lipid rafts. The raft model was originally proposed to explain sorting of components across the plasma membrane, as the differing properties of these regions aids in diversifying membrane functionality.[64, 65, 66] As well as affecting the function of membrane components, protein function may modulate the phase behaviour of lipid regions.[22] Different compositions of lipids produce complex phase behaviour with the addition of lipid species the phase transition temperature changes and the range over which they transition increases.[67] Phases can either be miscible and co-exist or they can separate into their respective phases, termed phase separation.[68] The phase transition of a bilayer can be controlled by a variety of condition changes including: a change in the temperature across the phase transition temperature, lipid-lipid or lipid-protein interactions, a phase transition in the opposite leaflet or binding of proteins or ions.[69, 70] Membrane phases are in a quasi-equilibrium that describes different areas of the membranes, the interfaces between these domains are known as the phase boundaries; sites where the properties change sharply.[22] Membranes can use these abrupt changes to arrange components on the cell surface by co-localising or separating them across the boundary. Reciprocally this phase behaviour can be affected by small changes in membrane make-up such as ion or molecule binding.[71] Proteins are particularly phase sensitive with any containing an alpha helical transmembrane domain showing preference to the liquid phase whereas hydrophobic matching drives a solid phase preference.[72, 73] When ordered and disordered regions are present most proteins partition into the disordered phase, Glycosylphosphatidylinositol anchoring proteins tend to generate an exception alongside Cavedin-1 scaffolding.[74] Whilst many proteins show preference for certain phases, they do not seem to show much preference to lipid compositions.[75] Membrane proteins generate local envi-

ronments from the surrounding lipids to support their function such as nucleation membrane rafts.[76] As well as the partitioning of proteins, cholesterol rich regions recruit cholesterol binding domains.[74] Anderson and Koeppe termed lipid rafts as an overall energy of interactions between the components generating small heterogeneity across the membrane.[77] These heterogeneities drive many membrane structures and dynamics which need to be studied further.

1.1.2.2 Lipid raft dynamics

Probing lipid dynamics includes investigation into the propagation and accumulation of molecular stress and it's role in influencing membrane bound mechanosensitive macromolecules.[78] These can be modulated through lipid-lipid interactions, as, in a membrane the phospholipids are packed closely enough that a displacement of one triggers oscillations that alter the dynamics of neighbouring domains.[79] It is currently thought that rafts form at random locations across the membrane consisting of increased stress whenever compression or shear waves travel over them.[80, 81, 82] Dynamics of membrane waves occur across a wide range of timescales and distances.[83] They can often be categorised as either thermal deformations or ATP-driven processes. These deformations often resemble waveform dynamics with wavelengths ranging from nm to μm scales, with larger scale fluctuations indicated to be at the cell edges and the basal membrane.[84, 85] All membranes basal or otherwise, also experience smaller thermal fluctuations which can be experienced down to a picosecond time scale and respond by solid like dynamics.[79, 86, 87, 88] Whilst fast paced fluctuations arise from small nanodomains and invaginations, slower moving waves (10s) are also experienced. These forces are found to be dampened after propagating over small distances which implies that the stress is well contained within rafts.[80, 82] The forces on the rafts demonstrate an elastic regime as induced stress dissipates and rafts lose their elasticity. This causes them to go through an elastic-to-viscous crossover leading to raft deconstruction.[89, 90] Rafts are formed via the accumulation of lipids carrying reduced stress after self-diffusing. Once they become trapped by van der Waals forces new rafts can form spontaneously.[91] This propagation, dissipation and reformation of rafts causes the stress to propagate in pulses resembling waves. The interfaces between the rafts are separated by densely packed lipids containing stress due to the non-linear coupling of longitudinal and transverse modes.[92] This propagation and its subsequent effect on the density of the membrane aids defining the rate of biological processes.[93, 94] The combination of compression and shear waves generate a membrane surface consisting of multiple optical vibrational modes. These create landing platforms which allow the passage and binding of small molecules, however, these can be broken down by the inclusion of hydrophobic molecules as they breakdown of out-of-phase membrane displacement patterns.[92] Whilst larger and slower waveform fluctuations are more widely understood we aim to target the less well studied small rapid fluctuations using our novel imaging technique.

1.2 Membrane observation

Conventional techniques for the study of lipid membranes consist of both direct observations of natural and model membranes and computer-based modelling. Early observations included the Langmuir trough, used to measure the surface area of a

known volume of phospholipids and electron microscopy images of a bilayer which together confirmed the presence of a bilayer.[95, 96] Computer based modelling techniques have made predictions over bilayer organisation, physical interactions in both simple and complex systems. Other studies have used spectroscopic measurements of hydrated bilayers to identify interactions such as those between phospholipids and cholesterol.[97, 98, 99]

1.2.1 Fluorescence

A large body of the work driving our understanding of lipid bilayers utilises fluorescence measurements. Direct observations of membranes have been carried out using fluorescence under different conditions to characterise various compositions and their behaviour. Some experiments use the auto fluorescence of cells these often have a low signal to noise level meaning that it is hard to distinguish the sample signal from the background. In a cellular environment, metabolic indicators such as Flavins and NAD(P)H emit in the green and blue range, respectively, while structural proteins collagen and elastin are excited in the 300-400 nm (UV - Violet) region.[100, 101] Other diagnostic structures such as lipopigments specifically lipofuscin are cited in ageing research and emit in the green to red region and porphyrins, which can accumulate in tissues during the disease progression of porphyrias. These can be measured in the red range and are therefore suitable for diagnostic imaging.[102, 103, 104, 105, 106] Whilst this provides a basis for imaging non modified systems there are methods, including those discussed in this thesis, that provide a better signal to noise than autofluorescence.[107] Some membrane proteins have intrinsic fluorescence from tryptophan residues however this is often too weak and difficult to distinguish from the background.[108, 109] Due to the hydrophobic nature of tryptophan it is likely to be found at the interface between tails and head groups and therefore suppressed. [110]

The majority of fluorescence work uses fluorescent probes known as fluorophores. Fluorophores can be used to both give a overall measurement of the movement of molecules alongside the measurement of the behaviour of individual labelled components.[111] In reality, measurements are generally made of populations of fluorophores to provide an insight into the behaviour of a single component. Techniques such as FRAP (fluorescence recovery after photobleaching) where the migration of lipids back into a photobleached area is measured, provides a measurement of lipid fluidity, and lateral diffusive rates of lipids under different conditions and of different membrane domains.[112, 113, 114] Measurements of the same characteristics can be carried out using fluorescence correlation spectroscopy (FCS) where diffusion and molecular interactions are measured as the fluorescence intensity is measured in a small observation volume.[115, 116] As discussed in Chapter 5 we can measure the movement of a water soluble dye across a membrane to identify membrane permeability and in our case the identification of pore formation. Other indicators such as calcium reporters can be used to measure membrane permeability as the fluorophores on one side of the membrane will only emit in the presence of calcium after passing through the membrane.[117, 118, 119] A similar proximity based fluorescence is utilised in FRET (fluorescence resonance energy transfer) where there are donor and acceptor fluorophores from which the energy is transferred inducing emission when they are in close proximity ($\approx 1 - 10$ nm) which allows measurements of lipid packing as well as the spatial distribution of other labelled components.[120] These high precision experiments can also be undertaken using single particle tracking

tracking the movement of lipid or protein molecules across a membrane.[121]

Fluorescence techniques tend to be limited by the diffraction limit of light, 200-250 nm laterally and 500-700 nm axially.[122] Single-Molecule Localisation Microscopy (SMLM) can achieve resolution down to 10-20 nm laterally and 50-60 nm axially by fitting the signal to identify the centre of the diffraction limited spot.[123] STED (Stimulated Emission Depletion Microscopy) improves resolution to 20-50 nm laterally by selectively depleting the fluorescence surrounding the focal point which reduces the effective excitation area hence improving resolution.[124] An alternative method for improving resolution is expansion microscopy where the specimen is labelled and embedded in a hydrogel. Enzymes are then used to partially digest the sample leaving the labelled components allowing them to be imaged at a greater resolution using a standard fluorescence microscope once the hydrogel has swelled, resolution of approximately 60 nm has been achieved.[125]

Fluorophores can pose difficulties as they are prone to photoblinking, photobleaching over time as well as causing phototoxicity in the system. The exact loci of the component of interest can also be ambiguous as the point spread function can be large leaving a large area for which the fluorophore could be, the attached fluorophores could appear at a slightly different location than the component of interest due to the linking mechanism and molecule size.[126, 127, 128] They also often require modification when they are applied to a system, this is not only laborious but can introduce artefacts. For these reasons the generation of label-free techniques are at the forefront.

1.2.2 Label free observation techniques

Recently interferometric scattering microscopy (iSCAT) has been used to detect reflected light from an interface underneath the sample to generate interference. A coherent light source is used to illuminate the sample from which the scattered light is collected with the reflection from the surface below the particle acting as a reference. When this light interferes with the sample reflection the signal is amplified and can be captured generating a high resolution measurement of the particle, specifically temporally as several thousand frames can be acquired per second (5 μ s).[129] Currently iSCAT is used to track molecules, these include molecular motors such as kinesin and dynein responsible for cellular cargo transport and how they move along microtubules and how proteins can assemble and aggregated which could be useful in the study of amyloid fibrils.[130, 131] The particle tracking can be applied to understand the size of extracellular vesicles which have been indicated in both intercellular communication and disease diagnostics and therefore have an application within biomarker analysis and has been applied to vesicles within a cell.[132, 133] The main potential of this technique and the previously discussed application is encompassed in nanoparticle tracking, with particle size and binding events with ligands on the surface able to be quantified.[134] Whilst this has proved instrumental in single particle tracking it has been limited to an axial tracking range of a few hundred nanometers with a recent advancement extending this to 4 μ m for small particles of 10 nm in diameter and over 30 μ m for larger particles of 80 nm diameter.[135] However for long range particle tracking this provides a limitation, which through the use of an external reference beam we mitigate when measuring with iGOR. This experimentation was also expanded into looking at how proteins and ligands move across a supported lipid bilayer and how they interact and how the membrane responds in terms of lipid packing and lateral movement. This also

provides a limitation as dynamics across the bilayers thickness cannot be measured and any static forces acting between the bilayer and the glass surface could be impacting the natural diffusive movements of the lipids.[136] The requirement of large supported bilayers and a glass water interface for this technique provides a limitation for observing dynamics as many of the membrane dynamics would be dampened by the surface.[136] As discussed in latter chapters 6 and 7 we can mitigate some of these limitations.

Other label free observation of lipid bilayers include chemical specific imaging such as Raman Spectroscopy. Raman spectroscopy measures the vibrational modes of chemical bonds after interaction with light.[137] Coherent Anti-Stokes Raman Spectroscopy (CARS) also probes these vibrations using coherent light as chemical bonds respond differently to light they can be classified into groups: Lipids, DNA, RNA, Proteins, Phosphates, Lipid-Proteins.[138, 139, 140] epi-detected heterodyne CARS (eH-CARS) is a further technique that can be used for nanoparticles and lipid bilayers using chemically specific image contrast. This has been shown to give topological information of a supported lipid bilayer to nanoscale resolution, however, it is a point scanning technique and therefore is limiting when measuring dynamics.[141] Currently work is being undertaken to reveal the behaviour of lipid rafts using an enhanced Raman spectroscopy; local field enhanced eH-CARS. This utilises the enhancing effect of gold nanoparticles to amplify the signal from the bilayer (unpublished). Plasmon-waveguide resonance has also been used to quantify the lateral segregation of lipids and proteins into microdomains using optically anisotropic systems to probe the refractive indices as well as long range molecular order.[142] Mass photometry is a recently published technique using iSCAT that allows label free tracking and mass determination of proteins present on supported lipid bilayers. They cite a mass resolution of sub-50 kDa which when paired with the tracking ability allows mass specific diffusion coefficients to be identified. With a temporal resolution of 3 ms these diffusion constants as well as association/dissociation events can be accurately quantified in terms of protein behaviour.[143] As these measurements are undertaken on a supported bilayer they dynamics of the lipid bilayer itself in response to these events remain un-probed. Atomic force microscopy (AFM) can be used to gain topological information from an immobilised lipid bilayer with additional components, this has been used on portions of bacterial membranes to analyse organisation of integrated components. AFM utilises a sharp probe that traces across the surface of the sample measuring any height changes present. AFM is an example of a contact based techniques are also used to observe membranes however these are often invasive and not compatible with suspended model membranes.[144]

1.2.3 Quantitative phase imaging

Quantitative Phase Imaging (QPI) is a group of techniques quantifying the phase shift of light due to interaction with a sample, namely biological samples. Often the phase shift is proportional to the dry mass content where the specific refractive increment quantifies this relationship. As previously mentioned qDIC utilises this to allow observation of organic samples.[145] A more simplified version is Phase Contrast Microscopy where the resulting amplitude changes equates to the phase shift caused by the refractive index distribution across the sample. Generally speaking QPI techniques can be organised into four primary approaches; interferometry, wavefront sensing, phase retrieval and digital holography.[145, 146, 147] Interferometry

measures the phase shift based in the interference between a sample and reference beam to produce an interferogram where the dry mass is the product of the total projected area and the average optical thickness, scaled with the specific refractive increment.[148] Digital Holography expands the analysis of an interferogram using diffraction to reconstruct the complex wavefront. This includes the intensity modulation of light as well as the phase shift, holography also changes the illumination direction.[149] Wavefront sensing doesn't use a reference to recover phase shift, instead the movement of an array of focussed light spots caused by aberrations allow phase shift to be recovered. Phase retrieval algorithms use images taken using differing conditions and computationally reconstruct phase shift. Both iterative and deterministic approaches can be utilised to solve for phase images.[146]

QPIs have been used in a wide range of biological studies including growth rate assays, neutron behaviour, drug screening and the determination of biophysical cell properties.[146, 150] Quantitative phase imaging has also been used when looking at cell growth to investigate how single cells regulate their volume during cell cycle phases.[151] These volume changes can also be tracked to understand how homeostasis is maintained and how the morphology of red blood cells change in disease conditions such as sickle cell disease and malaria.[152] This same theory can be applied when discussing the plasticity of neurons to look at the morphological changes in dendritic spines and axons in response to stimuli.[151] Cancer cell metastasis involves not only the movement of cells but cellular deformation which was assessed using QPI. Alongside understanding how these changes occur during disease progression it also a useful tool in drug discovery pathways as they also aim to monitor cell morphology and dynamics in response to drug treatments.[146, 153] In this way QPI is a useful tool in providing label-free insights into cellular structures and therefore our model membranes especially as it is a well-established tool in our lab with home written software streamlining analysis. For our uses, whilst it provides a high resolution for the measurement of membrane properties it requires multiple image acquisitions for the same region of interest and therefore is not suitable for understanding the dynamics of a membrane on a very short time scale.

1.2.3.1 Quantitative differential interference microscopy

Quantitative differential interference microscopy (qDIC) is a technique based on the changes in phase and in turn, optical thickness found in the sample and so due to the gradual change in phase at the top of the vesicle it would not be able to measure height fluctuations.[107, 154, 154, 155] qDIC in particular is further discussed in this thesis where it has been used to determine the optical properties of vesicles, namely the refractive index, lamellarity and internal solution. For our uses, whilst it provides a high resolution for the measurement of membrane properties it requires multiple image acquisitions for the same region of interest and therefore is not suitable for understanding the dynamics of a membrane on a very short time scale, however we have used it to gain a better characterisation.

1.2.3.2 Holographic imaging techniques

Digital holographic imaging relies on the production of interference patterns using a coherent laser source. This interference of a reference beam and a beam scattered by the sample encodes both amplitude and phase information of the light reflected by the sample.[149] This recorded interference pattern is termed the hologram and

allows the reconstruction of wavefront in 3D as we can simulate how the image would appear if it were observed at different depths or planes assuming free propagation. For samples which are not strongly scattering, this can be undertaken via either numerical propagation or phase recovery algorithms.[156] Numerical propagation is typically done using Fourier transformations. In Fourier optics the wavefront can be described using a sum of sinusoidal components with different spatial frequencies and a Fourier transform can be used to calculate how these components would evolve at different distances, effectively simulating how the wavefront behaves at different focal planes. After propagating the wavefront to the desired plane an inverse Fourier transform reconstructs the real space.[145, 149]

When employing these techniques for biological imaging the main areas are digital holographic microscopy (DHM) is where a digital sensor captures a hologram directly of transparent samples, optical coherence tomography (OCT) which uses low-coherence light to capture micrometer resolution images of biological tissues and Holographic Flow Cytometry which combines flow cytometry with holography to capture 3D images of cells in suspension.[149, 157, 158, 159] Overall holographic imaging provides non-invasive methods to obtain high spatial resolution 3D images of biological samples however it does often require complex set ups with minimal environmental vibrations and noise alongside powerful data processing computational power.[160]

1.2.3.3 Phase unwrapping

The phase of a wave is the description of a position in a repeating cycle of peaks and troughs. As the pattern repeats so does the phase within a range of -2π and 2π . Due to its periodic nature of the the phase of a field is only defined up to an integer multiple of 2π . In reality as the height of the membrane is not limited to this range with its true value being the number of cycles plus the phase of the current cycle. The measured phase is referred to as wrapped as is limited to the 2π range, the process of determining the true phase is referred to as unwrapping and described below.[161]

To achieve a continuous phase evolution across space and time, which is relevant when interpreting the phase as a surface height, integer multiples of 2π can be added, to avoid phase jumps above π . However, this is difficult in two-dimensional fields as the condition has to be met in two dimensions generating conflicting local conditions, requiring a non-local solution. Furthermore, phase singularities at points of zero amplitude occur, also called vortices, which can have a phase change of multiples of 2π when circulating around the point, this integer multiple is known as angular momentum or topological charge of the vortex.

There are many approaches that can be taken to phase unwrapping that include path following algorithms, branch cut algorithms, least squares and optimisation approaches, Fourier Transform and graph cut and energy minimisation methods.[161, 162, 163, 164, 165, 166, 167] Generally speaking the factors that will impact the efficacy of phase unwrapping are the noise in the data which can generate false discontinuities but can be minimised by high-quality data acquisition and noise filtering prior to phase unwrapping, the size of discontinuities in relation to the rate of change and phase impacts the complexity of the algorithm required. The more complex the algorithm required requires an increased processing power.[161]

1.2.4 Interferometric gated off-axis reflectometry

Interferometric gated off-axis reflectometry (iGOR) is a novel imaging technique developed by Wolfgang Langbein, Paola Borri, Tual Monfort and David Regan, as a sensitive label-free live imaging technique capable of single molecule sensitivity due to sub-nm resolution. As a form of digital holographic microscopy, it produces a hologram containing 3D information produced from the interference pattern. The interference pattern is produced from a complex reflected field containing reflections from a signal field and a separate reference beam. iGOR allows single particle observation and tracking, alongside measurement of thickness with angstrom resolution. The off-axis nature of this technique enables the amplitude and phase to be separated in the Fourier domain leading to the separation of the axial positions from the membrane thickness. This retrieval of the scattered field allows additional topography information with sub-nanometer sensitivity. The contrast is formed by the interference of the light field scattered by an object and the reference field. The complex field is measured in both the co- and cross- polarised channel. The incident light on the sample is co-polarised, the majority of the light is reflected with an unaltered polarisation and therefore the co-polarised channel. In contrast, the signal present in the cross-polarised state shows any in plane birefringence present.[168] iGOR is discussed further in Chapter 6 and Chapter 7.

Interferometric Gated Off-axis Reflectometry is being developed in our group. My role in the development was during the final stages and centred around producing pipelines for imaging and analysing lipid systems. This included final hardware changes as well as protocols to image suspended membranes and small unilamellar vesicles (SUVs). In terms of analysis I wrote analysis code to correct data and extract relevant parameters. I also collaborated in software design for more sophisticated analysis coded by David Regan.

iGOR collects the light scattered in the epi-direction by a sample. This light collected is combined with a reference beam with a matched path length. From measured interference the light field in amplitude and phase to be measured. For a flat bilayer sample the amplitude and phase of the reflected field in focus with the bilayer correspond to the thickness and height, respectively. Light can either be unpolarised or polarised, unpolarised light has no fixed orientation and oscillates randomly in all directions perpendicular to the propagation direction. Polarised light is light with a defined direction of oscillation, meaning it oscillates either parallel to the plane of incidence (p) or perpendicular to it (s). P and S are also known as co- and cross-, respectively. The light incident on the sample is p polarised, however we measure in both s and p polarisation. Once reflected from the sample the co- and cross- polarised light components have orthogonal linear polarisation. These are subsequently separated by a Wollaston prism before hitting the Basler camera. Separating these helps to resolve sample anisotropy which can arise from in-planar bilayer birefringence. Our set up can measure in a widefield configuration at 327 Hz.

1.3 Model membranes

Owing to the complexity of membranes, it is hard to generate suitable model membranes.[169, 170] Simple model membranes such as vesicles or supported lipid bilayers are typically made up to a ternary lipid composition however, they run the risk of demonstrating oversimplified dynamics and behaviour. More complex model

membranes such as GPMVs (Giant plasma membrane vesicles) are an extracted portion of natural membranes and fall between the classification of synthetic model membranes and living cell membranes.[171] Other model membranes include networks of vesicles connected by lipid microtubules, ruptured bilayers supported on solids from both synthetic and native membranes and membrane nanodiscs containing membrane proteins.[170, 172] Membranes can also be supported on surfaces using tethers such as DNA and lipid tubules, however the level of support the bilayers receive from either a surface or tether can alter the dynamics.[173, 174, 175] Nanodiscs are small regions of membrane surrounded by an alpha helical scaffold however, these fail to generate an internal volume and are therefore only suitable for lipid binding and not transmembrane transport.[38, 171]

An emerging field of research is bottom up biology where researchers aim to take fundamental components to combine and generate functional cells.[176, 177] These often start with vesicles of varying specifications and incorporation proteins such as Min protein systems and actomyosin rings to generate oscillations and contractions reminiscent of cellular functions.[178] The gradual addition of complexity to these models allows each layer to be analysed and understood from a biophysical perspective. Measurement of membrane linked behaviour can be undertaken on a single bilayer level using models such as vesicles and supported lipid bilayers or on a population basis using models such as liposomes or micelles.[112, 179, 180] These measurements would rely on a secondary indicator of membrane behaviour such as fluorophores or ion flow.

For use in iGOR setup free floating lipid bilayers are required as the observation region needs to be at least 30 μm from the surface to avoid interference from other interfaces affecting the signal from the lipid region of interest. The same concept applies to the vesicles and therefore to prevent the lower surface from interfering vesicles need to have a diameter of 30 μm or greater and not containing any internal structures or any structures attached to the vesicular surface. The vesicles are also required to be of this size so that the top surface appears near flat for observation. To observe the dynamics of a lipid bilayer we need a single suspended bilayer. It is for this reason we have developed a protocol for producing giant unilamellar vesicles and more supported half-sphere giant unilamellar vesicles (hs-GUVs) and droplet interface bilayers as simple model membranes to quantify their dynamics. These requirements for iGOR should not limit our ability to observe biologically relevant phenomena as it is a freely fluctuating bilayer with no limit on lipid compositions providing stable bilayers can be generated. This allows the observation of lipid bilayer fluctuations and potential lipid rafts. The main foreseen limitation is once additional components are added into the system the interferogram becomes more challenging to deconvolute due to the additional scattering objects, however by slowly increasing the complexity we can mitigate this. Whilst our temporal resolution is improved due to its widefield conformation we may not be able to measure phenomena that occurs faster than 3 ms such as ion channel opening, molecule diffusion across membranes, some lipid raft formation and dissolution.

1.4 Thesis outline

The methods used in this work alongside a description of microscopy techniques including relevant mathematics and optical set up and processing can be found in Chapter 2.

Chapter 3 details the optimisation of preparation protocols for the production of GUVs. We also discuss alternative bilayer models and their preparation. Initial fluorescence measurement are also discussed in this chapter.

Characterisation of these models using qDIC are described in Chapter 4. In this chapter the subsequent simulations and their incorporation into the analysis are also included.

Chapter 5 describes the preliminary experiments to confirm App6Aa1 protein insertion into our membrane models.

The use of iGOR for the measurement of membrane dynamics of GVs are detailed alongside the final optimisation of the method in Chapter 6.

An alternative use of iGOR for the tracking of organic nanoparticles in a 3D volume is demonstrated in Chapter 7.

1.5 Project aims

- Optimise GUV electroformation to produce stable, artifact-free vesicles suitable for iGOR analysis.
- Characterise membrane properties using epifluorescence and qDIC microscopy, with comparison to simulations.
- Use iGOR to quantify membrane dynamics in response to environmental changes and transmembrane protein insertion.
- Investigate lipid phase behaviour by altering membrane composition and analysing birefringence to infer phospholipid organization.
- Develop time-resolved iGOR measurements to monitor phase and amplitude shifts during transitions such as gel-phase formation or pressure loss.
- Assess membrane deformation following protein insertion and generate deformation maps based on steady-state membrane responses.
- Establish a validation protocol for protein insertion using internal fluorophore loss as a marker.

Chapter 2

Materials and methods

2.1 Lipid solutions

2.1.1 Lipid handling and storage

The lipids used were 1,2-dipentadecanoyl-sn-glycero-3-phosphocholine (DC₁₅PC), 1-palmitoyl-2-oleoyl-sn-glycero-3-phosphocholine (POPC) and 1-palmitoyl-2-oleoyl-sn-glycero-3-phosphoethanolamine (POPE). All lipids were purchased from AVANTI Polar Lipids (Alabaster, US), as 10 mg/mL solutions in chloroform, 25 mg was purchased at a time and delivered on dry ice. These lipids were kept in chloroform and a sealed nitrogen environment to prevent peroxidation. To maintain this, the stock solution was opened only in a nitrogen cabinet and stored in glass vials sealed with parafilm. Polytetrafluoroethylene (PTFE) cap linings were used to prevent the chloroform from degrading the plastic and contaminating the solution. The lipids were then stored at -20 °C and considered stable for approximately a year, in line with manufacturers guidance.

The fluorophore-labelled lipid used for fluorescence imaging was ATTO488-DOPE or ATTO425-DOPE having absorption and emission spectra shown in Fig. 2.1. They were purchased in powder form and were dissolved in chloroform at 1 mg/mL. Lipids were kept in a sealed nitrogen environment at -20 °C with an aluminium foil wrapping around the glass vial to prevent progressive photobleaching of the fluorophore. As the lipids were dissolved in chloroform, handling the solutions cannot be done with standard plastic syringes or pipettes as they would be degraded, and was instead carried out using glass syringes (700 series, Hamilton, US). The handling was done in a fume hood to remove chloroform gases. Any lipids containing a fluorophore were kept in a dark environment, typically by using aluminium foil wrapping, to avoid photobleaching.

2.1.2 Preparation of lipid solutions

A 4 mL glass vial was cleaned by 10 successive chloroform rinses. In a nitrogen cabinet the required volumes of each stock solution were added to the vial using the glass syringe, depicted in Fig. 2.2a. The volumes were defined by the mass required to produce the desired composition defined by a molar ratio. The resulting solution was dried to generate a thin film of lipid on the inner wall by placing the vial under a nitrogen flow directly from the tube placed just above the vial neck with sufficient flow that the solution surface is disturbed without forcing it up the wall. This was carried out on a hot plate set to 60 °C for 30 min, then stored under

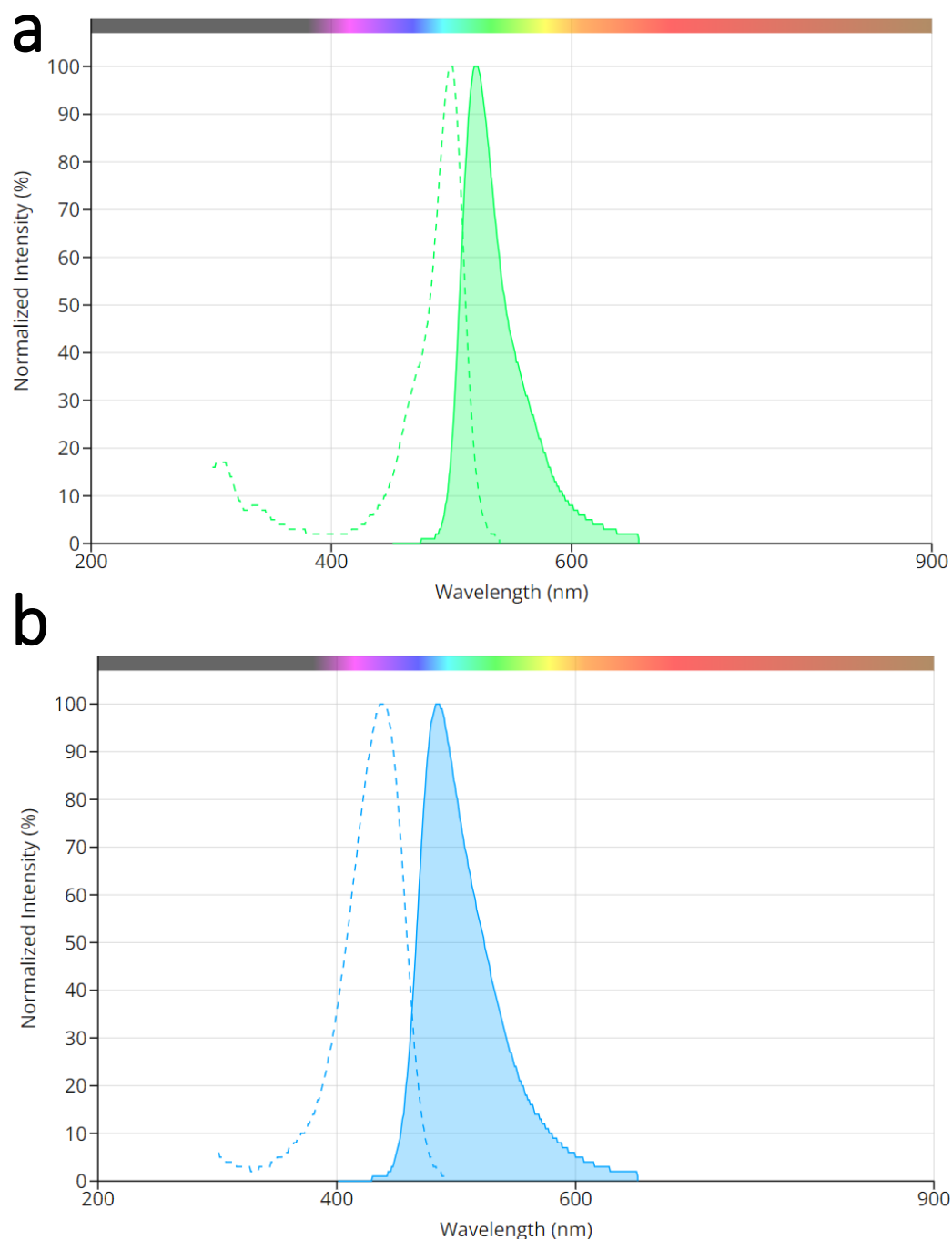


Figure 2.1: Fluorophore spectra Fluorescence excitation (dashed) and emission (solid) spectra for the ATTO488 (a) and ATTO425(b) fluorophores, respectively.[181, 182] ATTO488 shows an excitation maximum at a wavelength of 499 nm and an emission maximum at 520 nm, while for ATTO425 these wavelengths are 438 nm and 484 nm.

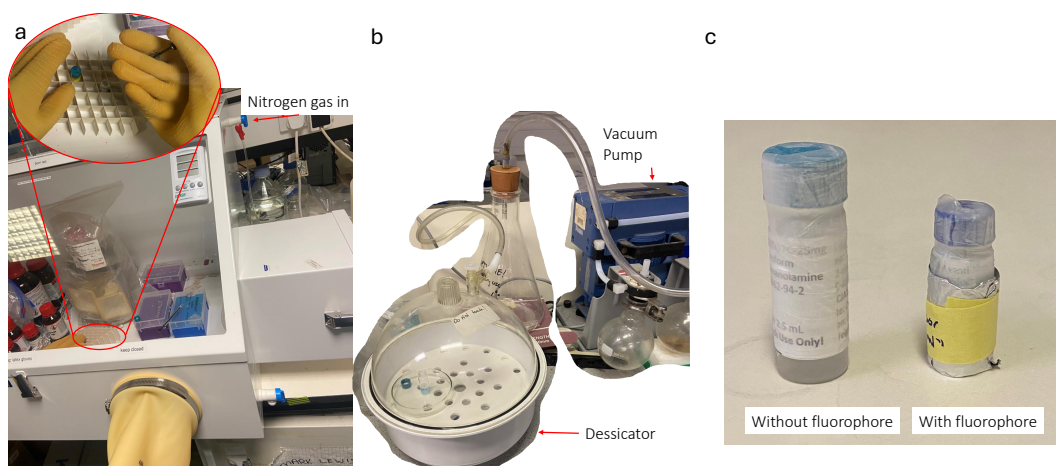


Figure 2.2: Lipid handling Pictures of steps in the preparation of lipid solutions. **a)** Nitrogen glovebox used and handling of solutions. **b)** Vacuum pump (Vacuubrand MZ 2C vacuum pump) to a minimum pressure of 7 mbar and desiccator used to store vial under vacuum. **c)** Storage conditions of lipid stock solutions both with and without fluorophore.

vacuum for an hour to remove the chloroform as depicted in Fig. 2.8. The resulting lipid film was then dissolved in a new solvent by adding this solvent into the vial under nitrogen and vortexed for 30 seconds using a Jencons VX-100 vortex mixer (VWR, USA) at an approximate rpm of 2000 with the vial closed. The solvent was chosen dependent on the phase of the lipid mixture at room temperature; for those in a gel phase isopropanol was chosen, for those in a liquid disordered phase a mixture of chloroform and acetonitrile (95:5 V/V) was used as determined by Regan.[155] The vial was then stored in a -20°C freezer sealed with parafilm and foil, as shown in Fig. 2.2c. Samples are stable for approximately a year. Fluorescently labelled lipids were added, at a 0.1% lipid molarity to allow observation of lipid structures under epifluorescence. This percentage provided sufficient fluorescence while not significantly changing the phase behaviour of the bilayers.[155]

2.2 Lipid bilayer sample formation

2.2.1 Giant unilamellar vesicles (GUVs)

The protocol for the formation of GUVs was developed within this thesis. More details on the development are given in Chapter 3.1. Here we describe the final protocol used for most of the results shown in this thesis.

2.2.1.1 Coating of electrode wires with lipid

A Tantalum wire, 1 mm in diameter, was cut into two sections of about 5 cm length each and held together by a home-designed 3D printed holder, design drawings shown in Appendix A.1. Under a directed nitrogen flow from the output tube, 5 μL of the 4 mg/mL lipid solution was deposited on each wire using the 50 μm glass syringe over 1 cm from the tip of each wire by slowly expelling lipid from the syringe and sliding along the wire as the solvent evaporates, shown in Fig. 2.3a. After application of the lipid solution the electrodes were vacuumed according to Section 2.2.3 in the

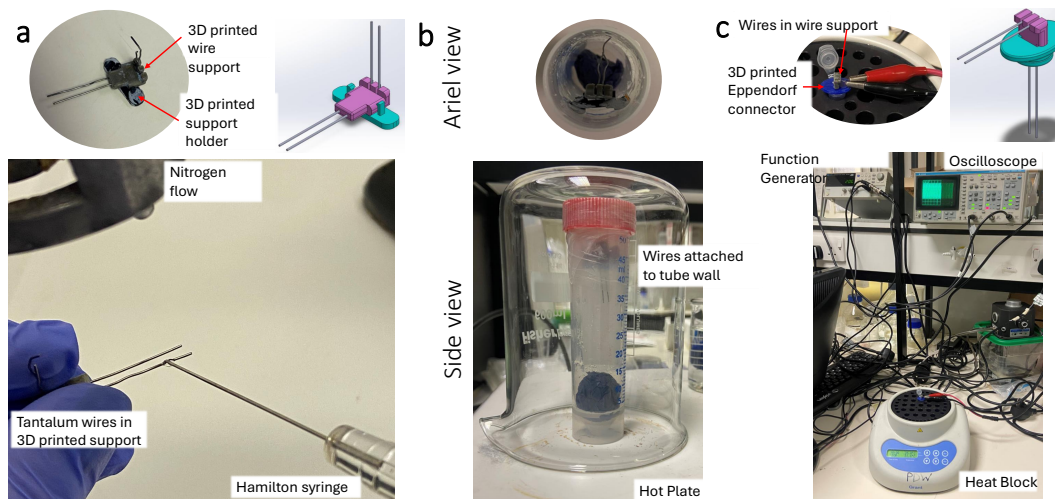


Figure 2.3: Pictures supporting the electroformation protocol a) 3D printed supports to maintain wire geometries and application of the lipid solutions onto the tantalum wires under nitrogen flow b) pre-hydration chamber with wire holder. c) electroformation in progress with the wires in the electroformation solution in an eppendorf tube and connected to the function generator and oscilloscope.

absence of light by placing inside a closed cupboard to ensure all of the solvent had evaporated. The wires were then pre-hydrated in a humid nitrogen environment for 1 h at a temperature at which the bilayer was in the liquid disordered phase. Pre-hydration was achieved using a wet paper towel in the bottom of a falcon tube, filled with nitrogen, sealed with parafilm and placed on a hotplate, at a temperature above phase transition temperature, covered with a large beaker as shown in Fig. 2.3b. The wire holder was fixed to inside of the tube using a wire clip affixed using blu tack as depicted in Fig. 2.3b. The wire clip is detailed in Appendix A.2. The electrodes were washed in 1.2 mL of distilled water (d.H₂O) twice for 10 min each by placing the holder in a 2 mL Eppendorf of 1.2 mL d.H₂O and then removing after 10 min and discarding the water.

2.2.1.2 Electroformation

A 2 mL Eppendorf tube containing 1.2 mL of 0.2 mM sucrose solution was degassed by vacuuming for 1 min. The holder with the lipid-coated wires were then inserted into the tube by clicking the wire holder in the eppendorf connector, as seen in Fig. 2.3c, with the wires spaced 2.5 mm apart, as dictated by the 3D printed support. The wires were connected to a function generator (Instek SFG-2010) and oscilloscope (Gould DSO 405). The solution was kept above phase transition temperature for the duration of electroformation using a hot block (Grant BTD Block Heater) to ensure the lipids remain in liquid disordered phase, this set up is depicted in Fig. 2.3c. A sine wave of 20 Hz and 2.5 V peak-peak was applied for 60 min followed by a square wave at 2.5 V peak-peak for 30 min at 5 Hz, 15 min at 2 Hz and 15 min at 1 Hz and at 4 V peak-peak and applied for 5 min.

2.2.2 Filtration

A filtration setup was assembled as shown in Fig. 2.4. A 5 mL Luer slip syringe (Medica, USA) with a 25 G, 16 mm long needle (BD,UK). The resulting flow rate of approximately 0.2 mL/min was depending on the liquid level of the syringe. The syringe was re-filled to the 5 mL mark after 2 mL had passed through the needle to control the rate. Under the needle a PluriStrainer Mini 20 μ L filter (43-10020-40, Pluriselect, Germany) was placed in a 15 mL Falcon tube (Corning, USA) containing d.H₂O. Cleanroom wipes (double-knit polyester wipes, 414004-518, VWR) were placed alongside the filter in the falcon tube to form a bridge into neighbouring empty 15 mL falcon tubes for the removal of d.H₂O via capillary action. 5 mL of d.H₂O was added to the top of the syringe and 200 μ L of the electroformation product was added to the top of the filter. After 1 mL of d.H₂O had passed through the filter another 200 μ L of product was added to the top of the filter. This was repeated until all sample has been added ensuring that the syringe was re-filled with d.H₂O keeping between 3 and 5 mL volume. After the last aliquot of sample was added and 2 mL of d.H₂O had passed through the syringe, using a pipette with a cut tip the sample was removed. The liquid height in the tube controls the sample volume remaining in the filter, if the capillary action was matched to the flow rate we recovered about 120 μ m into another empty Eppendorf tube. For experiments where the lipid was required to be kept above the phase transition temperature this process was carried out on the hotplate and under a thermally insulated beaker with wet paper towels placed directly on the hotplate to maintain humidity to ensure water flow, as seen in Fig. 2.5.

2.2.2.1 Cleaning of imaging glass

Using cleanroom wipes soaked in acetone the glass surface was repeatedly wiped until no marks remained on the glass. The wipes were exchanged either after 5 wipes or when they started leaving fibres. cleanliness was checked by holding up to a lamp and repeated if necessary.

2.2.2.2 Preparation of slides

An imaging spacer 13 mm in diameter and 0.12 mm in thickness (GBL654006, Grace Bio-labs SecureSeal, Bend) was added to a microscope slide (76 mm \times 26 mm, 1 mm thick)(Menzel-Gläser, Germany) cleaned as described in Section 2.2.2.1. If the sample was imaged on Ettore, the slide was cut down to fit onto our smaller stage with a diamond pen, the width of one slide was removed from the slide length. 20 μ L of the filtered sample was added to the centre of the spacer and the upper protective film removed. A clean (24 \times 24) mm² coverslip (Menzel-Gläser, Germany) was placed on top ensuring no air bubbles were trapped underneath, generating a volume of 21.2 μ L. The region of the coverslip exposed for imaging was cleaned using acetone after sealing. An example of the final sample can be seen in Fig. 2.6.

2.2.2.3 Funnel for imaging

A funnel was designed to help imaging of GUVs. This consisted of a central round chamber that the GUVs could be imaged in. Cone access for the transillumination allowed the sample to be placed in the middle well and imaged from below via reflectometry and epifluorescence and in transmission with DIC. 4 channels up the

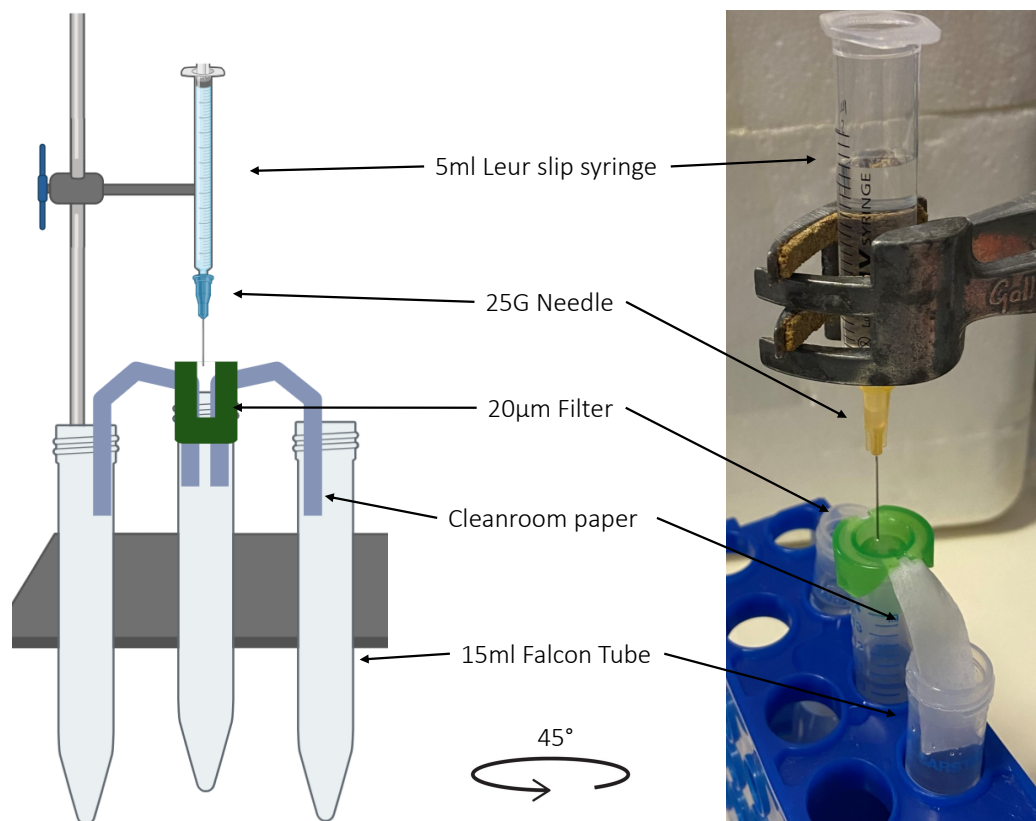


Figure 2.4: Filtration Sketch a) and picture b) of the filtration setup demonstrating the geometry of the components for filtration.

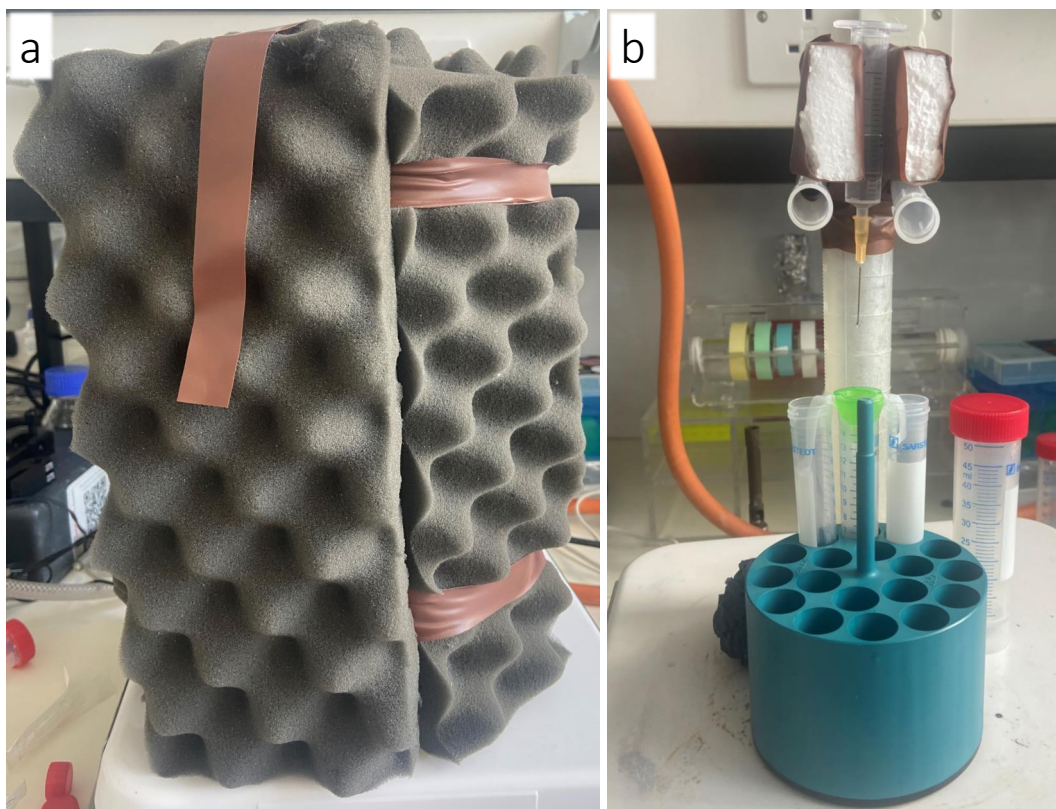


Figure 2.5: Pictures of heated filtration setup a) shows the insulation taped onto a 5 L beaker on top of the hotplate covering the modified filtration set up shown in b. The filtration set up was modified to allow it to fit under the beaker.

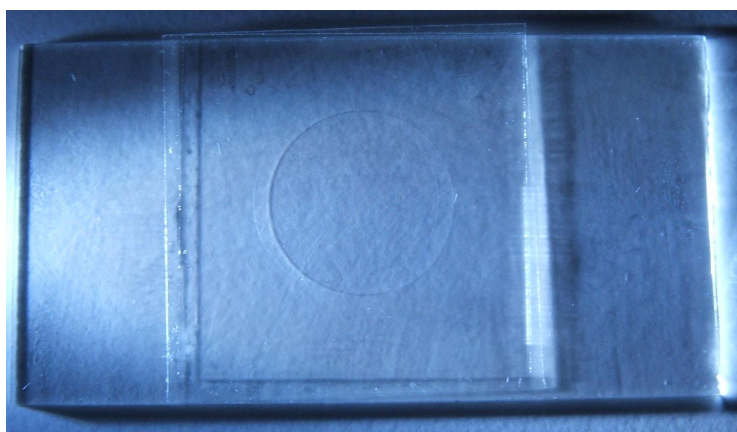


Figure 2.6: Sample slide ready for imaging An example of a slide made ready for imaging with a slide, coverslip and gasket.

sides allowed the addition and removal of solutions during imaging. The funnel also had slots allowing a 5 mm coverslip to be placed over opening which prevented evaporation. They were 3D printed using files shown in Appendix A.3. Funnels were printed using a BMF, S230 photon lithography printer using HTL Resin unless otherwise specified. The funnels were glued to a 35 mm dish with 14 mm² accessible glass (P35G-1.5-14-C MatTek, USA) after being cleaned using ethanol. Araldite "Standard" two component glue was added to the base of the funnel before being pressed into the central coverslip region of the dish. The dish was then turned upside down on top of a pillar to support the funnel from below with a small weight on top to maintain even pressure whilst the glue set overnight. About 5 μ L of GV solution was pipetted into the central well. A 5 mm diameter circular coverslip (AGL4605-1 Agar Scientific) was added on the lower ridge and a 16 mm diameter coverslip across the top. Additional solution was added as specified down the channels.

2.2.3 Desiccator use

A vacuum was established by connecting a Vacuubrand MZ 2C vacuum pump (Wertheim, Germany), with a minimum pressure of 7 mbar, to a desiccator for 5 min as seen in Fig. 2.8. The pump nozzle was attached to the desiccator and switched on, the valve was fully opened, identified by the loudest position representing maximum air flow. The valve was then turned 90° to its fully closed position. After 5 min the pump was switched off and the nozzle removed. This was left for the specified time and the desiccator was vented with air by turning the valve back 90° to its fully open position to re-establish atmospheric pressure.

2.2.4 Spin coating

The spin coater used was the Laurell Spin Processor, Model WS-650MZ-23NPPB attached to the Gast Vacuum Pump (0523-545Q-G588DX, electrical 5KH36KNA510X). The pump generated a vacuum which stuck the coverslip to the block inside, once the lid was shut the solution could be added through the hole on top as shown in Fig. 2.8. The spin settings are detailed in the individual protocols, and consist of acceleration, constant speed and deceleration periods. Nitrogen gas at 2 bar was used to flush the chamber and release the vacuum.

2.2.5 hs-GUV sample preparation

2.2.5.1 ITO-coated coverslip electroformation

This preparation was undertaken on coverslips that had been treated with H₂O₂ to increase hydrophilicity as described in Harlow *et al.* [183]

150 μ L of 1 mg/mL lipid solution was spin coated (6 s acceleration then 30 s at 3000 rpm, followed by a 6 s deceleration) in a nitrogen environment, onto a hydrophilic coverslip and incubated in a vacuum for 60 min after 5 min degassing, demonstrated in Fig. 2.8. A chamber was made using an imaging spacer, a clean (24 \times 24) mm² coverslip and filled with d.H₂O. The coverslip with the lipid bilayer was placed on top of the spacer to generate an enclosed chamber. The chamber was squeezed between two Indium Tin Oxide (ITO) coated coverslips ensuring contact between all coverslips. This was achieved using 3D printed support as discussed in Appendix A.4 and depicted in Fig. 2.7. The chamber was connected to a function generator

and oscilloscope. Hardware is detailed in Section 2.2.1.2. A sinusoidal 20 Hz and 2.5 V waveform was applied for 1 h.

2.2.5.2 PVA swelling

Long chain polyvinyl alcohol (PVA), average M_w 130 kDa (563900, Sigma) was prepared as a 5% (w/w) solution by stirring PVA in water while heating on a hotplate with a magnetic stirrer at 90 °C. This was diluted to produce the 1.7% solution.

For drop casting 150 μm of PVA solution at specified concentration was pipetted onto a H_2O_2 treated coverslips.[183] The pipette was used to spread the volume across the whole area before leaving to dry on a hotplate for 30 min at 50 °C.

For spin coating 20 μL of 1.7% (w/w) PVA, unless otherwise specified, was spin coated (10 s acceleration, 60 s at 2500 rpm, 1000 rpm to standstill deceleration) under nitrogen onto a hydrophilic coverslip. It was then dried at 50 °C for 30 min.

150 μL of a 1 mg/mL lipid solution was spin coated (6 s acceleration, 30 s 3000 rpm, 6 s deceleration), under a flow of Nitrogen gas, on top of the PVA layer, shown in Fig. 2.8. The lipid bilayer was vacuumed and pre-hydrated in the same way as discussed in Section 2.2.1.1. A chamber was made using an imaging gasket, slide and $\text{d.H}_2\text{O}$ and left overnight to allow rehydration of the PVA layer, details on how water was added is discussed in Section 3.2.2.3.

2.2.6 Droplet interface bilayers

2.2.6.1 Droplet interface bilayer sample preparation

The following method is taken from an internal first year PhD report written by Hannah Baird.

A set of four glass coverslips were exposed to an oxygen plasma treatment inside a reactor. Following this, one coverslip was secured to a vacuum platform within a spin coater. Onto this coverslip, 120 μL of a 7 mg/mL low gelling temperature agarose solution, previously melted and maintained at 80 °C was applied. The spin coating process was carried out for 30 seconds.

Once coated, the coverslip was carefully positioned agarose side up in the designated notch at the base of a custom micro-milled acrylic device. The entire assembly was then inverted and placed on a heat block set to 30 °C. Meanwhile, 35 mg of agarose was dissolved in 1 mL of a buffer containing 0.33 M CaCl_2 and 10 mM 4-(2-hydroxyethyl)-1-piperazineethanesulfonic acid (HEPES) at pH 7.35. This solution was also heated to 80 °C. A 170 μL aliquot was then gently dispensed into the acrylic device. To ensure quality, the agarose layer was examined under a stereo microscope for any imperfections.

Subsequently, the wells within the device were filled with a lipid solution composed of 8 mg/mL 1,2-diphytanoyl-sn-glycero-3-phosphocholine (DPhPC) dissolved in a mixture of 60% hexadecane and 40% silicone oil. Care was taken to eliminate visible menisci. A droplet-phase solution was then prepared by mixing 10 μL of 1.5 M KCl with 10 mM HEPES (pH 7.35), 4.4 μL of Chelex-treated water, and 0.6 μL of 10 mM Ethylenediaminetetraacetic acid (EDTA). This mixture was used to generate droplets in a trough containing the same lipid solution. Using a 1 μL pipette set to its minimum volume, tiny droplets were introduced into the trough and left to incubate. Afterwards, individual droplets were transferred into the wells of the prepared device.

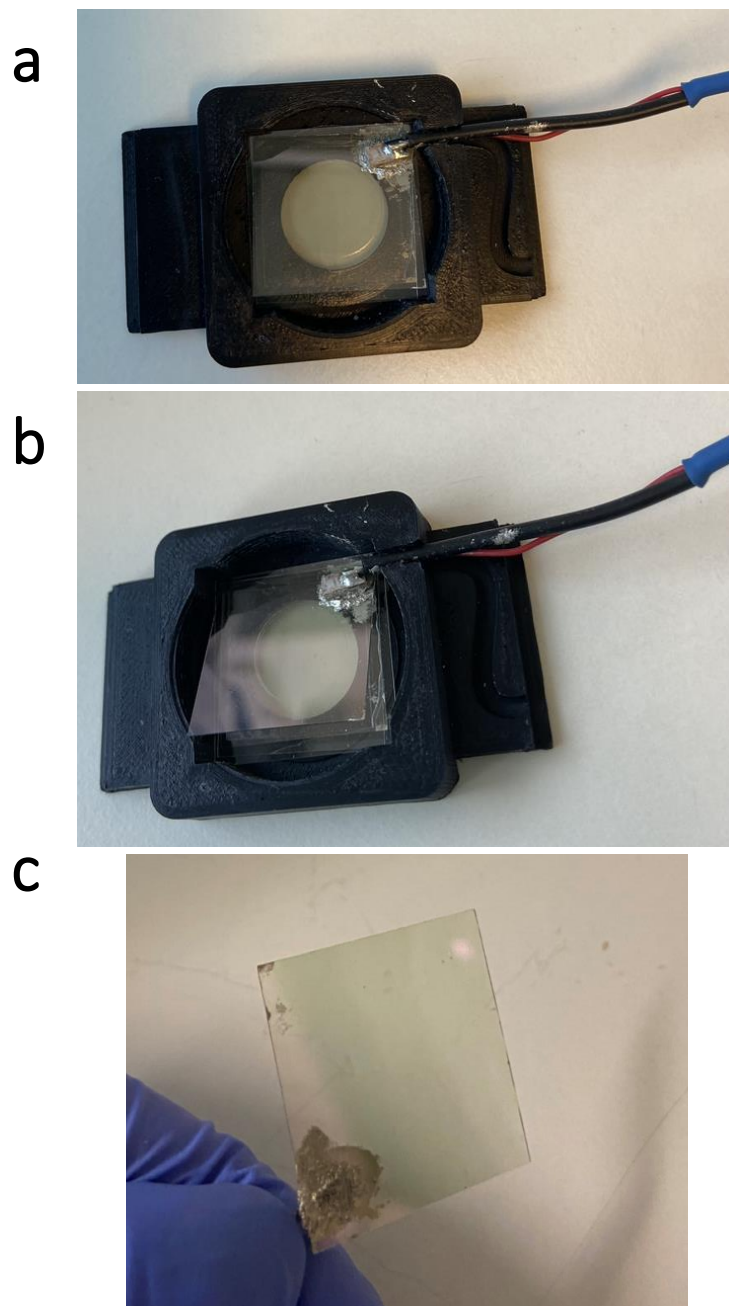


Figure 2.7: Pictures of the ITO mount Pictures depicting the stacking of the chamber containing lipid solutions between ITO coverslips into the mount in **a)** and **b)** with a close up of the wire connecting to the ITO coated coverslip (**c)**

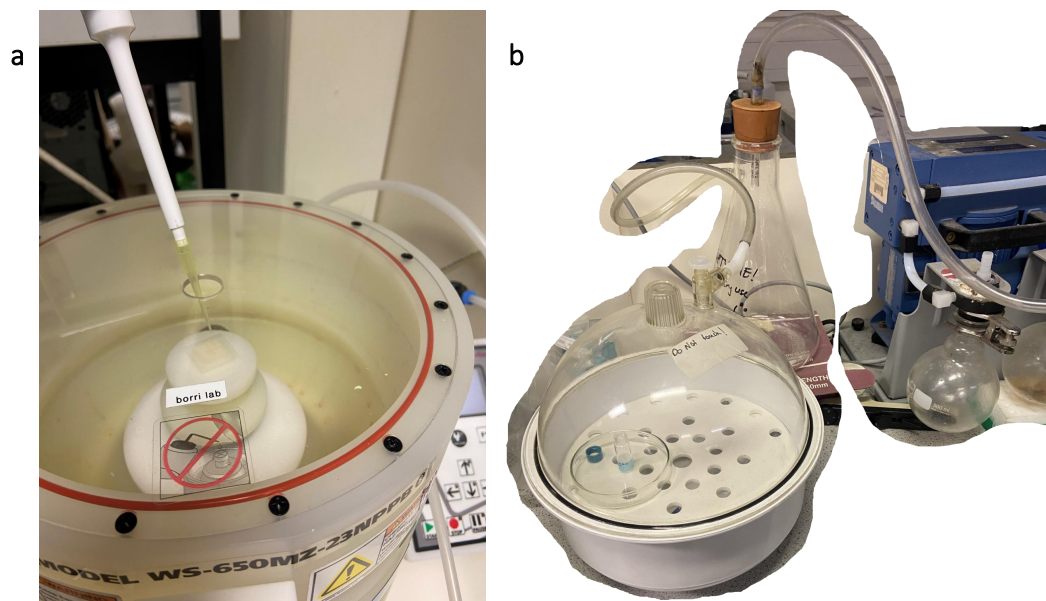


Figure 2.8: Spin coater and desiccator use a) The application of a solution onto a coverslip centered on the block of the spin coater. b) A vacuum pump attached to the desiccator to allow degassing.

2.2.7 Focal bead sample preparation

1 μL of polystyrene focal bead solution was added to 1 mL of 75% (v/v) glycerol solutions for each 100 nm (00876-15) and 200 nm (07304-15) polybead microspheres (Polysciences). Samples were sonicated in the bath sonicator (3510 MTH, Branson) for 20 min. Sample slides were produced as described in Section 2.2.2.2.

2.2.8 SUV preparation

A 4 mL glass vial was cleaned with six washes of acetone. 250 μL of a 4 mg/mL POPC:POPE(1:1) solution was deposited in the vial using a hamilton syringe, equating to 1 mg of lipid. Under directed nitrogen flow the lipid solution was dried whilst the vial was tilted and rotated such that the lipid dried in a film along the walls of the vial. The vial was placed under the vacuum for 30 min as described in Section 2.2.3. The vial was filled with 2 mL of d.H₂O and placed in an ice bath. The sonicator tip (Fisherbrand 12337338) was placed into the centre of the liquid volume and sonicated at 30% maximum power until the solution turned clear. The solution was split into 2 mL Eppendorf tubes and centrifuged at maximum power for 10 min. The supernatant was extracted using a pipette and deposited in another cleaned vial. The solution was diluted with d.H₂O at a 10:1 ratio and stored at 4-6°C. SUV solutions were diluted at a 100:1 ratio when incorporated into glycerol solutions at both 50 or 90%. Sample slides were produced as described in Section 2.2.2.2.

2.3 Quantitative Differential Interference Contrast Microscopy

2.3.1 qDIC optical setup

A full description of the qDIC set up can be found in papers written by Regan and Hamilton.[184, 185] It used a Nikon Ti-U inverted microscope with a motorised xy stage and objective focusing (Prior H117N2TE stage, H122 focus drive and a Proscan III XYZ controller). Together these produced a 0.04 μm microstep size with 250 microsteps per step and 200 steps per rotation of a 2 mm ball screw with a repeatability of 0.7 μm . Z focal position was controlled by the objective focus drive with 2 nm microstep size and 100 μm per rotation. The Z height was controlled using Micromanager software. Transillumination used a Nikon 100 W tungsten halogen lamp (Nikon V2-A LL 10 W) as source. Schott BG40 and Nikon GIF filters were used to select a wavelength of 550 nm with a full width at half maximum of 53 nm. A rotatable linear polariser and quarter wave-plate (Senarmont compensator and Nikon T-P2 DIC Polariser HT MEH51941, respectively) were used before a Nomarski prism (Nikon N2 DIC module MEH52400). The angle between the polariser and the wave-plate was defined as θ creating a phase shift of 2θ between the linear polarisation components split by the prism. A dry close working distance condenser (0.72NA, MEL56100) was used in conjunction with a 20x 0.75 NA (MRD00205) dry objective and 1.5x tube lens to focus light on the sample and collect and image light after, respectively. A second Nomarski prism (DIC slider MBH76220) and a linear polariser (Nikon Ti-A-E DIC analyser block MEN 51980) was placed between the objective and the tube lens. Light was detected using a Hamamatsu Orca 285 CCD camera producing images of 1344 x 1024 pixels.

2.3.2 qDIC data acquisition and processing workflow

qDIC images were acquired as batches of 256 with 0.1 s exposure. Polariser angles of ± 15 degrees were used sequentially generating a phase offset of ± 30 degrees. The image batches were averaged across the maximum number of frames over which the vesicle movement was acceptable. The images were cropped to 400×400 pixels with the vesicle in the centre.

In the analysis a contrast image was generated by the combination of images taken at a positive and negative phase angle using Equation 2.1. The phase, Φ , was measured across the shear distance, s , according to Equation 2.2 to generate a phase gradient.

$$I_C = \frac{I^+ - I^-}{I^+ + I^-} \quad (2.1)$$

$$\Delta r = \phi \left(r + \frac{s}{2} \right) - \phi \left(r - \frac{s}{2} \right) \quad (2.2)$$

The equation of the image shown in Equation 2.3 was inverted to calculate the gradient phase, $\delta(r)$, which in turn was Fourier transformed to gain the phase in the Fourier domain, using the polariser angle, ψ and the gradient phase δ .

$$I_c(\vec{\mathbf{r}}) = \frac{\sin(\psi) \sin(\delta)}{\cos(\psi) \cos(\delta) - 1} \quad (2.3)$$

This phase, $\phi(\mathbf{k})$, was extracted using Wiener deconvolution shown in Equation 2.6. In this equation ξ is the Fourier multiplier explaining how the gradient phase is related to the phase in Fourier space and was defined using Equation 2.5.

$$F(\delta(\vec{\mathbf{r}})) = \xi(\vec{\mathbf{k}})F(\phi(\vec{\mathbf{r}})) \quad (2.4)$$

$$\xi = 2i \sin\left(\frac{s\mathbf{k}}{2}\right) \quad \text{and} \quad \delta = \xi\phi \quad (2.5)$$

Subsequently the phase in real space $\phi(\mathbf{r})$ was retrieved using an inverse Fourier transform as shown in Equation 2.6. This phase was further analysed using the integrated phase.

$$\phi(\vec{\mathbf{r}}) = F^{-1}\left(\frac{F(\delta(\vec{\mathbf{r}}))}{\xi(\vec{\mathbf{k}}) + (\kappa\xi(\vec{\mathbf{r}}))^{-1}}\right) \quad (2.6)$$

This processing was implemented in an in-house developed software (qDIC). Unless otherwise specified, the parameters were as follows; a signal to noise parameter of the wiener filter (κ) of 10^6 , a background count of 192, a polariser angle, ψ , of 30° , shear vector magnitude, s , and direction were 238 nm and -45° respectively with a 550 nm wavelength. Dirt filters were applied manually to remove any debris close to the vesicle. Data was analysed in a home written software, using the apodisation method for integration, an example of this process can be seen in Appendix B.1.

The $\phi(\mathbf{r})$ images produced were used to plot phase profiles across the centre of the vesicle at a 45° angle.

2.4 Temperature control during microscopy

Temperature control on the microscope was carried out using the slide heater. This home-made technology was accurate to 0.1°C and heated up the slide by a resistive heater after the temperature had been set. Small wells on the both sides of the slide were available to hold dry ice, which allowed it to reach temperatures below room temperature, which also provided a CO_2 gas flow preventing condensation on the slide, this device can be seen in Fig. 2.9 where pictures were taken once mounted on the Ettore microscope. This device was compatible with both microscopes and used in conjunction with epifluorescence as described in Section 5.1 on Galileo and with iGOR as discussed in Section 6.10 on Ettore. To record the rate of change of temperature the data was taken as a time series and the frame was recorded manually in conjunction with the temperature from the slide heater.

2.5 Calibration of numerical aperture

Numerical apertures were calibrated for the 0.72 dry condenser using objectives of various NA (0.3, 0.45, 0.5, 0.75) and observing the filling of their back focal plane in transmission using a Bertrand lens and marking the position on the slider. Köhler illumination was set by adjusting the condenser to the correct height and lateral position to focus and center the field aperture image. The aperture diaphragm of the condenser was then adjusted to match the objective back focal plane size and the condenser aperture diaphragm lever position was marked on a paper attached close to the lever. The distances from closed were measured and graphed and interpolated to create a calibrated ruler that was attached to the condenser. The oil condenser had already been calibrated using the same protocol.

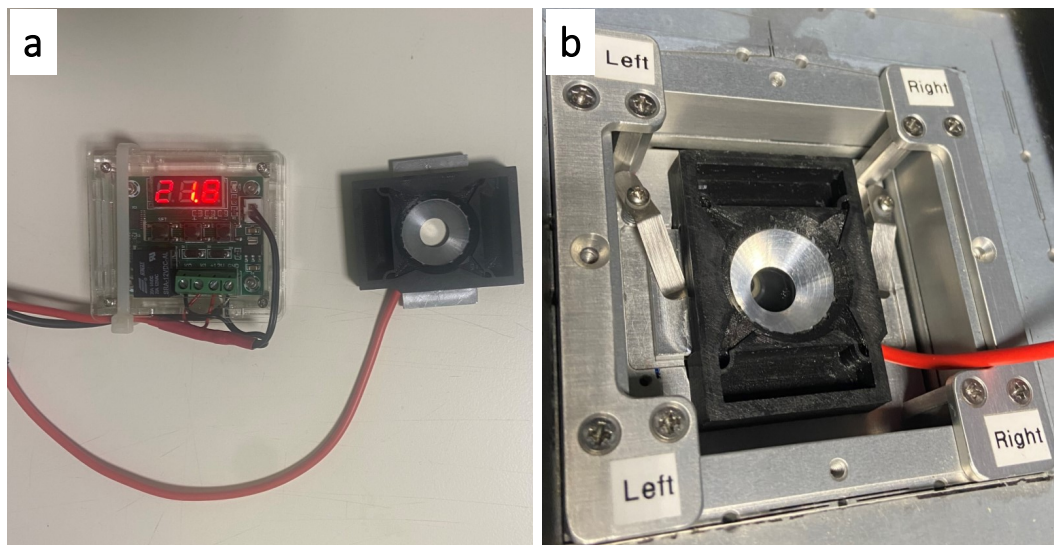


Figure 2.9: Slide heater a) Slide heater connected to the control unit. b) Attached to the microscope stage on top of the sample slide.

2.6 Protein insertion

2.6.1 GV sample preparation

GVs were produced using the protocol described in Section 2.2.1 with a lipid composition of POPC:POPE:ATTO-DOPE (50:49.99:0.01, w/w), with the ATTO being either ATTO 425 or ATTO 488 as detailed later. 50.2 mM Sucrose, 5×10^{-8} mM 5(6)-Carboxyfluorescein (Sigma-Aldrich, USA) was used as the internal solution. Filtration was carried out using 50 mM Tris-HCl pH 8.0 buffer.

2.6.1.1 Enclosed samples

Approximately 20 μ L of GV sample was pipetted into the well of an imaging spacer on a slide and sealed with a 22 mm coverslip both cleaned as described in Section 2.2.2.1. Purified App6Aa1 protein solution was provided by Lainey Wilson and added to the well, typically in the order of 5 μ L before sealing to generate the final concentration as specified.

2.6.1.2 Open samples

An 8 well (9 mm diameter and 0.12 mm thickness) secure seal imaging spacer (GBL65-4008, Grace Bio-Labs) was cut in half to provide a 2×2 well section. This was stuck to the inner circle of a plastic dish of diameter 35 mm. One 40 μ L droplet of GV solution was added to each well before imaging, as seen in Fig. 2.10. During imaging App6Aa1 protein solution was added by pipetting a droplet adjacent to the existing GV droplet allowing them to combine, to produce final protein concentrations as specified.

2.7 Epifluorescence imaging

Epifluorescence images were taken using the same microscope, referred to as Galileo, in Section 2.3. A metal halide light source (Prior Lumen 200) used at 100% power



Figure 2.10: Open samples for protein insertion An image to show the set up of the open samples with droplets applied ready for imaging in a plastic dish with a 35 mm diameter

with an exposure time of 0.12 s unless otherwise stated. A CLWD condenser (0.72 NA)(Ti-C-LWD Condenser Lens Unit in Ti-C Manual System Condenser Turret, Nikon), 10× objective (0.3 NA)(CFI Plan Flour, MRH00101, Nikon) and 1.5× tube lens were used.

Epifluorescence images were taken with Semrock GFP-A-Basic-NTW filter for 5(6)-Carboxyfluorescein and ATTO488 This filter had an excitation wavelength of 469/35 and a detection of 525/39. A Semrock Custom Blue filter was used for ATTO425, This filter had an excitation of 370/36, an emission of 447/60 and a Dichroic of 409. Filter spectra are shown in Fig. 2.11.

2.7.1 GV imaging during electroformation

The 3D printed wire clip, shown in Appendix A.2, was stuck to the base of a plastic dish using blu tack and the wires placed into the clip so they were lying flat just above the surface. Solution was added and the dish placed in the sample holder on the microscope.

2.7.2 GV imaging through protein addition

GVs in a well were imaged with both the GFP-Basic-NTW and Custom blue filters in quick succession. The App6Aa1 protein solution was added in a droplet adjacent but touching the GV droplet allowing it to form one larger droplet. The same imaging protocol was undertaken of all vesicles remaining in solution.

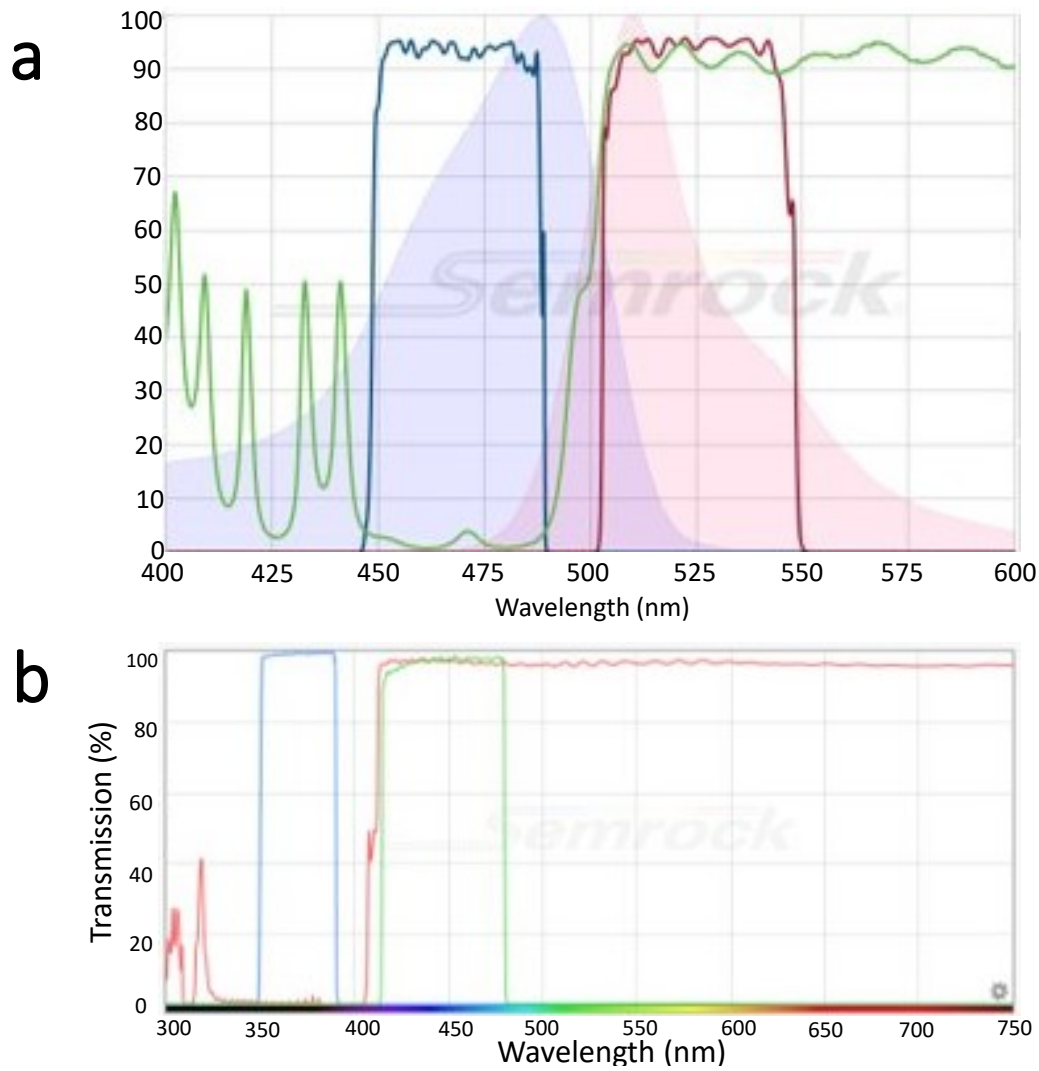


Figure 2.11: Epifluorescence filter specifications Exciter, emitter and dichroic transmissions are shown. (a) GFP-A-Basic-NTW, with the exciter, emitter and Dichroic shown in blue, red and green, respectively. (b) Custom blue filter which shows the Dichroic in red and the Excitation and Emission in blue and green, respectively. Spectra taken from manufacturers (Semrock, US).

2.8 Droplet interface bilayer sample imaging

DIB samples were imaged using qDIC, as described in Section 2.3 using the CLWD condenser with a 0.72 NA, $20\times$ 0.75 objective and a $1.5\times$ tube lens. Image batches of 256 with a 0.12 s exposure time were acquired for a single z plane. For z stacks, images were taken as a single snapshot of 0.12 s exposure in $1\ \mu\text{m}$ steps.

2.9 Interferometric gated off-axis reflectometry

2.9.1 Optical setup

This set up is shown in detail in Appendix B.2 detailing components. A simplified diagram is shown in Fig. 2.12.

The light source used in this set up was a femtosecond laser consisting of a Ti:Sapphire oscillator (Spectra Physics MaiTai HP) pumping an optical parametric oscillator (Inspire HF 100). We used the signal beam of the OPO at 550 nm. It had a pulse duration of about 100 fs, having a coherence length of $30\ \mu\text{m}$ in air. The horizontally polarised beam was coupled by a fibre-coupler FC1 (Thorlabs CFC-8X-A, $f=7.5\ \text{mm}$) into a single mode polarisation maintaining fibre (Thorlabs P1-488PM-FC-2) of 2 m length, with a polarisation axis aligned with the input polarisation. At the fibre output, with horizontal output polarisation, was collimated by a second CFC-8X-A. Any residual cross-polarisation was cleaned and passed through a Glan-Thompson Calcite Polariser (Thorlabs GTH5M) providing a horizontal linear polarisation with less than 10^{-6} vertical polarisation residual intensity. After this a beam sampler BS1 (Thorlabs BSF10-A1), a fused silica plate with 30 arcminute wedge, separated the reflections of the two sides and one side anti-reflection coated. This provided 1% reflection for horizontal (p) polarisation, which was used as the reference beam. The reference beam travelled through a delay stage (Linear stage Physik Intrumente M-403.82S, retroreflector BK7 Right-Angle Prism (Thorlabs PS915H-A)) to control the temporal overlap with the signal on the sample. It then passed through glass blocks SF2 of length adjustable in 3 mm steps used to match the chirp of the signal and reference beams at the camera to maximise their interference. The reference beam intensity was adjusted using a rotatable half-wave plate (CASIX WPA465-610) and a Glan-Thompson Calcite Polariser (Thorlabs GTH5M). The reference beam was then passed through a rectangular aperture (0.625 mm height and 0.879 mm width, cut from anodised aluminium foil) to define the reference beam area on the camera. The aperture plane was collimated by the lens L2 (achromat $f=50\ \text{mm}$, Edmund Optics #49-328), and coupled by a mirror (Thorlabs MRA15-P01) towards the camera at a far-field plane of the sample, offset from the centre to provide the off-axis holography. The beam transmitted by BS1 was guided via mirrors through a beam expander BE1, which controlled the size of the beam at the sample plane via a 2:1 beam size reduction (achromats $f=50\ \text{mm}$ and $-25\ \text{mm}$, Thorlabs ACN127-025-A, AC127-050-A). Coupling into the microscope occurred via a mirror 90 degrees up into an 3:4 beam expander ($f=-75\ \text{mm}$, $f=100\ \text{mm}$ acromatic lenses Edmund Optics #45-422 and 49-360), and a mirror deflecting the beam back into the horizontal direction into the Ti-U back port and is transmitted through a field aperture. Once collimated by a $f=160\ \text{mm}$ achromat (Edmund 67-334) it was reflected towards the microscope objective by a 20:80 R:T beamsplitter (Chroma 29008) held in a Nikon Ti-U filter cube. A $60\times$ 1.27 NA water immersion objective (Nikon, MRD70650) focussed the light into the sample which provided a

high lateral spatial resolution. Notably, the beam was adjusted by the 3:4 expander to have a focus in the back focal plane, to result in a collimated beam in the sample volume of $10\ \mu\text{m}$ beam diameter. The reflected light passed through the beamsplitter and a $1.5\times$ tube lens of the Ti-U, was deflected out of the right port by a port prism and the by mirror FM1 onto a near field aperture A2, which matched the reference beam aperture $0.9125\ \text{mm}$ height, $1.76\ \text{mm}$ width). Lens Spec L1 ($f=100\ \text{mm}$, Edmund Optics 49-360) then collimated the aperture as well as imaging the objective far field plane to aperture A3 (adjustable iris, Thorlabs SM1D12C) which defined the detected size of the objective far field. A Wollaston prism (0.75 degree split, Quartz, Altechna, Custom made) split the horizontally and vertical polarisations of the combined reference and signal beam vertically. All mirrors were protected silver, $\lambda/10$ surface figure, $>95\%$ reflection. After deflection by FM2, the light was focussed onto the imaging camera by lens L1 (Edmund Optics 49-360 achromat $f=400\ \text{mm}$) where the areas of horizontal and vertical polarisation were separated vertically by $5.24\ \text{mm}$. The camera was a Basler acA1920-155um with a Sony IMX174 sensor, 1920×1200 pixels, of $5.86\ \mu\text{m}$ size, $11.25\ \text{mm} \times 7.03\ \text{mm}$, 32 ke full well capacity, 70% QE at $550\ \text{nm}$, 7e read noise USB3, Global shutter. The camera was mounted with the longer side vertically, accommodating two regions of about $7\ \text{mm}$ horizontal by $5\ \text{mm}$ vertical for the two polarisations, corresponding to the imaged apertures A1 and A2 of reference and signal. The magnification on the Camera was 4 times the one of the microscope in its intermediate image plane.

2.9.2 Acquisition

This section details the iGOR acquisition pipeline. The data acquisition was controlled by a program written in Matlab called iGOR-C, developed in the group (Tual Monfort(2019-2020) and David Regan(2020-2024) guided by Wolfgang Langbein).

The field as was incident on the camera was a complex image represented by, \mathbf{E} , as the data was processed the notation changed as detailed in Equation 2.7.

$$\mathbf{E} = E(x, y), \quad \hat{\mathbf{E}} = \mathcal{F}(E(x, y)) = E(k_x, k_y) \quad (2.7)$$

This equation demonstrates the fast Fourier transform of the complex signal from the spatial domain into the Fourier domain also known as k space, (k_x, k_y) .

The intensity on the camera can also be described by the Equation 2.9 which provided the basis for the subsequent explanation, where k_r was the in plane vector of the reference describing k space as a frequency in spatial domain incorporating the refractive index, Equation 2.8, and $k_r \sin\theta$ was the reference wavevector in the camera plane, with θ being the angle between the signal and reference beams at the camera plane.

$$k_r = \frac{2\pi n}{\lambda} \quad (2.8)$$

$$\mathbf{I}_R + \mathbf{I}_S + \mathbf{E}_R \mathbf{E}_S^* e^{ik_r \sin\theta} + \mathbf{E}_R^* \mathbf{E}_S e^{-ik_r \sin\theta} \quad (2.9)$$

In the following discussion \mathbf{I}_A denotes the acquired image and \mathbf{I}_{AC} the calibrated image at that point in the protocol. Fig.2.12 shows a simplified iGOR diagram highlighting key areas of the set up that allow the extraction of data.

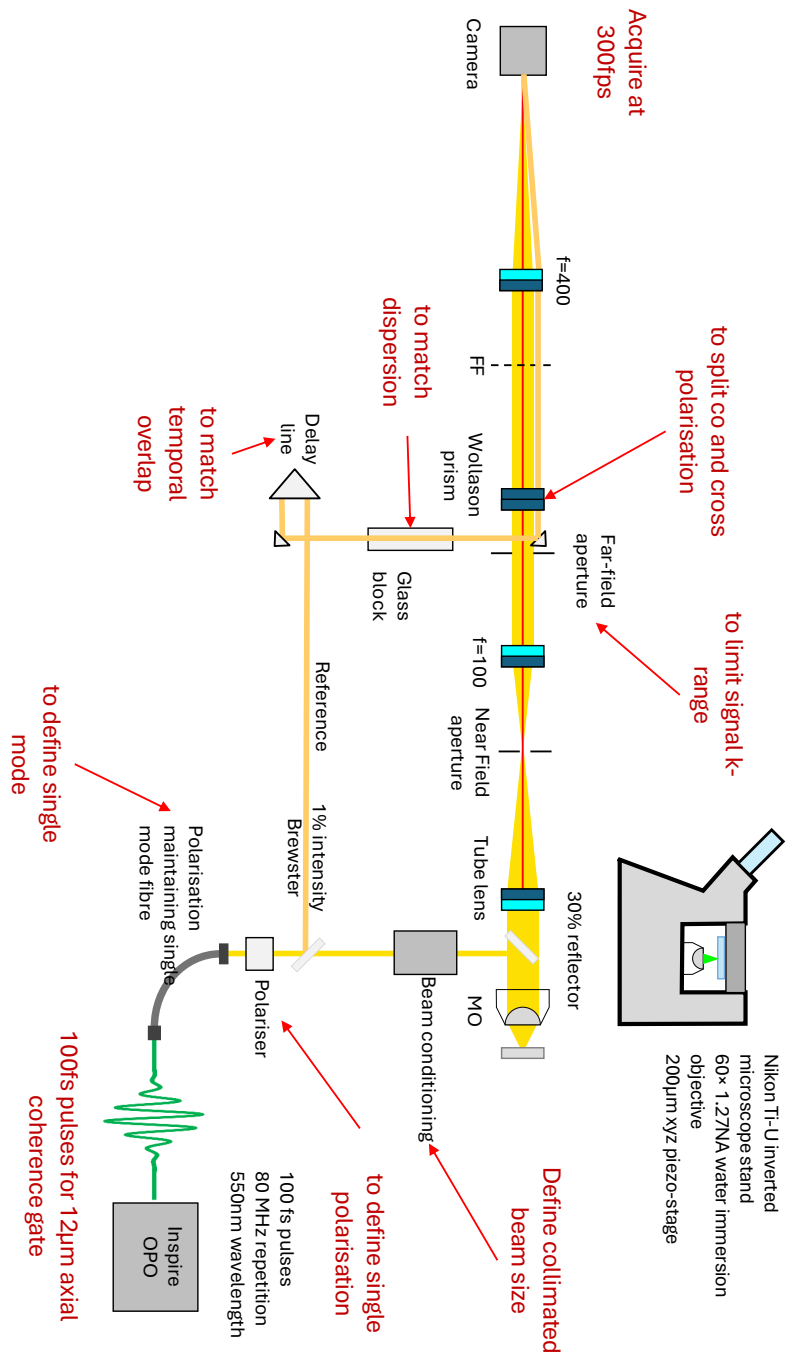


Figure 2.12: iGOR Optical Set Up A simplified schematic of the iGOR optical set up with highlighted components and their function detailed as presented by Langbein. [186]

2.9.2.1 Calibration images

The camera used in this set up was a CMOS camera that recorded the intensity incident on the camera over a given exposure time, typically in the millisecond range. It was a global shutter ensuring that the exposure period was equal for all positions, and allowing to read the camera while exposing another frame. The individual camera pixels could have had a varying sensitivity, which was corrected for in a flat field sensitivity correction. This calibration image (\mathbf{I}_{FF}) was measured and averaged over 30s using a homogeneous incoherent illumination prior to my involvement, and then loaded in for each subsequent imaging session. Equation 2.10 demonstrates how this flat field calibration was applied to an image (\mathbf{I}_{A}) via multiplication after subtraction of a dark field \mathbf{I}_{DF} , an image taken with both shutters closed.

$$\mathbf{I}_{\text{AC}} = \mathbf{I}_{\text{FF}}(\mathbf{I}_{\text{A}} - \mathbf{I}_{\text{DF}}) \quad (2.10)$$

The ultimate aim of iGOR was to be able to measure the reflected sample amplitude (\mathbf{E}_{S}) and phase (ϕ_{S}). This was done in two steps: isolating one of the interference terms and the removal of amplitude and phase contributions from the reference term.

To allow the isolation of the interference term first the zero order signal and reference beam were removed. The interference was in principle separated in k-space, but it was still better to subtract these first to reduce artefacts in the Fourier transform. This could be done via straight subtraction, these images were taken in a flat region of the sample with no additional structure at the interface. The reference (\mathbf{I}_{R}) and signal (\mathbf{I}_{SF}) reflections were measured separately by blocking the unwanted beams using shutters these were taken in both polarisations alongside an interferogram (\mathbf{I}_{RSF}). After subtraction of (\mathbf{I}_{R}) and (\mathbf{I}_{SF}) from the interferogram and division of the signal field ($\sqrt{\mathbf{I}_{\text{SF}}}$) as shown in Equation 2.11 the resulting field was as represented by Equation 2.12.

$$\frac{\mathbf{I}_{\text{RSF}} - \mathbf{I}_{\text{SF}} - \mathbf{I}_{\text{R}}}{\sqrt{\mathbf{I}_{\text{SF}}}} \quad (2.11)$$

$$|E_{\text{R}}|e^{-i(\phi_{\text{R}}+k_r r \sin \theta)}e^{i\phi_{\text{SF}}} + |E_{\text{R}}|e^{i(\phi_{\text{R}}+k_r r \sin \theta)}e^{-i\phi_{\text{SF}}} \quad (2.12)$$

2.9.2.2 Extraction of the first order interference term

The region of interest was selected in a user interface to extract the central portion of the raw display in both polarisations to ensure the centre of the signal beam was being imaged. Due to iGOR's off-axis configuration there was a separation observed in the Fourier domain, otherwise known as k space, this was due to a differing angle of incidence on the camera from the reference and signal beam, θ . This, in turn produced a shift in k space from which we could extract the first order interference term. We defined the region containing the first order term we extracted as $\hat{\mathbf{E}}_{\text{FO}}$ from the Fourier transform of the field shown in Equation 2.12.

In the user interface, a binary mask (M) was applied in k space which was one inside a user selectable ellipse and zeros outside. The user set the radius in k-space of the first order term. In theory the NA of the objective should've been equal to the radius of the first order term, in practice this was not observed and therefore the user had to select this range to ensure the first order term was correctly extracted as the edges could be clearly seen when imaging a region with high spatial frequencies.

This mask was used to select first order interference in the other images and shift the centre of this space to zero.

A Fourier image was formed via pointwise multiplication according to Equation 2.13 to isolate the complex field in the first order and was used in future calculations. This was also the image that the mask was applied to as shown in Equation 2.13, producing the first order term in real space. This section of k space was cut out, centred at zero wavevector, and then padded to the next highest power of 2 resulting in the correction field (\mathbf{E}_C). This acted as the final correction term for the first order term of any measurement data (\mathbf{E}_{FOM}) extracted using the same procedure as the calibration field, by dividing through to cancel out the reference left all phases relative to the flat signal field as shown in Equation 2.14.

$$\mathbf{E}_C = \mathcal{F}^{-1}\{M\hat{\mathbf{E}}_{FO}\} = \mathbf{E}_R e^{-i\phi_{SF}} \quad (2.13)$$

$$|\mathbf{E}_S| e^{i(\phi_{SF} - \phi_S)} = \frac{\mathbf{E}_{FOM}}{\mathbf{E}_C} \quad (2.14)$$

2.9.2.3 Further corrections prior to saving

The amplitude (\mathbf{E}_S) retrieved from Equation 2.14 was unscaled. To calibrate the reflected field into field reflectivity units it was calibrated to a known reflectance such as that of a glass/water interface. This glass/water interface calibration image was taken prior to sample imaging. It was used if the sample did not provide a well-defined flat interface which could be used to calibrate.

The power reflectivity, P_R , for p polarisation was calculated using Equation 2.15 and Equation 2.16 with NA set to 0.3, in the p polarisation, given by the chosen incident angle (in units of NA) and polarisation of the excitation beam at the sample. The angles of reflection and transmission at the interface (θ_R and θ_T) were given by the Equation 2.15 using the refractive indices of glass (n_g) and water (n_w) (or medium present).

$$\theta_R = \arcsin\left(\frac{NA}{n_w}\right), \quad \theta_T = \arcsin\left(\frac{n_w \sin(\theta_R)}{n_g}\right) \quad (2.15)$$

$$P_R = \left| \frac{n_g \cos\theta_R - n_w \cos\theta_T}{n_g \cos\theta_R + n_w \cos\theta_T} \right|^2 \quad (2.16)$$

This was applied to any further acquisitions according to Equation 2.17, where I_{GW} was the measured intensity image of the glass interface and R_{GW} was the intensity reflectivity calculated from equation 2.16.

$$\mathbf{I}_{AC} = \frac{R_{GW} |\mathbf{E}_S|^2}{\mathbf{I}_{GW}} \quad (2.17)$$

Power fluctuations of the Ti:Sa laser were corrected to the average signal detected on the camera. This was applied when measuring weak signals such as lipid bilayers and nanoparticles as we could assume the reference intensity was dominating and the fluctuations of the signal intensity due to sample changes could be neglected. The mean intensity of each frame was normalised relative to the 1st frame measured.

2.9.2.4 Phase unwrapping

An algorithm detailed in literature was applied to the data to remove phase jumps while the data was acquired.[187]

2.9.3 GV sample imaging

Suitable vesicles were located and imaged using DIC. GVs with a minimum diameter of 30 μm were selected. Therefore the sample was observed at 18 μm above the inner surface of the glass cover slip and explored laterally. Once a vesicle of sufficient size had been found it was imaged through it's axial positions using DIC to ensure that there were no internal structures. The measured diameter (D) was used to calculate the nominal top of the vesicle assuming the bottom was attached to the coverslip. This was checked by selecting vesicles which did not drift laterally, indicating their attachment. The focus was adjusted to the nominal top and observed in iGOR to ascertain the focal plane of the top surface. A convergence point could be seen under the top surface due to the focal point of the spherical top surface which occurs at a height of 3/4 of the diameter, the top surface was then adjusted by moving the focus upwards by $D/4$. Once at this height finer focus was achieved by looking at the fluctuations in the amplitude and minimising these. An offset was taken laterally shifted by some 50 μm in the same imaging plane to act as an additional reference. A typical data acquisition then used multiple focus positions to enable post-selection of the best focus plane, minimising the refocus distance required (see later). Vesicles were imaged as a time series containing batches of 1000 frames at a rate of 327 Hz with an exposure time of 3 ms. 1 batch was taken for each height imaged. Once the optimum focal height was chosen a time series of an extended length was taken, the exact time was dependent on the GPU function as at some point it no longer processed the data in real time and failed.

The camera was read in 8-bit mode for fastest read speed, lowest gain was used, for which a digit corresponded to about 120 electrons. To have a shot noise equal to this value, providing shot-noise limited detection, a reference intensity of approximately 120 counts was chosen by adjusting the half-wave plate (iG HWP)(Casix achromatic waveplate WPA465-610). The excitation intensity at the sample was chosen as high as possible within the available laser power, while not saturating the camera by the interference (allowing for a maximum signal intensity of about 20% of the reference). For single bilayers, the maximum available power was typically used provided total counts did not exceed 255, providing typically a few 10mW.

New surface reference images were taken in between vesicles.

2.9.4 Analysis pipeline

After the acquisition the data then showed the phase and amplitude in both the co- and cross- polarisation.

Linear approximation of a simple interface was used to determine the relationship between the measured reflectance (r) and thickness of a bilayer (d). Fig. 2.13 shows the relationship calculated according to Equation 2.20, where n_B is the refractive index of the bilayer. Linear approximation could be used in this case as the thickness was much smaller than the wavelength of light meaning that we could make certain approximations. Firstly, as the interference effects from different interfaces within the membrane were minimal and any phase shift from top and bottom was negligible

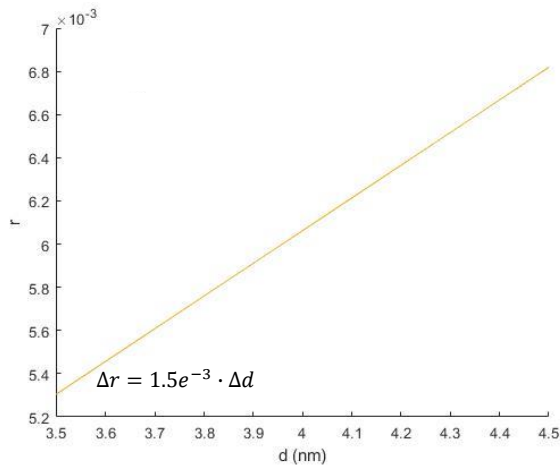


Figure 2.13: Linear approximation of bilayer reflectance Linear approximation of a lipid bilayer of the reflectivity of a lipid bilayer as function of thickness assuming a refractive index of 1.436 calculated using Equation 2.20

and therefore the overall reflection could be approximated with a simple model. We could also assume that despite the angle of incidence of the light onto the membrane it was small enough that the system could be said to have normal incidence as effects such as brewster angle and critical angle effects and the fresnel equations were simplified.[188]

Once loaded into the iGOR post analysis software (V_011) written by David Regan, a scaling option was used to convert the change of phase ($\Delta\varphi$) into a change of height (Δz) using Equation 2.18, where n_M was the refractive index of the medium, and amplitude (A) into thickness (d) using Equation 2.19, a scaling factor (α_d) was determined using linear approximation, which for a lipid bilayer is 1.5×10^{-3} . Any refocussing, cropping and phase unwrapping was also completed in this software.

To refocus data a propagation term was calculated and used to multiply data in the Fourier domain. Phase data was fitted to identify 2π jumps and these were iteratively removed. Processed images and videos were exported from this software.

$$\alpha_H = \frac{\lambda \Delta\varphi}{4\pi n_M} \quad (2.18)$$

$$\alpha_d = 1.5 \times 10^{-3} / nm \quad (2.19)$$

$$\alpha_d \approx \left| \frac{n_M - n_B}{n_M + n_B} \right| k \quad \text{where } k = \frac{2\pi n_B}{\lambda}, \quad \text{if } d \ll \lambda \quad (2.20)$$

A separate analysis code was written by myself to further process images and extract numerical values as described below. Processed images from this analysis were run back through the iGOR post analysis software (V_011).

2.9.4.1 Amplitude

Both a temporal, $\langle A \rangle_t$, and spatial, $\langle A \rangle_r$, median of the amplitude were used in accordance with Equation 2.21.

$$\langle \Delta A \rangle = \frac{A}{\langle A \rangle_t} \langle A \rangle_r \quad (2.21)$$

The time average normalised the time averaged thickness spatially which allowed the removal of any static artefacts, as we assumed that the thickness fluctuations were shorter range than the imaged size. The spatial average returned the value to the absolute reflectance of the membrane. Together these allowed the isolation of short- ranges spatial and temporal fluctuations. Image matrices were scaled using Equation 2.19.

To correct the amplitude we first made assumptions based on known characteristics of bilayers and spherical geometries. Primarily, we assumed that when averaged over the measurement time the membrane thickness is spatially homogeneous on average and we could therefore use the temporal average median $\langle A \rangle_t$ to remove any static or long range artefacts within the region of interest. Secondly, we assumed that the spatial average of the bilayer thickness was constant over time and therefore we should divide through by temporal average for each frame. Thirdly, we assumed spatial homogeneity of the bilayer in the region of interest, assuming a minimum vesicle diameter of $30\ \mu\text{m}$ the expected bending within a $10\ \mu\text{m}$ region at the top centre was less than $1\ \mu\text{m}$, these factors combined allowed us to treat the region of interest as homogenous and therefore calculate a spatial average $\langle A \rangle_r$ using the median value in space and time to renormalise the amplitude.

2.9.4.2 Phase

Further fitting was completed using 2D 2nd polynomial fitting for each frame. Within each frame if any given point was more than π from the fit it was corrected by 2π and the frame re-fit and corrected iteratively until no more corrections were required. Once the phase had been corrected the final fit for each frame was used to normalise the data and remove the overall curvature of the vesicle to better show the fluctuations of phase. Image matrices were scaled using Equation 2.18. This is further discussed in Section 6.4.3.

Chapter 3

Suspended bilayer generation

This chapter presents the protocols we developed to generate suspended bilayers for use with iGOR measurements. Due to the capability of the iGOR technique to observe fluctuations in thickness and position in suspension, we aimed to produce a stable suspended bilayer. Importantly, the bilayer needed to be separated from any other interfaces present in the sample by at least the coherence gate length of iGOR, approximately 30 μm , so as to suppress unwanted background signals that would compromise the quantitative interpretation of the data.

Several membrane systems were considered in the development process, each offering different strengths and limitations. Supported lipid bilayers (SLBs) are easy to prepare and well suited for high resolution imaging, but their close contact with a solid substrate can dampen membrane fluctuations and would be too close to the glass surface for iGOR.[189, 190] Planar bilayers formed over apertures (e.g., black lipid membranes) allow for suspended configurations but are mechanically fragile and poorly suited for long term measurements.[191, 192] Droplet interface bilayers (DIBs) offer excellent control over bilayer size and composition, including asymmetric leaflet formation, and they are compatible with electrophysiological and optical techniques.[193, 194] However, standard DIBs are often supported by agarose or formed at the oil-water interface, both of which can interfere with sensitive optical measurements like iGOR due to signal damping or refractive mismatch.[195] Giant unilamellar vesicles (GUVs) are widely used as their free standing bilayer structure avoids substrate interactions, preserving natural membrane fluctuations and mechanical behaviour, ideal for techniques like iGOR.[196, 197] They offer precise control over lipid composition, enabling studies of phase separation, membrane heterogeneity, and lipid-protein interactions. GUVs are also compatible with protein reconstitution and allow solute encapsulation, making them suitable for mimicking cellular environments and processes like membrane deformation, fusion, and tension regulation.[16, 197, 198, 199] For our uses they provide a simple model that can be made more complex as imaging with iGOR is optimised.

We focused on developing two main systems: GUVs and a modified DIB system, with our aim being to generate a stable suspended bilayer that we could use for iGOR measurements.

A protocol to generate GUVs was developed, building on an existing method used in our lab by Craig McPhee [107]. The original protocol, however, was intended for applications less sensitive to vesicle size and stability, and it did not yield vesicles suitable for our specific needs. GUVs, as spherical and fully enclosed lipid bilayers, are sensitive to changes in internal pressure. This affects membrane tension and can

lead to structural instabilities, particularly during liquid to gel phase transitions. When attempting to produce larger GUVs, we encountered instability caused by internal pressure loss.[200, 201, 202] To mitigate this, we also developed protocols to form half spherical GUVs (hs-GUVs), which are formed and measured on the same substrate. These offer improved stability and positional control compared to free floating GUVs.[203]

In parallel, we adapted a DIB system. DIBs are formed by bringing two lipid coated aqueous droplets into contact in an oil medium, such that a bilayer spontaneously forms at the interface.[195] This method allows precise control over lipid composition in each leaflet, supports electrophysiological measurements, and produces flat, planar bilayers, features that are ideal for iGOR imaging.[193, 194] In our implementation, we modified the DIB platform to ensure that the bilayer was fully suspended in aqueous buffer rather than being supported by low percentage agarose. This adjustment aimed to reduce fluctuation damping and eliminate optical artefacts introduced by the agarose layer. The DIB system is being developed in collaboration with Emma Bopp's MPhil thesis project.

Together, these methods were designed to create bilayer systems compatible with the high spatial and temporal sensitivity of iGOR, enabling reliable quantification of membrane dynamics under controlled experimental conditions.

3.1 GUV electroformation

The generation uses deposition and drying of lipids onto tantalum wires to generate a lipid film, prehydration in a humid nitrogen environment to organise the lipids into well-formed bilayers, washing off excess lipid, electroformation to produce vesicles and filtration of the GUVs to remove lipid debris as illustrated in Fig. 3.1. A detailed description of the protocol is given in Section 2.2.1. The main challenge was reproducibility of sample yields and quantity of debris in or attached to GUVs being observed after using the same nominal procedure. Protocol changes were introduced to control parameters and conditions to limit this, including the 3D printed supports to control the distance between the wires and in turn the capacitive effect of the electric field.[204] The support is described in Section 2.2.1.1. This alongside further development of the protocol is discussed in this section. We note that in literature the best parameters for electroformation are widely disputed likely due to the differing specifications for the wide range of applications these model membranes have alongside loosely controlled conditions.[205, 206, 207, 208, 209]

3.1.1 Generating a lipid film

To generate a lipid film on the tantalum wires a glass syringe was used to spread 4 mg/mL lipid solution over the lower centimetre of each wire while the wires were held horizontally in the wire support as described in Section 2.2.1.1. Glass syringes were used as they are resistant to the chloroform that some lipids are stored in and provided a better controlled expulsion than pipettes. This was done under a gentle flow of nitrogen to assist drying and to prevent lipid oxidation in line with manufacturers guidance. To ensure that all the solvent had evaporated the wires were placed in a vacuum for an hour immediately after application of the lipid, as it is known that any remaining solvent, here isopropanol, interferes with the electroformation process.[196] The resulting film quality was evaluated by imaging the wire during

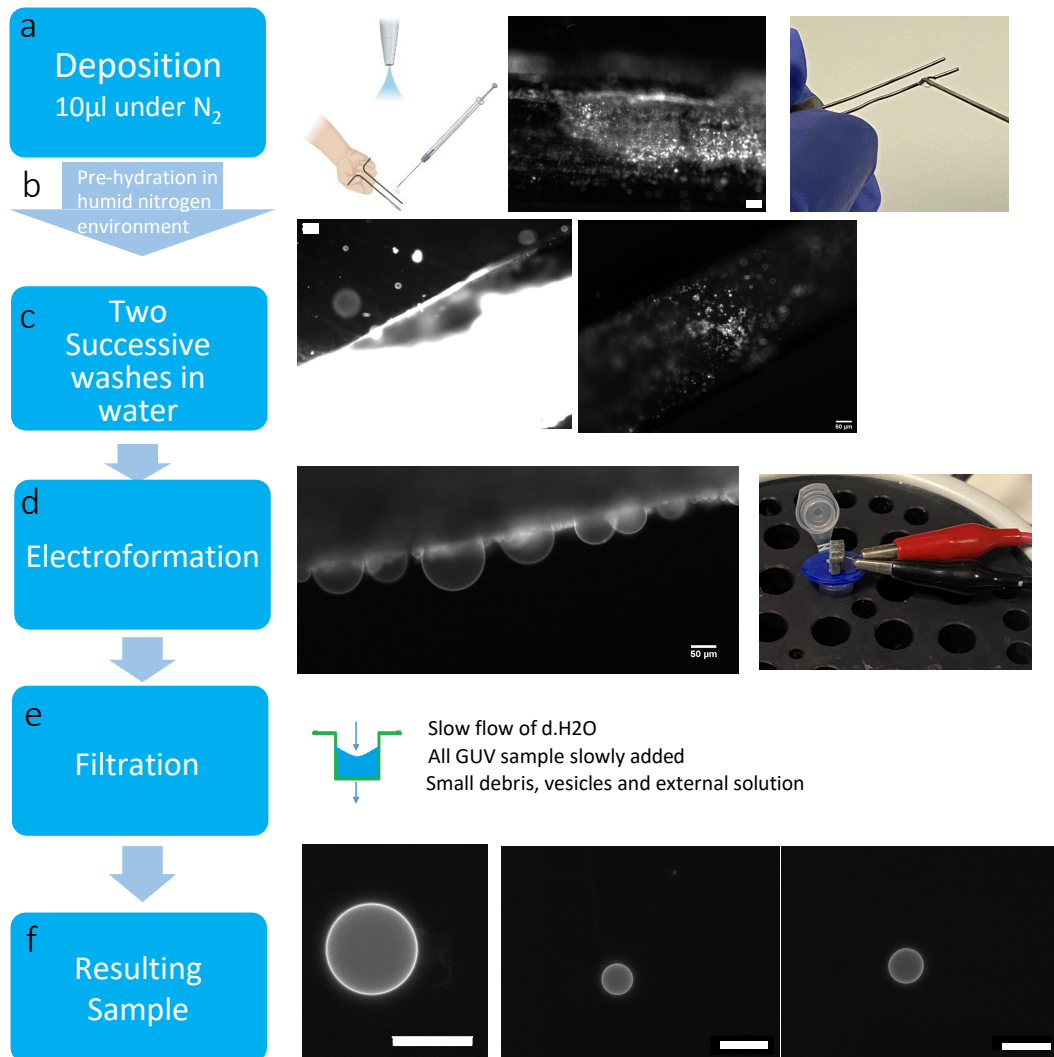


Figure 3.1: GUV development images A schematic showing the preparation protocol with epifluorescence images of highlighted steps. **a)** Deposition of lipid onto wires and an image of the lipid on the wire. **b)** Pre-hydration step which facilitates the self-organisation of lipids into bilayers. **c)** The loss of lipid debris off wires during the first and second washes. **d)** Domes produced on the wires from the bilayers alongside the electroformation set up. **e)** A schematic of the filtration used. **f)** Examples from a resulting sample containing clean vesicles. All scale bars represent 50 µm.

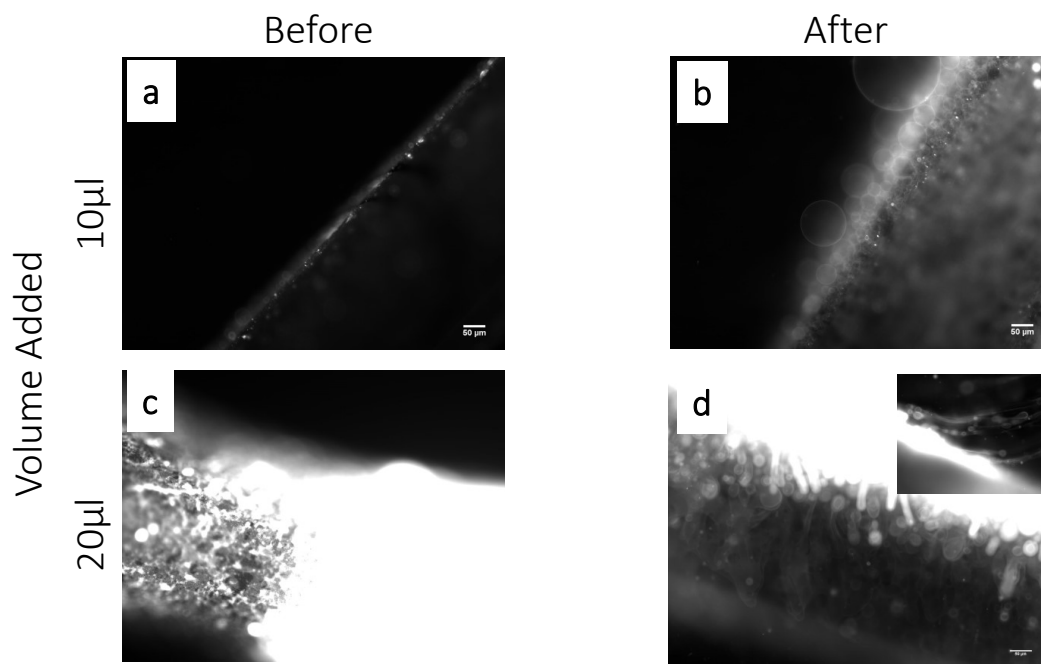


Figure 3.2: Volume of lipid applied to electrodes Epifluorescence images showing the results of electroformation alongside their starting bilayer confirmation. **a)** the initial bilayer when $5\ \mu\text{L}$ lipid was applied and the clean vesicles it produced in **b)**. In contrast **c)** shows the thick lipid layer produced with $20\ \mu\text{L}$ and its resulting messy conformations and elongated tubes in **d)**

electroformation, using fluorescence of labelled lipids (see method Section 2.7) we could compare the appearance of the lipid bilayer and its performance in electroformation of vesicles. The influence of the lipid volume applied to the wires is shown in Fig. 3.2 which shows the epifluorescence images acquired. This characterisation shows the lipid bilayer on the surface of the wires prior to electroformation and the resulting vesicles on the wire. Also shown is how these results change with a differing initial amount of lipid, with a higher volume of initial lipid $10\ \mu\text{L}$ per wire shown in Fig. 3.2c and d, the overlap of vesicles can be seen which results in multilamellar and vesicle in vesicle conformations. Elongated hs-GUVs were prone to pinch off to form smaller vesicles, however, these vesicles often never fully pinched off so formed a beads on string conformation creating a mesh, leading to aggregates. For a reduced volume of lipid of $5\ \mu\text{L}$ per wire the domes formed more cleanly, improving the sample clarity, by reducing non-GUV lipid structure as seen in Fig. 3.2a and b. From these results it was concluded that an increased thickness of lipid layer was causing fewer clean hs-GUVs on the wire and therefore a volume of $5\ \mu\text{L}$ of lipid solution per wire was chosen which as also shown in this panel generated a thinner lipid bilayer and clean vesicles on the wires.

Lipid structures were also found to form immediately after immersing the wires into water. Previously when creating lipid bilayers on surfaces, a similar effect was found to be reduced by incubation of the lipid from its dried out state, in 100% humidity, to form bilayers.[155] We therefore introduced such an incubation step as it was hypothesised the messy lipid structures observed forming were due to the lipid molecules being in an unorganised state. Lipids in an unorganised state will aim to eliminate water by forming structures such as tubes of varying diameter and

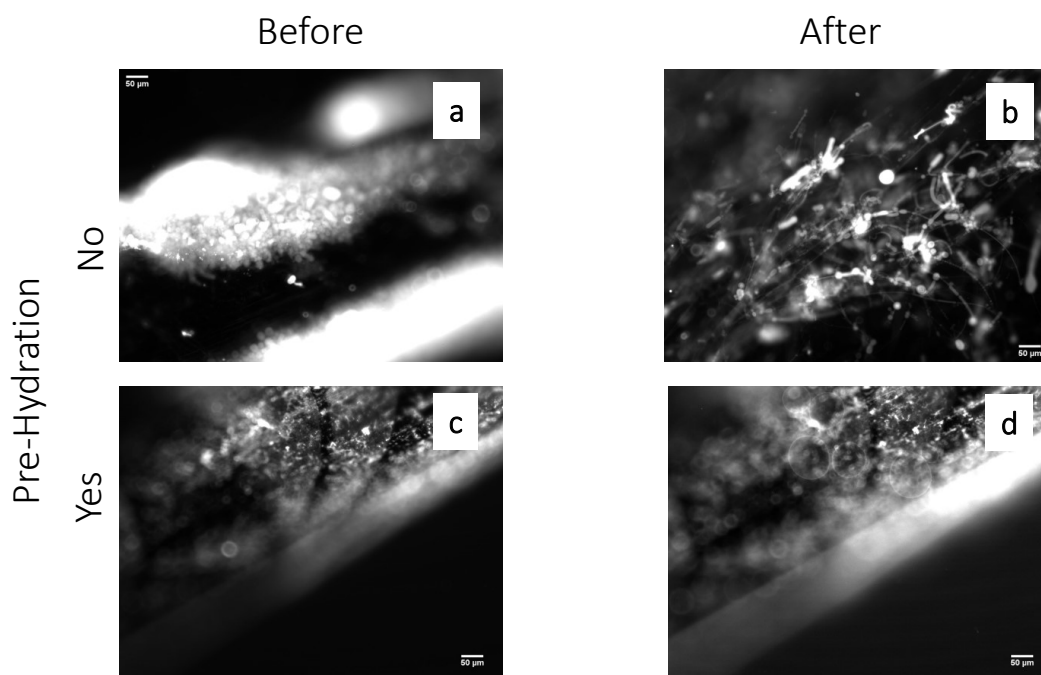


Figure 3.3: The addition of pre-hydration Epifluorescence images showing the results of electroformation alongside their starting bilayer confirmation. **a)** The initial bilayer when no pre-hydration was carried out producing no GUV conformations as demonstrated in **b)**. In contrast **c)** shows the clearer lipid layer produced with pre-hydration and its resulting spherical vesicles observed on the surface **d)**

small vesicular aggregates.[210, 211] To drive this self-organisation into a series of bilayers on the wires, the hydrophobic effect was utilised by exposing the wires to a humid environment causing the tails to orient together away from the water vapour leading to bilayer formation on the wires. A description of this step can be found in Section 2.2.1.1. To prevent peroxidation of the phospholipids nitrogen was also added to the environment. The duration of the pre-hydration was varied and the results shown in Fig. 3.3 a where the clear disorganisation of lipid on the surface can be seen alongside the resulting lipid structures not resembling vesicles in Fig. 3.3 b. Pre-hydration steps of 1,2 and 24 h were used. It was found that the increasing the time above 1 h did not improve the effect. Considering the drawbacks of longer incubation on preparation time and risk of lipid peroxidation 1 h was chosen going forward.

Wash steps were introduced prior to electroformation to remove any lipid structures spontaneously leaving the wires upon immersion. The wires were immersed into d.H₂O and left for 10 min, as described in Section 2.2.1.1. This was trialed as it could be seen in Fig. 3.4 a, that even in the absence of a current when wires are immersed in d.H₂O lipid debris was directly observed being removed into solution. However, when these wires were subsequently placed into the electroformation solution lipid debris could still be seen diffusing into solution. It was therefore decided that a further wash would be introduced using the same method as before which proved sufficient in preventing spontaneous loss of lipid debris from the bilayers upon submersion in the electroformation solution.

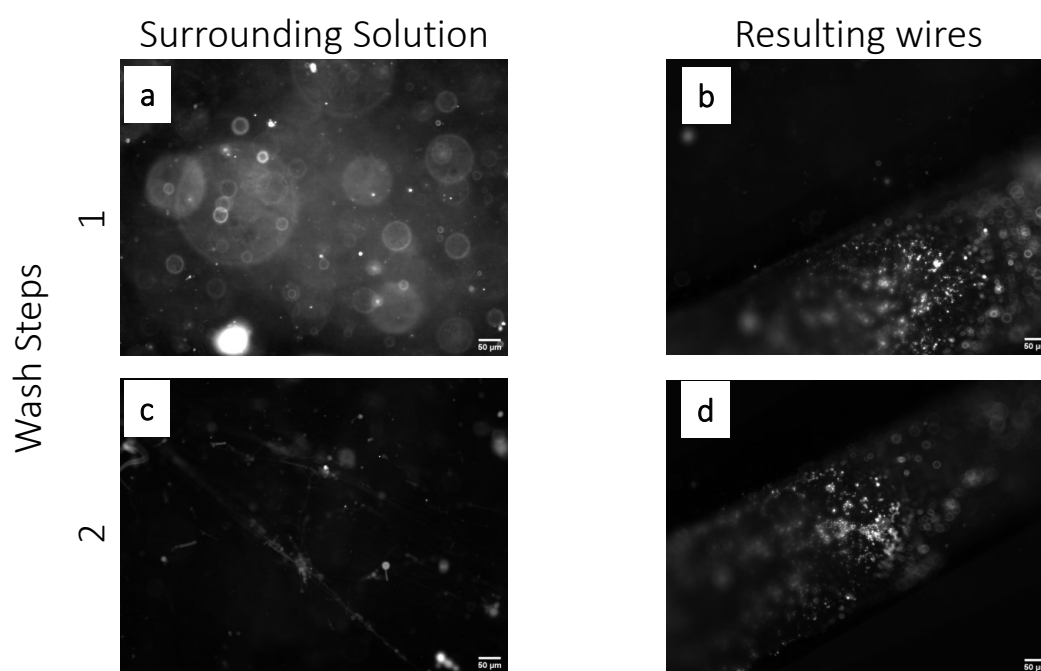


Figure 3.4: Wash steps prior to electroformation Epifluorescence images showing the results of wash steps. **a)** the surrounding solution after wires submerged during the first wash step with no current applied showing the lipid debris present. **b)** The lipid bilayer once submerged in the second wash from which debris could still be observed leaving the wires and the surrounding solution again contained debris as seen in **c)**. **d)** Shows the bilayer after a second wash from which no lipid debris was observed leaving the surface

3.1.2 Electroformation

For electroformation, as described in Section 2.2.1.2, the wires were immersed in a 0.2 mM sucrose solution and a voltage was applied to the tantalum wires. Exposure of the lipid bilayers on the wire surface to this time dependent electric field generated electrostatic forces within the lipid film destabilising the bilayer spatial distribution which allowed the structure to reshape, removing frozen-in structures of high curvature which are energetically unfavourable. It also provided sufficient energy to allow separation of flat bilayers in close proximity and lateral motion to form larger blisters which, over time, transformed into increasingly complete spherical vesicles. This made it easier for them to separate and detach from the wires. Subsequent to the separation of the bilayers they tended to form an enclosed vesicle however the mechanism for this is disputed. The prevailing theories include the field exerting a force on the lipid bilayers forcing them to separate or the water being forced in between the bilayers.[212, 213] Electrostatic interactions could also cause the fusion of smaller vesicles and incorporation of other lipids to ensure vesicles of sufficient size.[214] As the bilayers begin to separate to form vesicles, the medium surrounding the wires fills the space now created between the bilayers causing the electroformation solution to therefore become the interior solution of the vesicles once they are formed.

As discussed in the literature both the frequency and waveform type control speed and clarity of GUV production.[205, 206, 215] In terms of frequency as we were aiming for defect-free vesicles we are not using high frequencies (>100 Hz) as although they produce uniform vesicles they tend to be on the smaller side with more defects.[205] A decreased frequency increased the time to produce lipid structures however they were more likely to be defect-free and of sufficient size as they provided the same force for a longer time, allowing for larger movements of the bilayer. Sinusoidal waveforms consist of a gradual change from positive to negative peaks and therefore cause minimal abrupt forces on the membrane producing more uniform and defect free vesicles. A square waveform on the other hand is a sharp transition between a positive and a negative set value. This promotes faster vesicle formation with a higher probability of multilamellarity and internal structures.[215, 216] From the literature and previous experiments within the lab group, our starting point was a procedure with a first step applying a sinusoidal waveform at 10 Hz, 2.5 V peak-peak to grow clean hs-GUVs on the wires for 120 min and a step using a square waveform lasting 60 min with a decreasing frequency to encourage full GUV formation and vesicle release. We also used lower frequency square oscillations for the expulsion of vesicles into solution. The balance between these parameters for maximal vesicle yield and highest average diameter is widely disputed with references to many combinations cited in the literature.[205, 207]

During the optimisation, the addition of extra steps increased the duration of the procedure, over which the lipid structures could destabilise. Keeping the protocol short was crucial as induction of internal structures upon destabilisation associated with increased time would cause interference. Therefore, any steps had to be made as short as possible as shear stress during GUV formation caused defects which limited the maximum voltage which could be used.

3.1.2.1 Sinusoidal waveform to grow large bilayer domes

As a first step, medium frequency (20 Hz) sinusoidal oscillations were used for growing vesicles on the wire surface by flattening bilayers and separating them in some places to form domes, pulling the bilayers laterally and peeling the bilayers away from one another. In the original protocol this step was a 2 h, 10 Hz, 2.5 V yielding domes in excess of 30 μm size. Longer production times were detrimental as previously mentioned and thus we reduced the time to 1 h and doubled the frequency to 20 Hz. This ensured that the same number of waves pass across the bilayer and produced comparable results as demonstrated in Fig. 3.5.

The resulting domes on the wires after this step had radii in excess of 30 μm and therefore this growing step was deemed suitable for our purposes, see Fig. 3.5a-c.

3.1.2.2 Square waveform

The square waveform step had a dual purpose: to shape the hs-GUVs into GUVs on the surface of the wires and then detach them from the wires. This section of the protocol consisted of a 2.5 V waveform at 5 Hz for 30 min followed by 2 Hz for 15 min and 1 Hz for 15 min. When observing electroformation we could see that this regime was successful in generating full GUVs on the wire surface as shown in Fig. 3.5d-f.

Three steps of decreasing frequency were used to create large GUVs. A lower frequency was used to allow the bilayers more time to respond to the altered voltage, thereby giving them more time to peel off and the bilayer on the surface to reform in the space meaning when the voltage changes and the dome returned to the surface the more complete configuration was maintained and more stable. The slow progression through 5 Hz, 2 Hz and 1 Hz resulted in rounded GUVs on the wires as seen in Fig. 3.5d-f. Fig. 3.6b shows the effect of the square waveform at different frequencies of vesicles on the surface. Kymographs show how a section of pixels in an image change over time. They are a line cut taken for a set x value across the y axis of the image. This same line cut was taken for all frames in the time sequence to provide the z axis. The y axis is plotted against z to show how this line changes with time. We took a line cut of the suspended bilayer, the lower bilayer and the wire across a 1 s, 1000 frame time period. An example of this process is shown in Fig. 3.6a. These results show that the bilayers responded to the current and were experiencing a shift away from the wire and back. Interestingly, whilst most vesicles responded to the applied field, on some occasions, such as that shown in Fig. 3.7, some vesicles remained on the wire. This was taken at a low frequency of 1 Hz allowing the domes sufficient time to respond to the change of direction and a high voltage (10 V), however some areas of the bilayer were not responding in the same way by being pushed away from the wires and remaining on the bilayer surface. It has not been determined as to why this occurs as it does not appear to be size dependant, but could have been due to tethering to the surface via a tubular structure.

A very low frequency (0.1 Hz) was trialled to detach formed vesicles from the wire, increasing the voltage with time. 2 minutes at 2.5, 4, 5, 6, 8, 10, 12, 14, 16 and 20 V were used in this sequence, which did work in some cases, an example can be seen in Fig. 3.9b where a vesicle can be seen being pulled off the wire during a sharp and sustained increase in voltage at 5 V. This effect preferentially affected small vesicles as can also be seen in Fig. 3.9b. In other cases, as in the example demonstrated in the series Fig. 3.9a the sharp changes in voltages caused the deflation of hs-GUVs.

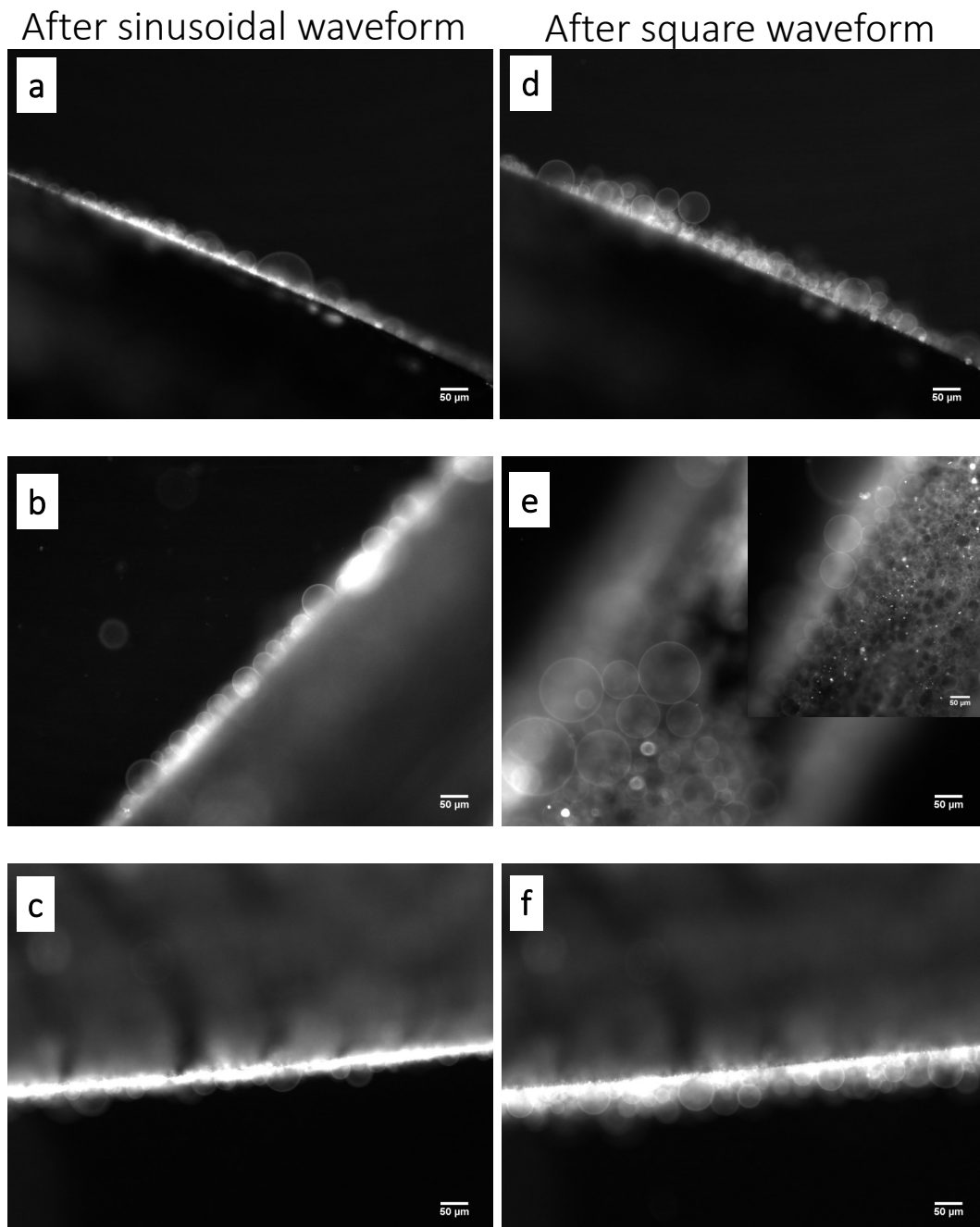


Figure 3.5: Results of the sinusoidal and square waveforms Epifluorescence images showing the results of electroformation for the same regions of wire after the sinusoidal waveforms demonstrating the generation of hs-GUVs on the surface. They are shown alongside the same domes after they had experienced a square waveform designed to push them up into vesicles on the surface of the wire ready for expulsion. **a-c)** show the domes after the sinusoidal waveform with their corresponding regions shown in **d-f)** after the square waveform

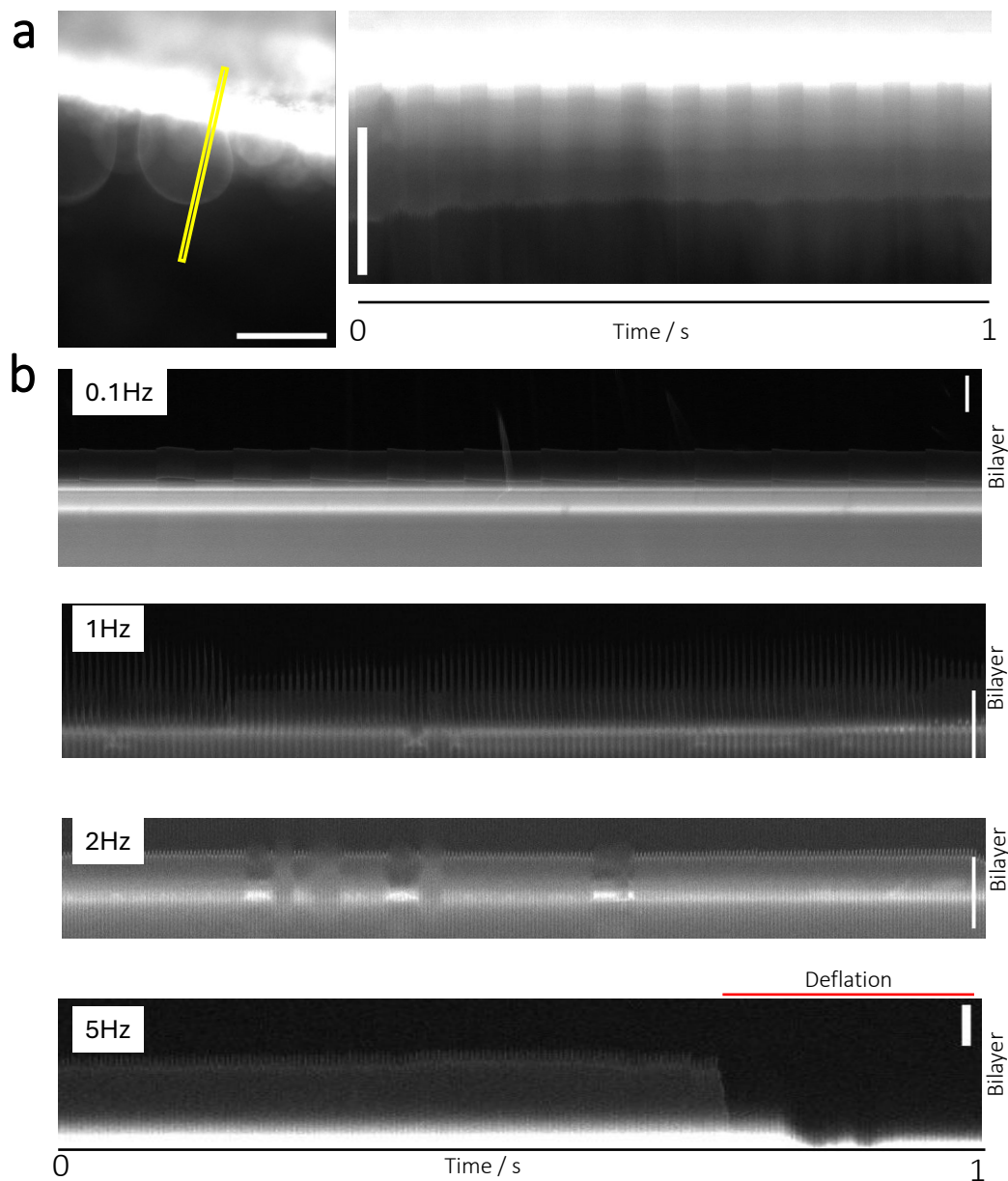


Figure 3.6: Effect of the square waveform a) Shows an example of a kymograph produced from the image shown using the section highlighted in a yellow box which becomes the y axis. The z axis shows how this region changes with time. b) Kymographs of bilayers experiencing an increasing frequency of square waves across a 1 s, 1000 frame time period, images acquired at 8 Hz. These demonstrate the effect of the waveforms in forcing the vesicles away from the wire. Vertical scale bars represent 50 μm .

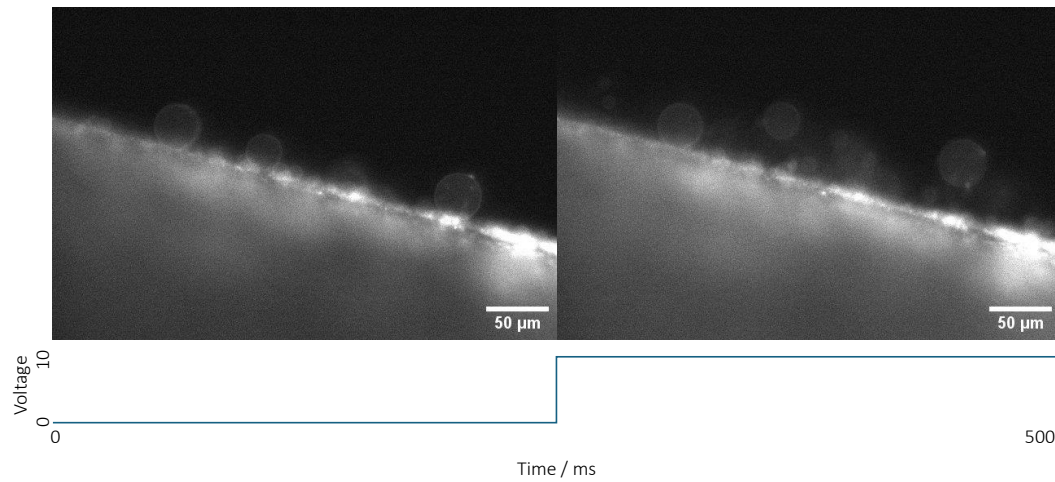


Figure 3.7: Differing responses of vesicles to high voltages Epifluorescence images showing an area of bilayer on the wire experiencing a 10 V 1 Hz waveform. Shown underneath is the waveform when each snapshot was acquired. Some vesicles can be seen responding to the applied field whilst one remained on the wire surface despite being acted on by the same field, see supplementary media file M_1_3

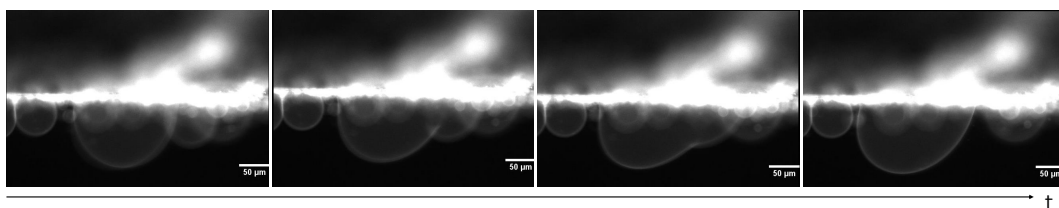


Figure 3.8: hs-GUVs combining on wire surface Epifluorescence images showing an area of bilayer on the wire where two hs-GUVs joined generating a larger hs-GUV, data taken using an amplitude of 5 V and frequency of 0.1 Hz, see supplementary media file M_1_2

It is worth noting that in both examples there were also vesicles that withstood a low frequency high voltage regime. To avoid a sharp change of amplitude deflating the hs-GUVs we used a steady increase of amplitude between specified amplitudes, where over the course of 2 min the voltage is progressively increased. An example of these results, Fig. 3.9c, shows a similar range of results with some that deflated whilst still on wires and some that remained on the wires withstanding 20 V at 0.1 Hz. Whilst it was clear that expulsion of hs-GUVs from the surface is possible via the progressive increasing of amplitude it was decided that due to the risk of deflating the vesicles and reducing the yield to keep the parameters of the square electroformation the same as original utilising a gentle knocking of the 3D printed support to expel the GUVs off of the wires to maintain a reproducible protocol.

This effect of both deflation and joining was observed when looking at a range of half-domes experiencing square waveforms as can be seen in Fig. 3.8. It was thought that by increasing the voltage of the waveforms and thus the distance from the wires, it would provide more space for full circularisation of the vesicle ready for the expulsion of them off the wire. Our measurements, however showed that the increased distance and time from the wire induced by increased voltage at the lower frequencies used, induced a range of responses such as deflation, joining the hs-GUVs together increasing their size and a minimal effect in some cases. Whilst some of these effects aid generating larger vesicles easily lost to solution, we also saw similar results at lower voltages without the loss domes via deflation, therefore a lower voltage was chosen for the final protocol as we could produce vesicles of a sufficient size, as seen in Fig. 3.5d,e and f with less chance of unwanted loss of hs-GUVs on the surface.

3.1.3 Internal solution

Sucrose has been widely used in combination with glucose as a method for generating either a sinking effect by using equal molarities or a concentration gradient across the membrane to provide osmotic pressure. This concentration gradient acts to immobilise the vesicles as glucose has a lower mass and therefore via gravity the sucrose inside the vesicle causes it to sink and generates internal pressure to improve stability.[217, 218] We found it to be just as effective to use sucrose as an internal solution with d.H₂O as an external. This proved more beneficial in the immobilisation of the vesicles as the effective mass difference between sucrose and d.H₂O is greater than that between sucrose and glucose, therefore, so was the force acting on the vesicle keeping it in close proximity to the lower glass interface when imaging. When we decreased the sucrose concentration gradient to 0.2 mM, as latterly discussed, we still observed immobilisation of vesicles on the lower glass surface that were over 30 μ m in diameter. This prevented the need for tethering using biomolecules, such as Biotin-Streptavidin binding mechanism, which could interfere with any binding and insertion events in future experiments.[219]

Using our preparation protocol we are able to generate a different internal solution to external as during filtration we exchange our external solution replacing with our filtration solution as described in Section 3.1.4. For the most part we used d.H₂O to generate a maximal concentration gradient. For our protein insertion this was altered as described in Chapter 5. 0.5 mM was initially used before we estimated the maximal molarity and resulting osmotic pressure potential that a vesicle could withstand without rupturing. This was based on a value of 5% for the maximal expansion of surface area of a vesicle. The energy in strain equation

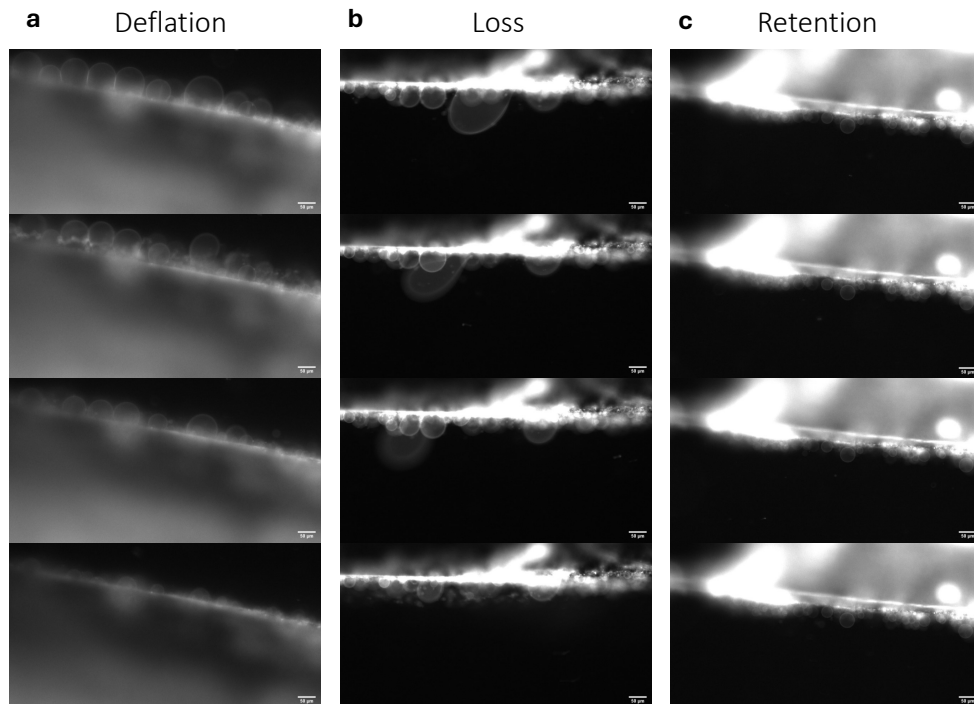


Figure 3.9: Expulsion of hs-GUVs from wires using square waveform Epifluorescence images showing the response of lipid bilayers to a high voltage (10 V), low frequency (0.1 Hz) regime in an attempt to expel hs-GUVs from the wire surface. **a)** Large scale deflation can be observed, the top image shows domes on a wire and their gradual deflation to the bottom image where very few small domes remain. **b)** The loss of vesicles from surface at 1 Hz, 10 V. A large vesicle can be seen being expelled from the wire across the series as well as many small vesicles in the bottom image. **c)** Retention of vesicles at 10 V 0.1 Hz showing an example where minimal change was observed. Supplementary media files corresponding to **a)** M_1_1, **b)** M_1_4 and **c)** M_1_5. Scale bars represent 50 μm .

(Equation 3.1) at equilibrium with the work done by pressure (p) (Equation 3.2) is shown in Equation 3.3, letting $A - A_0$ become a derivative of $4\pi r^3$.

$$E_s = \frac{1}{2}K_s \frac{(A - A_0)^2}{A_0} \quad (3.1)$$

$$p \cdot 4\pi r^2 dr = dw \quad (3.2)$$

$$dw = dE_s \quad E_s = \frac{1}{2}K_s \delta_r \left(\frac{(4\pi(r^2 - r_0^2))^2}{4\pi r_0^2} \right) dr \quad (3.3)$$

Equation 3.3 was simplified to Equation 3.4. By recombining the equations and making dw equal to dr using the equation for pressure (Equation 3.2) we arrived at Equation 3.5.

$$8\pi K_s r_0 \left(\left(\frac{r}{r_0} \right)^2 - 1 \right) \frac{r}{r_0} dr \quad (3.4)$$

$$pr = 2K_s \left(\left(\frac{r}{r_0} \right)^2 - 1 \right) \quad \text{let } x = \frac{r}{r_0} \quad \text{and } a = \frac{2K_s}{r_0} \quad (3.5)$$

Once we substituted as shown in Equation 3.5 we were left with a quadratic as shown in Equation 3.6

$$ax^2 - px - a = 0 \quad (3.6)$$

The quadratic formula was then used to find solutions and it was assumed that the solution was greater than one as we were looking for expansion, corresponding to an increase in radius (x). We also assumed a small change in radius, corresponding to stretching in the order of a few percent. This made the solution Equation 3.7.

$$x = 1 + \frac{p}{p_0} \quad \text{where } , p_0 = 2a = \frac{4K_s}{r_0} \quad (3.7)$$

Using Equation 3.7 and a K_s of 250 mN/m, $r_0 = 50 \mu\text{m}$ gives a p_0 of 0.2 bar. [220] A maximum expansion of 5% was used in our calculation to maintain a $p/p_0 < 5\%$ as the relationship is linear for small changes in radius, and $p < 0.01$ bar.

$$pV = Nk_B T \quad (3.8)$$

The osmotic pressure was calculated using Equation 3.8, assuming ideal gas law, as we were aiming for an estimate. This gave a pressure of 24.8 bar, rounded to 25 for future calculations. The critical molarity m for a $50 \mu\text{m}$ radius could therefore be described using Equations 3.9 and 3.10.

$$0.2 \text{ bar} \cdot \frac{50}{r} \cdot 0.05 = 25 \text{ bar} \cdot m \quad (3.9)$$

$$m = 20 \frac{mM \mu m}{r} \quad (3.10)$$

Thus the critical molarity, m , is 1 mM for $\varnothing = 2r = 40 \mu\text{m}$ and therefore we used concentrations below 0.4 mM for $\varnothing = 100 \mu\text{m}$ vesicles.

After generating these vesicles using an internal solution of 0.5 mM Sucrose we were still experiencing stability issues. The question we still needed to answer is

whether the the osmolarity is conserved which is further discussed in Chapter 4 where qDIC was used to further characterise vesicles. We hypothesised that the 0.5 mM sucrose was producing an internal pressure too great for one bilayer to withstand and therefore the sucrose concentration needed to be decreased. Once we decreased the sucrose concentration to 0.2 mM we observed an increased stability and clarity of our samples. An example of a sample we produced using this method is shown in Fig. 3.12 b, which shows a series of images of vesicles in this sample. The datasets analysed and discussed in Chapter 4 are a representation of samples quantitatively measured with the diameters all vesicles of a measurable size ($>3 \mu\text{m}$) represented in the histogram in Fig. 3.12 a. These samples were produced with a variety of sucrose concentration gradients.

3.1.4 Filtration

Filtration was required to decrease the density of the sample and remove small lipid structures to prevent additional interference when imaging. A filter with a mesh pore size of $20 \mu\text{m}$ was used to filter out any debris or vesicles smaller than this from the solution and to exchange out the outer liquid, full description of the method is given in Section 2.2.2. The sample was added to the top of the filter and maintained in the volume of the funnel above the mesh. A solution, in our case $\text{d.H}_2\text{O}$, was passed through the filter slowly enough not to push the GUVs into the mesh which would've destroyed them. Large enough vesicles did not pass the filter and remained above the mesh whilst smaller vesicles and other lipid structures passed through. The resulting solution that was removed from above the filter should've therefore only contained vesicles above $20 \mu\text{m}$ in diameter. The density and characteristics of the sample prior to filtration affected filtration efficiency as tubular networks and aggregates could cross-link and block the filter. This was suppressed by a cleaner initial sample which was achieved by the previously discussed procedures.

Initially to minimize the shear stress on the vesicles during filtration a directional flow through the filter was omitted. However, the reliance on diffusion through the filter via brownian motion, gravity and convection proved insufficient and the samples required multiple 12-hour filtration steps which resulted in vesicle degradation by formation of internal structures, as discussed earlier. The filter was placed in the top of a 15 mL falcon tube cut off at the bottom and placed in a 50 mL falcon tube to allow dispersal of lipid under the filter into a large volume. This was left for 12 hours and then the water exchanged and repeated. When we calculated the expected diffusion of a $20 \mu\text{m}$ vesicle relying on diffusion and gravity it would've taken 18.5 hours to move 2 cm.

To speed up the motion through the filter we added a gentle flow. This greatly reduced the time required for filtration whilst achieving a high level of filtration with a purification factor of 60, as demonstrated in Fig. 3.10. A flow rate of 0.2 mL/min was achieved and provided a flow rate that was sufficient without incurring too much force on the vesicles which could press them against the filter causing them to be lost against the filter mesh. Successful filtration is seen in Fig. 3.1. To limit the concentration of non-GUV lipid structures when filtering a large volume of unfiltered solution was limited. The volume was added sequentially in 0.2 mL parts, with each being filtered by a 1 mL flow to remove the major part of the non-GUV lipid before adding more solution.

Filtration was also used to increase the concentration of GUVs, to increase the likelihood of observing a suited GUV in the sample volume (about $15 \mu\text{L}$). As the

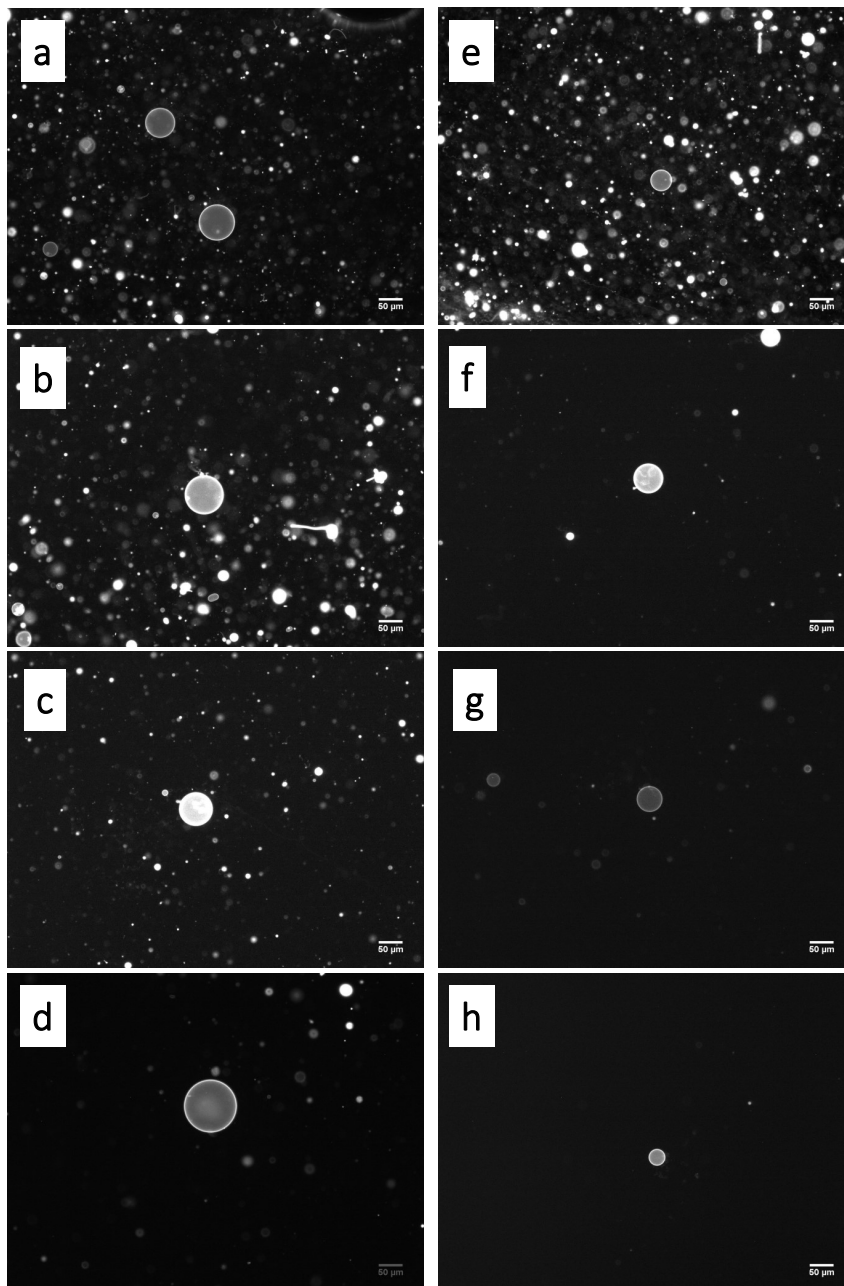


Figure 3.10: Filtration results Epifluorescence images showing filtration effects on the resulting sample relying on Brownian motion in the first column where the filter. Regions to be imaged were centred on a GV to evaluate surrounding debris. **a-d)** show the results relying on brownian motion, **a)** is the unfiltered with **b)** after the 1st 12 h filtration, **b)** and **c)** after 2nd and 3rd 12 h filtration, respectively. **e-h)** results produced using additional flow from an unfiltered sample (**e)**) to samples filtered with 5 mL (**f)**), 10 mL (**g)**) and 15 mL (**h)**) wash volume at a 2 mL/min flow rate. Clearly visible is the improved clarity when using flow as well as the improved required time taken to achieve each concentration of debris.

filtration step preferentially removed small lipid structures the subsequent sample contained an increased density of large vesicles. The sample prior to filtration was 1.2 mL which was reduced to about 0.1 mL after this filtration step. To achieve the final volume of 0.1 mL the filter was lifted up to allow the excess to flow through and ensured that the correct volume was removed from the sample, during filtration about 250 μ L was maintained above the filter. The sample was removed using a pipette tip that had been cut off at the end. As well as increasing density, the filtration step replaced the external solution and could remove soluble components such as dyes and sucrose that were in the electroformation solution. This allowed us to have different internal and external solutions, and for the osmotic pressure to be adjusted. This was useful for other experiments such as the pore insertion experiment discussed Chapter 5. Chapter 4 discusses the further characterisation of the internal solution and its impact on lamellarity leading to the reduction of sucrose concentration gradient to 0.2 mM.

3.1.5 Gel-phase lipid bilayers at room temperature

To adapt the protocol for lipid species with a phase transition temperature above room temperature, and therefore in gel phase at room temperature, we used DC₁₅PC having this transition around 32 °C. We prehydrated, washed and electroformed the vesicles at a temperature above the transition, in this case 40 °C, however we cooled the sample down before filtration and saw conformations as seen in Fig. 3.11, where the vesicle was in gel phase and contracted causing deformation. The conformations observed show that they had been cooled down below phase transition temperature while staying liquid since the area is conserved preventing the gel phase transition, and then ripped open, and immediately solidifying as they were already colder than the phase transition temperature. Whilst this protocol produced vesicles that weren't suitable for imaging as cooling of the vesicles during filtration caused destabilisation, it does show compatibility with our preparation protocol up until the filtration step as vesicles of a sufficient size were produced. It is worth bearing in mind that the filtration had not been fully optimised at this point. To maintain a liquid disordered phase during the formation of vesicles with such lipids we modified our filtration set up so we could carry it out at a controlled temperature above room temperature (see Section 2.2.2). Alongside the filtration the heat block was also set to 40 °C to keep the unfiltered sample plastic and glassware to the desired temperature. The microscope was set and maintained at a temperature of 40 °C as described in Section 2.4. To transport samples steel pillars were pre-heated to 40 °C on the heat block and pressed against the slides whilst they were being moved to the microscope. This protocol was successful in maintaining a liquid disordered phase in DC₁₅PC with a phase transition temperature above room temperature. This is demonstrated and further discussed in Section 6.10.

The resulting protocol as described in Section 2.2.1 produced samples with a sufficient density of clean vesicles as demonstrated by the histogram and fluorescence images shown in Fig. 3.12. Further characterisation of these results including lamellarity and internal sucrose concentration determination is discussed in Chapter 4. Whilst this was successful in the end we experienced stability problems which were resolved once the internal solution was investigated. For the sample preparation used in the later chapters of this thesis we could reliably produce suitable quantities of clean vesicles stable for approximately 5 hr, suitable for our work. However, alongside this we considered alternative approaches, discussed below.

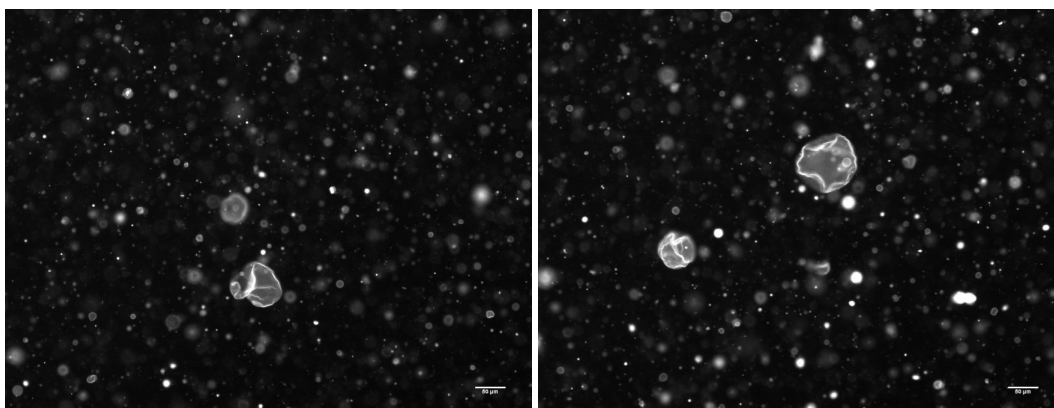


Figure 3.11: Compatibility with DC₁₅PC Epifluorescence images showing the production of vesicles using our protocol and DC₁₅PC lipid species imaged at room temperature. Images show collapsed vesicles in the gel phase characterised by the wrinkled and faceted vesicle surface.

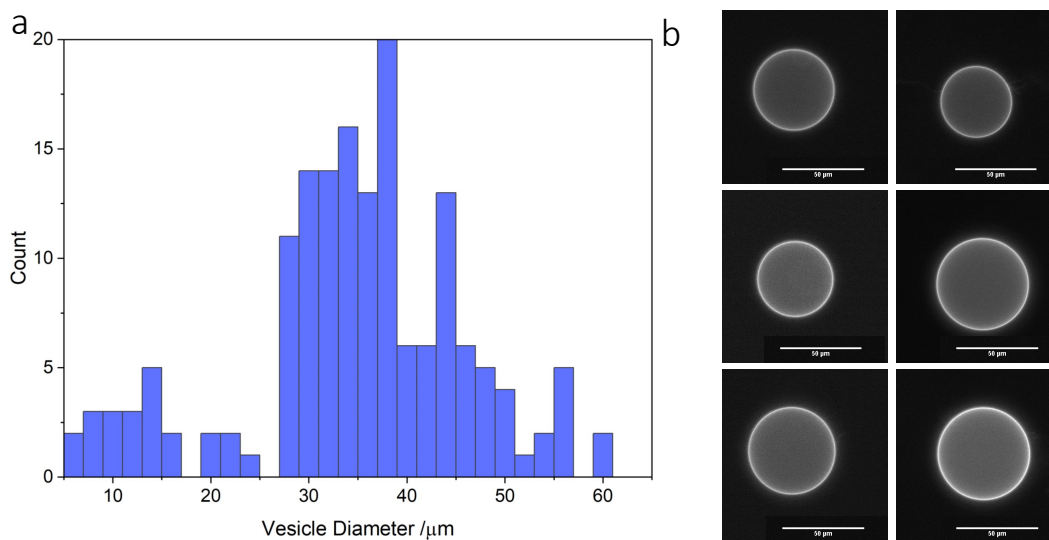


Figure 3.12: Diameter distribution of GVs a) A histogram showing the distribution of a cross-section of samples that were later used in qDIC imaging. Samples prepared using the protocol described in 2.2.1 with sucrose concentrations between 0 mM and 0.5 mM, demonstrating sufficient clean vesicles above our 30 µm threshold. b). Epifluorescence images of some clear GUVs that would be suitable for iGOR imaging. Sample was a POPC:POPE:ATTO488-DOPE (50:49.9:0.1) lipid composition. Scale bars correspond to 50 µm

3.2 hs-GUV protocol development

Considering the limitations discussed above regarding GUV samples, we considered alternatives including supported membrane models. Here, we discuss the preparation of samples providing a half-sphere conformation of lipid bilayer remaining attached to a glass surface, which can be formed in situ and are inherently immobilised on the surface. The preparation of these sample reduced handling and preparation time; found to be important when producing GUVs as discussed in the previous section.

These samples are still required a bilayer 30 μm from surfaces to be suitable for iGOR. Due to the hs-GUV conformation a diameter in excess of 60 μm was required.

When measuring the size of the hs-GUVs produced on the wires during electroformation, many of these fulfilled the size requirement as can be seen in Fig. 3.1. Therefore, by altering the electroformation parameters for example by only using sinusoidal waveform, and using them on a lipid bilayer supported by glass we should have been able to produce a similar sample to that of the hs-GUVs on the wires, in a similar way to that achieved in the McPhee and Regan paper.[107, 154] The method is described in Section 2.2.5.1 and results discussed in Section 3.2.1.

We also made efforts to optimisation the gel assisted swelling method to produce GUVs presented by Weinberger *et al.* [203]. Transferring this protocol to make it compatible with our techniques required a couple of significant changes discussed below in Section 3.2.2 with methods detailed in Section 2.2.5.2.

3.2.1 ITO electroformation

Whilst previous work in our lab produced hs-GUVs via an ITO electroformation method we found that this was not reproducible using our lipid compositions. Initially we followed the same protocol as described in the McPhee thesis.[221] For detailed methods refer back to Section 2.2.5.1. When using 300 μl DOPC lipid at a 2 mg/mL concentration spin coated onto an etched coverslip, the surface appeared patchy from which the hs-GUVs are produced. This meant that aggregates containing vesicles and lipid debris were primarily produced as seen in Fig. 3.13a. Therefore, pre-hydration and wash steps were introduced as discussed for the wire electroformation method in Section 3.1.1 with the coverslip being placed vertically in the centre of the falcon tube on top of the tissue. This caused any lipid debris that was not organised in neat bilayers on the coverslip surface to be removed.[155] The wash step was adapted and the coverslip surface was flooded and water removed before the chamber was made. Fig. 3.13b shows surfaces for which this was undertaken where distinct bilayers can be seen, with spatially homogeneous regions of fluorescence of different intensity. This shows the formation of regions with a well-defined number of bilayers in the 20-100 μm size range. Fig. 3.13b also shows a line cut across this epifluorescence image showing the distinct lamellarities observed. Whilst these bilayers looked suitable for electroformation when the current was applied minimal change was observed across the membrane with only a few aggregates being formed at the edge of the bilayers. It was also observed that there were gaps in the bilayer across the coverslip surface, which, alongside the ineffectuality of the electroformation suggested that additional bilayers were required. A higher concentration of lipid was spin coated (4 mg/mL) onto the surface however this was effective to varying degrees, with coverslips showing between one and three bilayers, and a PBS environment produced a wave confirmation across the surface. In some experiments,

seen in the bottom row of Fig. 3.13d, hs-GUVs were produced however they exhibited a low density with disordered confirmations, and in other places no hs-GUVs were produced (Fig. 3.13c). After the experiment, shown in Fig. 3.14, where during the course of electroformation the lipid layer could be seen progressively dissolving off the coverslip into solution generating debris, it was decided that we would not continue optimising this protocol and divert to developing the PVA swelling method described below.

In summary, the ITO electroformation protocol did not produce sufficient results for consideration. We could spin coat the lipid onto a coverslip to generate a sufficient bilayer on the surface but once a current of 20 Hz, sine wave with a voltage up to 2.5 V had been applied, we saw next to no change or the breakdown of the lipid bilayer as it came off the coverslip surface. The optimisation of this method was discontinued as the PVA swelling method was showing more promise as a technique for the preparation of hs-GUVs.

3.2.2 PVA swelling

Weinberger *et al.* shows the production of supported domes on a dried PVA layer, which, once re-hydrated pushes the lipid layer into hs-GUVs.[203] A stack of lipid bilayers are formed on top of a dehydrated lipid bilayer. A chamber is formed around the system and hydrated, once the water is drawn into the PVA layer the bilayers also become separated by water and swell up into domes. This protocol should inherently avoid overcrowding as, if vesicles are of a sufficient size ($>30\ \mu\text{m}$ tall), with a cross-sectional diameter of $60\ \mu\text{m}$, the distance between the top of neighbouring hs-GUVs enough. However, in practice the observed hs-GUVs did not have a spherical cross-section and therefore in some places overcrowding was an issue. This method required optimisation of wash steps beyond our time restrictions and was therefore discontinued. When imaging, samples were scanned by eye using fluorescence to gain an understanding of the whole surface, representative images were then taken for further analysis.

3.2.2.1 Establishing the PVA layer

The Weinberger protocol we based this preparation on utilised a spreading technique of $100\ \mu\text{L}$ a 5% PVA solution to generate a specified thicknesses of PVA on a coverslip, ranging from 40 to 160 nm. Work had already been undertaken in our lab to generate specified thicknesses of PVA on a hydrophilic coverslip using a spin coater to generate a homogenous layer. It was also decided that due to the geometrical constraints of our iGOR technique, the intended objective only had a $200\ \mu\text{m}$ working distance, and the PVA layer is likely to cause some degree of scattering, the thinner this layer is whilst still enabling hs-GUV production would be the best for our intended use. From this prior knowledge, we had preliminary experiments of 5% PVA solution both spin coated and spread, hereafter referred to as drop casted and described in Section 2.2.5.2, and spin coating of a 1.7% and 5% PVA solution. Fig. 3.15 shows the resulting lipid structures from these respective conditions after incubation for the hour suggested in literature. From previous measurements we know there is a 5 fold increase in PVA thickness on the coverslip between the spin coating methods with 1.7% yielding 20 nm and 5% yielding 100 nm, as discussed in work published from our group.[222] It was understood that the spin coating methods generated PVA layers much thinner than the reference material (about $7\ \mu\text{m}$),

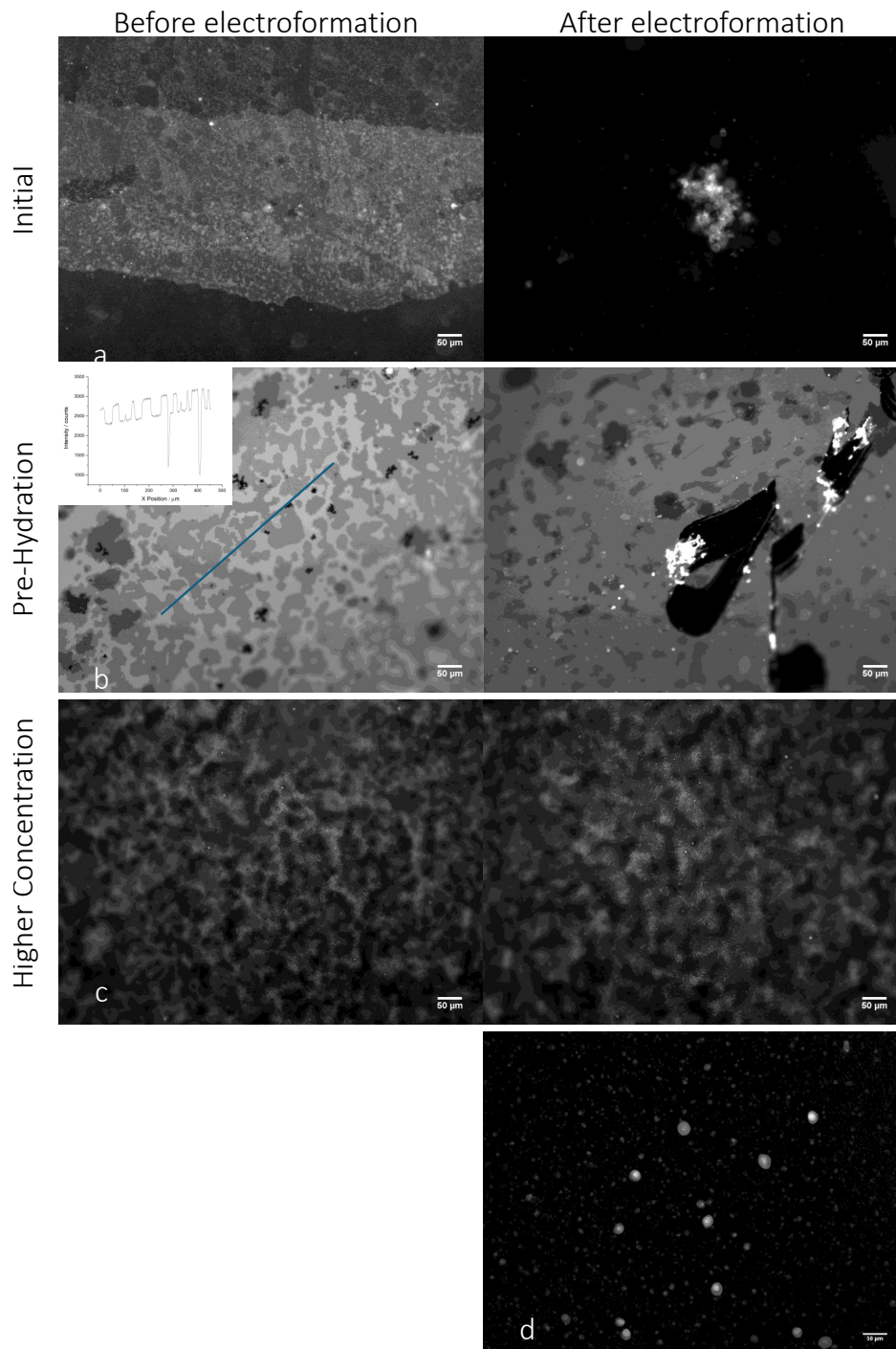


Figure 3.13: ITO electroformation development Epifluorescence images showing the electroformation results arising from a lipid bilayer produced with the nominal procedure (a) where neat bilayers can be seen with slight patching across the surface. However, after electroformation only a lipid aggregate was present. The addition of a pre-hydration step (b) produces clearly visible neat bilayers with the integrated graph showing the intensity measured along the blue line. This highlights the organisation of the surface in bilayers although it can be seen it produced only lipid aggregates. Samples produced with a higher concentration of lipid (c) and d) show lipid bilayers present prior to electroformation and an area with no *hs-GUVs* and another with a low density and disordered conformations.

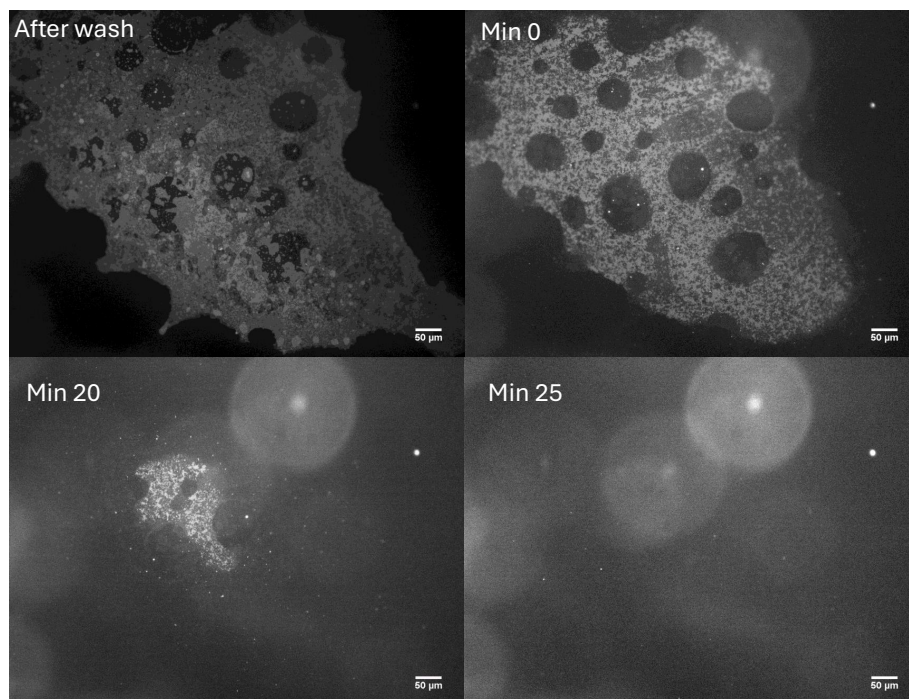


Figure 3.14: Loss of lipid from ITO surface Epifluorescence images showing an ITO surface over 25 min with no applied voltage. The images show a progressive loss of lipid into solution and the disassembly of suitable lipid bilayers for electroformation.

however if it was sufficient to support lipid swelling behaviour it would be a more reproducible method. It can be seen in Fig. 3.15a that the 1.7% PVA spincoating method produced a layer sufficient to support hs-GUV growth with vesicles of a suitable diameter formed. Fig. 3.15b and c show the results when using 5% PVA in both spin coating and drop casting methods for which the structures produced include large vesicles which are no longer supported on the surface but suspended in inflated tubular networks. As these results were produced using the same lipid concentration it could be concluded that this was due to the PVA thickness. 1.7% spincoating is the only sample that did not cause over inflation of the vesicles whilst supporting vesicle growth. Going forward these were the conditions used as the spincoating method reproducibly generated a smoother surface.

In terms of volume applied to the spin coating it was observed that a 5 fold volume increase, from 20 μL to 100 μL , of PVA solution does not impact the resulting thickness of the layer that is produced.[222] It was determined that the lower limit of volume required depended on the centring of the coverslip on the spin coater. Any imbalance caused more solution to spin off one side leaving an uncoated region opposite, one such boarder left from this can be seen in Fig. 3.16. To avoid this a volume of 100 μL was used going forward. This could also be assessed prior to the application of the lipid bilayer by eye as a tide mark type edge could be seen if held up to the light.

3.2.2.2 Establishing the lipid bilayer

Weinbergers protocol used 10-20 μL lipid at a concentration of 1 mg/mL spread onto the PVA layer, generating a thickness in the order of 5 μm , as with the PVA layer we

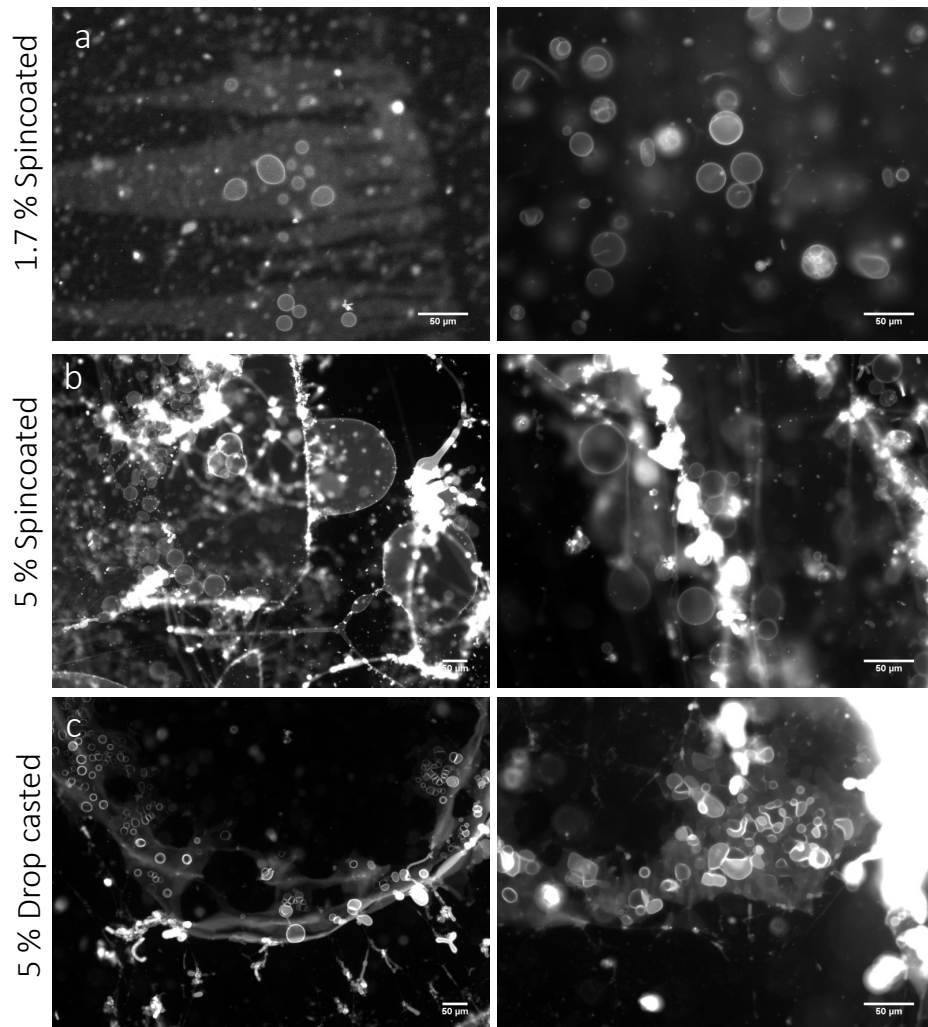


Figure 3.15: Establishing a PVA layer All samples contained 1 mg/mL lipid spin coated on top and incubated for 1 h **a)** Resulting sample after 1.7% spincoated lipid demonstrating *hs-GUVs* present on the lipid surface. **b)** and **c)** 5% PVA solution applied using spincoating (**b)** or drop casting (**c)** where similar aggregated and tubular conformations can be seen suspended from the surface to a lesser extent after using drop-casting and producing large networks after spin coating.

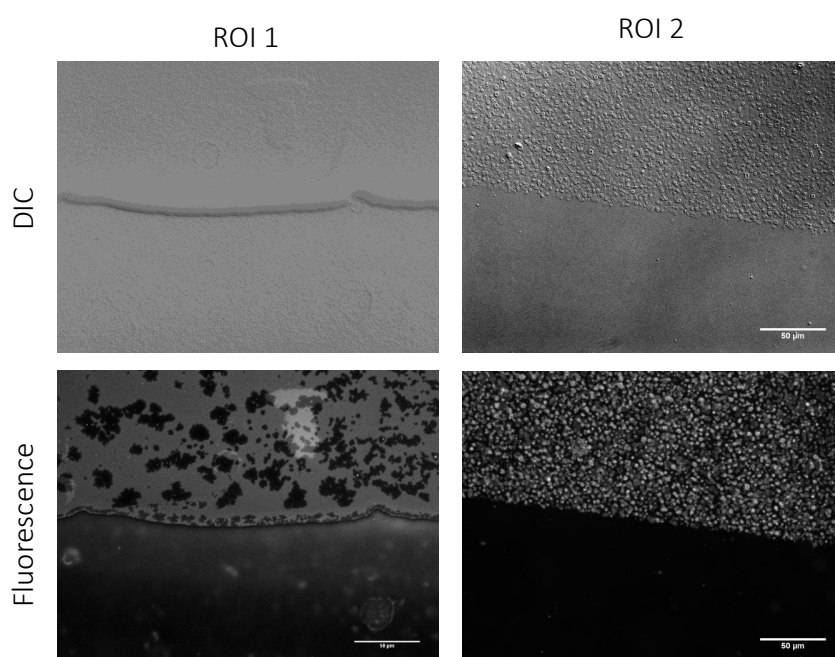


Figure 3.16: PVA sample heterogeneity A PVA border seen in both qDIC and epifluorescence in **a)** in contrast to **b)** where an apparent border seen in epifluorescence, but not in qDIC. This suggests it is not a PVA border just an border where the lipid bilayer stopped forming. qDIC images taken using 20x 0.75 NA objective with a 1.5x tube lens, averaged over 256 images, 100ms exposure time.

introduced spin coating to increase the homogeneity of the layer. A concentration series of 1, 2 and 4 mg/mL was used. This was in line with methods producing suitable lipid layers in ITO experiments (see Fig. 3.13b) discussed above, where we spin coated a 2 mg/mL to generate a lipid bilayer as discussed in work to produce supported lipid bilayers. The spin parameters were taken from this work.[155] It can be seen in Fig. 3.17 that 1 mg/mL was insufficient to generate a homogenous layer on the PVA surface. Some areas were sufficient for hs-GUV formation however, there are also areas with no lipid coverage. Contrastingly, 4 mg/mL of lipid produced results shown in Fig. 3.17c which demonstrates a too dense lipid coverage which generated non spherical protrusions with some resembling tubes. These would have top surfaces not still enough for intended imaging. Whilst the lower, wider structures highlighted in red would generate suspended freely fluctuating bilayers as intended, smaller protrusions and vesicles can be seen forming underneath which would render these structures unsuitable for iGOR. The 2 mg/mL samples did not exhibit a homogeneous lipid layer, however, in sufficient areas across the membrane hs-GUVs were observed. However, alongside this, production of lipid debris increased which, after the later discussed wash steps could not be removed and therefore 1 mg/mL was used to minimise this effect.

As pre-hydration steps have been shown to improve the organisation of lipids on a surface, discussed in Section 3.2.1. We added steps in the same way to this protocol to establish bilayer organisation on the coverslips using the method proven effective in both wire and ITO electroformation, consisting of a 1 h incubation in a humid nitrogen environment. Confirmation that this is effective in this protocol is shown in Fig. 3.19 where a reduction of tubes and non vesicular lipid structures can be seen.

One observation made from the data shown in Fig. 3.17 was that the vesicles produced were of insufficient size and the top surface of hs-GUVs would be within 30 μm of the surface and therefore cause interference. After leaving the domes to develop for a longer period of time, examples of which can be seen in Fig. 3.20 where b) shows that the hs-GUVs produced within 20 minutes were of a sufficient diameter but not of sufficient height, a) shows hs-GUVs that were considerably smaller however both did grow overnight as seen in the data taken 24 h later. Row c) shows an area from which at least one hs-GUV was of sufficient height. What can also be seen from these 24 h experiments was the large scale phase separation observed from the compartmentalisation of fluorophore in some areas of the domes. This effect is discussed further in Section 5.1.2. After 24 hours a possible cause of this is oxidation of the lipid. It could also be that the fluorophore was expelled from the edges showing a more gradual gradient and upper part of the vesicles as highlighted in the zoomed region. The sharp rings at the edges suggests that the bilayer was nearly vertical at this point, which also implies that the height of the vesicle should've been sufficient, but when refocussing there was nothing to see. The fluorophore appeared to be going into regions of higher curvature which had two leaflets of different packing density as the fluorophore, DOPE could've partitioned into one where it would've been better accommodated as demonstrated in Fig. 3.18. This effect was not seen in Fig. 3.19 where vesicles were imaged after a short incubation and at a significant height above the surface, seen as the surface bilayer is defocussed.

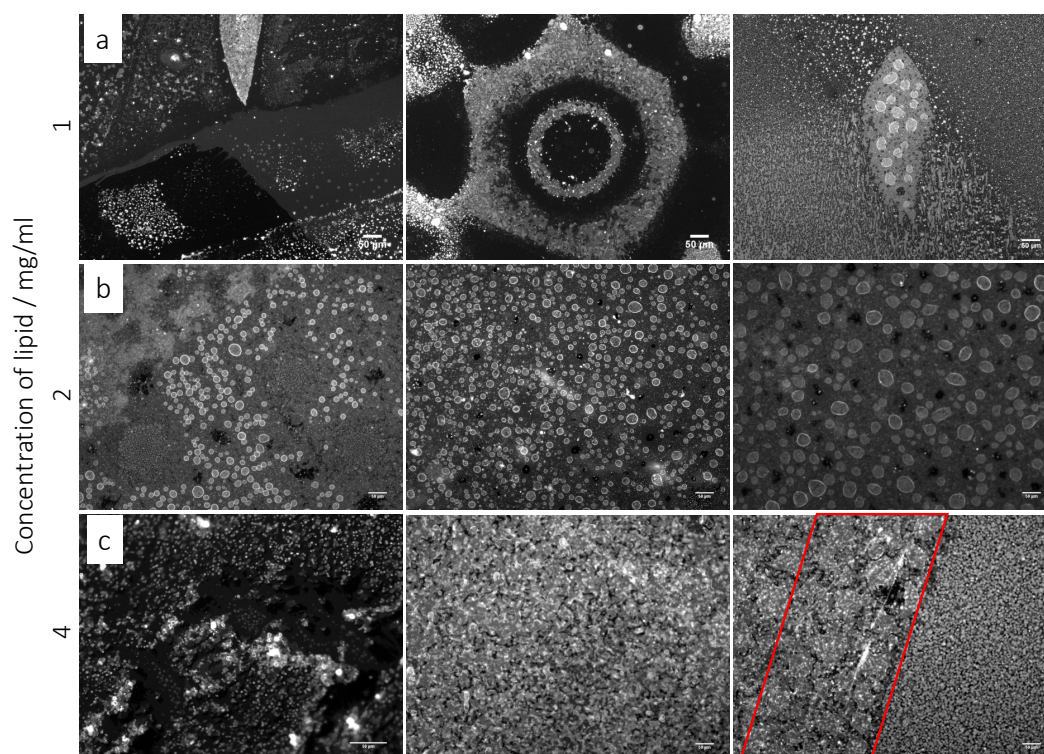


Figure 3.17: Establishing a lipid bilayer ontop of PVA Images of the resulting surface after the nominal PVA swelling procedure described in Section 2.2.5.2 with varying concentrations of lipid spin coated, 1 mg/ml (**a**), 2 mg/ml (**b**) and 4 mg/ml (**c**) with a highlighted region showing the large low domes discussed. No wash steps were in place at this time. **a**) shows a heterogeneous surface with areas of patchy lipid and areas with no lipid present and only a few that produced hs-GUVs. **b**) shows a more contiguous lipid layer despite being patchy. It also demonstrates the ability to produce hs-GUVs of sufficient size and density across a larger area of the surface. **c**) demonstrates a thicker lipid layer which, in the places where lipid structures were formed, formed over-inflated structures with other lipid debris underneath. However, it can also be seen that there was still heterogeneity present in these samples.

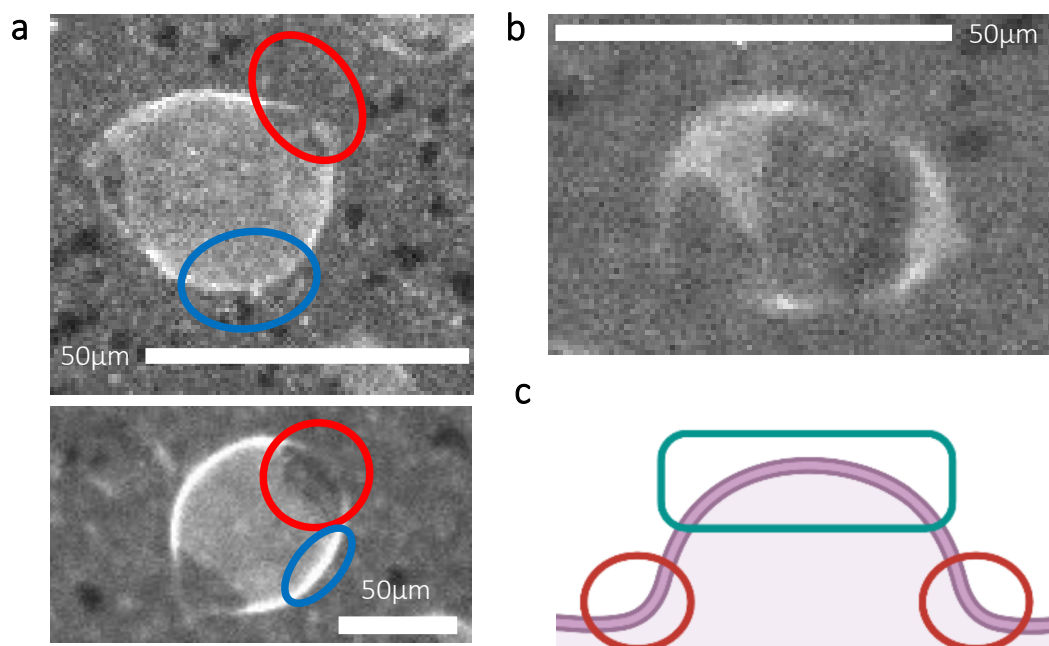


Figure 3.18: Partitioning of fluorophore into areas of differing curvature **a)** Partitioning of fluorophore into regions of high curvature (blue) and out of regions with gradual gradient (red). **b)** Partitioning of fluorophore out of top surface of *hs-GUV*. **c)** schematic showing areas of high curvature across the top (cyan) and edge (red) of *hs-GUVs*.

3.2.2.3 Washing methods

As determined from the wires for electroformation lipid debris was released from the surface upon the addition of solution. This debris would cause interference in iGOR. To remove this debris from solution, the wetting step was refined and followed by washing steps. This required a compromise between aggressive enough washing to remove loose lipid without it disrupting the layer established after pre-hydration. The wetting procedure originally consisted of the coverslip being gently pressed down onto a pre-filled imaging spacer to create a chamber.

Adding a drop of solution on a surface tilted to a 45° angle which subsequently slides down the surface caused the complete loss of liquid in the path of the droplet (Fig. 3.22b). Submersion of the coverslip into water horizontally with the lipid layer face down also resulted in disruption of the lipid bilayer in a way that prevented large *hs-GUV* formation as there was not a large enough contiguous area to support such a formation. In other samples it proved insufficient in removing debris and appeared to lead to the production of small tubular structures, likely arising from the smaller areas of continuous surface lipid, as seen in Fig. 3.22a.

By putting the gasket on the lipid covered coverslip first instead of the slide it allowed a different wash step to be introduced. This was done by adding an excess of water (50 μL) to the well, leaving for 10 min and removing the majority, leaving the 20 μL required to fill the chamber. Whilst this did not significantly disrupt the lipid surface aside from the generation of a concentric circle pattern due to the force of water being pulled up from the centre it also proved insufficient in removing debris from the surface for iGOR imaging (Fig. 3.22c). The addition of extra agitating via triturating the excess water before removal from the gasket provided extra force for

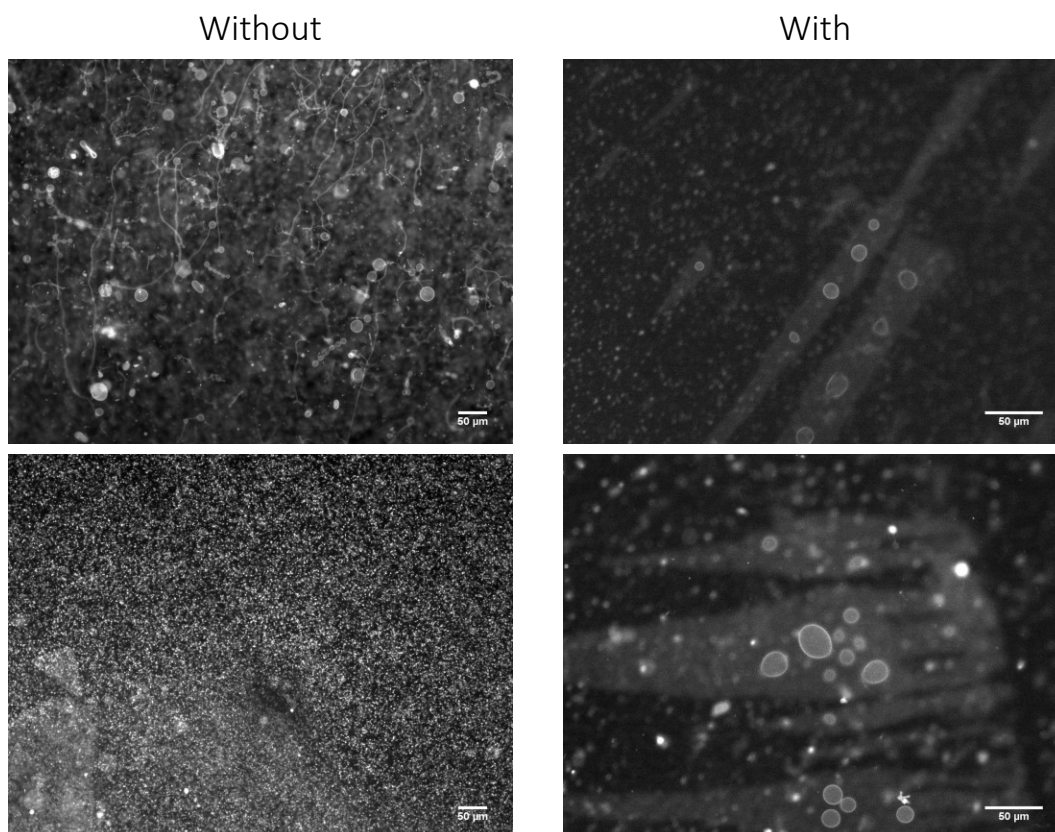


Figure 3.19: Introducing pre-hydration to PVA swelling Epifluorescence images taken after 1 h PVA swelling nominal procedure described in Section 2.2.5.2 either with or without a pre-hydration step, no wash steps were in place at this time. Without pre-hydration the formation of tubular structures can be seen as well as small lipid structures produced on the surface which rendered the samples unsuitable. For the samples with a pre-hydration step fewer small lipid structures can be seen with more hs-GUV conformations observed.

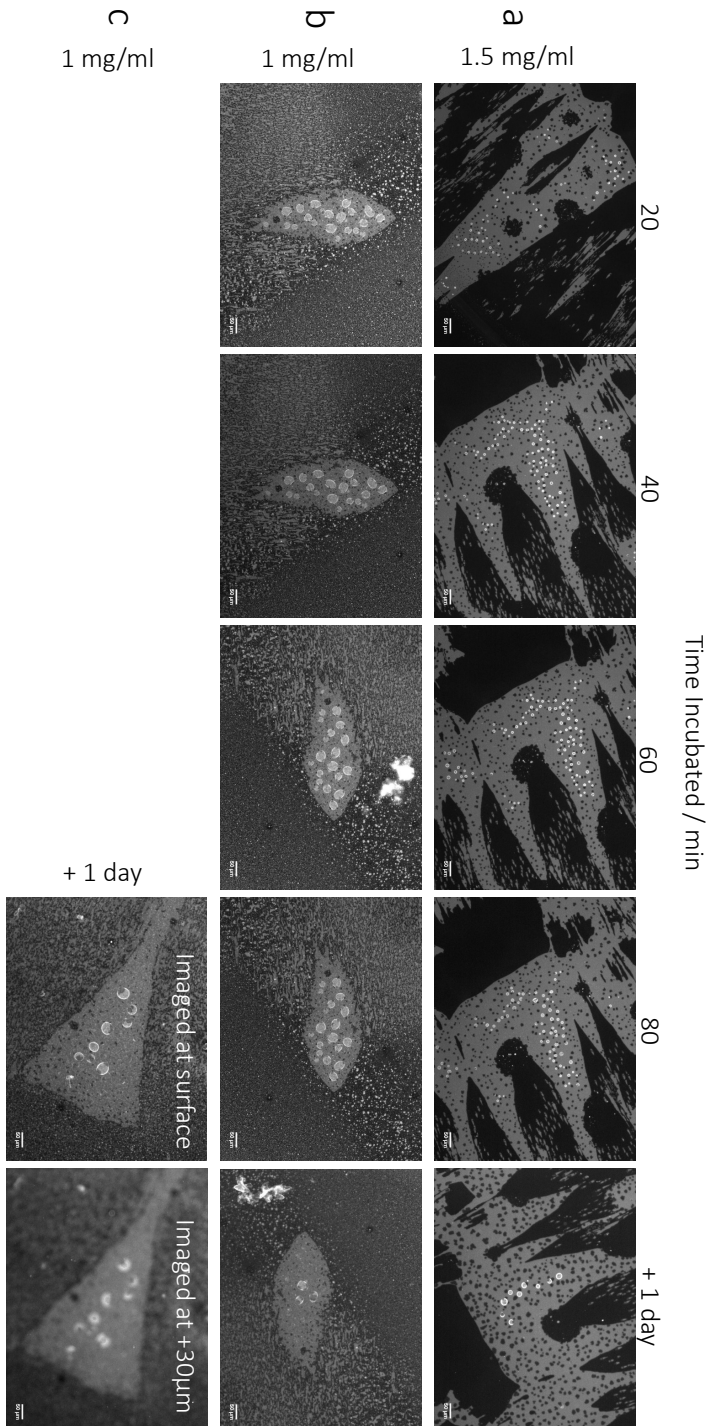


Figure 3.20: Results of longer incubation time PVA and lipid surfaces after incubation times ranging from 20 min to 24 h, results shown **b)** produced with a higher lipid concentration. Otherwise protocol was as described in Section 2.2.5.2. A trend of increased *hs-GUV* size can be observed across the examples shown with the example in **c)** having a surface 30 μm above the surface. However, it was accompanied by a decrease in *hs-GUV*s present and phase separation across the dome surface.

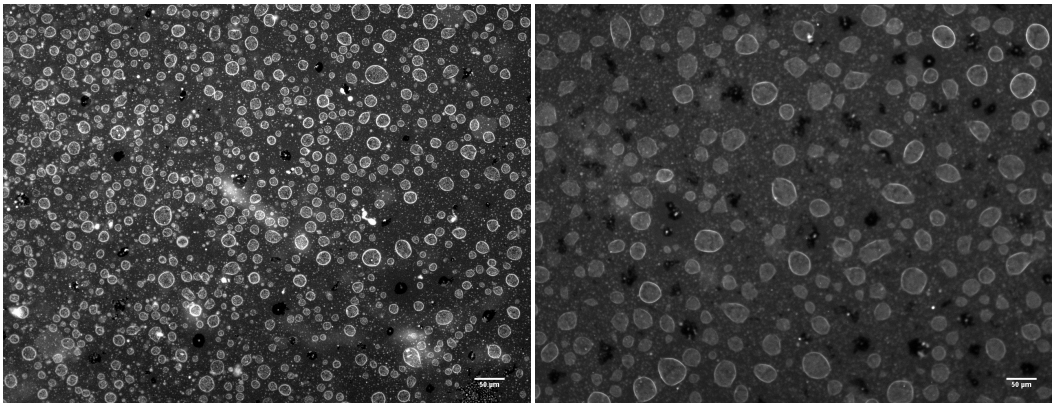


Figure 3.21: PVA hs-GUV production Epifluorescence images of a suitable sample, however this was not reproducible enough for our uses. A suitable sample was characterised by spatially separated hs-GUVs with multiple within a field of view. They were also confirmed to have surfaces at least $30\ \mu\text{m}$ from the lipid layer.

the removal of those lipids not formed into bilayers. This trituration method was deemed sufficient for our methods using epifluorescence as seen in Fig. 3.22d where we were able to produce minimal debris and bilayers that could support larger hs-GUVs, however once higher magnification images were taken using DIC it could be seen that the hs-GUVs produced were of insufficient size and contained a significant proportion of vesicle in vesicle structures.

A more gentle method was attempted to generate large hs-GUVs by creating a small channel in the imaging spacer which was placed in a slightly under-pressured environment allowing the chamber to fill slowly. This method is depicted in Fig. 3.22e. An under-pressured environment was generated by placing in a dessicator and degassed for 5 min to have the air diffuse through chamber and allow the water to slowly enter, then once fully wetted, the liquid can flow to the large surrounding volume to diffuse the lipid debris away from the surface. This solution was left for varying periods of time in an effort to remove any lipid debris that would spontaneously fall off into solution however this produced a patchy lipid surface that could not support sufficient dome formation, this was observed in multiple attempts with a representative image shown in Fig. 3.22e.

3.2.2.4 PVA swelling summary

When observing the hs-GUVs produced from the final protocol in Fig. 3.21b that were of a suitable size we found they often phase separated overtime, which is not necessarily an issue for iGOR. However, the smaller hs-GUVs like those seen in Fig. 3.20a did not show the same phase separated conformation. We have presented potential methods to wash the bilayers in an aim to create minimal debris in solution. Whilst we could not reach a suitable level of reproducibility for continued use we could generate hs-GUVs of a sufficient size and density, highlighted in Fig. 3.21b.

Inconsistencies appeared to be due to the spin coating of both the PVA and lipid solution as this base-layer appeared different in the samples, resulting in drastically different hs-GUV conformations. Spin coating was used to provide a well defined film with the same parameters as those specified in Section 2.2.5.2. The same volumes

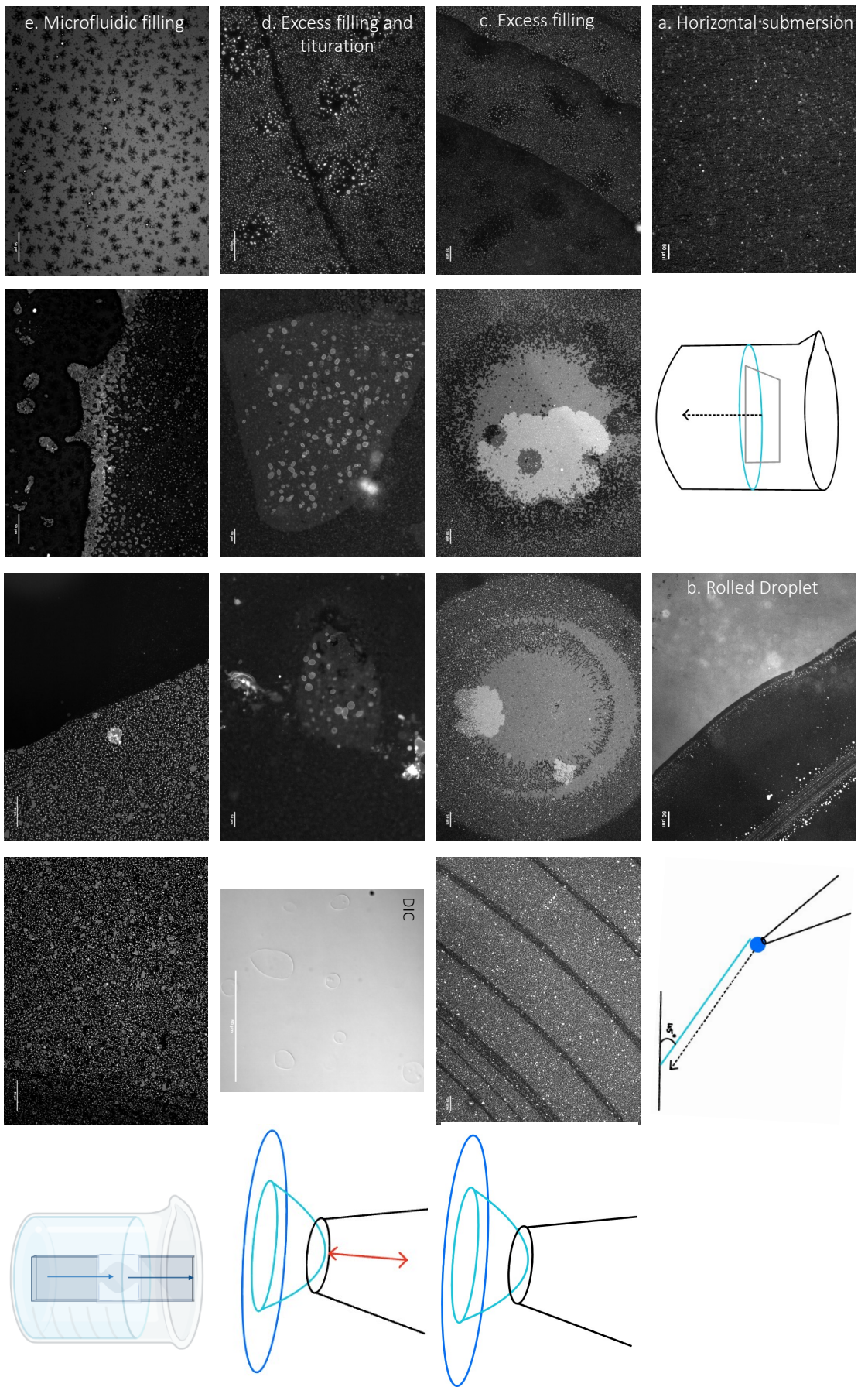


Figure 3.22: Washing method for PVA supported lipid bilayer Epifluorescence images of lipid surface after the prescribed washing method alongside sketches of the method used including horizontal submersion (a), rolled droplet (b), excess filling (c), excess filling with titration, with a DIC image of higher magnification at 30 μm from surface (d) and microfluidic filling (e)

and compositions were applied every time to a coverslip that had been cleaned with a hydrogen peroxide treatment that made the surface hydrophilic, in work described in [222], this aided PVA spin coating. When looking at the qDIC images of borders found within the sample (Fig. 3.16) some could be seen in fluorescence and qDIC, indicating that there was a lack of either PVA or lipid bilayer in this area. However, some were not accompanied by a change in DIC signal. This lack of fluorescence was therefore likely caused by a large scale phase separation of the lipids with the fluorophore separating into one. This could be seen by the gaps in fluorescence that were not present in qDIC indicating that there was still lipid in these regions. The separation could be observed in samples within an hour of production. The reason for this large scale separation is unknown but meant that we wouldn't always know the composition of any hs-GUVs present, it also seemed that only one lipid species supported hs-GUV which could've limited future work.

3.3 Droplet interface bilayers

Starting from the experience of the Castell lab we adapted their droplet interface bilayer (DIB) samples to make them compatible with iGOR.[195] Phospholipids form a monolayer at a water/oil interface due to their amphipathic nature. A monolayer was formed on a low percentage agarose gel covered by oil/ phospholipid solution where phospholipids self assembled with tails facing into the oil. Small droplets of isotonic buffer (KCl^-) were placed into solution in the well of the incubation tray and phospholipids oriented around the edge of the droplet. This droplet was transferred into the well of the device as close to the agarose layer as possible. When this droplet interacted with the monolayer at the bottom of the well a bilayer was formed as shown in Fig. 3.23a. The agarose was 0.1% (w/v) which, whilst did not impact the total internal reflection fluorescence (TIRF) used in their experiments, it would have caused interference when imaging using iGOR. The main drawback with this method for observing dynamics is the damping that the membrane will experience from the agarose.

3.3.1 Unmodified device

Initial characterisation of the device used by the Castell lab was undertaken using their protocol to generate DIBs as described in Section 2.2.6.1 and is depicted in Fig. 3.23a. The purpose of this study was to measure the bilayers produced using DIC and design the updated device and methods for use, for this reason we used a DPhPC lipid as it is well established in the Castell lab which allowed us to focus on device design. As seen in Fig. 3.23b and c we could produce stable droplets that joined with each other to form bilayers away from the surface freely fluctuating and isolated bilayers at the bottom of the wells that formed bilayers with the monolayer supported on agarose. As the droplets were larger the edges and top of the bilayer, the regions we are not intending to use, were well outside our coherence length and therefore suitable for iGOR. When the lipids droplets broke down they formed lipid inclusions on the agarose surface which was easy to see in DIC, meaning we could identify when the droplet had started degrading. These results were obtained using DPhPC and imaged with a total phase offset of 15° . We also observed that wells containing multiple small droplets tended to be less stable with droplets often fusing to form large droplets that only contained a bilayer at the lower surface. It was also

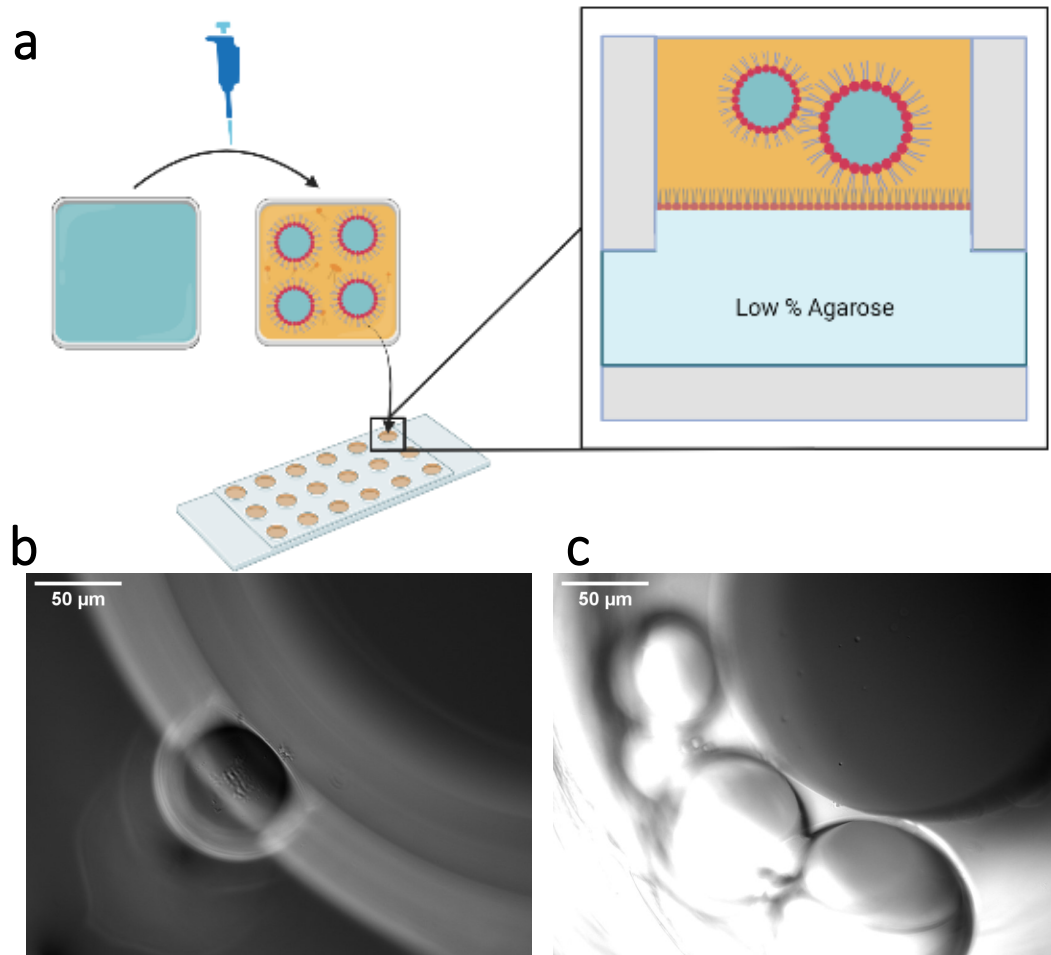


Figure 3.23: Droplet interface bilayer samples a) A schematic showing the preparation of Droplet Interface Bilayer samples as previously described and the resulting lipid bilayer observed in **b)** and **c)**, produced with DPhPC and imaged above the surface of each droplet using DIC with images taken at an angle of positive 15° . The image in **b)** shows a sharp interface between droplets indicating the presence of a lipid bilayer. **c)** shows a sharp interface at the base of the large droplet, characteristic of a lipid bilayer where the monolayer on top of the agarose layer formed a bilayer with the monolayer of the droplet.

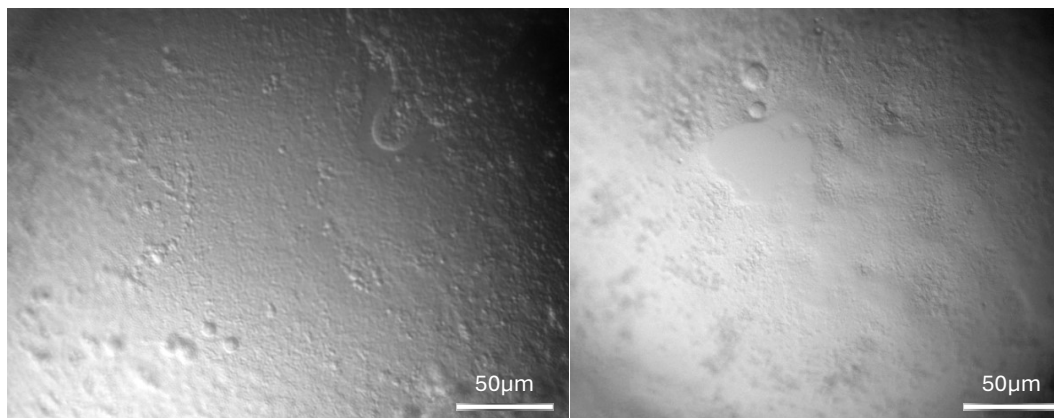


Figure 3.24: DIC images of agarose Layer DIC images taken at $+15^\circ$ showing the surface of the agarose layer within the modified DIB device. It can be seen that the surface is not smooth and would subsequently cause interference when using iGOR.

observed that the interfaces of interest were not all clear with aberrations either in the agarose layer or adjoined to the membrane.

In response to these results we, alongside the Castell research group, designed a modified device to make these model systems compatible with iGOR. These designs are discussed below.

3.3.2 Device with deeper agarose layer

The original device was designed by the Castell group for use on their TIRF system, where the agarose layer was as thin as possible. For use with iGOR the distance between the coverslip and the monolayer needed to be larger than $30\ \mu\text{m}$ which meant that the modified device had to have a larger indent for the agarose above the coverslip. The sketches for this design are shown in Appendix A.5.

As a main advantage of iGOR microscopy is the ability to observe suspended lipid membranes. We intended to use 2 methods for the generation of suspended bilayers: an aggregation of small droplets that interact with each other to generate bilayers away from the surface supported monolayer or stamping the gel to generate areas of the bilayer that are unsupported and can fluctuate more freely.

There were problems encountered when trying to mill the device in the usual way: cutting plastic away to mould the device, where drill bits kept breaking. To overcome these challenges multiphoton lithography was used to print the new device. In this way a new device was created with a space for $50\ \mu\text{m}$ agarose underneath the monolayer.

Despite this device producing a lipid system with the required dimensions, after imaging with iGOR it highlighted that the agarose layer despite being low percentage was not smooth enough to treat as a surface for referencing Fig. 3.24. The device also showed significant decay once cleaned and was therefore no longer useable. Although these limitations could be overcome it was decided that a device utilising a monolayer formed on top of a buffer solution in a much smaller device would be the better way forward. This is discussed below.

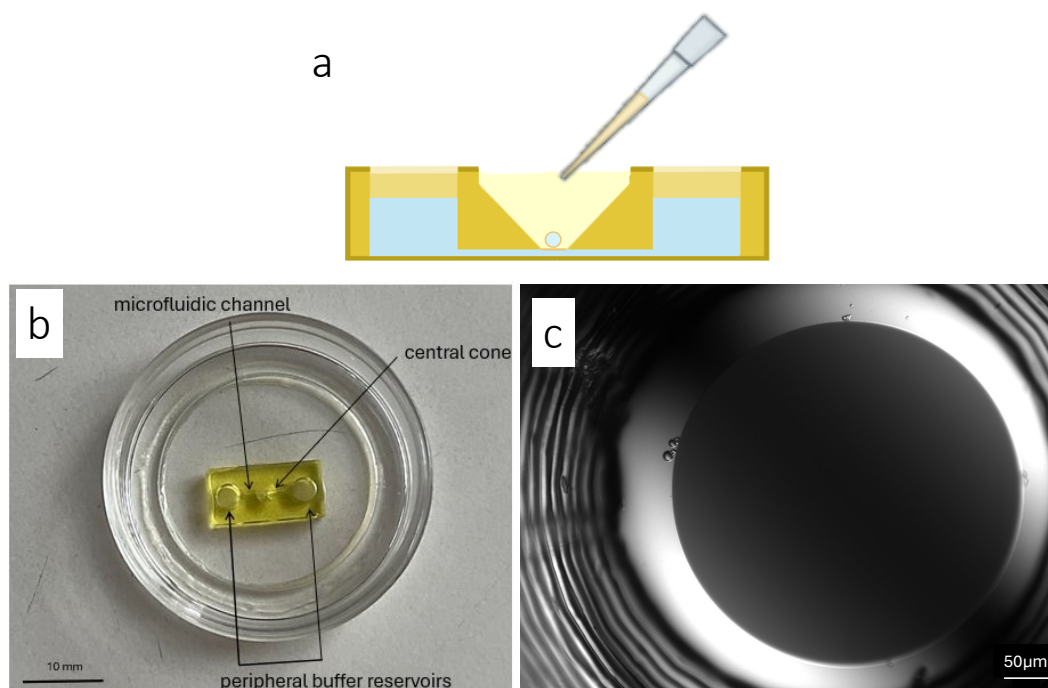


Figure 3.25: DIB using a buffer supported monolayer a) Sketch showing DIB device design and intended use. b) Picture of device glued to a dish ready for use. c) DIC image of bilayer produced at the interface where a clear interface can be seen characteristic of a bilayer that forms at the interface between the buffer and the oil. Work produced in collaboration with Emma Bopp.

3.3.3 Device utilising a buffer supported monolayer

A new iteration of the device was designed by reducing the number of wells from a 4×4 array to one well above a microfluidic channel through which buffer could be added, an oil/lipid solution could be added on top to generate a monolayer to which the droplets were added and a bilayer produced. A schematic is shown in Fig. 3.25a. In this way we generated a bilayer that could freely fluctuate at a suitable height above the glass interface. As the solution within this volume was a 0.5 M KCl 10 mM HEPES buffer it was much less likely to scatter the light than the agarose, making it a preferable system for iGOR. This device was printed and glued to a MatTek dish in the same way as described in Section 2.2.2.3. Sample preparation from here was undertaken by Emma Bopp but has shown progress with a smooth, stable bilayer having been produced as shown in Fig. 3.25. Full details can be found in an unpublished Cardiff University MPhil thesis.

3.4 Discussion

Our GUV preparation protocol is one that reliably produces clean GUVs with diameters in excess of $30 \mu\text{m}$ albeit with varying density. These GUVs were suitable for measurements over a short-time frame, owing to their instability when observed after more than about 5 hours. This was observed as the loss of a spherical confir-

mation and the emergence of defects in the vesicles. Initially increased fluctuations in the membranes were identified and the vesicle deemed to be unstable and no longer measured, data not shown. Due to thermodynamic reasons they lost internal pressure and started to form tubular structures. With work described in Chapter 4 this instability was greatly improved with reliable measurements being able to be taken for at least 5 h. The membrane still became more fluctuating due to reduced internal pressure, however, as we introduced a higher initial internal pressure the time before this occurs was increased and therefore we observe large scale deformation less frequently. This process gave us a model where we could measure surface tension and thus fluctuations, over time due to loss of internal pressure as well as a time frame where the membrane as a whole was not fluid and the finer dynamics could be probed. Whilst this method hasn't been stringently trialled with different lipid composition the compatibility with our 1:1 POPC:POPE composition is a good indication of large scale compatibility due to the destabilising nature of the POPE, as well as demonstrated compatibility with DC₁₅PC and DOPC. The main limitations for this method are the stability and limitations when using charged lipid species and dyes as these affect the diameter of GUVs produced from electroformation, evidenced by our work with Rhodamin-6G as discussed in Chapter 5 and literature.[208] This didn't limit our work too greatly as the main biologically relevant lipids (PC,PE and SM) are zwitterionic and therefore compatible with our protocol especially as we could still incorporate a water soluble dye into our systems which allowed for epifluorescence measurements. [223]

hs-GUVs as model membranes work to improve stability as the vesicle was supported by PVA and glass around the centre. Whilst this has been shown to make an improvement as the hs-GUVs have been measured over the course of 2 days, the images in Fig. 3.20 were taken after 24hrs. When they were observed using DIC the hs-GUVs were taller than expected with longer sides. This caused more movement in the membranes and encapsulated lipid debris. Therefore, a wash step would be necessary to prevent this debris interfering when using iGOR, however this was not achieved and was an area not worth pursuing as GUVs were proving suitable model membranes and in the interest of time this optimisation was stopped. The elongated nature of some of the hs-GUVs caused the hs-GUV top surface to be more mobile which would have led to blurring if imaging with iGOR. If a wash step were to be established the PVA thickness could be adjusted with an aim to achieve the correct degree of swelling and in turn hs-GUV height. This method could be worth pursuing if we were to require a model membrane containing charged lipids due to the incompatibility with wire electroformation. Even at this stage of optimisation this gives us more flexibility with lipid compositions that we can use.

In summary we have presented various methods for the production of suspended bilayers to varying levels of optimisation. Having the different potential conformations that we have shown allows versatility when trying to observe different behaviours and investigating alternative lipid compositions. For our primary lipid composition of POPC:POPE, the GUVs hold an advantage when looking to observe homogenous phase behaviour as at a temperature above its phase transition temperature there was no phase separation visible in fluorescence although there may have been nano- or transient domains present that are insufficient in separating out the fluorophore. This method also allowed us to observe the effect of protein insertion on phase behaviour. hs-GUVs could be an advantageous model for the stability of vesicles. The droplet interface bilayers under optimisation in collaboration with

Oliver Castell and Hannah Baird could bridge this gap and provide stable bilayers where protein could be added whilst under observation.

We have concluded that the GUV sample preparation was developed sufficiently to reliably produce vesicles suitable for iGOR imaging and the protocol limitations established. DIB systems were also suitable for iGOR imaging with the system still in the process of testing although we have a device that is ready for testing with iGOR. The hs-GUV development was discontinued as it showed less promise than other system development.

Chapter 4

Characterisation of giant vesicles using qDIC

Whilst the primary aim of this project is to use iGOR to study the fluctuations of lipid bilayers, we first needed to develop a reliable GUV preparation protocol. As discussed in Chapter 3 we experienced stability issues for which we employed a sucrose concentration gradient. This gradient across the membrane aimed to improve GUV stability and facilitate sedimentation.[217, 218] However, even with this gradient, the vesicles remained stable only for a few hours, necessitating a reliable method to confirm the presence and maintenance of the intended internal gradient. qDIC allowed us to measure the phase gradient across the equatorial plane of individual vesicles.[107] Because the contributions from lamellarity and internal sucrose concentration differ spatially, the former confined to the membrane surface, the latter distributed throughout the vesicle interior. These two parameters could be disentangled through analysis of the phase profile.

qDIC was chosen for its unique capability to provide spatially resolved maps of the optical thickness gradient across a sample.[154] This was particularly useful for assessing key physical properties of vesicles, such as lamellarity and the internal solute concentration. Unlike conventional DIC, qDIC enabled quantitative phase information to be extracted, which was essential when characterising the optical properties of GUVs and validating sample quality prior to iGOR measurements. qDIC is an existing technique previously developed in our group meaning imaging and analysis protocols were already in place providing an accessible method.[155] Initial analysis of this data proved insufficient for determination of lamellarity and sucrose concentration and therefore we simulated the measurements to allow improved analysis. The simulations were used to calculate parameters which were applied to measured data to deconvolute using the whole profile improving results. They were also utilised to correct profiles for effects such as defocus.

Section 4.1 provides a brief overview of the qDIC technique and outlines our method for extracting phase profiles across GVs. Section 4.2 summarises literature values for key lipid properties. In Sections 4.3 and 4.4, I describe how we extracted lamellarity and sucrose concentration from the measured phase profiles. An improved analysis pipeline using numerical simulations is introduced in Section 4.6, with fitting procedures discussed in Section 4.8.3.2. Corrections based on simulated defocus effects are presented in Section 4.7.2, and the interpretation of both simulated and experimental phase profiles is further explored in Section 4.9.

4.1 Quantitative differential interference contrast microscopy

qDIC is a method that measures the phase changes across a sample.[107] The set up is as described in 2.3.2.

A protocol was developed within our lab for the acquisition and analysis of qDIC images of GUVs. A standard qDIC image acquisition was undertaken as previously developed.[107, 224] A home built software was used to integrate the image, (described in Section 2.3.2 and shown in Appendix B.1), from which a phase profile of the background and across the vesicle diameter was plotted. The fit was generated as a linear fit from the scatter plot outside of the region corresponding to the vesicle, shown as $w = 0$ in Fig. 4.1, this region was weighted zero in the fit and shown in the black bracket. The phase change at the centre of the vesicle was calculated by subtracting the background fit from the measured phase in the region indicated by the red box, corresponding to the change of phase caused by both top and bottom bilayer as well as the internal solution as seen in Fig. 4.1d. Analysis of this phase change allowed us to characterise the sucrose concentration and in turn, internal pressure and lamellarity. Data was taken at varying sucrose concentrations and numerical apertures.

Phase changes observed in qDIC are related to changes in optical thickness which is the product of the refractive index and thickness. For the integration we determined using a κ value of 10^6 was suited providing sufficient large extension of the phase tails, which can be seen in Fig. 4.3.

4.2 Refractive index of sucrose solution and lipid bilayers

For the analysis, we required the refractive indexes of the materials involved. We used a POPC:POPE mixture but there are currently only values for a POPC bilayer available in literature.[226, 227, 228] There were four values ranging between 1.4725 and 1.4776 with an average of 1.4751 ± 0.0014 which was in line with the reported standard error for each value, although the refractive index of our bilayers was not expected to deviate too much. Reported refractive indices were measured using lipids in a hydrated state using in-plane polarised 589 nm light. Calculation of bilayer optical thickness required the use of the membrane thickness, this is also a value that has not been reported in literature for any POPC:POPE composition membranes, but has been reported for both individual lipid species. For POPC they ranged from 3.70 to 3.98 nm and POPE ranged from 3.95 to 4.34 nm. [226, 227, 228] This produced an average of both components of (3.92 ± 0.076) nm. The systematic error introduced through the membrane thickness and refractive index was about 3% of the optical thickness between 1,2,3 bilayers and was therefore insignificant when determining the lamellarity due to the much larger change of optical thickness and corresponding phase by an additional membrane. A summary of the literature values used for the membrane thickness and refractive index of POPC and POPE is shown in Table 4.1 and Table 4.2. The refractive indices used in analysis for the sucrose concentration are shown in Fig. 4.2 where the refractive index was fitted using a linear fit.[225]

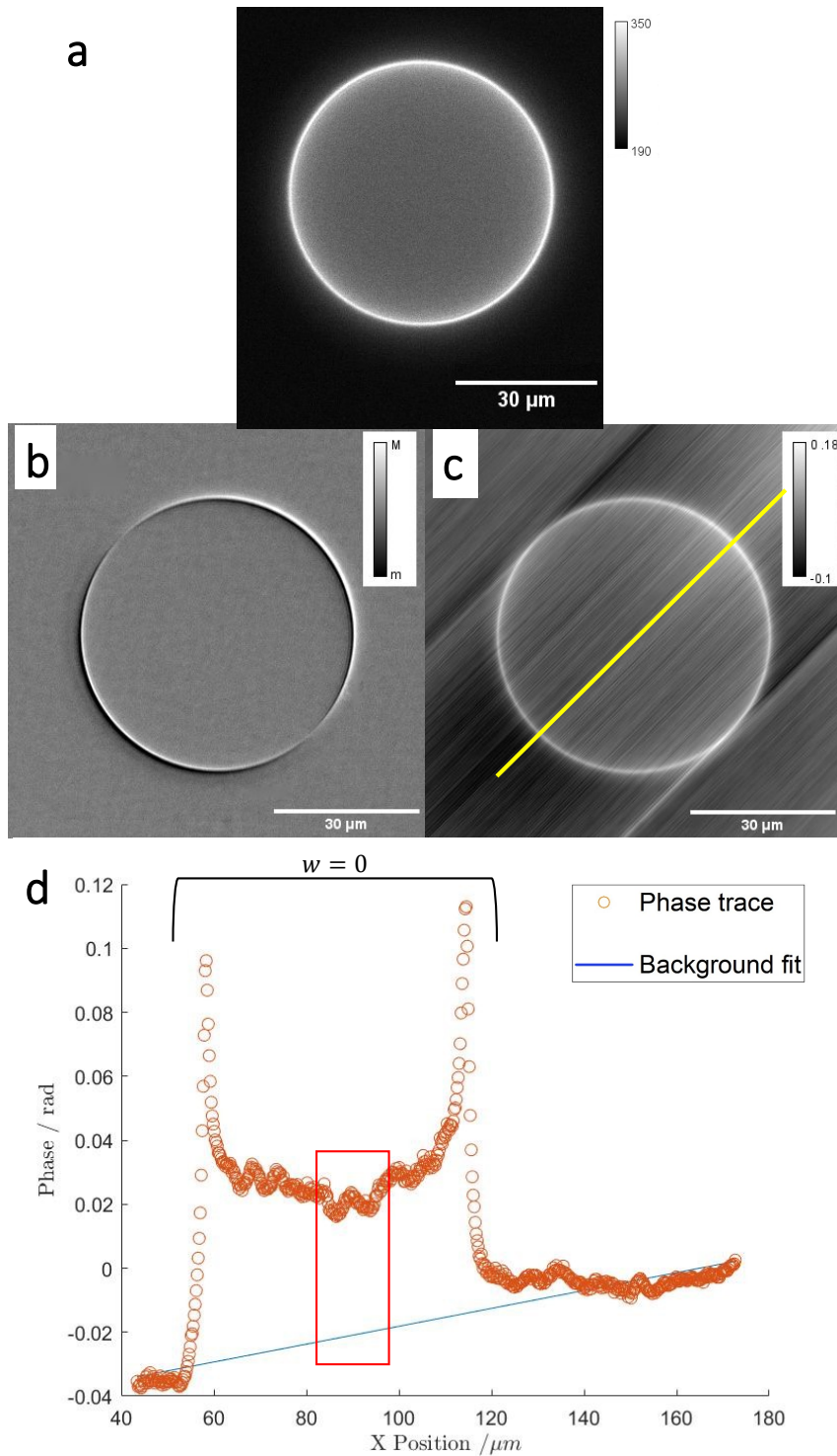


Figure 4.1: Analysis of qDIC images a) Epifluorescence image of the GV b) corresponding Δ image ($m = 35$, $M = 235$) c) phase image resulting from qDIC integration for $\kappa = 10^6$. d) The phase profile along the line cut shown in yellow in c) and the background fit shown in blue. The red box shows the central region used in further analysis. The black bracket demonstrates the region used to weight the background fit.

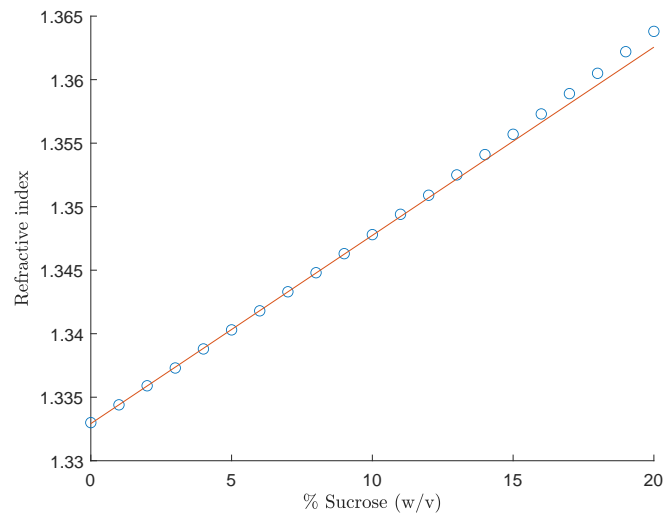


Figure 4.2: Relationship between sucrose concentration and refractive index Refractive index of a sucrose-water solution versus sucrose content as sucrose percentage (blue circles) taken from [225]. The data was fitted linearly over the range of 0-20 % (w/v) yielding $n_{\text{su}} = 1.333 + 0.001482c_{\text{su}}$ where c_{su} is the %(w/v) concentration of sucrose

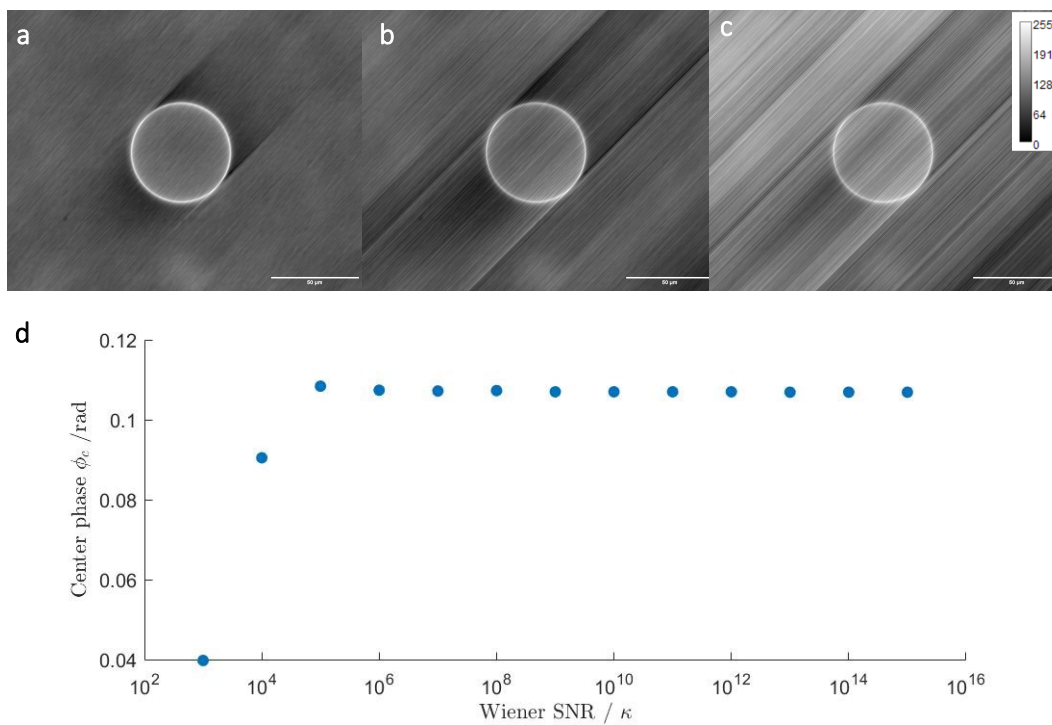


Figure 4.3: Phase images as function of Wiener filter SNR κ a),b) and c) show the phase images of a vesicle calculated with a Wiener filter SNR of 10^4 , 10^6 and 10^8 , respectively. d) shows the values measured from the central column for an increasing value of κ , Clearly demonstrating that no κ dependant changes are seen after 10^6 . Scale bars represent $50 \mu\text{m}$.

4.3 Measuring refractive index and lamellarity

To determine the refractive index of a POPC:POPE (1:1) bilayer, the optical path length for GVs without concentration difference was determined, and compared with the nominal path length for a given lamellarity. For this we used the central region to analyse data for normal incidence on the bilayer. The central column was defined as ± 5 pixels equating to $1.08 \mu\text{m}$ from the central point defined as halfway between the peaks. The background was fitted using a linear fit and a weighting which masked out the signal from the vesicle, which in this instance was selected as the position of base of the peak by eye, this is shown in the black region demonstrated in Fig. 4.1. The fit was then calculated for the entire profile and subtracted and the mean taken for all values within the central column to yield $\Delta\varphi$. When calculating the refractive index of the bilayers (n_{B}), Equation 4.1 was used where d is the bilayer thickness and b is the number of bilayers in the optical path.

$$\Delta n_{\text{B}} = \frac{\Delta\varphi\lambda}{2\pi bd} \quad (4.1)$$

For a unilamellar vesicle this was two due to the bilayers, at the top and at the bottom of the vesicle. In order to determine the lamellarity the refractive index was calculated according to Equation 4.1 for b values 2, 4, 6 and 8. From this the resulting refractive index closest to the expected literature value was assigned as the correct lamellarity.

Vesicles generated using only d.H₂O allowed the determination of the refractive index of the bilayer. The change of phase measured was used alongside the literature values for membrane thickness and the equations detailed above to produce the change of refractive index due to the bilayers present at the centre. When looking at the average measured change of refractive index for Fig. 4.4, we calculated a value of 0.1469 ± 0.002 , $n = 44$, which we compared to the literature value of 0.1411 ± 0.001 to which showed a comparable error. However, with simulation and fitting analysis undertaken, as described below, we improved our standard error by using an optimised analysis protocol.

The systematic error was evaluated by calculating n_{B} for each vesicle using the minimum, maximum and average membrane thickness shown in Table 4.1. For this analysis we used the minimum, maximum and average for each value to establish a systematic error of 4% present in our measurements. These can be seen in the graph shown in Fig. 4.4a, where the average change of refractive index for exemplar GUVs are shown in bars one to four with error bars representing the standard error calculated for differing literature values. The calculation of each bilayer had an associated systematic error meaning a multilamellar vesicle was less reliable than a GUV, consisting of one bilayer, as it had the lowest associated systematic error and therefore GUVs were the most reliable for the calculation of n_{B} .

4.4 Measuring sucrose concentration and lamellarity using central column

The change of phase at the vesicle centre was used to calculate the concentration of sucrose in the internal solution, the change of phase extracted from the central column of graph was input into Equation 4.2 alongside the assigned lamellarity (b) to retrieve the refractive index of sucrose (n_{S}) where r is the radius of the vesicle,

Lipid composition	POPC /nm	POPC:POPE /nm	POPE /nm
	3.7		4.34
	3.75		3.95
	3.8		4.1
	3.77		
	3.98		
Average	3.8		4.13
Standard error	0.047854		0.087977
Total average		3.92	
Standard error		0.0764605	

Table 4.1: Summary of the membrane thickness literature values A summary of the literature values for the membrane thickness of both POPC and POPE and the resulting average and standard deviation for the data.[226, 227, 228].

Refractive Index	Error	Corrected Refractive Index
1.4728	0.0017	0.1388
1.4776	0.0017	0.1436
1.4774	0.0016	0.1434
1.4725	0.0026	0.1385
1.4751	Average	0.1411
0.0014	Standard error	0.0014

Table 4.2: Summary of the refractive index literature values Summarises the literature values for the refractive index of POPC. [226, 227, 228]

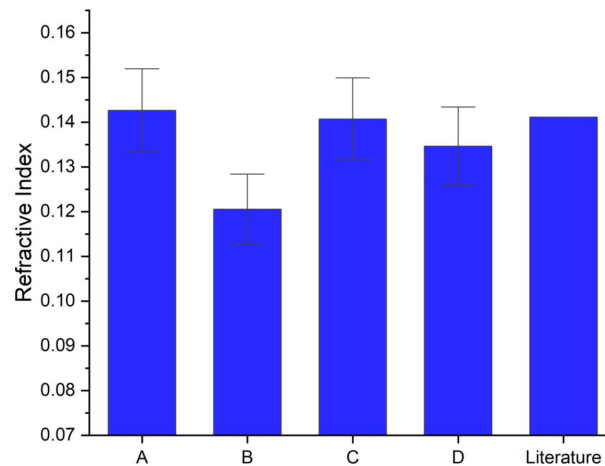


Figure 4.4: Refractive index analysis of POPC:POPE bilayers Refractive index difference of the lipid bilayers to water measured for exemplar vesicles and the literature value for POPC. [226, 227, 228] Error bars represent the standard error calculated from the minimum and maximum literature membrane thicknesses for vesicles A-D.

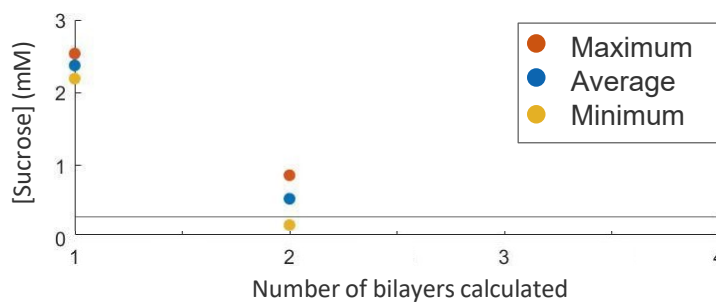


Figure 4.5: Sucrose concentrations of measured vesicles Graph showing the calculated sucrose concentration for different assumed lamellarities for an exemplar vesicle. The sucrose concentration could be thresholded between 0.3 and 0 mM indicating that the vesicle was bilamellar. The different series plotted are the range of values calculated using the minimum and maximum literature values of both membrane thickness and refractive index to show systematic error. Calculated values for 3 and 4 bilayers have been omitted as the produce sucrose concentrations below 0 mM which is not experimentally accessible.

this was repeated for assigned lamellarities 1,2,3 and 4. The refractive index of the sucrose was converted to percentage sucrose using the fit in Fig. 4.2. This percentage was then converted to mM using Equation 4.3 and the lamellarity could be identified by thresholding the data using the known maximum concentration difference of sucrose initially in solution. As we knew the sucrose concentration we put into the electroformation solution and subsequently the vesicle, and the fact that the external solution is d.H₂O, we knew the maximum concentration gradient possible which was equal that of the electroformation solution.

$$\Delta n_S = \frac{\Delta\varphi\lambda(2\pi)^{-1} - bd\Delta n_B}{2r} \quad (4.2)$$

$$C_{su} = \frac{10000}{342.3} c_{su} \quad [mM]/[\%w/v] \quad (4.3)$$

The sucrose concentration gradient was calculated for b values 2 to 8 representing uni- to quad- lamellarities. The maximum sucrose concentration gradient possible was used to exclude lamellarities in Fig. 4.5. We were then able to allocate lamellarity based on which value fell within our threshold. Vesicles were made and measured with internal solutions of sucrose concentration (C_{su}) 0, 0.1 ,0.2 ,0.3 and 0.5 mM, for each concentration vesicles were classified based on lamellarity. Fig. 4.6 shows the distribution of calculated lamellarities for each concentration of sucrose.

Whilst we were initially looking to quantify the internal sucrose concentration to confirm we were achieving the planned 0.5 mM sucrose concentration gradient, surprisingly, when we analysed the vesicles containing 0.5 mM sucrose all vesicles were at least bilamellar, despite appearing unilamellar in epifluorescence. From these results we theorised that the internal pressure was too great for a single bilayer to withstand. We made a calculation discussed in Section 3.1.3 to inform the maximum concentration gradient implemented. From this we calculated 0.4 mM for diameters up to scaling as 1/diameter. For our purposes we needed a single bilayer and therefore we needed to reduce the internal sucrose concentration and in turn the internal pressure to be able to produce stable, unilamellar vesicles. To reflect

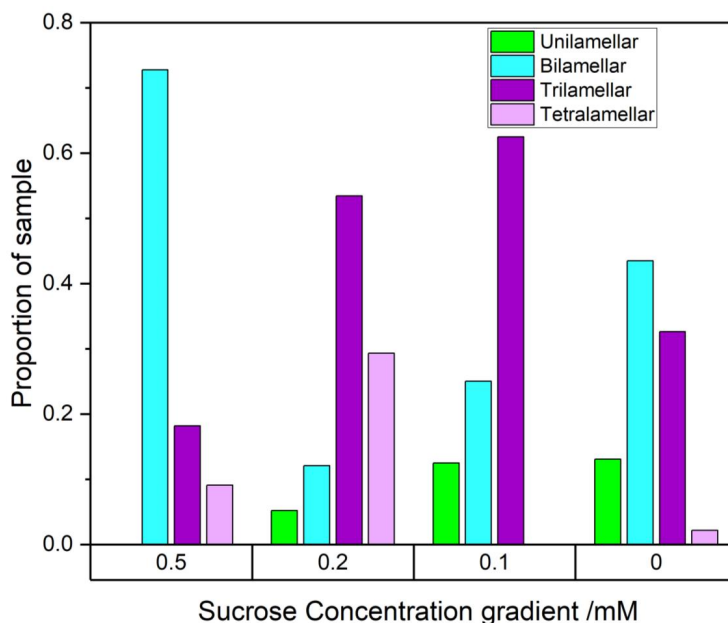


Figure 4.6: The dependency of lamellarity on sucrose concentration A histogram showing the proportion of lamellarity in the sample upon various internal sucrose concentrations with zero external sucrose concentration.

the heterogeneous nature of the vesicles within a sample we refer to them as GVs unless lamellarities have been defined.

To get a better idea of the effect of systematic error in this data from both the membrane thickness and refractive index, values were calculated with combinations of the minimum and maximum of both values. The range of values were plotted around the average value as a separate series. It can be seen from the graph in Fig. 4.5 that whilst the error was too large to determine the sucrose concentration, it was sufficient to determine the lamellarity as bilamellar. These results suggests that both 0.5 mM and 0.3 mM sucrose produce an internal pressure to great to sustain stable unilamellar vesicles. $d.H_2O$ only vesicles were analysed primarily to determine the refractive index of POPC:POPE (1:1) lipid composition and as can be seen in Fig. 4.6 it facilitated the production of unilamellar vesicles. As we calculated the maximum value to be 0.4 mM we trialled 0.3 mM however this only produced bilamellar vesicles. Once we reduced the concentration to 0.2 mM we saw the emergence of unilamellar vesicles demonstrating that the internal pressure was sufficient to support such morphologies. This was also observed in 0.1 mM samples, it was accompanied by an increase of higher lamellarities namely trilamellar. Whilst this was a surprising result it can be understood as due to the nature of wire electroformation pulling bilayers off the surface it could easily produce multilamellar vesicles and as these additional bilayers would have provided additional stability they could withstand higher internal pressures. This meant that their existence was independent of the sucrose concentrations in the range we were using and therefore doesn't affect the validity of the conclusions made in this section. Using the results discussed above we implemented 0.2 mM sucrose as the electroformation solution and therefore internal solution going forwards for the production of GVs in an aim to facilitate the production of unilamellar vesicles.

4.5 Summary of initial qDIC analysis

In an effort to produce stable GUVs we had to find the maximum concentration difference that produced unilamellar vesicles. As seen in Fig. 4.6 even with no concentration gradient present across the membrane we expected a range of lamellarities due to the inherent variability of the preparation protocol as discussed in 3.1. Therefore, provided the chosen sucrose concentration could support unilamellar vesicle synthesis and stability, which was seen when using a 0.2 mM concentration gradient it was suitable for our experiments. The cause of the increase in trilamellar vesicles upon decreasing below 0.5 mM sucrose is unknown however it is likely to be statistically irrelevant as we had a small sample size. In light of this and the error previously discussed, improved fitting using a robust fitting method for these phase profiles gave more confidence when characterising the vesicles as well as accounting for various parameters and features seen. One of these is birefringence which is the influence of intra-bilayer lipid organisation on the qDIC signal, where slanted lipids have an effect on the light.[229] This birefringence manifested as an effective refractive index which could've been adding to our error, therefore the later discussed method was utilised to improve our characterisation.

Secondary to this fitting there was a gradient across the vesicle that became evident upon normalisation (shown in Fig. 4.21). This is thought to be due to birefringence. This birefringence is the difference between in-plane and out of plane, and the polarisation of the two DIC sheared beams probes birefringence for polarisations along versus across the shear. Going forward this will be incorporated into the simulation to allow GV data to be analysed for this effect, giving us another measurable characteristic for GV analysis. When looking at phase profiles, the central column showed greater variance than the peaks corresponding to the bilayer edge, this could be due to the central column being further from the fitted region and a lower signal increasing the signal to noise, producing additional error. For this reason the peaks were incorporated into analysis via simulations to reduce error as described in the following section.

4.6 qDIC GV simulations

As previously discussed, we expected a range of lamellarities independent of sucrose concentration when forming GVs due to the inherent variability of the protocol. Therefore, we needed a more robust method for the separation of the signal caused by the bilayers and that caused by the internal solution. To do this we simulated the overlap integrals expected upon interaction of a light cone with GVs. A full description of the protocol is in Section 4.6.1.

This gave a direct calculation of the overlap integrals across the GV and allowed us to calculate the resulting phase profiles to compare to those generated from the experimental data. This simulation was calculated for the lipid bilayers and internal solutions separately and then scaled for different lamellarities and internal concentrations and summed to provide the total path difference. By generating the bilayer and an internal solution profiles separately it gave us a full profile to compare to our measured data to allow lamellarity and sucrose concentration gradient of vesicles to be determined.

4.6.1 Simulation methodology

All simulations were carried out using MATLAB 2021b.

4.6.1.1 Formation of the GUV matrix

A $50,000 \times 50,000$ matrix was initially filled with GUV dimensions at a given z height for both the bilayer and the internal solution separately with a 1 nm in plane resolution then binned out to give a 100 nm resolution slice, this resolution could be changed using a scaling factor. We modelled a $30 \mu\text{m}$ unilamellar vesicle. A bilayer thickness of 4 nm was used close to literature values as discussed in Section 4.2. A refractive index of 1.47 was used, hereafter referred to as n_{BL} . The refractive indices for interior and exterior solutions for this matrix were defined as n_i and n_e , respectively. These were set at 1.333, the refractive index of water as default, with any sucrose concentrations calculated using Equation 4.3 and the fit in Fig. 4.2.

The matrix was filled by coordinate for every z plane, each coordinate had a radius calculated using $r = \sqrt{x^2 + y^2 + z^2}$. If $r > r_{GV}$, $n = n_e$, if $r > r_{GV} - d$ then $n = n_{BL}$, otherwise $n = n_i$. Each z plane was then averaged in x and y to form a 500×500 matrix. Upon completion of 100 z planes the $500 \times 500 \times 100$ matrix was averaged in z into a 500×500 matrix representing a 100 nm thick slice. On completion of half the GUV ($500 \times 500 \times 250$) slices, the second half was created using mirror symmetry.

Interior only matrices were filled using the same method as described above with only the coordinates within the inner radius given a value other than that of water, n_i .

4.6.1.2 Formation of the cone matrix

A 3D matrix for the cone was produced to the same 10 nm resolution as before and averaged to 100 nm. The x-y radii of the cone r_{illum} at each z height was defined using $r_{illum} = \tan(\theta_O)z$ corresponding to the opening angle (θ_O), dictated by a numerical aperture of 0.72 in this case 0.57205 and a z being the distance from the centre of the vesicle in μm . The values within these radii were calculated for each plane to give a normalised cone given by $\frac{1}{\text{Number of pixels in cone area}}$.

4.6.1.3 Generating overlap integrals

The overlap integrals are the dot products of the cone matrix at different positions of the GUV Matrix, which represent the response of the GUV to the light in terms of phase shift caused. The light cone was centred at the central plane of the GUV matrix and shifted across its diameter to generate a phase profile. The GUV matrix was padded with external medium points of value n_e , which allowed the cone to start completely outside of the GUV. The cone was moved through the centre of the GUV calculating the total overlap integral at each point by calculating the dot product of both matrices and summing all values in x , y and z . A profile was produced using the total overlap integral at each x position at y position 250. The overlap integrals for different positions along x were calculated using the circshift function to shift the cone position without recalculating the matrix. By calculating the interior and bilayer only profiles separately it allowed scaling of the interior by weighting the x profiles with the changing $n_i - n_e$.

The resulting phase profiles also showed the expected shape and scaled suitably as seen in Fig. 4.8a and b, Fig. 4.8c shows a logarithmic plot of the edge of the vesicle for both bilayer and internal volumes. The phase for each simulated pixel was plotted against the distance from the edge of the signal start. From this we deduced that at the point where the centre of the cone reached the vesicle edge the overlapping area of the bilayer scaled as the square root, while the overlapping volume scales with the power 3/2 as expected.

Fig. 4.9a and b show the difference in simulated and calculated phase for the centre of each plot for bilayer and internal volume only plots, respectively. The phase at this position was calculated using the method detailed in Section 4.4 for our simulated values. These were plotted alongside the phase at the centre of each plot and showed good agreement in values. The calculations were undertaken assuming perfect imaging and therefore didn't account for the fact that the radius of the light cone was different at differing axial positions as seen in Fig. 4.7d. Accounting for this we are confident that our simulations were a suitable quantitative representation of our imaging system, this was further supported by the simulations discussed in Section 4.9.2 where the central value changed with numerical aperture suggesting that beam radius impacted this value. The effect that resolution had on these profiles can be seen in Fig. 4.9, where the inner and outer integrals against resolution for bilayer (c) and internal volume only systems (d) are shown. From this we determined that the resolution had a significant effect on the integral value, for this reason we extrapolated using the 10 and 50 nm measurements to the value at 0 nm, the true integral value used for further profile determination as discussed below. These linear fits were also used to correct any simulations undertaken at lower resolutions. As our minimum resolution was 10 nm no positional consideration was required when scaling for bilamellar vesicles as any thickness changes of the bilayer (± 4 nm) were below resolution. Once scaled to trilamellar and tetralamellar models the effective thickness change was still considered negligible.

4.6.1.4 Defocus dependency

Phase profiles were calculated with the light cone matrix centred at an increasing distance from the central focal plane of the vesicle. The illumination radius was calculated at each z height according to $r_{illum} = \tan(\theta_O)z_s - z$ where θ_O is the cone opening angle, z_s is the centre of the cone shifted by defocus amount.

4.6.1.5 NA dependency

The cone matrices were simulated for numerical apertures of 0.3, 0.5, 0.72, 0.95, 1, 1.15 and 1.25. Profiles of the overlap integrals were produced in the same way as described above. Full GUV profiles were produced by summing interior and bilayer profiles.

4.6.2 Profile analysis

A main motivation for the completion of these simulations was to evaluate the out of focus effects of the light cone where the radius was larger. This was initially undertaken to explain the edge effects where the peak didn't start as sharp as one would've naively expected, it was also realised that this could improve our calculations of lamellarity and sucrose concentration as we incorporated the peak edges

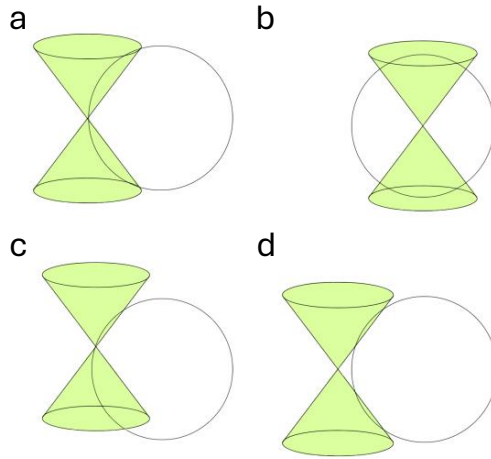


Figure 4.7: 3D overview of the illumination light cone and GV volume Sketches to demonstrate the interaction of the light cone in different orientations relative to the GV. **a)** shows the light cone focussed on the vesicle edge at a point where the light at the cone centre is on the centre of the vesicle, this generates a high optical thickness and the start of the GUV signal. **b)** shows the light cone focussed at the vesicle centre, this generates an optical thickness consisting of the upper and lower bilayers and internal volume. **c)** represents the out of focus conformation where the light cone is shifted above the central focal generating an asymmetric response. **d)** shows the cause of the edge effects where the higher and lower larger radii of the cone reach the GV before the centre inducing signal prior to the peak

which were less influenced by the background. The experimental profiles showed a slower increase when reaching the edge, as can also be seen in Fig. 4.16. Initially we hypothesised that this was due to effects from where the cone is broader as it hit the vesicle edge first out of the focal plane as illustrated in Fig. 4.7d. Later defocus effects were considered as represented in Fig. 4.7c. Fig. 4.13 shows a defocus series up to a defocus of 16% of the diameter ($0.16D$) where it can be seen that the edge had a more curved response however it was not to the degree observed in the experimental profiles. We undertook simulations up to $0.334D$, but we limited analysis and corrections to the former as we discarded such measurements, this was reinforced when looking at the high defocus profiles the internal geometries were altered too greatly to be the full cause of the additional curvature of the profile edge. The more curved response observed experimentally was therefore not solely due to out of focus effects as we couldn't describe it fully. To better describe this effect we looked at the point spread function (PSF), an artefact arising from imaging out of the focal plane or other beam broadening effects as latterly described. Beam broadening is due to diffraction limited resolution creating deviation from the ray-picture. Through fitting we aimed to quantify these effects to enable incorporation back into simulations.

When modelling the signal for the simulations it was the optical thickness at each voxel (Thickness \cdot Refractive Index) that contributed to the overlap integrals via addition. This allowed the direct scaling of signal as increases in optical thickness at each voxel scaled linearly, meaning the complete profile could be multiplied up as the thickness change was compensated by the effective refractive index change. Once

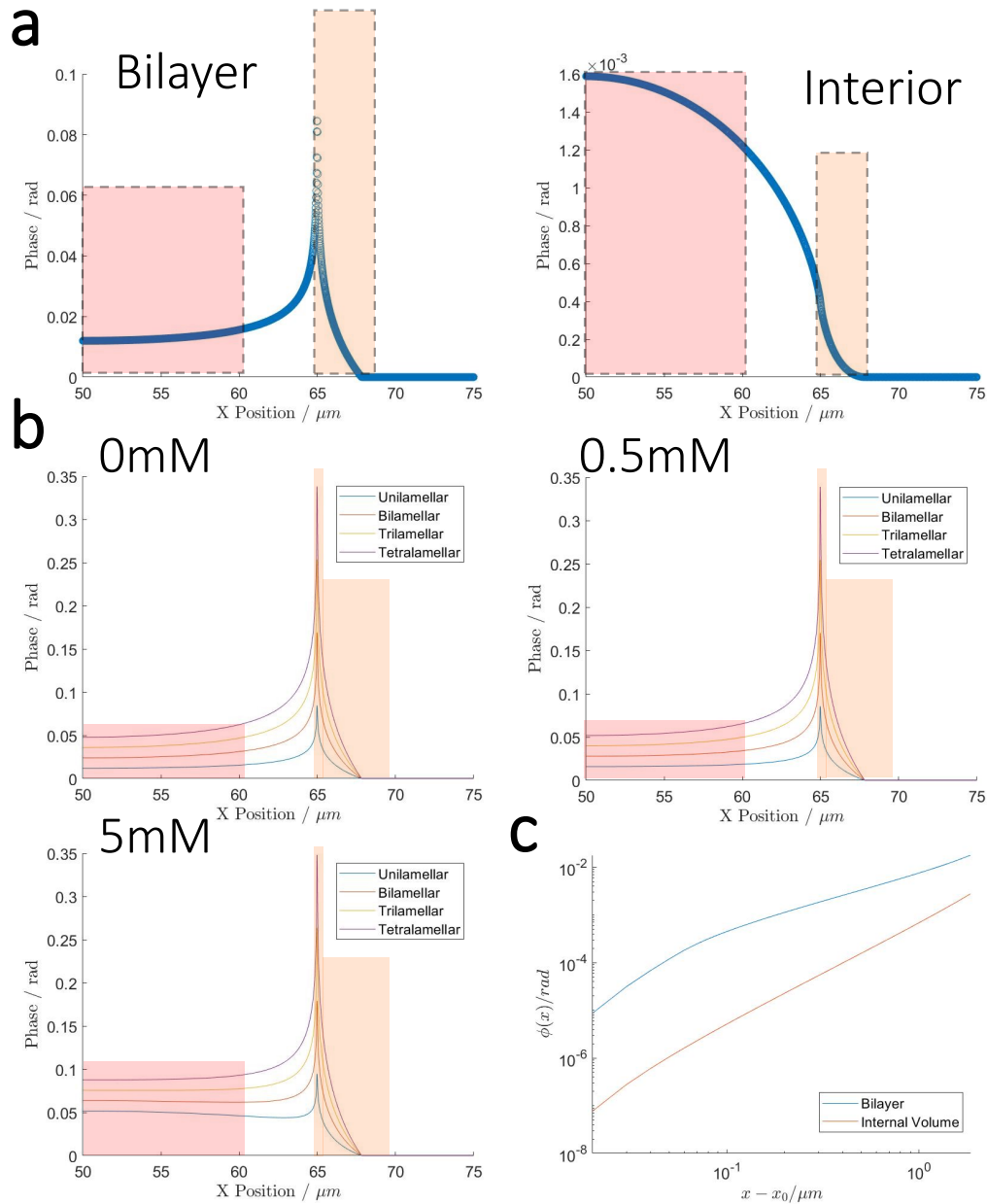


Figure 4.8: Simulated GV phase profiles a) shows the simulated phase profiles for the bilayer only simulation as well as the interior solution only (0.1 mM sucrose) which were summed and scaled to produce the profiles shown in b) where the differing ratio of central and peak heights can be seen. Simulations were carried out for a 30 μm vesicle with a 4 nm POPC:POPE(1:1) bilayer. The highlighted regions are those used in the generation of integrals from simulated phase profiles and their dependency on lamellarity and sucrose concentration gradient which were later used for the fitting of experimental data. c) shows a log log plot of the phase of a given pixel against the distance from the start of the signal highlighting the expected scaling for a volume (3/2) and for a surface (1/2) of a sphere.

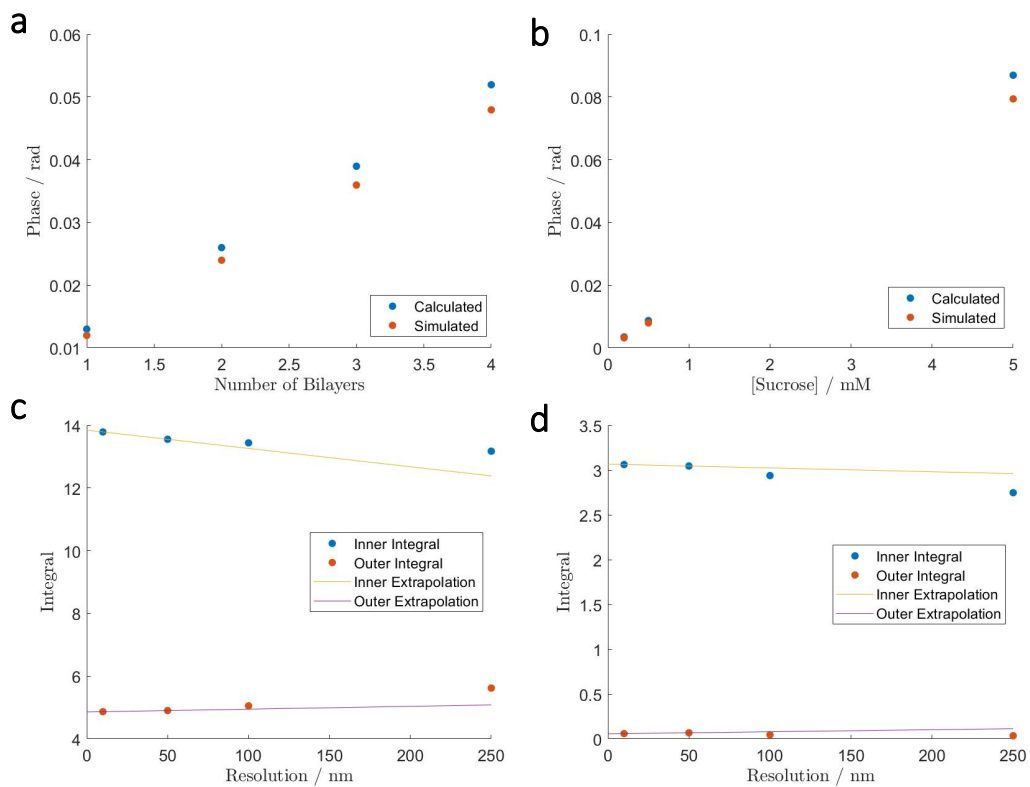


Figure 4.9: Evaluating simulation accuracy a) and b) display a comparison of the calculated and simulated values for the centre of a vesicle containing only bilayers and internal volume, respectively. c) shows the effect of resolution on inner and outer integrals for a unilamellar vesicle. The extrapolation shown was calculated based on the 10 nm and 50 nm results and show the values used going forwards. d) shows the same data for a 0.2 mM sucrose internal volume.

profiles had been generated for the lamellarity and sucrose concentrations, shown above, the ratio between the height of the peaks and central region was altered as can be seen in Fig. 4.8. The ratio was therefore, a parameter we used for fitting to determine both lamellarity and sucrose concentration as discussed in Section 4.8.3.2.

The profile was integrated across the regions highlighted in Fig. 4.8 and a fitting method for the integrated profile has been developed utilising the previously mentioned ratio change. When discussing the profiles, C was the centre of the vesicle and defined as halfway between the peaks $P1$ and $P2$ which were the positions of the highest value on either side of the profile. For symmetrised plots C was the first value and $P2$ the max, with D , diameter, defined as $2 \cdot P2$. The edge of the vesicle E was the position for which the vesicle signal returned to 0 and as directed from the simulations was defined as $E = 1.57D$. The range that integrals were calculated from were defined as inner, $C : C + 0.35D$, and outer, $P2 : E$ and calculated in $\text{rad}/\mu\text{m}$. When interpreting these integrals and comparing experimental and simulated values further scaling was undertaken as described in Section 4.8.3.2. Our first model contained no PSF, beam broadening or birefringence parameters. We fitted the background using linear regression using the same methodology as discussed above, then integrated the profile further across an area in the centre and the peak to generate parameters for comparison with simulations.

4.7 Identifying integrals for experimental comparison

When integrals were taken of both experimental and simulated profiles further integration was carried out for different intervals across the profile. When combined into various ratios they were used to make different inferences and corrections to the measured data. The integrals used and discussed further in this section are shown in Fig. 4.10. The primary aim of this analysis was to use the ratio between peak and central regions to determine lamellarity and sucrose concentration as discussed in Section 4.8.3.2. However we also used a peak broadness ratio to measure the level of defocus present in the sample as discussed below in Section 4.7.2 in order to correct any defocus errors present in our measurements.

The peak broadness and the ratio of inner and outer integrals as indicated in Fig. 4.10 were used to understand the profiles and the systems they arose from. These were calculated from the profiles that had been fitted and cleaned using the pipeline described in Section 4.8. Integrals for which both the sucrose concentration and lamellarity impact were used for sample analysis whilst a ratio calculated from within the outer region allowed the correction of any defocus present as well as any artefactual broadness as discussed below.

Upon the addition of sucrose into the system the profile became more variable. The more of the profile between the peaks incorporated the more the ratio became dependant on the sucrose concentration and less on the defocus as shown in Fig. 4.12.

4.7.1 Peak broadness

Peak broadness is a measurement of the spreading of signal across the peak corresponding to the edge of the vesicle. The peak broadness was measured by the ratio between $P \pm 0.015D$. Variation in peak broadness could have arisen from a multitude of factors not all accounted for in our simulations. Parameters of particular interest included point sample defocus, sucrose interior or the NA used. For all

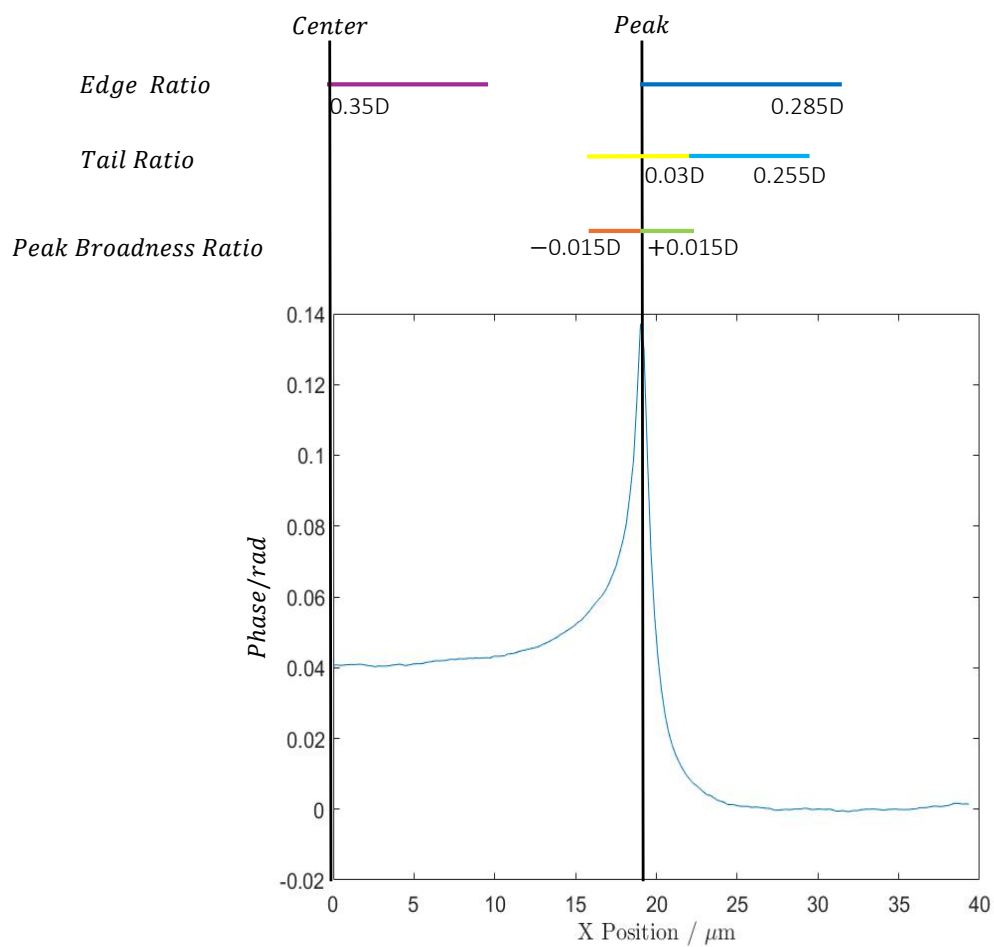


Figure 4.10: Integral determination from profiles Experimental graph showing the regions for which the integrals were calculated in relation to the centre and peak values of a specified vesicle to produce the ratios discussed.

samples the PSF should have remained constant due to the resolution of the system. These effects could most effectively be evaluated in samples only containing d.H₂O as both an internal and external solution.

The effect of resolution on GV phase profiles can be seen in Fig. 4.9 where the integrals of simulations with different scaling are compared, extrapolation was undertaken to determine the integral value as unaffected by resolution. For further analysis fitting parameters calculated from simulations with a matching resolution to the system were used and, as all values in the following analysis were used as either a ratio or percentage change they required no further correction due to resolution.

The increasing peak broadness observed with increasing NA in both simulated and experimental data was due to the increased opening angle of the light cone which caused increased signal from outside the focal plane. As the illumination NA was controlled and set at 0.72 for all the experimental datasets, apart from those investigating NA, out of focus effects were attributed to defocus and subsequently corrected. This change is discussed further below. When correcting for this defocus we also corrected for other peak broadening effects such as NA calibration.

PSF effects were seen as a peak broadening identified primarily at the edge of the profile as the GV signal returned to the background. This was seen as a step at the edge of the profile as highlighted in Fig. 4.16.

A generalised peak broadness parameter was evaluated using an integral ratio $\eta_{PB} = (P + 0.015D)/(P - 0.015D)$ consisting of integrals taken across the identified peak position and compared to the same simulated integral ratio. This relationship is shown in Fig. 4.12a alongside the experimental data for this ratio, measured with varying sucrose concentration gradients, demonstrating that the peak broadness shows negligible dependency on sucrose concentration. We also calculated a mean peak broadness of 0.8407 ± 0.0876 which suggested minimal dependency on defocus which was supported by Fig. 4.11 which shows the defocus plotted against peak broadness ratio for our simulated defocus series. The difference between our calculated mean and that from the simulations of 1.0061 ± 0.02 provided us with a measure of those factors not incorporated into our simulation. This created a factor of 0.8356.

4.7.2 Evaluation of the effect of defocus

Simulations were undertaken shifting the centre of the cone up relative to the vesicle as demonstrated in the sketch shown in Fig. 4.7c, the results can be seen in Fig. 4.13.

As previously mentioned artefactual peak broadness arising from defocus was corrected via comparison to a simulated integral ratio. The tail ratio, η_{tail} , was taken largely of the outside of the peak as well as some across the inside to be able to incorporate a degree of peak broadness. For this tail ratio, $\eta_{tail} = (P - 0.03D : P + 0.03D)/(P + 0.03D : E)$ as shown in Fig. 4.10, we take most of the integrated area from the outside of the peak as it is less likely to be affected by the inner sucrose concentration as seen in Fig. 4.12. Fig. 4.12 also shows the intervals from which the integral ratio was calculated. This ratio was fitted to the simulated defocus following a power log law with an R² value of 0.9962 as seen in Fig. 4.14a. By comparing to the measured ratio we determined the level of defocus and therefore the degree to which we needed to correct as discussed below.

The change of inner and outer integrals compared to the zero defocus case as a function of defocus can be seen in Fig. 4.14. Fig. 4.14b-d show the effect of defocus on the profile was present in the regions used in the subsequent lamellarity calculations.

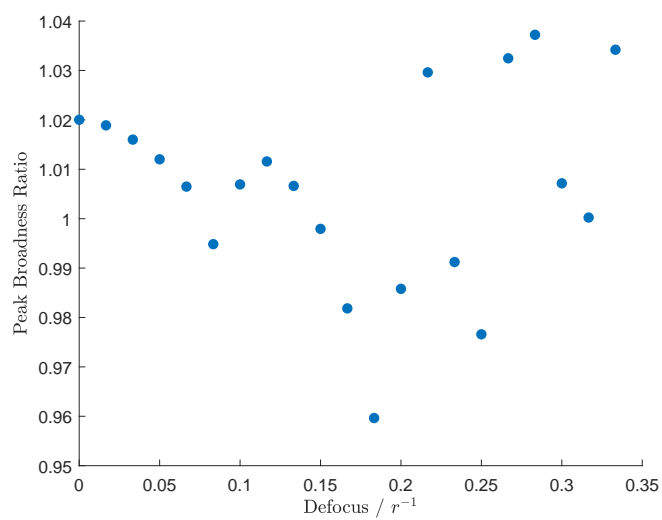


Figure 4.11: Effect of defocus on peak broadness A graph to show how the peak broadness ratio was affected by defocus levels, the ratio was plotted against the defocus level in units of the radius. These simulations were carried out on a 30 μm vesicle.

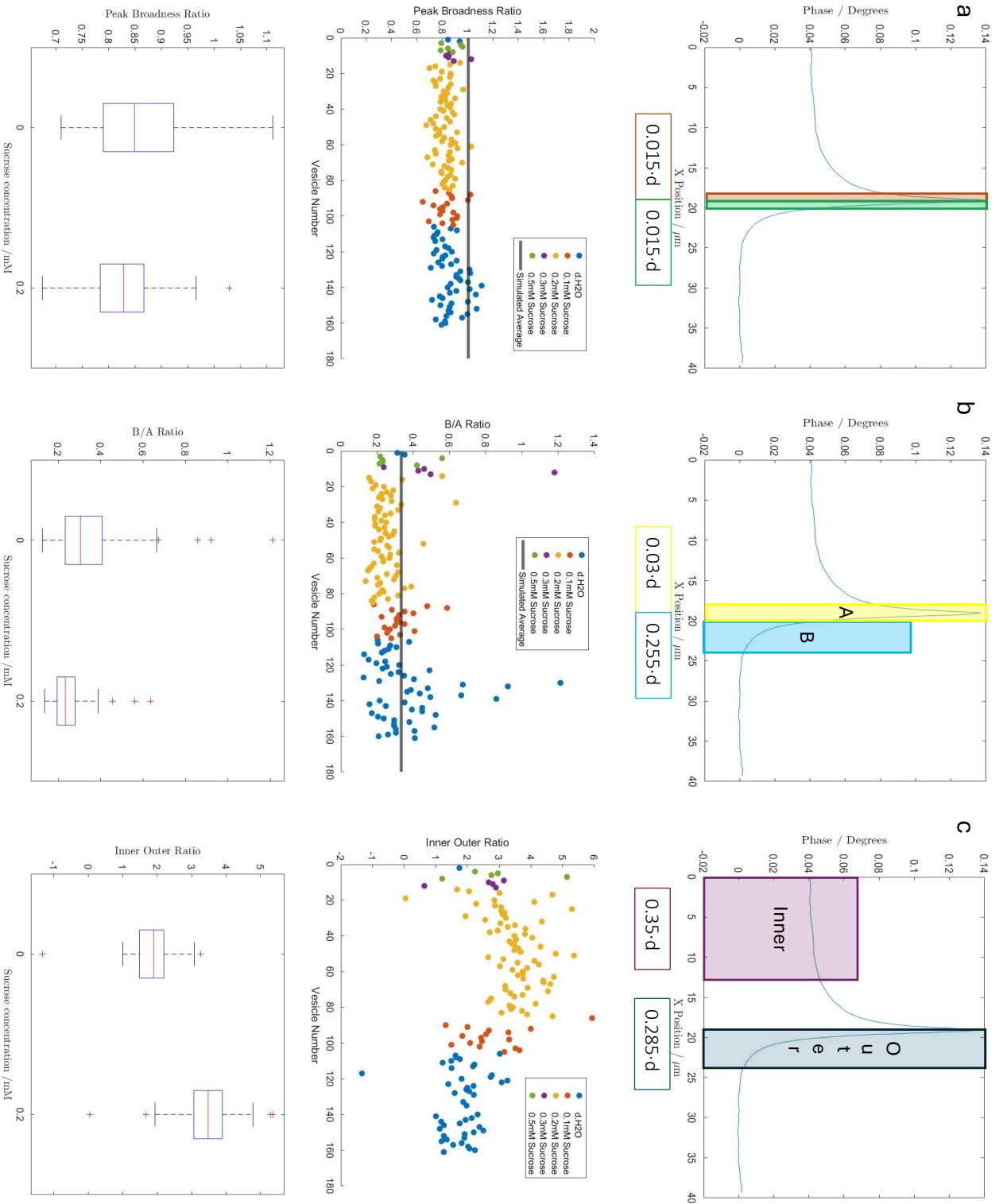


Figure 4.12: Integral Ratios The graphs in the top row show a phase profile with the regions included in the ratio highlighted and described as a proportion of the diameter D . **a)** shows the peak broadness ratio which provided a measure of peak asymmetry. **b)** shows the tail ratio used to determine the level of defocus present in the sample. **c)** is the edge ratio consisting of the inner and outer integrals used to determine the lamellarity and sucrose concentration. The scatter and box plots demonstrate the dependency of each ratio on sucrose concentration. The yline in each scatter plot shows the simulated value for the ratios in **a)** and **b)**.

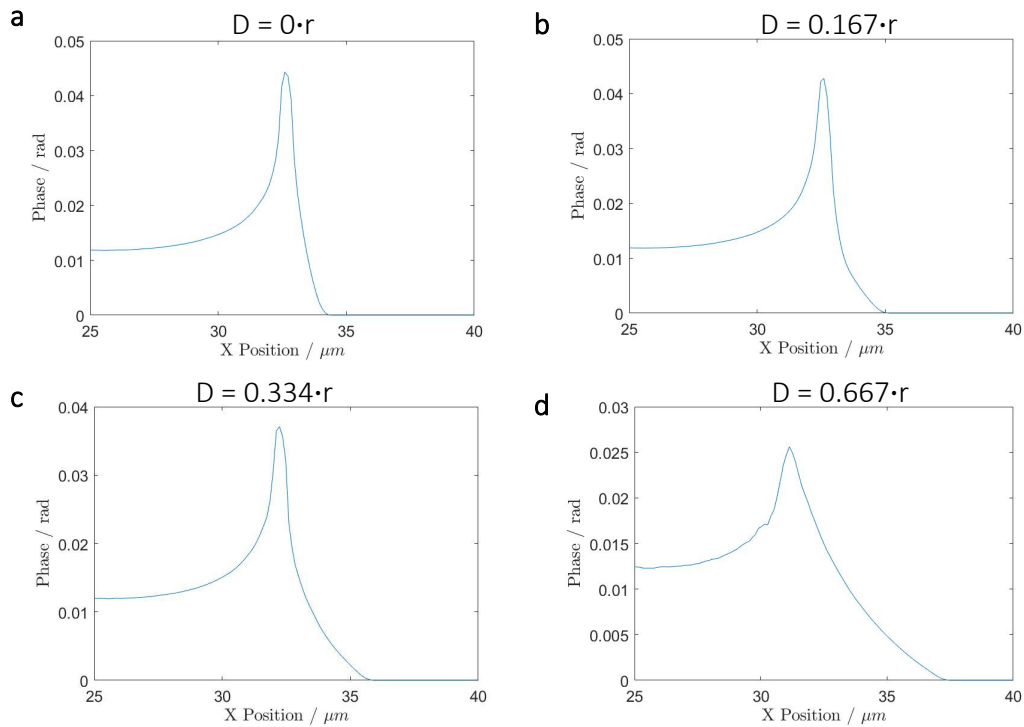


Figure 4.13: Defocused GUV Phase Profiles A series of plots showing the phase profile as the imaging became more defocused. Simulations were carried out using a $30\ \mu\text{m}$ unilamellar vesicle that was defocussed by $0\ \mu\text{m}$ (a), $2.5\ \mu\text{m}$ (b), $5\ \mu\text{m}$ (c) and $10\ \mu\text{m}$ (d). As the radius was $15\ \mu\text{m}$ these defocus levels (D) equated to 0 , $0.167r$, $0.334r$ and $0.667r$, respectively.

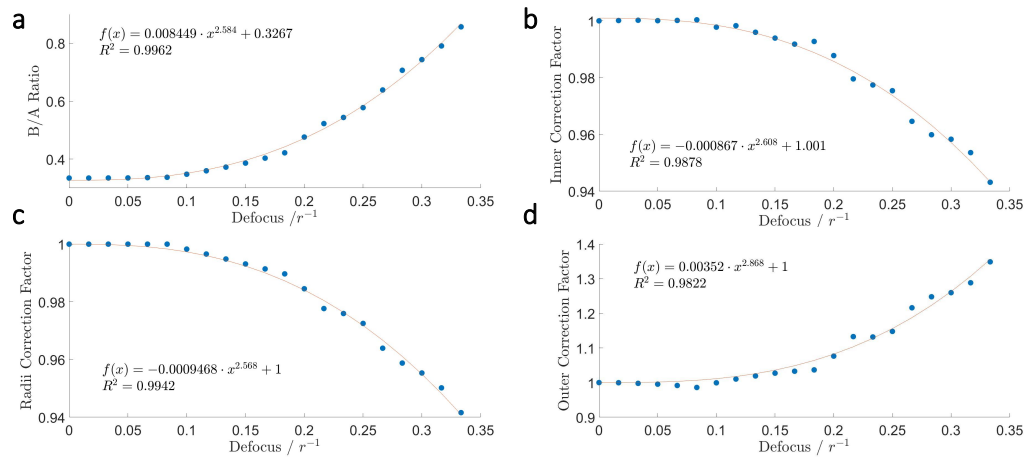


Figure 4.14: Dependencies of profile measurements on defocus A series showing the effect of defocus on measurements including the B/A ratio used for determining the level of defocus present in our samples in a). b) shows the inner integral changes with the outer integral shown in d). c) demonstrates how radii change with an increasing defocus level.

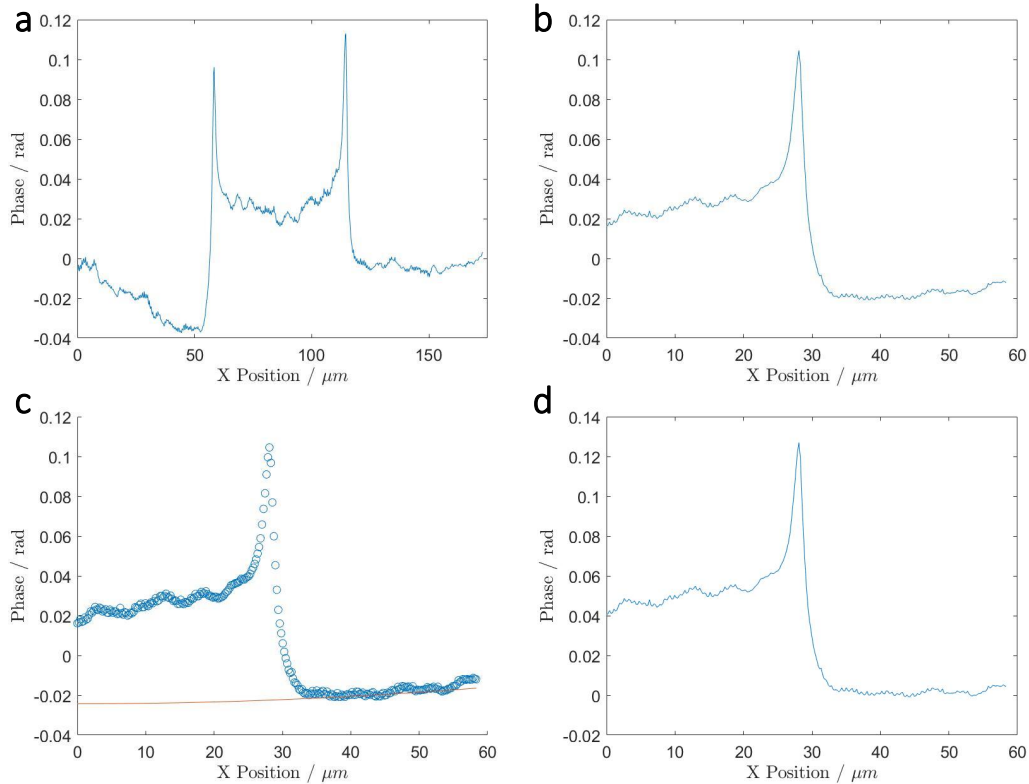


Figure 4.15: Example data pre-processing a) shows the phase profile as measured directly from the phase image. b) shows the profile once symmetrised with either side of the profile averaged together. Robust fitting was then undertaken to produce the fit seen in c) which once subtracted left the profile in d)

The inner and outer regions that were used in lamellarity and sucrose concentration determination are shown in Fig. 4.8 and consisted of the first 35% of a symmetrised profile and the peak to the edge of the profile equating to 28.5% of the diameter. It can be seen that the inner and outer integrals changed with defocii according to the fits shown in Fig. 4.14, with both fits having an R^2 value upwards of 0.99.

4.8 Comparing simulations to experimental data

4.8.1 Symmetrisation

As previously mentioned birefringence within the sample caused an asymmetry between the two halves of the profile. Whilst this was a quantity we aimed to quantify, in this first instance we aimed to remove these effects to allow quantification of the lamellarity and internal concentration. A symmetrisation step also removed any linear background slope present in our data. The profile was split in half about the centre, C , with the first half being flipped in the x axis. In this way we created an average between the two halves to remove the effect of birefringence. This is hereafter referred to as the symmetrised profile and is shown in Fig. 4.15b.

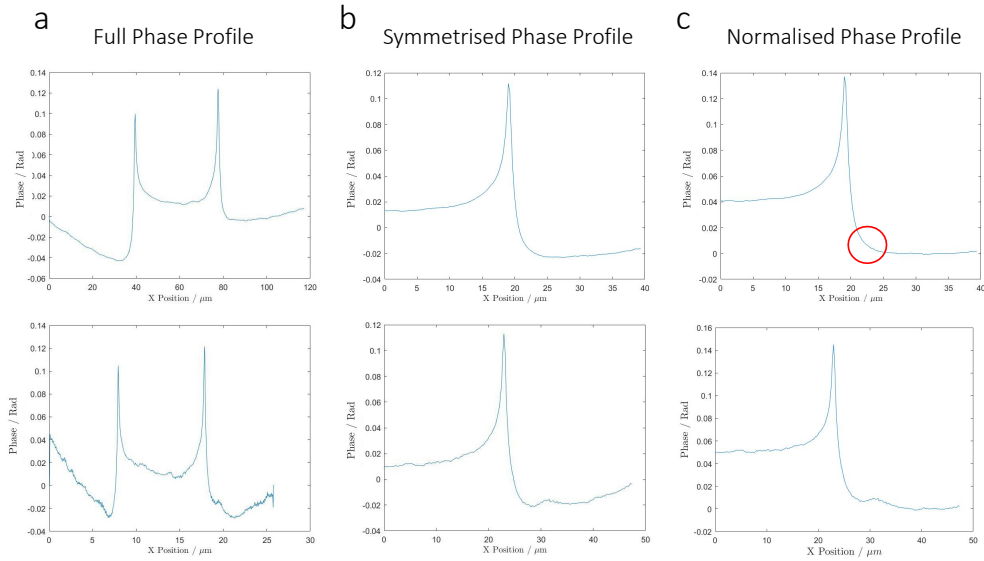


Figure 4.16: Normalised profiles A series showing the progression of an experimental dataset to the profile used to calculate lamellarity and sucrose concentration. **a)** shows the full phase profile of the line cut from the phi image. **b)** shows the profiles one they had been symmetrised where the first half of the profile was flipped and averaged with the second half to mitigate any birefringent effects. The background was then fitted and removed to produce the normalised profiles shown in **c)**.

4.8.2 Background fitting

Robust fitting and normalisation of profiles allowed integrals to be calculated and compared to simulations. This background fitting removed any offset and remaining background aberrations from the qDIC phase retrieval. Robust fitting was the method used to fit the background of the profile without being as influenced by any artefactual signal. As we knew that the background was our true baseline any artefactual signal always appeared as additional signal. We could therefore fit the background from underneath ignoring deviations for a set width, in this way we fitted the background whilst being largely unaffected by additional signal. The vesicle signal was omitted from fitting via masking with the edge of the mask set as $C + (0.595D)$. Fitting was undertaken from this edge value up until $1.75E$. Once the background had been fitted it was subtracted from the data to produce normalised phase profiles. An exemplar of this process is shown in Fig. 4.15c and the code used is in Appendix C.1.

4.8.3 Defocus correction

Utilising the previously calculated defocus for each vesicle the factor required to correct the inner and outer integrals was calculated. Once we started to investigate this defocus correction in comparison to our experimental data we adapted to better represent the data collected and artefacts introduced by our set up. As vesicles are symmetrical about the focal plane in z a negative defocus value that is differentiable from the positive is not possible. Therefore, our tail ratio, which increased with defocus, could not be lower than the minimum observed. As previously discussed

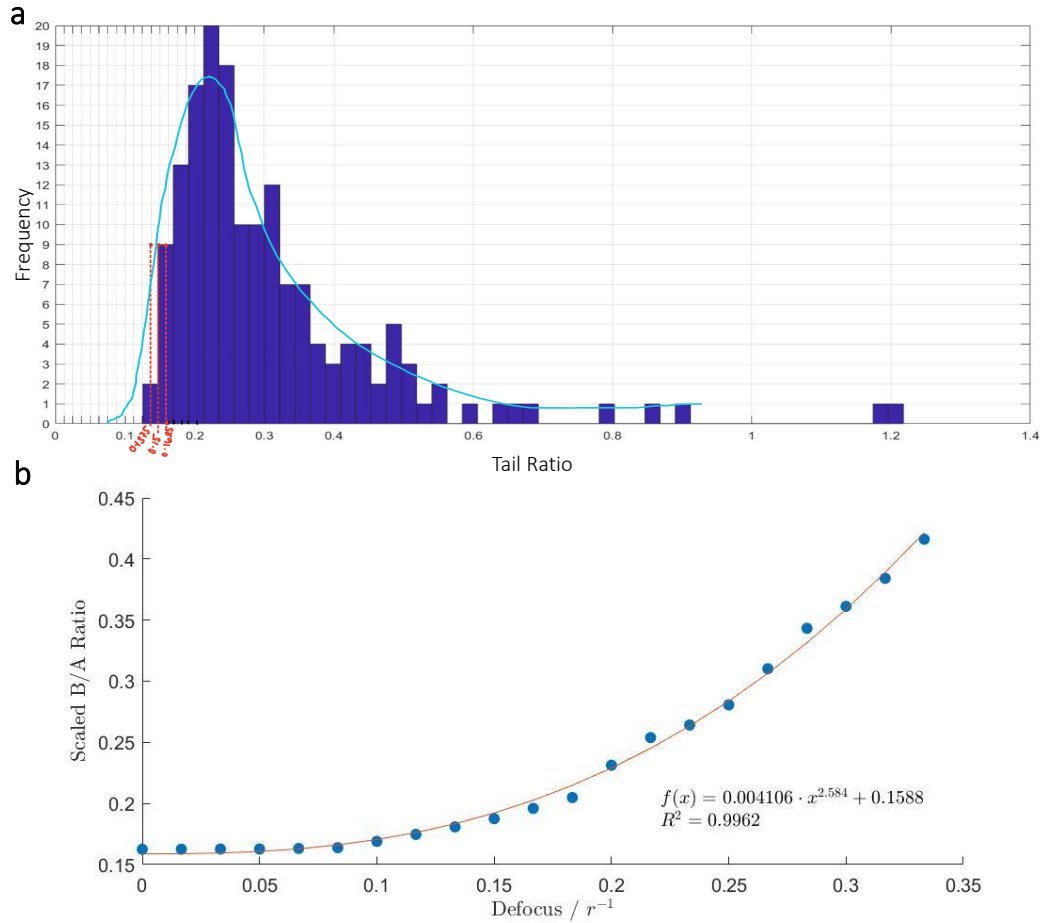


Figure 4.17: Scaling the defocus response a) shows the histogram of the tail ratio of all vesicles measured with the half maximum value shown. This value was used to scale the defocus relationship as shown in b). It was this relationship that was used to determine vesicle defocus.

there were some effects that we could not simulate for and therefore, save for artefactual and badly fitted datasets, we could account for some of these effects by using the minimum dictated by our data. Fig. 4.17a shows the distribution of the tail ratio of our measured data. The half maximum of the lower tail of the histogram was taken as the value for 0 defocus and the simulated fits were scaled accordingly as shown in Fig. 4.17b, with the original data shown in Fig. 4.14. Once calculated the defocus was used to select suitable data with vesicles with a $D > 0.28r$ being removed from further analysis. Further selections are discussed below. Remaining data sets were corrected according to their assigned defocii for both inner and outer integrals to generate the edge ratio that was used to determine lamellarity and sucrose concentration as discussed in Section 4.8.3.2.

The resulting defocus for all vesicles analysed is shown in Fig. 4.18a prior to thresholding. Fig. 4.18b shows the same measurement after thresholding.

4.8.3.1 Further thresholding

Data was further thresholded by disregarding any vesicles with a diameter lower than $15\mu\text{m}$. As the robust fitting was designed to reduce the influence of background interference, as discussed above, we also used it as a measure of the interference

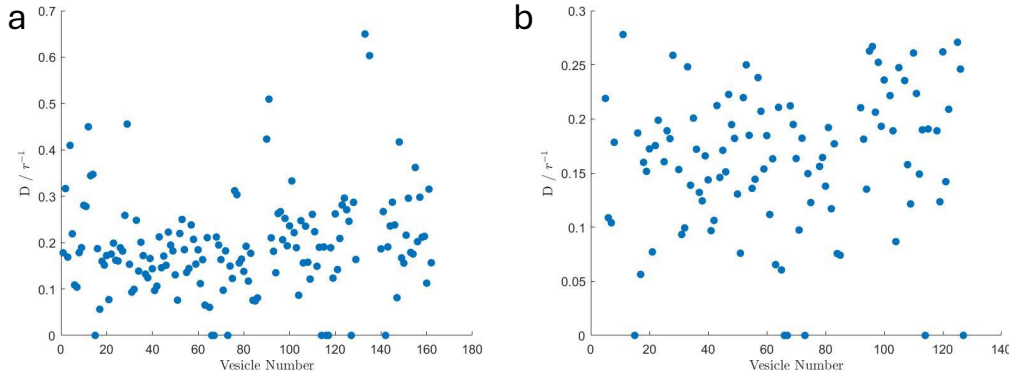


Figure 4.18: Sample defocus Scatter plots showing the resulting defocus D for all vesicles measured (**a**) and selected data for further analysis in **b**).

present in the data. It follows that if there was a lot of debris in the background there was likely to be some in the optical pathway across the vesicle. To quantify, the proportion of 'well fitted data' was measured. A threshold was set at a 5 mrad difference between the fit and data, this was set after comparison of well fitted dataset and poorly fitted dataset. The percentage of the fitted region that was outside of this set threshold was calculated with any datasets containing less than 70% of data points with differences below the threshold being disregarded. Visual thresholding was also undertaken where, by eye, any profiles that obviously were an incorrect shape were disregarded and likely arose from a high background signal generating an inability to fit and normalise the profiles correctly.

4.8.3.2 Fitting phase profiles

Remaining experimental phase profiles were integrated according to Equation 4.4 where 0.35 and 1.285 correspond to 35% and 128.5% of the vesicle diameter, respectively. The integrals were defined as Inner phase (φ_I) and Outer phase (φ_O). The relationship of inner and outer integrals with lamellarity is plotted and the gradient of each returned the coefficients found in Equation 4.6, which, from our simulations were $a_{in} = 13.79$, $a_{out} = 4.781$, $b_{in} = 15.31$ and $b_{out} = 0.2921$.

$$\int_{0.5}^{0.85} f(x)dx = \varphi_I \quad \int_1^{1.2850} f(x)dx = \varphi_O \quad (4.4)$$

In turn, these were combined into the matrix used for data fitting according to Equation 4.7. r_0 is the radius of the simulated vesicle which in our case was $15 \mu\text{m}$ and r being the radii of the measured vesicle, this correction term $\frac{r_0}{r}$ was used to correct the integral difference for radii scaling. This had been simulated to show it was a linear relationship as demonstrated in Fig. 4.19a for lamellarity and quadratic for the internal volume (Fig. 4.19b). For this analysis the integrals of the measured vesicle were combined into the vector $\vec{\varphi}$ as defined in Equation 4.5.

$$\vec{\varphi} = \begin{pmatrix} \varphi_I \\ \varphi_O \end{pmatrix}. \quad (4.5)$$

$$\varphi_I = a_{in} \cdot L + b_{in} \cdot S \quad \varphi_O = a_{out} \cdot L + b_{out} \cdot S \quad (4.6)$$

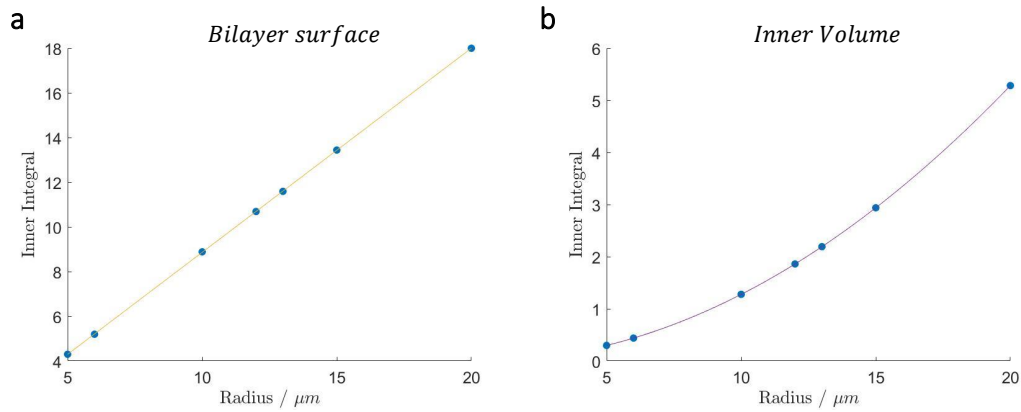


Figure 4.19: Radii dependency of integrals Simulations were undertaken to determine the effect of radius on integral values, **a)** shows the linear dependency of integrals with lamellarity in contrast to the quadratic dependency shown in **b)**

$$\begin{pmatrix} L \\ S \end{pmatrix} = \vec{\varphi} \begin{pmatrix} a_{\text{in}} & b_{\text{in}} \\ a_{\text{out}} & b_{\text{out}} \end{pmatrix}^{-1} \quad (4.7)$$

$$\text{Lamellarity} = L \left(\frac{r}{r_0} \right) \quad [\text{Sucrose}] = S \left(\frac{r}{r_0} \right)^2 \quad (4.8)$$

The resulting lamellarity and sucrose concentrations from this analysis is shown in Fig. 4.20 and indicated that the vesicles we were measuring were predominately unilamellar. It is clear there is still error in these measurements as we expect our measured lamellarities to be an integer, however we could assign vesicle lamellarity nonetheless. As our vesicles were predominately unilamellar Fig. 4.12 demonstrates we had the sensitivity in our technique to identify the difference between vesicles containing 0 and 0.2 mM sucrose. As discussed previously we observed differences between simulated profiles and experimental as broadening effects arising from imperfect imaging. Although we have used these to try and correct the data through defocus correction it could still be that these effects were causing additional area under the curve and hence the additional signal attributed to lamellarity. Another possible cause of the error observed here was arising from the symmetrisation step as the averaging removed the effect of birefringence it could have led to some additional signal where the background wasn't constant and averaging was insufficient to remove this. These results showed an improvement to the method initially used as we determined the lamellarity and sucrose concentration with more confidence and a smaller range of lamellarities which, when looking at the peak height didn't appear to be the case. We also determined a difference in sucrose concentration and therefore determined that we were successfully establishing the intended 0.2 mM sucrose concentration gradient as evidenced by Fig. 4.12c. In this way we were able to confirm our GUV preparation protocol was working correctly, to improve the ability to interpret this data additional components could be added to the simulations as the better the simulations represent the experimental data the less error is introduced.

4.9 Further interpretation of phase profiles

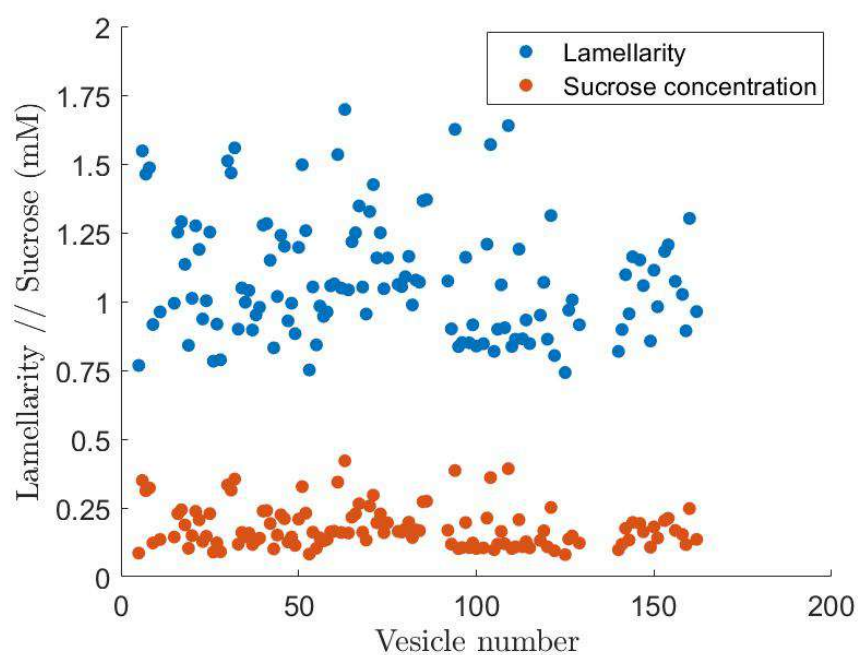


Figure 4.20: Measured lamellarity and sucrose concentration A scatter plot showing the results from the comparison of experimental data with simulated values. This plot shows that the majority of our vesicles were unilamellar and contained under 0.2mM sucrose.

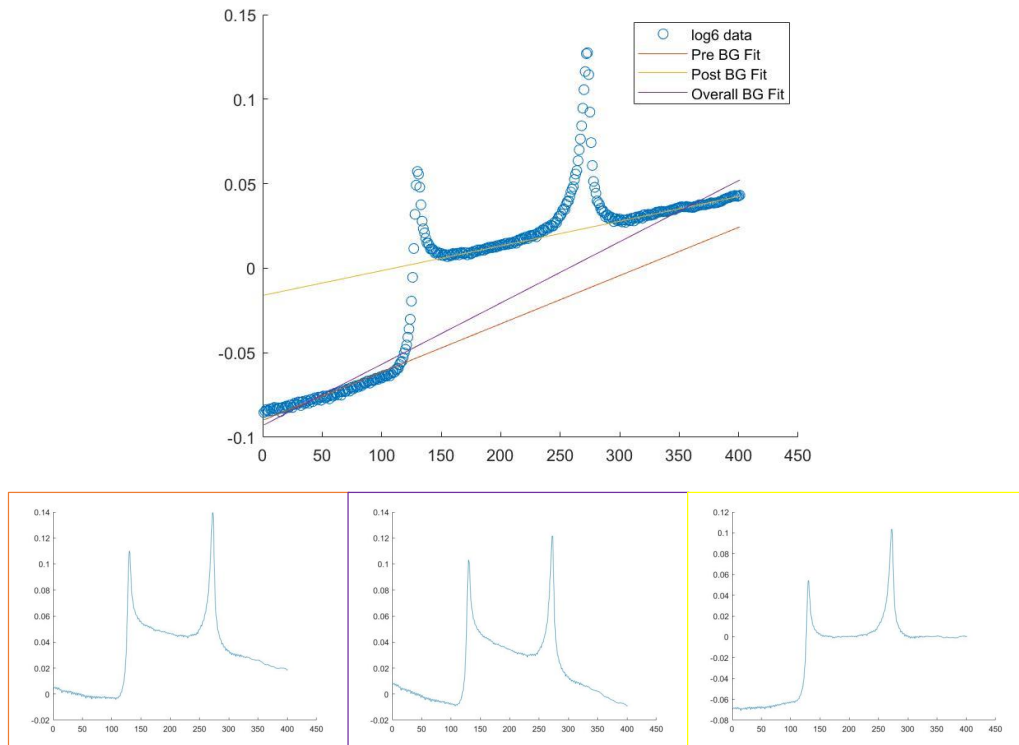


Figure 4.21: Birefringence effect on normalisation Graphs showing the overall background fitting and subsequent normalisation (Purple), background fitting before the vesicle (Orange) and background fitting after the vesicle (Yellow), highlighting the step change across the vesicle.

4.9.1 Birefringence

To fit experimental data all phase profiles were normalised. When carrying out this step for the NA data set we found a directional offset still in the data with one peak higher than the other (Fig. 4.21). When looking into the data at different κ values it became clear that there was a step change across the vesicle accompanied by a gradient present in between the peaks that was not present in the simulation. Upon further analysis the gradient of the interior matched that of the post vesicle background whilst the first peak was distorted. This could have reflected some birefringence found across the sample akin to that we have measured in lipid rods (unpublished data). For lamellarity calculation and general characterisation of the profiles it was decided that symmetrisation of the profiles would remove this effect for the remainder of the analysis to allow lamellarity and internal solution determination. As seen in Fig. 4.22, in an exemplar vesicle this change can be easily seen and measured at 0.02 which is in line with expected. To fully quantify this effect it would need to be incorporated into simulations and used to interpret experimental profiles. A plan for these simulations is discussed in Chapter 8.

4.9.2 NA dependence

4.9.3 Acquisition of numerical aperture data

Data was acquired using the same acquisition parameters whilst NA was varied. 0.3, 0.5 and 0.72 were acquired using the dry close working distance condenser and 0.3,

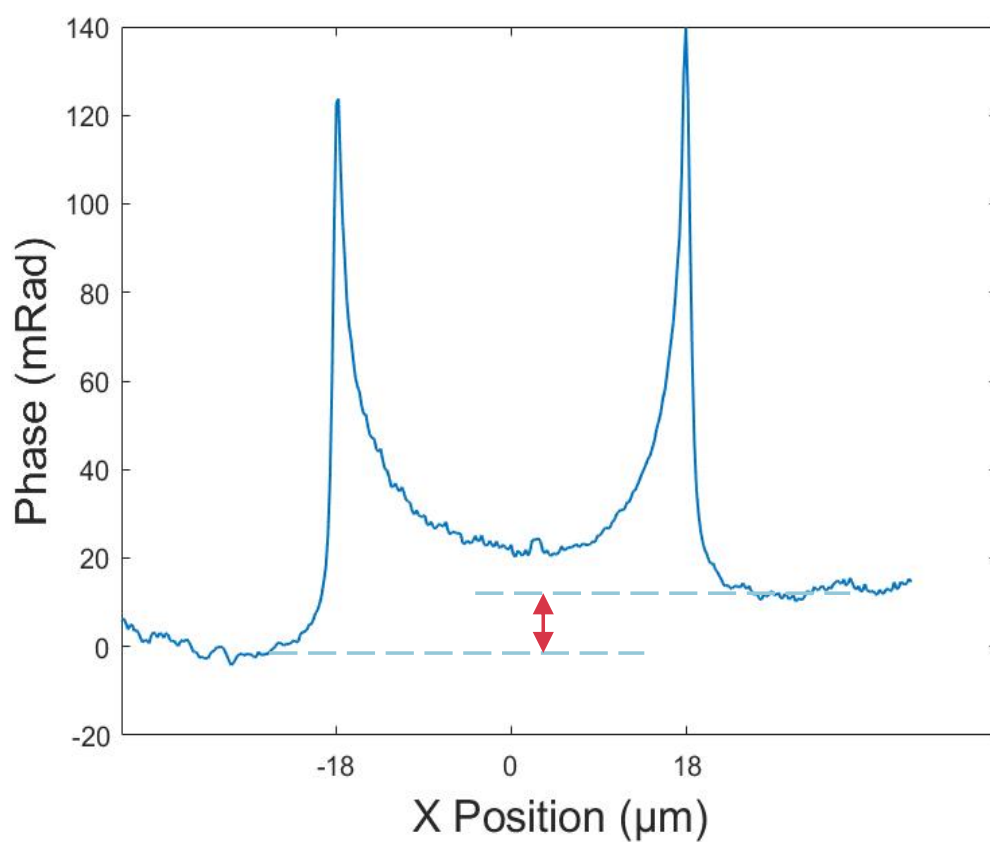


Figure 4.22: Measured birefringence A normalised profile with minimal background is shown where the birefringence was measured as indicated by the arrow. In this case it was measured at approximately 0.02

0.5, 0.72, 0.95, 1.00, 1.15, 1.25 and 1.34 were taken using the oil condenser.

4.9.4 Comparison of numerical aperture data

To allow corroboration of our simulations we took data with varying NA sizes. Areas of the profile highlighted for comparison were the height and shape of the outside edge of peaks. In the simulated profiles the peak height decreased with an increasing NA. To normalise the experimental data robust fitting and symmetrisation was undertaken. As can be seen in Fig. 4.23a the profiles appeared to scale in the same way with numerical aperture changes, a noticeable difference was the difference between the peak height of increasing NAs in comparison to the overall peak height. As highlighted in Fig. 4.23b the data taken with the oil condenser appeared to follow the observed trend of an increasing peak height with a decreased NA, however, the range over which this change occurred was significantly reduced. This suggested that there were other effects inducing beam spreading and that a narrow beam experimentally did not confer the same resolution, further evidenced by the height of the peaks being altered. Fig. 4.23b and c also showed a similar trend where the oil experimental data followed the simulated trend to a different scaling. The difference in values seen between simulated and experimental data meant it became difficult to make alterations for the error induced by the numerical aperture. Large changes to the NA set experimentally did not incur the degree of augmentation of the profile expected from the simulation. This meant small errors in this value were unlikely to impact results as much as could be corrected for indicated by simulations. For this reason no corrections were made based on these simulations.

4.10 Discussion

When calculating the refractive index of the bilayer we calculated $n_w + 0.1346 \pm 0.0036$, leading to a total refractive index of 1.468. The standard error was greater than that cited in literature (~ 0.0016). [226, 227, 228] Seeing as this value was reliant on using the membrane thickness, which for this composition had not been determined, meant this was an additional source of error. Quantitative analysis of iGOR data from these membranes will allow us to determine membrane thickness for POPC:POPE, and subsequently reduce this error. The systematic error arising from the uncertainty in this value was reduced when measuring vesicles with fewer bilayers as was used with a lesser frequency during analysis. Other sources of error for this method could be blurring of the vesicles arising from vesicle movement during image acquisition. This was reduced by manually cropping images stacks in all dimensions to improve vesicle alignment in each frame prior to averaging. Analysing all κ values simultaneously reduced error arising from incorrect line placement. An important consideration was deformation, as any deformation could have introduced additional bilayers or increased membrane fluidity which could have added blurring of the image. By imaging as soon as the GUVs had been produced, we minimised the chance of this occurring. The epifluorescence images confirmed that this had not occurred.

The systematic error for the measurement of sucrose concentration gradient was similar to that of the refractive index change expected for the concentrations we are using. However, by using the measured value of refractive index change due to the bilayer we effectively eliminated this as any systematic error in the membrane

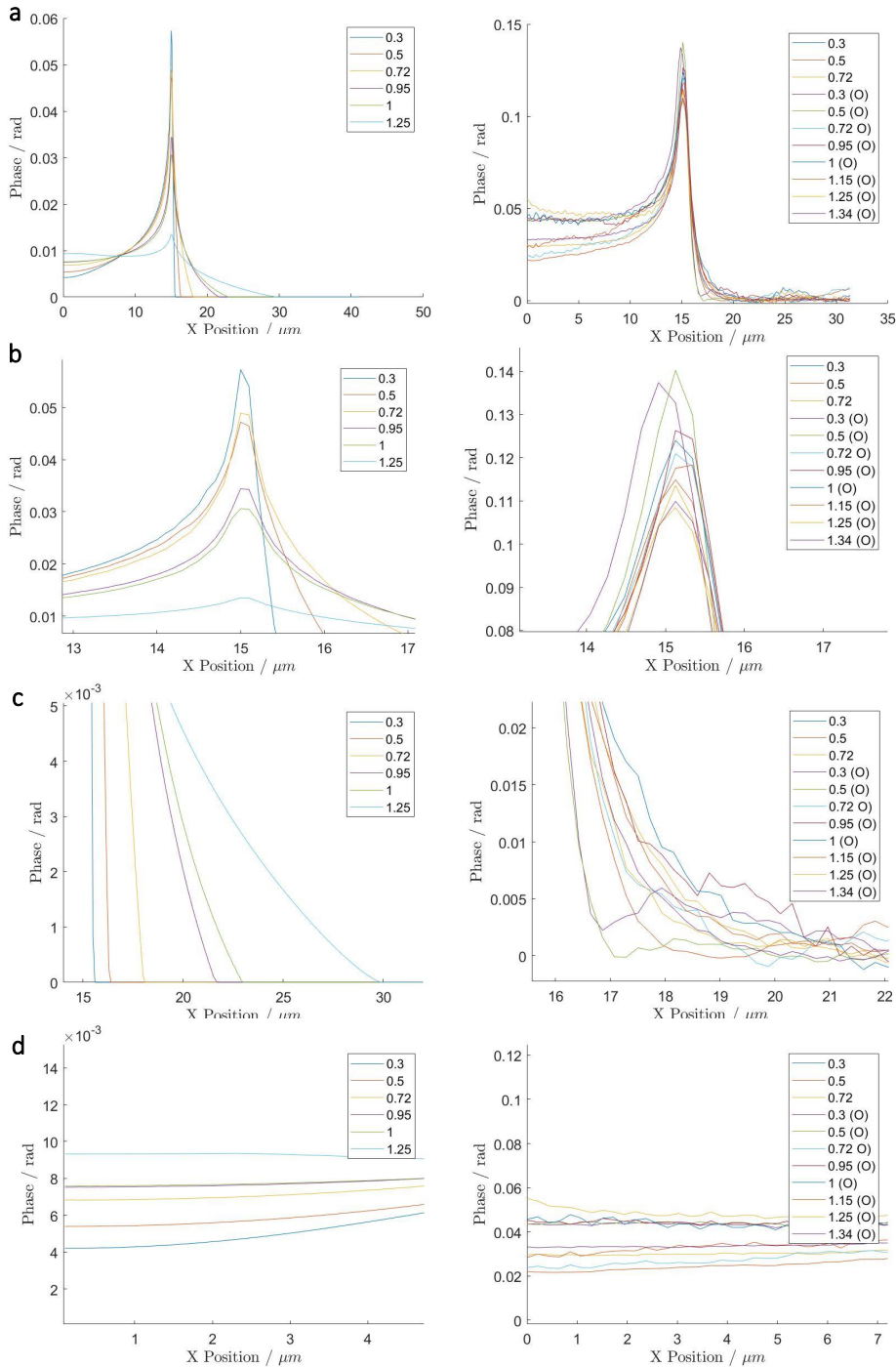


Figure 4.23: Comparison of simulated and experimental NA variation The simulated effect of a changing numerical aperture shown in the left panel with the corresponding experimental data in the right. **a)** is a comparison of the full profiles demonstrating the same shape with a changing numerical aperture. It also shows that the peak separation wasn't present in the same magnitude as the simulations, suggesting the NA was not the only parameter responsible for peak broadening. This is highlighted in **b)** where the same graphs are shown zoomed to the peak region. **c)** shows a zoom in of the outer region of the GV signal where the same spreading trend can be seen again to a different magnitude. **d)** shows the region corresponding to the central region of the GV where the same dependency of NA can be observed.

thickness used was compensated by the refractive index calculated. This meant that if the same membrane thickness and refractive index were used in the sucrose calculation then the change of phase attributed to the bilayers should have not been affected by this systematic error and be largely correct. This can be implemented as a scaling factor in the simulations once we have robustly fit the background of the phase profiles and have confidence in the measured phase change. Other sources of error could have arisen during the preparation of sucrose solutions as they were very low masses and could have been inhomogeneous. These sources of error did not affect the determination of the lamellarity as the corresponding change of phase caused by this error was insignificant when considering that caused by two bilayers, corresponding to an increase in lamellarity.

Analysis of the 0.5 mM sucrose data showed that the vesicles observed were predominantly bilamellar. This was unexpected and highlighted a problem with the GUV preparation protocol regarding the sucrose concentration gradient. We hypothesised that this was due to the internal pressure being too great for a single bilayer to withstand. To enable the production of stable unilamellar vesicles we have determined the maximum sucrose concentration gradient that a single bilayer can withstand to be 0.2 mM which has led to improved stability. It is also important to ensure we were only observing one bilayer during quantitative analysis of the membrane as this is the conformation of membranes within nature and therefore the most biologically relevant.^[230] For this we are in the process of generating fitting methods for our simulated models to allow us to characterise a range of parameters that influence qDIC response: Lamellarity, concentration gradient across membrane and birefringence.

After incorporation of simulations into our analysis protocol we were able to analyse experimental data using the whole profile. This improved our interpretation as the peaks were less likely to be impacted by poor background fitting. To improve our background fitting we implemented robust fitting which allowed us to be less affected by background artefacts and therefore better fitting. This also provided a measure by which to threshold the data as any datasets with many background artefacts were discarded.

Comparison to the simulations allowed us to incorporate defocus fitting and correct for any defocus present in the sample. An increasing level of defocus showed the spreading of the peak signal alongside changes to the inner integral. The outside of the peak was used to determine defocus level as this was less affected by any internal volume however both integrals were corrected by a factor determined by the simulations allowing us to more accurately determine the integral size. The ratio of the centre and peak heights were used after this correction to determine the lamellarity and sucrose concentration of the vesicles. In this way we highlighted the error in our initial work and gained confidence that our GUV preparation protocol was working in the way we expected and predominately producing unilamellar vesicles containing up to 0.2 mM sucrose.

There are still slight errors present in this data as the measured lamellarities are not integers, further simulations to incorporate other features of the vesicles into the simulations such as birefringence could improve our experimental interpretation. Further simulations could also provide additional information into bilayer composition as in a POPC:POPE membrane differing ratios are likely to produce different birefringent effects as POPE is more likely to change the polarisation state of the light. Despite the fact that the lipid bilayer on the wire prior to electroformation is

a 1:1 composition it may be that the vesicles do not have a the nominal composition.

This work provided an analysis pipeline for qDIC vesicle measurements to allow development of the preparation protocol and understand the populations of vesicles we are producing. It also provides scope for future work to further quantify features identified from the profiles.

Chapter 5

Protein insertion into GUVs

To enable future work to observe membranes upon protein insertion, the protein insertion into our model membranes had first to be developed and verified. To observe the insertion of proteins into a membrane using iGOR, a protein of sufficient size needs to be used. The following was undertaken as a collaboration with Colin Berry's group in line with their work on insecticidal proteins for food production. For ease of incorporation into our experimental procedure App6Aa1 (historically known as Cry6Aa1) was chosen as it also had been indicated to spontaneously insert into bilayers at very low concentrations and was a protein of interest they had successfully purified. It is a decameric protein predicted to have a 4 nm inner pore diameter due to its similarity to ClyA.[231] It is therefore expected to be observable using iGOR. As the protein was known to insert into a binary lipid composition POPC:POPE, that we have shown can exist as a homogeneous bilayer or a phase separated state under stress, it, combined with our model membrane was expected to provide a functional model to observe its dynamics and phase behaviour.

App6Aa1 is a *Bacillus thuringiensis* toxin that forms pores in the epithelial cell membrane of the midgut lumen of insects without the need for receptors. This provides a toxic effect as once ingested and inserted, the pore destabilises the membrane permeability to various ions causing colloid-osmotic lysis.[232, 233, 234] The protein consists of 475 amino acids and has a similar structure to other pore forming proteins such as ClyA.[235, 236, 237] The protein has been shown to insert into the membrane at concentrations as low as 100 fg/mL during electrophysiology experiments. The protein was inserted into POPC:POPE (1:1) membranes in the presence of n-decane.[238] pH has been shown to have minimal affect on insertion with pH 5.5 and 7.5 slightly more effective than 9.5, however a pH of 10 is optimal for protein solubilisation.[238] The protein has a stable secondary structure across a pH range of 3 to 11. This secondary structure consists of 10 helicies and 2 beta sheets, with the structure cross-linked by disulphide bonds. These overall generate a head subdomain consisting of the residues closer to the C-domain which also contains a beta-tongue and a tail domain from residues in the N-domain. The transmembrane region is formed after a conformational change to release the head domain containing the putative transmembrane region.[236, 239] The structure can be seen in Fig. 5.1

The protein insertion can be modelled on the structural studies undertaken on the ClyA protein. The monomer undergoes a conformational change upon contact with lipids where the beta tongue becomes a helical extension in the protomer. This protomer then oligomerises to form a pore. The pore is formed from 12 monomers and stabilised by 25 Hydrogen bonds and 13 salt-bridges. The transmembrane re-

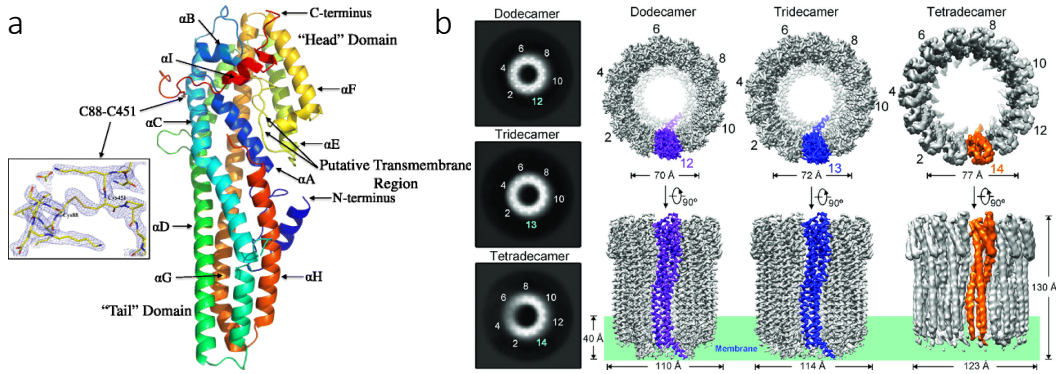


Figure 5.1: App6Aa1 protein structure a) The protein structure as determined by Dementiev *et.al.* [239] b) Cryo-Em structures of pore forming ClyA proteins as presented by Orth *et.al.* [240]

gion consists of the beta tongue and the amphipathic helicies. These allow polar residues to line the inside of the pore to allow the maintenance of the biophysical properties, the non-polar residues allow the pore to insert.[231, 241] Prior to observation using iGOR we needed to confirm that the App6Aa1 pore was inserting into our model membranes under our experimental conditions and to determine a suitable concentration for our purposes. The ideal concentration would be one resulting in one pore (12 monomers) per region of interest, which for our field of view in iGOR was about $64\mu\text{m}^2$. This posed difficulties as the vesicle density was highly variable and therefore this concentration would change dependent on the vesicle density. In this chapter I will discuss our preliminary experiments towards insertion protocols.

Upon the realisation that we could observe phase separation using epifluorescence during protocol optimisation, discussed in Section 3.2.2, it was hypothesised that we could use this to identify protein insertion as proteins have been shown to alter the phase behaviour of lipid systems. Therefore we compared the measured phase transition temperature (T_m) before and after addition of protein into the GUV solution.[15, 22] This reflexively aided our protocol development as we measured the phase transition temperature of the POPC:POPE (1:1) lipid composition which had not been fully characterised. By confirming the phase transition temperature we incorporated it back into our preparation protocol to ensure the lipid was always in liquid disordered phase during GV formation.

An epifluorescence approach was then undertaken using a water-soluble fluorophore in the vesicle centre. Pore formation was visible as a loss of internal fluorescence as the fluorophore exited through the pores over time. In principle, the lowest observable rate of fluorophore loss from the vesicles should be a suitable concentration. The proof of principle study was undertaken by myself and the preliminary study as it currently stands was undertaken during a BSc project with Oscar Hummerstone although it is first presented here as analysis was undertaken after his involvement. After the optimisation of the GV preparation protocol described in Section 3.1, GV samples stable for a time frame suitable for this experiment could be prepared.

A GUV funnel was developed to facilitate the addition of protein during imaging, as discussed in Section 5.3.

5.1 POPC:POPE bilayer phase transition

For our preparation protocol to be effective our samples needed to be produced with the lipid bilayer in its liquid phase. For our lipid composition the gel-liquid phase transition temperature was not known. Thus a protocol was designed and carried out to determine this transition temperature.

The phase transition temperature of lipid mixtures lies between those of the individual species involved. As well as changing the transition temperature, the addition of lipid species into a composition broadens the transition in temperature.[67] It was hypothesised that insertion of the App6Aa1 would alter the phase transition temperature and could therefore be used to confirm insertion for subsequent experiments. The change didn't prove to be sufficient for a conclusion to be drawn. Further work to confirm insertion is discussed in 5.2.

5.1.1 Phase transition temperature in literature

Whilst many lipid compositions have been fully characterised, POPC:POPE in a 1:1 ratio has not to our knowledge. The pure lipids have transition temperatures of -2°C for POPC and 35°C for POPE as given by manufacturers. A partial phase diagram for POPE with the addition of POPC up to a molar fraction of about 0.22 is reported in [242] and shown in Fig. 5.2. By extrapolation of this graph to pure POPC an approximation of the phase transition temperature was defined by the equation: $T = -26.913(\text{Molar fraction of POPC}) + 25.064$. This gave an approximation of 11.6°C , Fig. 5.2. The increased range of temperatures that the lipids transition over means that this temperature was approximate.[242]

5.1.2 GV morphology during phase transition

Fluorescence and DIC imaging was used to observe the morphology of GVs and identify effects of a phase transition. Liquid-gel phase transitions of vesicles could be measured by altering the temperature during imaging as described in Section 2.4. A phase separation was observed, Fig. 5.3d, due to the partitioning of the ATTO488-DOPE into the POPC fraction. Once the temperature dropped to below the phase transition temperature for POPE it started to transition into the gel phase. This transition caused the POPE in the gel phase to separate out from the POPC, to some degree, as it transitioned at a lower temperature. ATTO488-DOPE has a lower phase transition temperature and was therefore more likely to be contained within POPC regions. This partitioning caused dark patches across the surface as the POPE regions contained minimal fluorophore. Alongside this the membrane surface took on a different conformation, with the surface becoming faceted as areas of gel phase lipids formed as seen in Fig. 5.3a and b. The gel phase is quite stiff, and it is energetically favourable to have flat regions and edges of disorder between them, maybe still containing the liquid phase lipid.[243] The phase transition from the gel phase to the liquid disordered phase was seen after re-heating from below phase transition temperature. Once the vesicle transitioned out of the gel phase it destabilised and increased the fluctuations observed as the surface area expanded, so it became non-spherical, and the liquid phase was flexible, so it could fluctuate in shape. It was seen when the vesicle became destabilised and the membrane began to fluctuate to a much higher degree often causing deformation events such as that observed in Fig. 5.3c, and on a lesser scale in c. This change was due to the

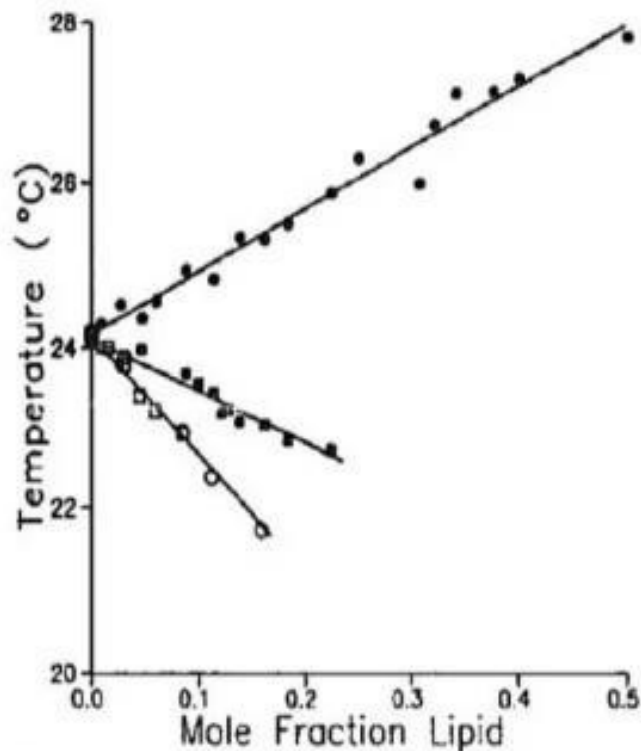


Figure 5.2: Partial phase diagram for POPC/POPE The partial phase diagram used to determine composition phase transition temperature - "The gel-to-liquid crystalline phase-transition temperature of POPE as a function of the percentage of POPS (black square), POPS plus 10 mM CaCl₂ (black circle), POPC (square), or POPC plus 10 mM CaCl₂ (circle) added to the membrane". [242]

constriction of the vesicle when it was cooled causing the loss of internal solution which upon expansion of the membrane once heated caused destabilisation.

The phase transition was observed upon cooling by a phase separation across the surface of the vesicle or a change in the appearance of the membrane. This was repeated for samples containing 0.08 mg/mL App6Aa1 protein. Protein sample preparation was undertaken by Lainey Williamson and Colin Berry.

5.1.3 Determining 1:1 POPC:POPE phase transition temperature

A vesicle at room temperature (20°C) was cooled using the slide heater described in Section 2.4 and dry ice where required. The temperature was decreased to 10°C or beyond if no change had yet been observed. Image series were taken at 1 s intervals, as described in Section 2.7, as the temperature was decreased and recorded manually. Once gel transition had been observed, either by membrane dimpling or phase separation, such as those seen in Fig. 5.3a,b and d, the process was repeated

whilst warming the sample using the slide heater until the membrane was observed destabilising as in Fig. 5.3a and e. The rate was determined by the slide heater, the goal temperature was set and the maximum rate achievable used. On average this was about 40s per degree when cooling and 10s per degree when heating. Dry ice was used for cooling trying to maintain a slow cooling rate to ensure the temperature could be recorded.

The lower limit of the phase transition temperature was defined by the lowest temperature a change was observed upon heating and the upper limit was defined by the first temperature a change was observed upon cooling. Under observation the phase transition temperature of the POPC:POPE:ATTO488-DOPE (50:49.9:0.1) was measured as between 14.5 to 12.5°C. The lower limit was averaged out over three heating experiments and the higher over three cooling experiments. These replicates were all independent as after each vesicle had been through a cooling and heating protocol the vesicle was destabilised and deformed.

5.1.4 Phase transition temperature upon App6Aa1 insertion

Based on the literature, initially a concentration of 2.5×10^{-12} g/mL App6Aa1 was chosen.[238] However, the phase transition temperature was measured as between 12 and 14.8°C showing no change to the control given the accuracy of our method. When the concentration App6Aa1 protein was increased to 0.35 g/mol we observed vesicles experiencing high levels of deformations, an example of which is seen in Fig. 5.4. Using a range of protein concentrations (0.008, 0.04, 0.0825 and 0.175 g/mol) the lower limit of transition was observed at around 10°C and a higher limit change between 15 and 16°C $n = 10$, but a clear trend could not be deduced as there were vesicles in the sample showing changes of membrane phase at temperatures within the control range. All experiments using the range of concentrations were used together as no distinction could be made. These vesicles could be those without a protein, however this was deemed not sensitive enough to confirm the protein insertion.

5.1.5 Summary

The results gained from this study did indicate a change due to the protein insertion and with more sensitive recording equipment, such as in conjunction with iGOR, this could be a viable method for the measurement of protein insertion. However, due to the human error involved with this protocol mainly the recording of the temperature change with frame this protocol was sufficient to find a range for the GUV preparation but the error meant that the change for protein insertion was insufficient to make any conclusions.

5.2 Pore formation probed by leakage

Vesicles in this section were prepared using the nominal procedure as described in Section 2.2.1 with 0.5 mM sucrose and the specified concentration of fluorophore as an internal solution. The lipid composition was POPC:POPE (1:1) unless otherwise stated.

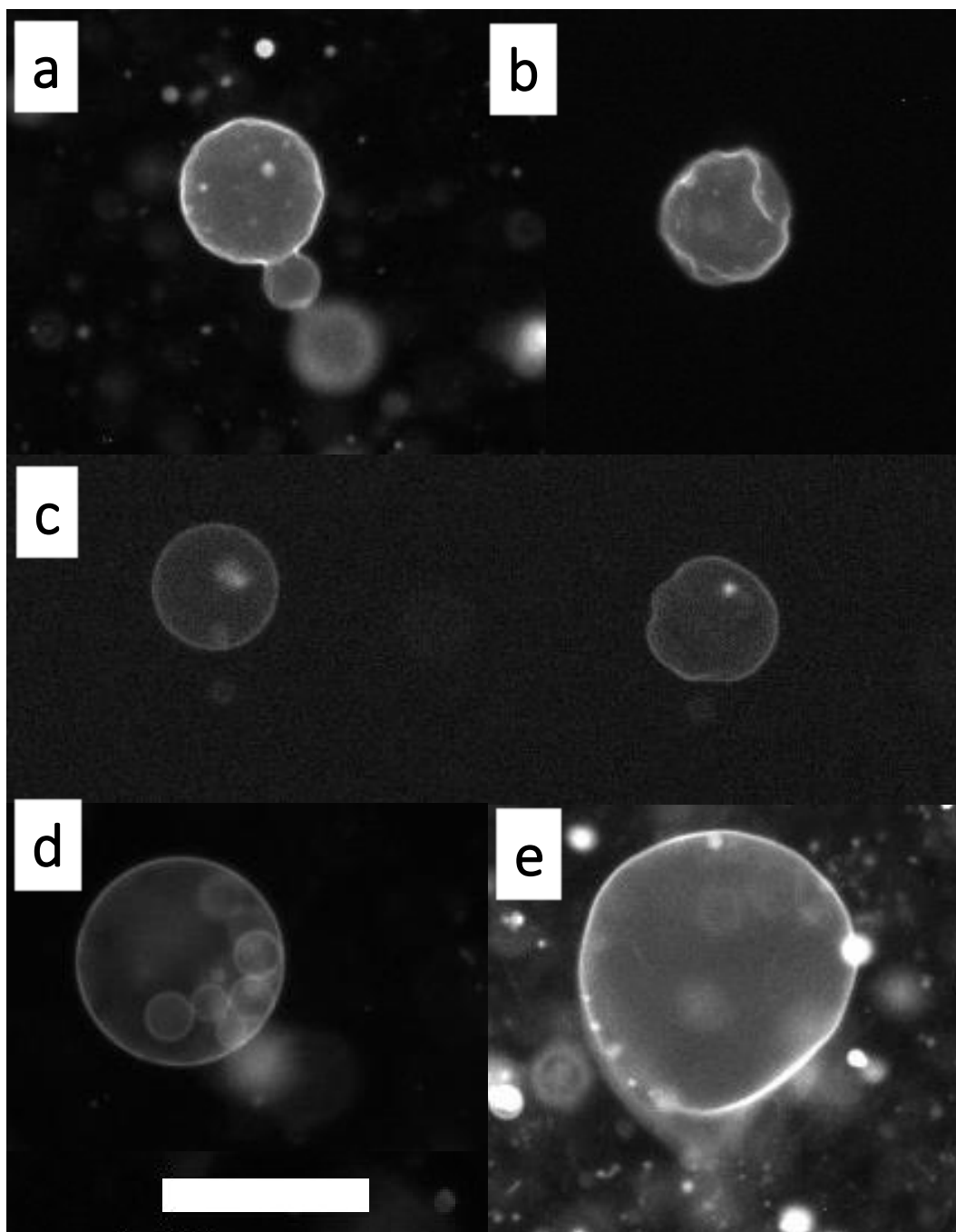


Figure 5.3: Phase transition Fluorescent images Fluorescence images of POPC:POPE 1:1 GUVs in solution prepared at 20°C with an internal sucrose of 0.5mM demonstrating the morphological membrane changes observed indicative of a phase transition. **a)** Upon cooling the membrane below 12°C was seen to gain an irregular, faceted surface as some of the lipids transitioned into gel phase while phase separating into different mole fraction mixtures, for which a more pronounced effect was seen in **b)**. **d)** A phase separation could be seen across the surface of the vesicle by the dark patches. Upon heating, deformation was seen in **c)** of a vesicle destabilising across a temperature increase also shown in **e)**. The scale bar represents 50 μm for all images

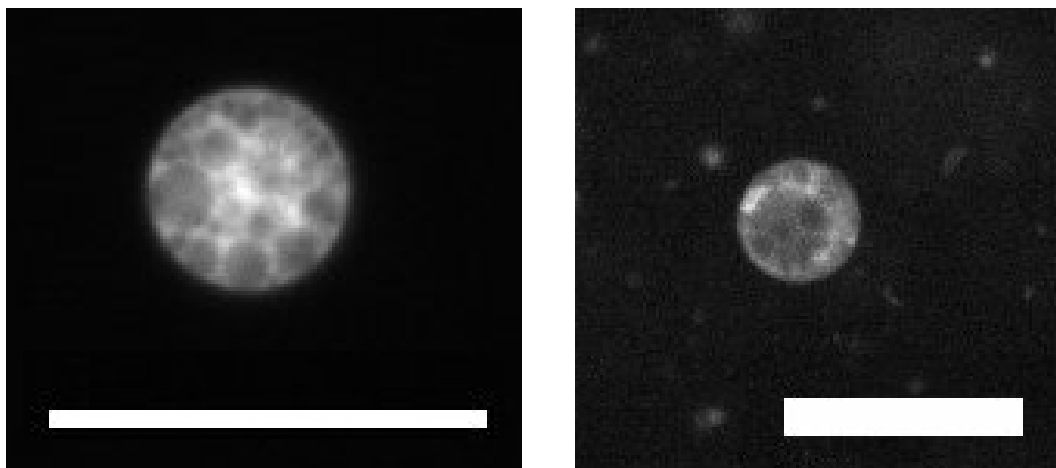


Figure 5.4: Deformation with high protein concentration Epifluorescence images of vesicles observed in solution with 0.35 g/mL App6Aa1 protein showing deformation. Scale bars represent 50 μm .

5.2.1 Fluorophore choice

When using the negatively charged fluorophore Rhodamine-6G at a concentration of 30 nM we found disruption to the electroformation as demonstrated in Fig. 5.5a, where samples did not contain vesicles of a sufficient diameter. Images were taken as described in Section 2.7, the membrane was probed with ATTO488-DOPE to allow vesicle membrane to be observed. This effect was seen even at low concentrations of 70 pM. When we switched to a neutral dye we were able to maintain the efficacy of the electroformation procedure. As the dye had an overlapping fluorescence spectra with the membrane pore, it has an excitation wavelength of 492 nm and an emission of 517 nm, no membrane fluorescence probe was used. Images were taken as specified in Section 2.7 using 10% lamp power. Co-localisation of the 5(6)-Carboxyfluorescein and vesicles using DIC is shown in Fig. 5.5b, where the DIC data was acquired as an average of 256 frames with a 0.12 ms exposure time and an angle of $+15^\circ$. This confirmed that this water-soluble fluorophore could be internalised into vesicles without disrupting the electroformation. We used the filtration to remove the fluorophore from the outside solution as described in Section 3.1.4. We required a concentration gradient of the fluorophore large enough that any changes were easily observed. It was also important that when a pore was produced the fluorophore moved down its concentration gradient into the external solution, where it became insignificant due to the sample volume. This was mostly dictated by the fluorescence intensity being well observable. The osmotic pressure was negligible, and the relative concentration inside/outside was dictated by our filtration step. As we used a flow, our minimum reduction in this step was a purification factor of 60 from which the fluorophore in the outside medium was small enough to provide suitable contrast as seen in Fig. 5.7 and have negligible effect on osmotic pressure. A 5(6)-Carboxyfluorescein concentration of $5e^{-7}\text{M}$ proved sufficient for these purposes as indicated by the low background and high vesicle signal seen in the intensity profiles as shown in Fig. 5.5c and d. This also shows that the filtration method was exchanging the outside medium effectively. In this experiment, to date, we have shown that 5(6)-Carboxyfluorescein could be incorporated into vesicles as an internal solution, removed from the external solution and remained there over the course of 24-48 h for GVs which were stable over that

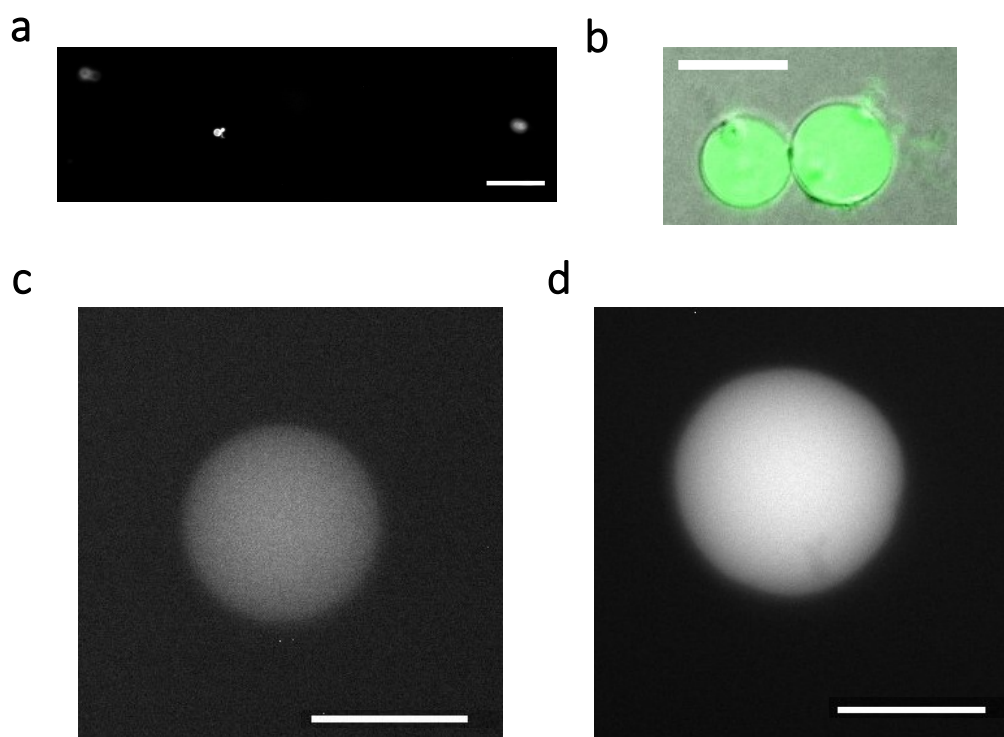


Figure 5.5: Fluorescence and DIC images of dye filled GVs **a)** represents the sample as produced in an electroformation solution of Rhodamine-6G demonstrating the inability to form vesicles of a suitable size. **b)** is a composite images demonstrating colocalisation of the internal 5(6)-Carboxyfluorescein dye and DIC images containing no bilayer fluorophore. **c,d)** show examples of vesicles with 5(6)-Carboxyfluorescein dye showing we could generate a contrast between internal volume and background. Scale bars represent 50 μm

interval.

5.2.2 Imaging protocol

The problem of photobleaching is highlighted in the graph shown in Fig. 5.7c of a vesicle imaged at the same place 1 minute apart using a lamp power of 100% using the 10x objective with Fig. 5.7d showing the reduction of photobleaching when using 10% power. To limit the effect of photobleaching no technical replicates were taken on the same vesicle as different vesicles in the same sample were considered independent repeats. The main cause of uncertainty during this experiment was the deformation of the GVs observed during protocol optimisation. Line cross-sections of each vesicle were compared as shown in Fig. 5.7a and b. This is indicated in the graph in Fig. 5.7e where the maximum intensity of all vesicles with diameter above 5 μm were measured. This graph appears to show that the day 2 vesicles were smaller. This could be indicative of loss of internal volume and subsequent loss of membrane as budded vesicles, resulting in a smaller vesicle. It could also be due to measurement bias and the instability meaning different vesicles were measured each day. There were a differing number of vesicles on each day which also indicated instability. To be able to separate the effects of deformation and photobleaching the

stability issue of the GVs was corrected as discussed in Chapter 4.

5.2.3 Maintaining fluorophore concentration in GUVs

When analysing the control samples containing only GVs and 5(6)-Carboxyfluorescein the intensity profiles of the vesicles were compared. These profiles and their corresponding vesicles are shown below in Fig. 5.7a and b these show that the fluorophore remained within the vesicle and could not cross the membrane. The retention was difficult to estimate due to factors such as photobleaching and the difficulty measuring the same vesicle populations due to sample change over this time frame. An average maximum intensity of 143.31 and 105.02 for day 1 (n=10) and 2 (n=8), respectively demonstrated a loss of 27%. An anomalous result was the vesicle showing a maximum intensity of 250 on day 2, higher than any from day 1. One explanation for this could be the loss of bilayer material through small tube production as this would not have taken internal volume. The ability to measure vesicles on day 2 with a measurable contrast to background due to 5(6)-Carboxyfluorescein provided confirmation that the membrane was impermeable to the fluorophore in the absence of external factors.

5.2.4 Loss of fluorophore upon pore formation

Vesicles prepared for the experiment using 0.08 mg/mL protein were a POPC:POPE:ATTO488-DOPE (50:49.9:0.1) lipid composition, with those prepared for 0.7 mg/mL remaining as POPC:POPE (1:1). Protein addition and imaging was undertaken as described in Section 2.6.1.1 in enclosed samples. Fig. 5.7e and h are examples of vesicles taken 1 day after the addition of 0.35 mg/mL and 0.08 mg/mL Cry6Aa1 respectively and show the loss of fluorophore from the vesicle and an extensively deformed vesicle, the sample contained no such morphologies on day 1. However, these images were taken when we had possible contamination and at low sample sizes we could not reliably make conclusions on the causes, however it did indicate that this methodology should work.

The large-scale deformation seen in Fig. 5.7e with many internal vesicles was likely to be due to the protein insertion as there was no indication that bacteria would cause this effect. This conformation was not observed in samples not containing protein but likely contaminated. It was a much larger effect than seen due to GV instability. A possible mechanism for this was the destabilisation of the membrane due to protein insertion causing additional fluctuations which were minimised by an invagination event causing a vesicle filled with external solution to form, as it was seen that the internal vesicles contained significantly less fluorophore. A schematic of this hypothesis can be seen in Fig. 5.6. In this way the membrane minimised the effect of the pores without losing all internal volume as we also observed pockets of high fluorescence within the structure. This explanation assumed the loss of pore upon the deformation event as otherwise the internal volume would have had a near homogenous distribution of fluorophore however there is evidence for short pore lifetimes.[238] These results gave us a ball-park figure for the tolerance of the GVs for protein insertion.

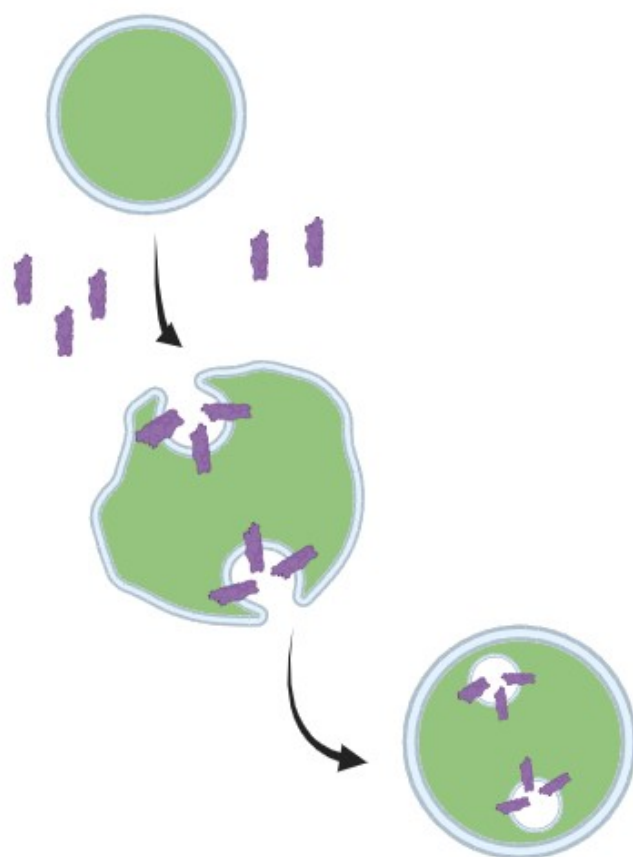


Figure 5.6: Schematic of hypothesised mechanism forming internal vesicles containing no fluorescence A schematic where the fluorophore filled vesicles are in a protein environment (purple) leading to a destabilised and invaginating membrane causing internal vesicles to form containing no fluorescence.

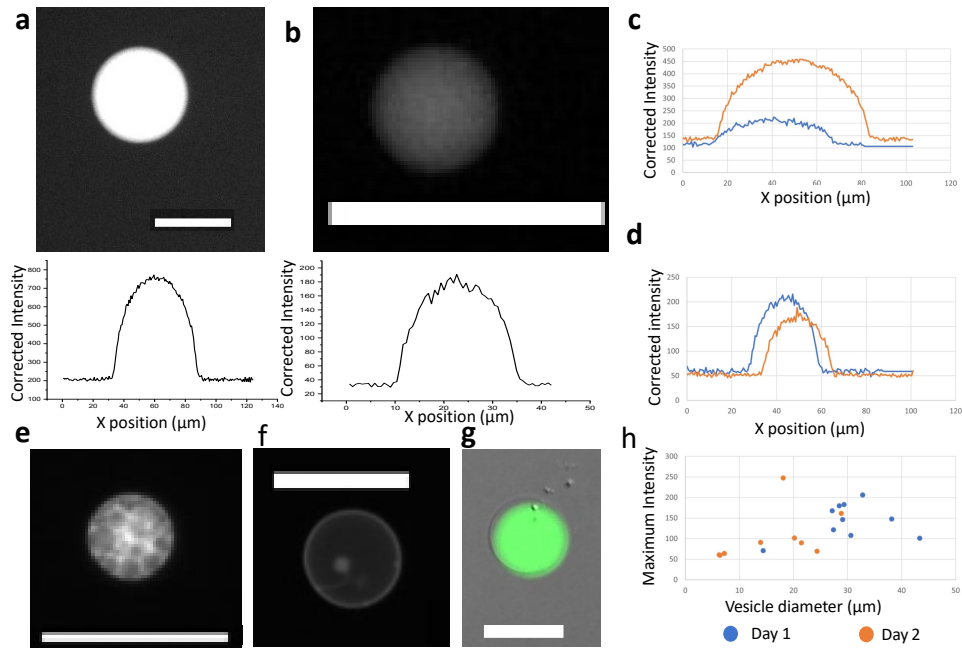


Figure 5.7: Summary of Cry6Aa1 insertion experiments a) and b) Epifluorescence images and their corresponding intensity profile across the middle of the centre of the vesicles from day 1 and 2, respectively, containing only 5(6)-Carboxyfluorescein. a) Shown in high contrast to highlight clear background. c) Effect of photobleaching intensity of the same vesicle after 1 minute at 100% lamp power as compared to d) 10% lamp power under continuous illumination. Intensity is shown after dark counts (192) had been removed. d) shows the vesicle centre intensity and diameter of a sample from day 1 to day 2, prepared using nominal procedure. e) and f) Effect of 0.35 mg/mL and 0.08 mg/mL Cry6Aa1 addition, respectively, vesicles also contained ATTO488-DOPE in the membranes. g) Co-localisation of 5(6)-Carboxyfluorescein with the vesicles using a composite of an epifluorescence image and a DIC image of the same frame of interest. h) A comparison of the maximum intensity measured for each vesicle on day one and day two showed an average decrease in intensity.

5.2.5 Drawbacks and limitations

When observing the control, we identified that the stability issues we were experiencing with the GVs were rendering these results unreliable. With varying degrees of GV deformation occurring in the sample, the internal volume of vesicles changed and therefore so did the concentration of internal dye independent of the protein. This could have occurred via various processes such as the formation of internal vesicles containing external solution and decreasing the internal volume, and the loss of internal solution within vesicles. Another effect of the deformation was the inability to correlate the vesicles from different imaging sessions especially at low leakage rates and longer time intervals. This was challenging as these were the conditions we were most interested in.

5.2.6 Preliminary study

A similar approach was taken as before where 0.5×10^{-7} mM 5(6)-Carboxyfluorescein was added to solution before electroformation and therefore incorporated into the vesicles and subsequently filtered out of the external solution. Controls were established and taken through the same protocol as the samples with the App6Aa1 protein added. This allowed us to observe protein insertion. It is worth noting that both the 5(6)-Carboxyfluorescein and the ATTO425-DOPE could be measured when using the GFP filter but only the bilayer probe with the custom blue. A sterile environment was introduced in the preparation of these samples eliminating contamination, this was confirmed by checking samples for bacteria in DIC. These experiments were repeated in excess of 20 repeats however for many of the experiments the vesicles although measured did not produce data suitable for analysis either through lack of measurable internal fluorescence signal or unstable vesicles with either internal defects or insufficient size. This left a small sample size of approximately $n=10$ independent replicates and therefore an example of a control and protein sample were chosen and analysed to demonstrate proof of principle as discussed below.

The introduction of "Open samples" reduced the need for controls as we could measure the vesicle before and after protein addition meaning vesicles could act as their own controls. This is seen in Fig. 5.8a where vesicles were holding an observable amount of 5(6)-Carboxyfluorescein for at least 40 min and subsequently losing it after addition of $7 \mu\text{g}/\text{mL}$ protein. There was a decrease in counts in the green channel in the centre of the vesicle, where intensity was predominately from the internal solution. At the same position the intensity of the blue channel decreased less suggesting that this effect wasn't solely due to photobleaching. In the control, the maximum value of the green channel showed an 8.01% reduction, compared to 1.62% for the blue after a 40 min incubation. The vesicle to which $7 \mu\text{g}/\text{mL}$ had been added showed a 7.57% reduction in the blue channel corresponding to the bilayer and a 68.23% reduction of the fluorescence observed in the green channel. These results can be seen in Fig. 5.8c, a change of shape can clearly be seen, before the protein was added the signal was dominated by the internal volume in contrast to the shape corresponding to a bilayer dominance after addition. These were compared to the shapes observed in the control sample where the dominance of internal and bilayer volumes did not change for each channel. They could also be compared to the shape of profiles simulated and analysed in Chapter 4.

An observation during the protein insertion was the phase separation observed on the bottom of the vesicle Fig. 5.9c, where the fluorescence was seen separating out

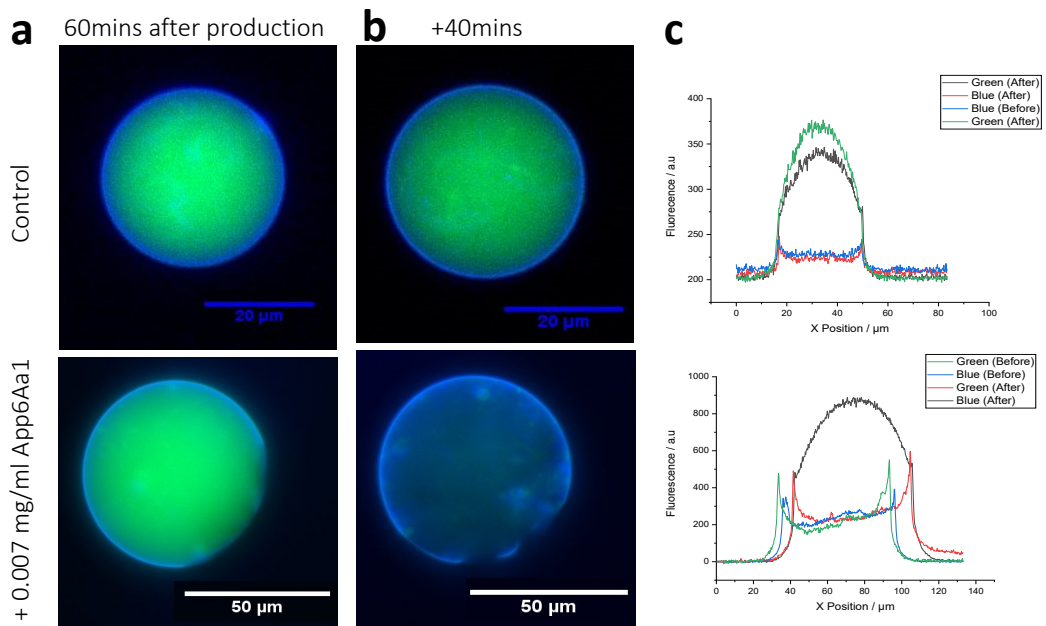


Figure 5.8: 5(6)-Carboxyfluorescein loss from GV after App6Aa1 addition **a)** False colour epifluorescence composite images before protein addition with **b)** showing the same GVs imaged 40 min later showing retention of fluorophore in control samples in contrast to the loss observed after the addition of 0.007 mg/mL App6Aa1. **c)** shows the graphical representation of the fluorescence cross-section in both channels for all vesicles. The internal volume can be seen dominating in the green channel in the control vesicle both before and after in contrast to the bilayer dominance seen in the green channel after protein addition.

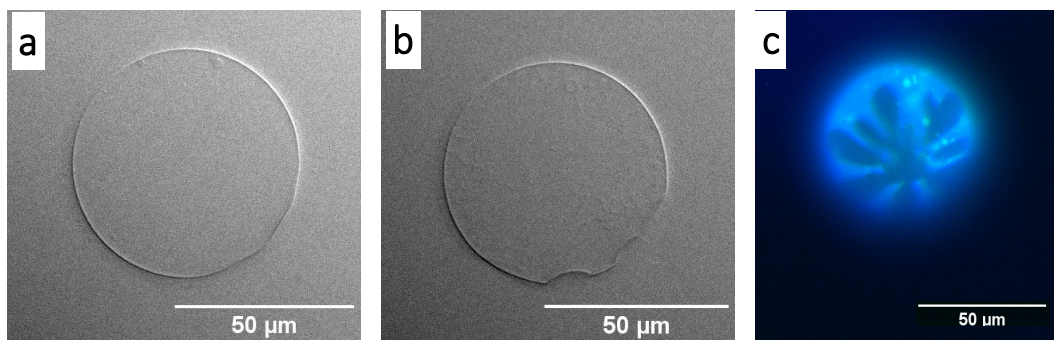


Figure 5.9: GV morphology from GV after App6Aa1 addition a) and b) DIC images of vesicle before and after 0.007 mg/mL App6Aa1 addition, showing the induction of a non spherical conformation of the vesicle cross-section. c) False colour composite image of the lower surface of the vesicle after addition demonstrating extensive phase separation of the membrane in this region.

of areas. This effect was predominately the bilayer probe. Fig. 5.9a and b, show the DIC images measured at an angle of $+15^\circ$ before (a) and after (b). A clear change in the membrane was seen where an area of inverse curvature was observed. Whilst this could be an example of membrane conformation change due to pore insertion it can be seen in Fig. 5.9a that before protein insertion the bilayer was already not spherical in this area. It is therefore unknown whether this was a protein effect or a due to the open conformation of sample imaging, however as shown in Fig. 5.10 this phase separation was observed in other protein samples.

The maintenance of intensity in the green channel had been measured across different control samples as seen in Fig. 5.8 where we had established that vesicles could hold onto 5(6)-Carboxyfluorescein. This figure displays results that demonstrated a clear difference between the control and protein samples. However, insufficient samples sizes were acquired during this short term BSc project to confirm insertion in a statistically relevant way. When we tried to repeat this experiment to gain additional data sets for statistical analysis we encountered solvent contamination arising from this project, delaying this work.

5.3 Use of imaging funnels

To improve the use of 'open' samples and prevent oxidation effects we aimed to generate a smaller contained volume with additional stability. This was required as a droplet on a surface relying on surface tension was not a reliable system for these experiments. Any disturbance would have caused the droplet to spread causing the loss of sample. By containing the sample droplet in a funnel we were able to produce a stable imaging volume that we could add to and manipulate. This also allowed us to better control the concentration of GVs as we could manipulate the GV solution during imaging using a small volume pipette through channels on the side. This was kept to a minimum as any manipulation could have damaged GVs. This is also an imaging system that can work across the both microscopes making it compatible with iGOR imaging which is the goal after protein insertion into vesicles is confirmed.

We designed a few iterations of funnels aiming to allow the exchange of solution during imaging. These are shown in Section 2.2.2.3. Initially it was designed with

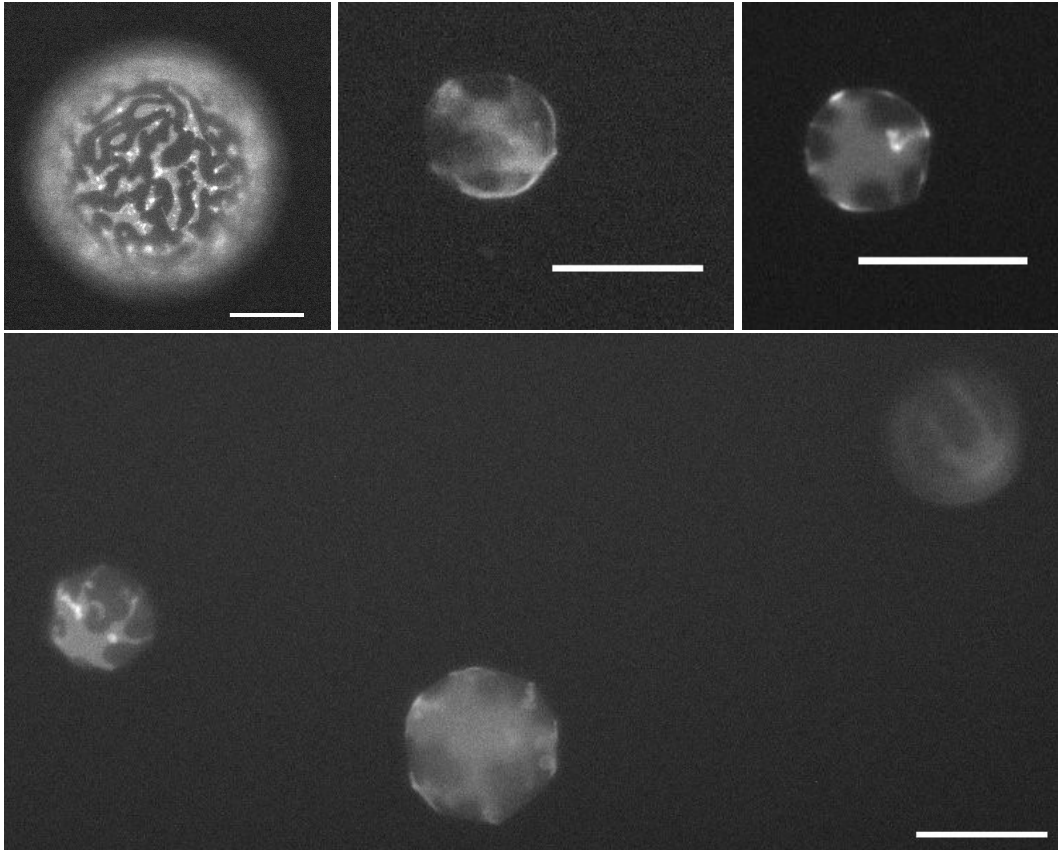


Figure 5.10: Epifluorescence images of phase separation after App6Aa1 Epifluorescence images of phase separation in GV samples after $7\ \mu\text{g}/\text{mL}$ App6Aa1 was added. All examples show regions of differing fluorophore concentration with some having excluded it completely, indicative of phase separation. Images were acquired using the GFP filter. Scale bars represent $50\ \mu\text{m}$.

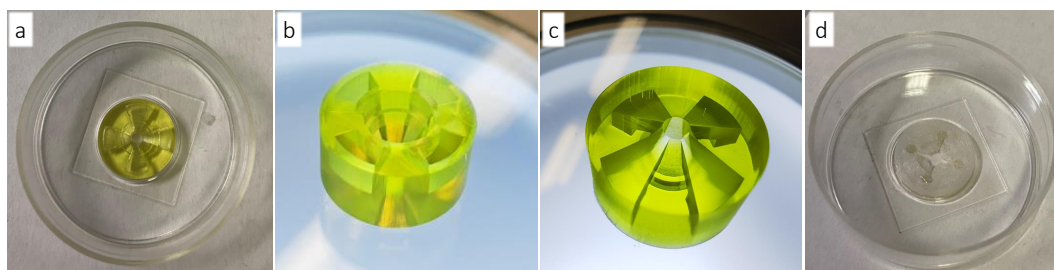


Figure 5.11: 3D printed funnel used for GV imaging Images a-c) show the original funnel printed with a) glued to a dish. d) shows a modified design designed to prevent unwanted capillary action.

four channels connecting at a central well. It was this central well into which solution was added and a small coverslip placed on top to avoid evaporation and air flow perturbations. When using this iteration of the design, capillary action of the channels was sucking the liquid out of the central well and away from where we could image. To combat this we changed the design to make the top of the channels start further back, however, we encountered the same effect still causing capillary action. For imaging, this device was used with a greater volume of sample to completely fill up its volume preventing loss from the central well. In this way we were able to maintain a volume suitable for imaging however this volume extended beyond where we could image meaning diffusive movements could take GVs outside an observable region.

Further iterations to remove the effect of this capillary action involved removing the top of the channels all together. However, to still generate a ledge onto which the small coverslip could be placed the channel had to be shallow otherwise we found we were still generating the unwanted capillary action. In the funnel shown in Fig. 5.11d we were able to generate an imaging volume into which we could add GV solution. This was then used in an attempt to obtain better controls for the preliminary study. The maintenance of an internal dye could be measured over a time frame of 1.5 h to provide the controls for the data such as that shown in Fig. 5.8. When this was attempted we found that in preventing the capillary action we were not sealing off the funnel efficiently enough and therefore inducing movement of vesicles upon imaging. This movement was too great to obtain images of a sufficient quality as our minimum exposure time was 100 ms and even at this temporal resolution blurring was observed. As we had identified 5(6)-Carboxyfluorescein as being susceptible to photobleaching the increased time involved in gaining a good image of a moving vesicle would have rendered results inconclusive as the internal solution would have been likely to photobleach. A further iteration was developed in which only one channel remained, reducing the circulation that could occur in this system, thereby reducing the movement of vesicles. This was found to be insufficient with vesicles still exhibiting blurring effects although in this case it seemed to be induced upon illumination of the sample. In theory with careful imaging and limited exposure times we could use this iteration for protein controls.

These results show a pipeline for the analysis of protein insertion into lipid vesicles once the funnel has been developed. The funnel will give us a suitable imaging system for which we can produce sufficient controls to fully confirm protein insertion into our vesicles and take onto iGOR imaging. Design changes planned include altering the gradient of the channels and using 2 channels to allow the flow

of solutions through the channel with a sufficient seal to prevent unwanted movement of GVs.

5.4 Discussion

Results from measuring the phase transition temperature did not show sufficient accuracy to determine a change upon protein insertion. This was due to the extended range of the phase transition due to their binary composition.

An alternative protocol was developed to identify pore formation by observing the loss of an internal fluorophore. Initial experiments allowed us to develop the protocol to produce vesicles containing an internal solution that was removed from the background. We assessed methods of imaging with an aim to minimise photobleaching effects for which we established that the bilayer fluorophore was more photostable than the 5(6)-Carboxyfluorescein and methods for which we can quantify to correct the effects. Upon realisation our samples were contaminated and we were still experiencing large scale deformation events these results were disregarded.

By eliminating sample contamination we were confident that any loss of fluorophore seen was due to protein pores. This loss of fluorophore remained hard to quantify due to the effect of photobleaching which was not necessarily even across all samples due to varying imaging times. Using DIC to locate and initially image these vesicles reduced this effect as it used a wavelength which was not absorbed and a much lower intensity. In principle, we could quantify concentration of fluorophore inside the vesicle using the approach discussed in Chapter 4. Another method to avoid photobleaching the 5(6)-Carboxyfluorescein was looking for vesicles using the blue filter cube as the transmission region didn't overlap with the fluorophore. We would therefore only be photobleaching the bilayer fluorophore which was more stable and not used in further quantification. It also reduced sampling bias that might have occurred in samples with less fluorophore in their interior which would also be the case when using DIC to locate vesicles.

We have shown that we can observe a change in loss rate of fluorophore across a lipid bilayer upon the addition of protein, these results indicated protein insertion into our model membranes. These results show that we have a working protocol to assess protein insertion into lipid bilayers, however we did not have sufficient controls to conclude in terms of concentration dependency. Improvements to this technique are being undertaken in terms of imaging funnels as discussed, with new devices designed to generate a more stable way of measuring these samples. Once working we can add to our control dataset to gain statistically significant results and transition to imaging with iGOR.

Chapter 6

Interferometric gated off-axis reflectometry

Interferometric Off-axis reflectometry (iGOR) is a form of digital holography that measures the complex field a signal using its interference with a reference beam. A plane wave (a focussed beam with a large beam waist compared to the wavelength, here typically a few $10\ \mu\text{m}$ size) is used to excite a sample, here a GV which scatters light in all directions, as shown in Fig. 6.1. The light scattered in the epi-direction is collected, generating the signal field. As iGOR is a wide-field technique that, in our case can be retrieved at a frame rate of 327 Hz, it provides a fast, label-free method for probing dynamics. The signal is measured in both co- and cross- polarisation directions, co- and cross-polarised to the excitation field. The signal can be refocused using the known field propagation in space. This refocusing capability is enabling three-dimensional tracking of organic nanoparticles as described in Chapter 7. In terms of the GV measurements this provided an opportunity to shift the focal plane to the top of the vesicle. The frame rate provided a temporal resolution of 3 ms, which, coupled with sub-nm resolution in membrane thickness and axial position provides a step change in label-free biological imaging.

By using an external reference beam we avoided the requirement of techniques such as iSCAT to measure objects within a few microns of a glass-water interface, allowing the measurement of a suspended region of the model membrane unveiling the true dynamics of a membrane without a support.[131, 133, 134] The incident light on the membrane was here chosen linearly and the primary analysis was undertaken on the data measured in the co-polarised channel. This is because it was

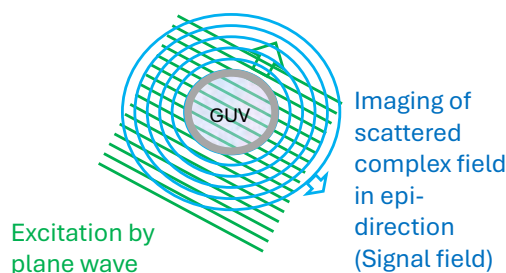


Figure 6.1: Sketch of GV excitation A sketch illustrating the excitation of, and the scattering from a GV when imaging using iGOR

created by the bilayer independent of in-plane birefringence or surface curvature. The image observed in the cross-polarised channel required a change of the polarisation state of the light, which, in the context of GUVs could be attributed to the in plane birefringence of the bilayer. This arises from an anisotropic molecular organisation of the bilayer such as tilted lipids in the bilayer or the geometry due to the curvature leading to a reflection plane different from the polarisation plane of the excitation.[229]

Suspended model membranes are a biologically relevant class of models whose dynamics are not well reported in literature, the suspended nature of these membranes mean they can freely fluctuate restricted only by the edge walls and remainder of the model. This makes them biologically relevant as it would be the same fluctuations experienced by the upper surface of a cell.[244] In terms of the label free techniques they generally require either a high level of averaging, such as qDIC, reducing the temporal resolution, or a supported lipid bilayer which dampens the observed fluctuations, such iSCAT.[129, 130, 131, 185] For our studies we primarily used the lipid mixture POPC:POPE (1:1) relevant in biology as PC and PE lipids are major components of eukaryotic membranes, as this is a binary composition has the capability of phase separation or domain formation on a smaller scale.[245] To study a sharp gel liquid phase transition we used DC₁₅PC as it has a phase transition temperature above that of room temperature. We could control the sample across the phase transition using our slide heater as described in Section 2.4 without the need for dry ice. A minimum vesicle diameter of 30 μm was required to isolate the signal from the top surface from the bottom surface for the coherence length of the excitation used.

Power spectral analysis was also undertaken on this data to study the spatiotemporal frequency content of the signal. The time domain signal is decomposed into its constituent frequencies.[246, 247] A dispersion relation curve (ω, k) was plotted. The power spectral density versus omega and k shows the spectral power of angular frequency (ω) and wave number (k) representing the oscillation rate of the wave against the spatial frequency of the wave. This graph and its subsequent analysis provided information about the waves propagating across the membrane including the phase velocity (v_p) which is the ω/k , also attainable is the group velocity (v_g) which is the gradient $d\omega/dk$ which describes the propagation speed of a wave-packet.[248] The dispersions observed within these plots could be categorised as either linear dispersion, representing a non-dispersive wave for which phase and group velocities are constant.[249, 250, 251] Those waves for which the phase and group velocities vary with frequencies are observed as a curved line representing a dispersive medium. These results are discussed in Section 6.6.

In this chapter I will initially give a brief overview of the processes involved in data acquisition describing the process by which iGOR works. I will also outline data analysis processes, mainly data filtering processes generating phase and amplitude time traces of the region imaged taken forward for further analysis. In this section I will also describe the assumptions and equations which allowed us to extract the thickness and height of the membrane from the amplitude and phase, respectively. In Section 6.2 I set out the expected geometries of a GV imaged using iGOR and how the vesicles we measured were compared. The refocusing of the vesicle is discussed followed by further analysis undertaken on vesicles including the power spectral analysis which aimed to identify dominant frequencies or waveforms within the membrane surface. Within this chapter I discuss data acquired using the

iGOR software as time series at a frequency of 327 Hz. The software handled the data as batches of 1000 frames therefore, in this chapter I will refer to the data in terms of time series, batches and frames according to this classification.

6.1 Data acquisition

The iGOR data processing workflow is detailed in Section 2.9.2. The intensity measured on the camera is shown in Equation 6.1 where the terms on the left side of the equation are the combination of the signal field and the off-axis reference field, \mathbf{E}_S and \mathbf{E}_R , respectively. The interference term in the middle of the right hand side represents the term extracted from the Fourier domain and used in further analysis of the amplitude and phase.

$$\left| \mathbf{E}_R e^{i\Phi_R} + \mathbf{E}_S e^{i\Phi_S} \right|^2 = \mathbf{I}_R + \mathbf{I}_S + |\mathbf{E}_R| |\mathbf{E}_S| e^{-i\Phi_R} e^{i\Phi_S} + |\mathbf{E}_R| |\mathbf{E}_S| e^{i\Phi_R} e^{-i\Phi_S} \quad (6.1)$$

Fig. 6.2 shows a summary of the processes involved in producing amplitude and phase images from the raw images recorded by the camera. The laser used for this acquisition was time gated to a 100 femtosecond pulse duration which limited the coherence length. For interference to occur the separation had to be below the coherence length as calculated from Equation 6.2 where L is the coherence length, c the speed of light, Δf is the spectral bandwidth and n the refractive index.

$$L = \frac{c}{n\Delta f} \quad (6.2)$$

This gating acted to suppress the scattering from other surfaces away from the region of interest. Shown in Fig. 6.2a is the raw display of the camera with the co and cross- linear polarisation region that was cropped out highlighted. A Fourier transform of the each region was then taken to produce the image in k space as shown in Fig. 6.2b, where the cut out shows the masked and cropped region. This region represents the first order interference term highlighted in the equation above. The separation from the zeroth order term is clearly visible. Once the region had been cropped and masked out an inverse Fourier transform was carried out to return the amplitude and phase as shown in Fig. 6.2c.

When interpreting the amplitude and phase we could translate them into height and thickness as the difference in phase was caused by the difference in optical path length causing a phase shift. As can be seen in Fig. 6.3a, the relationship between phase and height was as described in Equation 6.3 where Δ_z is the change in height and n_M is the refractive index of the medium.

$$\Delta_z = \frac{\lambda \Delta \varphi}{4\pi n_M} \quad (6.3)$$

The amplitude modulation was caused by a much smaller phase shift from the light reflecting off either side of bilayer. To quantify this we calculated the linear approximation of a thin layer as the thickness of a bilayer was much smaller than the wavelength of the excitation light. This can also be seen in Fig. 6.3a. To calculate the magnitude of this dependency of reflectance (r) Equation 6.4 was used, from which the graph shown in Fig. 6.3b was produced. The linear dependency was evaluated as 1.5e^{-3} per nm.

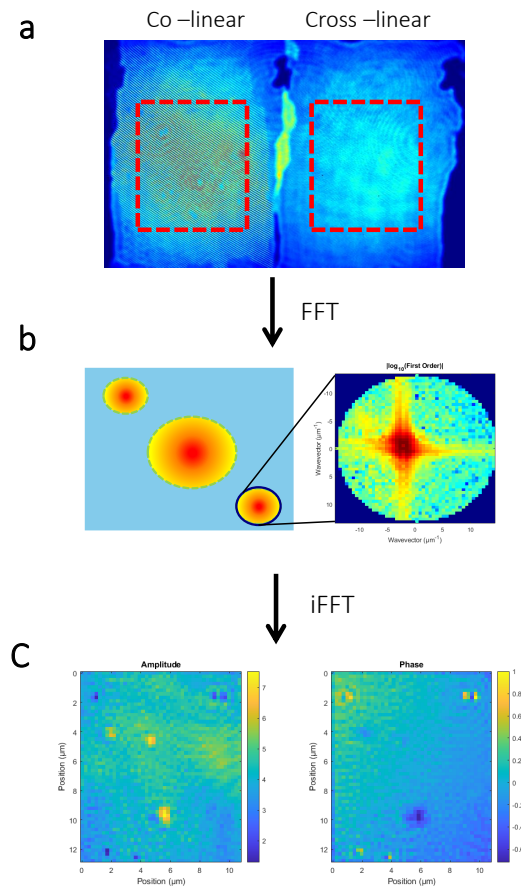


Figure 6.2: Simplified iGOR workflow A summary of the steps involved in extracting the amplitude and phase from the image recorded on the camera, this image is shown in **a)** with the highlighted regions being those Fourier transformed to produce image shown in **b)**. This shows the full image in k space on the left showing the zeroth order alongside the first order terms as well as the region that was cropped out and masked to extract the first order term, which, was in turn inverse Fourier transformed to produce the images shown in **c)**.

$$\Delta_d = \left| \frac{n_M - n_B}{n_M + n_B} \cdot k \right| \quad \text{where } k = \frac{2\pi n_B}{\lambda}, \quad \text{if } d \ll \lambda \quad (6.4)$$

6.2 Expected geometries

When observing a GUV using iGOR we used expected results to determine the focal plane and inform any further data correction required for the analysis. The focal plane was the height for which the amplitude had the least variance as in this region there should have been no local interference effects. The local interference effects of the bilayer occurred when the reflections from the membrane interfered with each other as they were propagating in different directions due to the membrane non flatness in close proximity to the bilayer. Whilst we aimed to image at the focal plane, identifying this in session was challenging and therefore data was taken at a higher axial position to allow the refocusing of data down to the focal plane. The focal plane could also be identified by considering the reflections of a spherical GUV. There was a convergence point half its radius below the surface. Once this point had been identified, its axial position above the glass water interface, onto which the GUV is attached, was increased by 1/3 to give the axial position of the membrane.

The expected membrane curvature of a spherical GUV within our field of view was calculated by the use of the Equation 6.5 where the radius (r), as measured laterally in DIC, was used to determine the difference in axial position (z_h) from the centre to the edge of our region of interest (E_C).

$$z_h = r - \sqrt{r^2 - E_C^2} \quad (6.5)$$

This expected curvature provided a measure to compare the shape observed co-polarised phase to, as seen in Fig. 6.4 the overall expected shape of the vesicle was observed in the co-polarised phase. The expected z_h for this vesicle of about 0.75 μm , was also seen. To measure the bending of a membrane over time we measured the height using phase and fit a radius of curvature to it using a 2D 2nd order polynomial fit produced in Section 6.4.3. From this fit the radius was calculated to allow a frame by frame analysis and was compared to the radius measured in qDIC prior to iGOR image.

We expected that when the radius of the local curvature fluctuated, the thickness of the membrane would have fluctuated in the second order of the extension which is very little. We did, however see longitudinal density waves not related to the curvature, possibly coupled to the curvature due to the spherical geometry. When the vesicle stretched and increased the surface area we expected the thickness to decrease as the same number of lipid molecules had to occupy a greater surface area.

6.3 Resolution

To assess the noise present in our data we analysed a time series of a glass water interface as shown in Fig. 6.5. To assess the noise in both thickness and height units we converted using the same linear dependency calculated for bilayers and Equation 6.3. This produced a measure of effective bilayer thickness which, when taken of a glass water interface for which there was no true movement we found an rms of 0.02 nm with a noise level of 0.1 nm. For the height we found an rms of 0.1 nm.

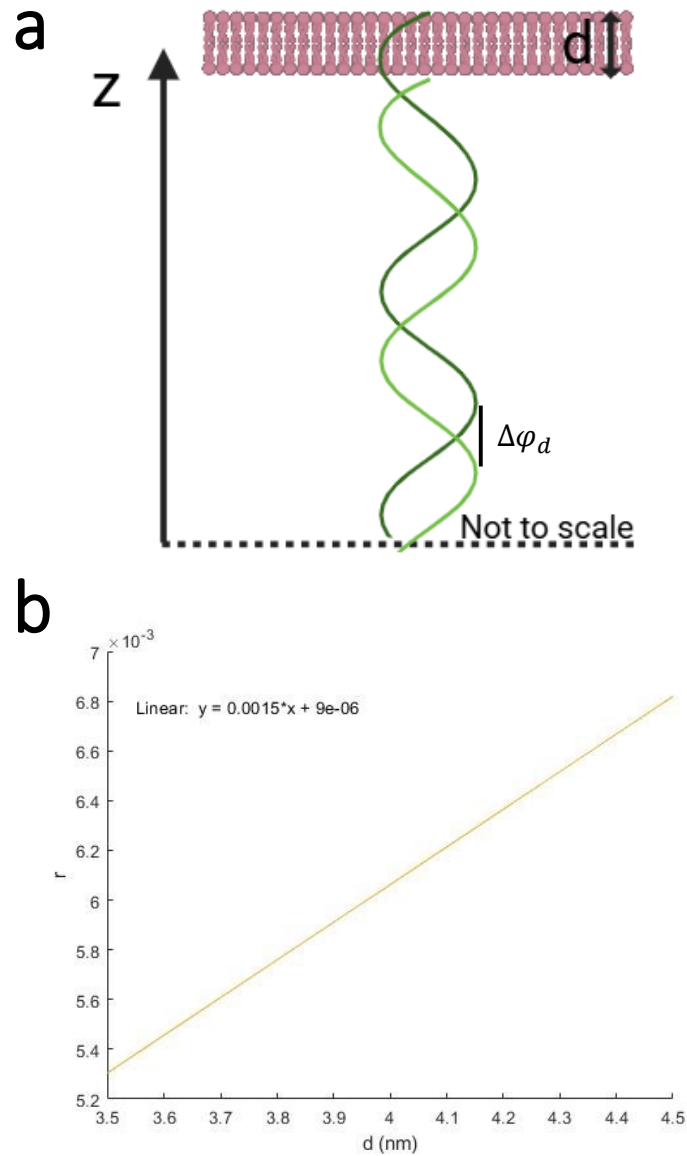


Figure 6.3: Amplitude and phase relating to membrane height and thickness a) shows how a reflected wave was modulated after interaction with a membrane and thus how we can relate phase with height and amplitude with thickness. It can be seen that there was a small change caused by each side of the bilayer as it was much smaller than the wavelength of light. This could be measured as a change in amplitude. The additional distance the light travelled from the matched reference beam at the glass to the bilayer was in excess of the wavelength and therefore was measured as a change in phase. b) shows the field reflectivity as a function of membrane thickness for $n_M = 1.3334$, $n_B = 1.4776$.

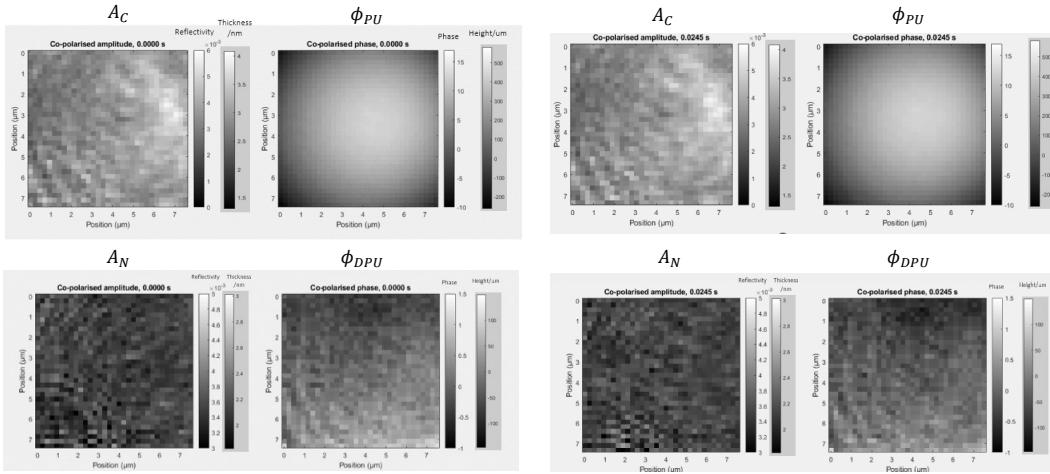


Figure 6.4: Fitting iGOR data Non-consecutive frames of the corrected (Φ_{PU} , A_C) and normalised (Φ_{DPU} , A_N) phase and amplitude. Data is only shown for the co-polarised channel.

From these results, paired with the noise observed in the results discussed later in this chapter taken on lipid bilayers, allowed us to confidently measure with a sub nanometer thickness and height resolution.

Our spatial resolution of $0.168 \mu\text{m}$ was limited by the objective and diffraction limit, meaning our field of view was covered by about 40 pixels which was cropped from the full camera image.

6.4 Data filtering processes

6.4.1 Power correction

The above mentioned measurements on a glass interface also demonstrated the improvement in data quality when looking at amplitude traces where oscillations of the power were corrected as described in Section 2.9.2.3. The fluctuations of the laser were accounted for, seen in Fig. 6.6, where the signal was much more stable and the fluctuations above noise were eradicated. Any observed behaviour of membranes above expected noise was therefore due to membrane fluctuations as opposed to artefactual laser fluctuations which could have arisen from the OPO cavity length stabilisation.

6.4.2 Offset

In an effort to reduce background artefacts, additionally to the reference images, we took an offset frame at the same axial position as the data acquisition, laterally shifted so as not to contain the GUV. From this we evaluated and removed height-dependent artefacts. A new offset frame was taken for every data set from an area local to the region of interest (approximately $20 \mu\text{m}$) at the same focal plane and subtracted prior to the data being saved. The offset frames were also saved to allow reversal of this process. We also evaluated the artefacts and how they changed with axial position. An example of this can be seen in Fig. 6.7 where a decreasing number of artefacts were observed as axial height was increased, however, there were regions

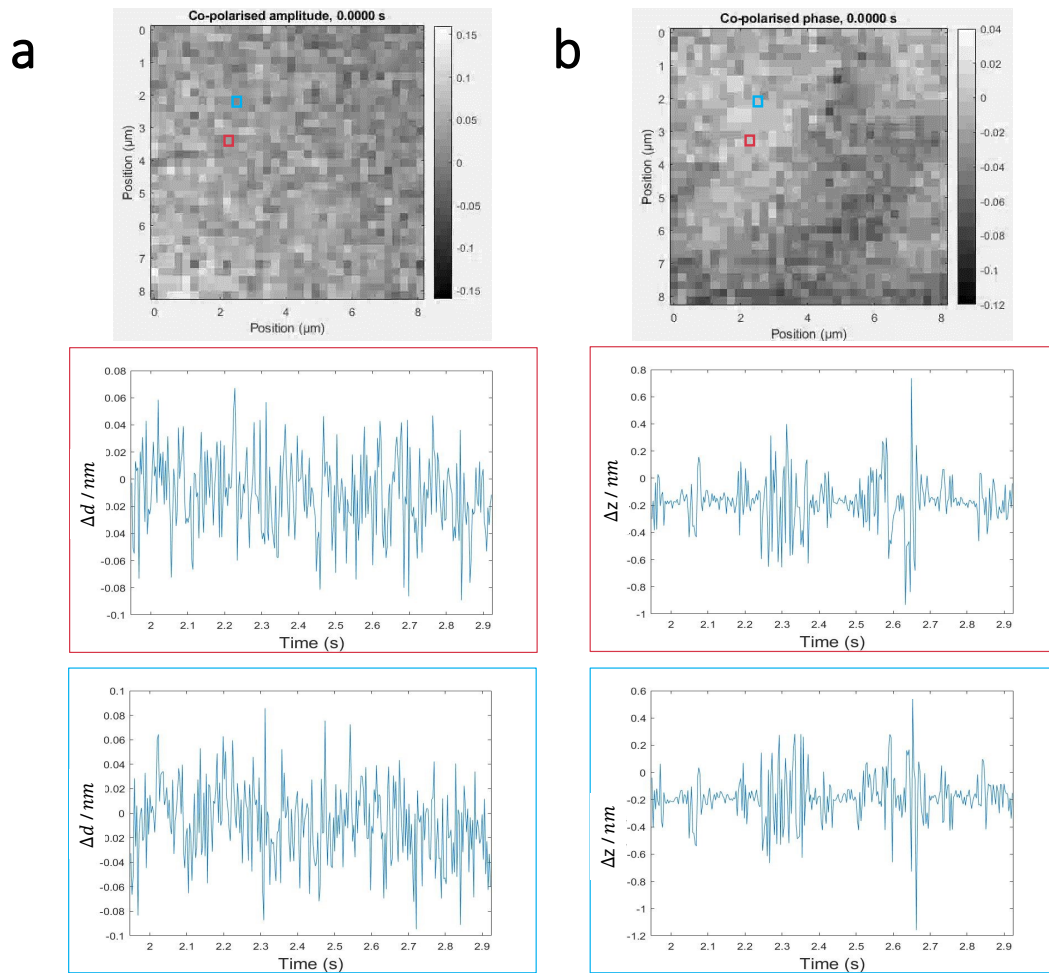


Figure 6.5: Reflectivity and phase measurements of a glass water interface Reflectivity and phase were converted to thickness and height using the same factors as for bilayers alongside a median correction step. **a)** contains a frame of the reflectivity corrected to thickness of a glass water interface alongside time traces of the highlighted pixels. These time traces demonstrated a noise level of 0.02 nm. **b)** shows the height fluctuations of a glass water interface in the same way indicating a noise level of 0.1 nm.

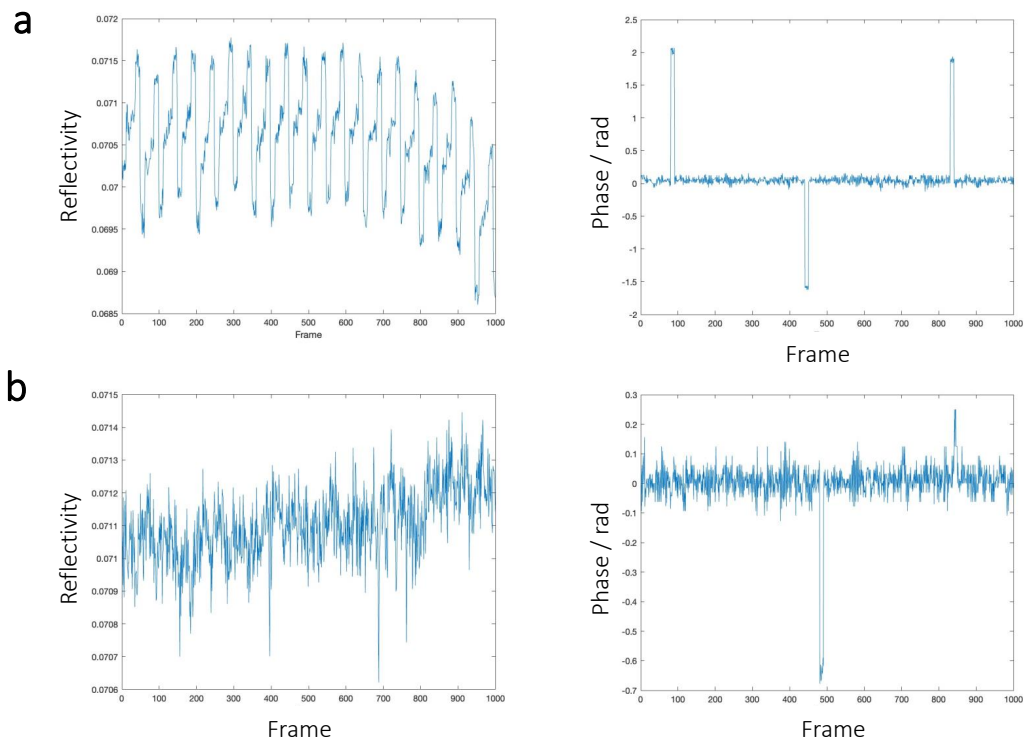


Figure 6.6: Effect of power correction on iGOR traces a) reflectivity trace of a randomly selected pixel measured without using the power correction where an oscillating noise can clearly be seen in the amplitude. This was removed as seen in b) for which the data was obtained using the power correction. No other corrections were carried out on these traces

where the artefacts persisted seemingly independent of height. This highlighted the necessity of these offset images in our data correction.

6.4.3 Phase unwrapping

Phase is an inherently cyclic quantity meaning when measured directly the phase is a 'wrapped' quantity meaning all values are between $-\pi$ and π . Once the phase increases beyond π the value becomes $-\pi$ generating a phase jump.[161] To provide a continuous phase representing the height of a continuous surface an algorithm was applied that is detailed in an upcoming publication from our group, but involves the moving the image through Fourier transforms with a radial fitting to remove the phase discontinuities. [187]

As can be seen in Fig.6.8 this process removed the majority of the phase discontinuities. The places in which this failed were either on a small scale over a few pixels or large lines of phase breaks. Corrections of these errors were undertaken using a sequence of methods as discussed below.

As the shape of the phase was close to spherical with a maximum in the centre of the field of view, it could be fitted with a two dimensional 2nd order polynomial fit. Using this fit we identified pixels with an erroneous phase as any pixels with a difference to the fit greater than π . To correct, we simply added or subtracted 2π to bring the phase back within a wrapped range from the fit. This was carried out as an iterative process with the corrected data being re-fit and corrected until no more corrections were performed. Whilst this was successful for the small phase discontinuities as seen in Fig.6.8b in the cases of large 'phase breaks', Fig.6.8, it was insufficient to correct likely due to the lack of continuous dome for the fitting. To correct this we initially fitted the region in the centre which was less affected by the edge of the field. This region was taken through the previously discussed fitting from which the final fit for each frame was saved and extended to the whole frame. Once calculated, the remainder of the frame was corrected in reference to this central region which facilitated the removal of large scale phase discontinuities. As shown in Fig. 6.8a, the result of this correction was closer to a contiguous dataset it was easier for the phase unwrapping algorithm to handle. Another iteration of the phase unwrapping algorithm proved beneficial for attaining the correct phase. The result of a complete phase correction sequence for a region of large phase break is shown in Fig.6.8c. This data was saved and referred to as ϕ_{PU} hereafter.

The final iteration of the fit was used to normalise the phase. This removed the overall curvature of the membrane and was therefore expected to be within a $-\pi$ and π range. A simple addition or subtraction of 2π for points outside this range corrected any remaining phase discontinuities. This generated time traces with minimal error arising from phase unwrapping issues, hereafter referred to as ϕ_{DPU} .

As shown later in this chapter when the top surface was highly fluctuating the phase unwrapping was not removing phase jumps effectively from both the algorithm or by the fitting. The fitting was no longer as effective as the top surface was much less symmetric and didn't have a suitable top curvature in most frames. Whilst these phase breaks were easy to observe they obscured the analysis of the underlying fluctuations. To reduce the effect of this it was calculated that for the phase breaks at π or $-\pi$ the corresponding height was 103.15 nm, therefore for the purposes of this analysis these were omitted from the data.

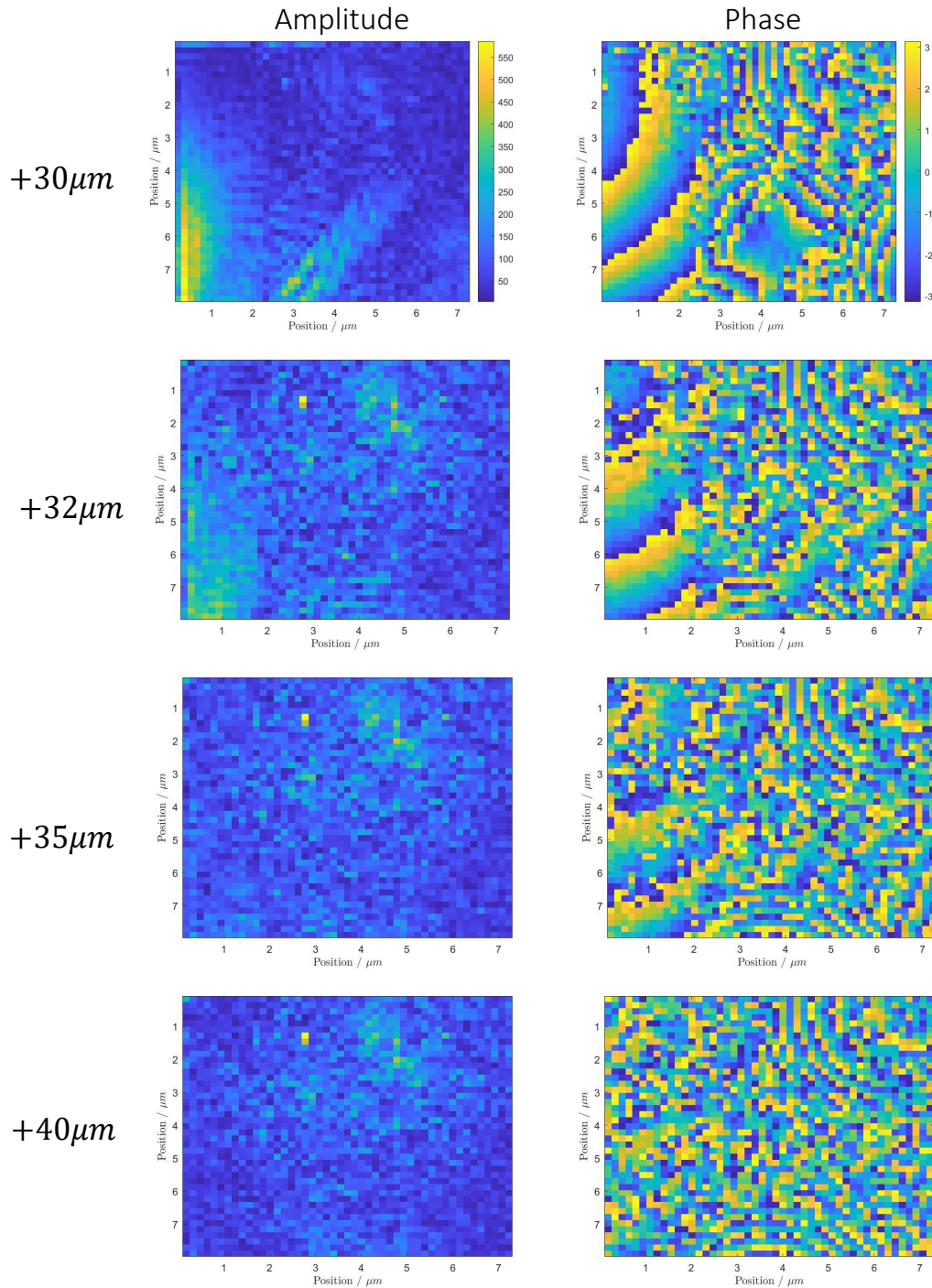


Figure 6.7: Offset frame dependant on axial position Offset images used in image correction for both amplitude and phase at an increasing axial position. The phase is as yet unwrapped in this example as taken directly from the complex field. These images show artefacts that persisted through the axial range as well as those more local to the focal plane that were not removed by standard referencing.

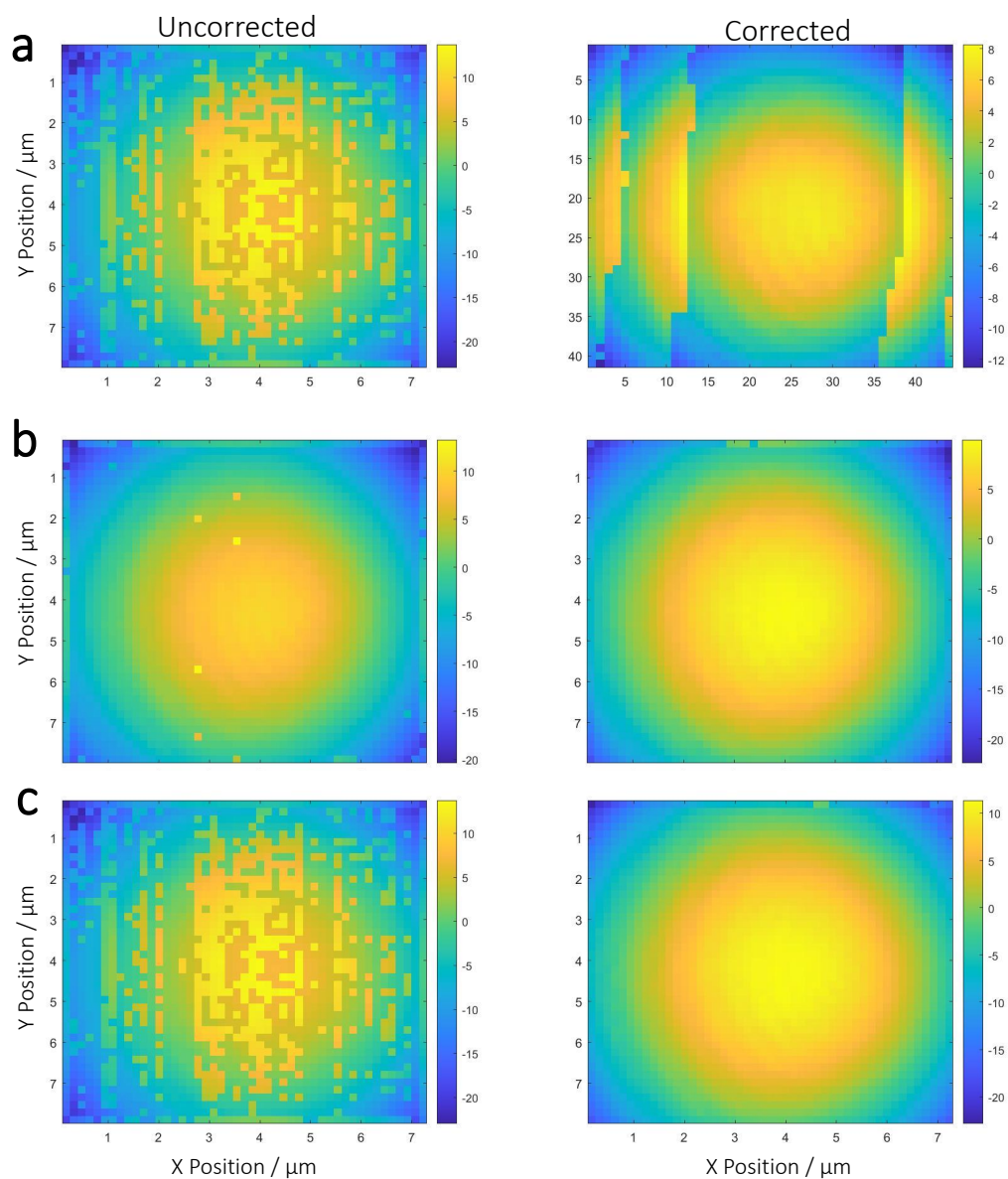


Figure 6.8: Efficacy of phase unwrapping The left column shows the result of the first phase unwrapping algorithm, termed uncorrected. **a)** case of a large phase break when corrected just using the polynomial fitting with **c)** showing the result after a second round of phase unwrapping. **b)** example of phase errors on small scale. Example was a 33 μm POPC:POPE (1:1) GUV

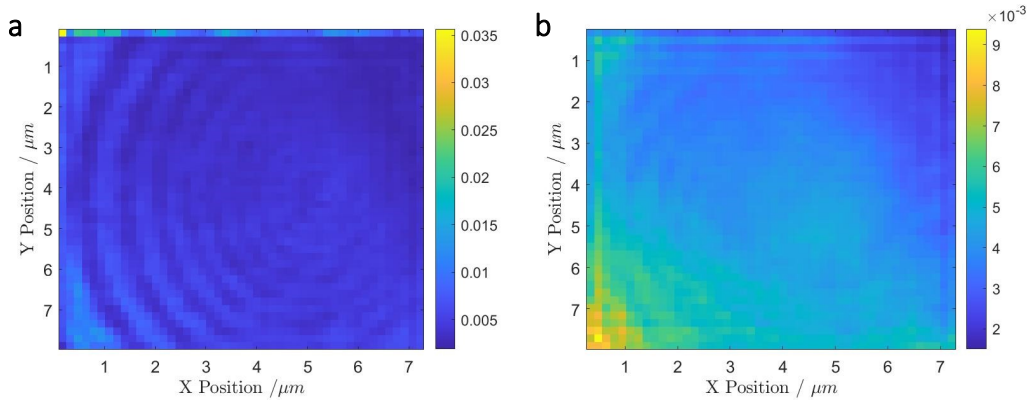


Figure 6.9: Temporal median amplitude average Temporal median averages taken of the amplitude across one batch in **a)** and the whole dataset(129 batches) in **b)**. **a)** shows the ringed artefact of the GUV as well as a stripe of hot pixels at the top in contrast to **b)** where a gradient across the field of view dominated with minimal contribution of the ringed artefact.

6.4.4 Amplitude correction

Analysis of the amplitude data was a more straightforward pipeline as its main aim was to remove spatial artefacts and generate a normalised image of the thickness across the sample. A temporal median for each pixel calculated in the time dimension was removed on a pixel by pixel basis, $\langle A_T \rangle$. To return the corrected amplitude to it's absolute value, an overall median value was calculated in all dimensions of a central cropped region, $\langle A_S \rangle$ and used to multiply the reflectivity. The central region used in the calculation of the value was restricted to a size calculated from the expected bending, using Equation 6.6 with a maximum of 100 nm axial change (B), where r is the radius, and L is the radius of the central region.

$$L = \sqrt{r^2 - (r - B)^2} \quad (6.6)$$

These calculated averages were used to modify the amplitude (A) to generate a corrected version of amplitude (A_C) according to Equation 6.7.

$$A_C = \frac{A}{\langle A_T \rangle} \cdot \langle A_S \rangle \quad (6.7)$$

Fig. 6.9a shows an example of a temporal median frame taken from the first batch of the data. In this frame a static artefact can be seen alongside a background gradient. Fig. 6.9b shows the median average over all of a large time period of up to 129 batches. In this long range average image, only the background gradient remained which was independent of membrane features as the vesicle had drifted around within this time, in the order of $2 \mu\text{m}$ in both x and y. Static membrane features were observed in the averages calculated on a batch by batch basis. Thus, by removing an average from both time frames we removed non-fluctuating spatial artefacts.

For analysis of membrane fluctuations the calculated temporal median was subtracted from each frame to reveal the amplitude changes (A_N) present in the sample centred around 0 as shown in Equation 6.8.

$$A_N = \frac{A}{\langle A_T \rangle} \quad (6.8)$$

This was taken further by initially subtracting the amplitude in the very centre of the frame or the peak of the quadratic fit discussed in Section 6.4.3 which generated a central referenced frame and therefore the changes of thickness in reference to the central value.

6.4.5 Excitation beam expansion

A large excitation beam illuminated not only the region of interest but the entire vesicle diameter which induced scattering from the sides of the vesicles. In turn, this generated local interference in the centre of the vesicle in a region local to the membrane. The original diameter of the beam can be observed in Fig. 6.10a. To combat this we reduced the area of excitation by closing the backport field aperture from 1.6 mm down to 0.7 mm to reduce the illumination size on the sample to approximately 12 μm in diameter, which was just about the same size as our frame height. Whilst this improved local reflections causing interference it can be seen that the beam was diffracting at the aperture generating light in a wide range of propagation directions causing aberrations as seen in Fig. 6.10b. By reducing the size of the beam with a beam expander before the aperture we limited the diameter of incident light without encountering diffraction issues as well as increasing the intensity by approximately 4 times. The result of this was a smaller, more intense and homogenous signal beam as seen in Fig. 6.10c. This helped to improve imaging as the beam incident on the sample was more homogenous.

6.5 Refocussing

6.5.1 Interference issues

As previously mentioned imaging below the nominal top of the GUV caused interference as the reflections from the bilayer interfered at the measured plane, this was worse for reflections coming from non parallel bilayers. Whilst the focal plane could be corrected post acquisition via refocussing the ability to do this without artefacts was decreased with excessive local interference. To minimise this the signal beam was reduced in size whilst keeping it collimated as a gaussian beam as described in Section 6.4.5 to reduce the number of reflections off the side walls of the vesicle.

The identification of the correct focal plane during imaging was important as the local interference effects were minimised. For a stable vesicle this was close to zero as the entire region of interest remained within the focal plane. For highly fluctuating vesicles this membrane was moving in and out of the measured focal plane generating pockets between the portion of the membrane above the focal plane and the focal plane where local interference could occur. This was the most likely source of error for membrane fluctuations.

Initially, the nominal top of the GUV was calculated using the DIC image where the diameter was treated as the nominal height of the vesicle top surface above the glass surface. An image series showing the effect of the signal appearance on axial position, Fig. 6.11a shows the image at the nominal top. After refocusing the image and adjusting the focal plane by $-3 \mu\text{m}$ the signal could be seen as not filling the field of view, indicating a focal position below the nominal top Fig. 6.11b. Fig. 6.11c shows the signal after refocusing by $+3 \mu\text{m}$. Identification of the focal plane was hard as the image contained artefactual signal from refocusing, disrupting the appearance of the

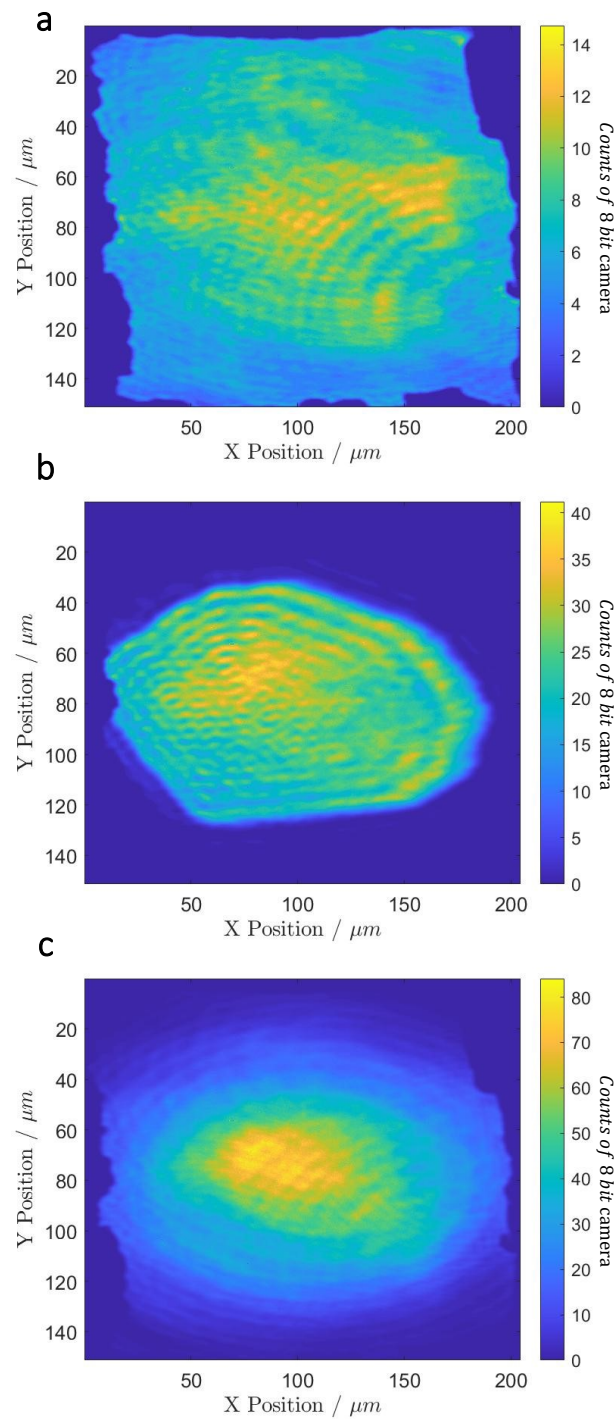


Figure 6.10: Signal beam attenuation Glass water reference images (signal beam only) taken at a glass water interface using an unrestricted beam as shown in **a)** and after the aperture was restricted to 0.7 mm in **b)**. **c)** shows the signal beam after the addition of the beam expander leading to a decreased diameter without causing diffraction.

bilayer. This highlighted the interference occurring locally to the surface disrupting the ability to refocus.

As described in Section 6.2 the nominal top surface focal plane could also be assigned using the convergence point $1/4$ of the GV radius from the top. Deviation from this value may have occurred through the vesicle being distorted in the region where it was in contact with the coverslip. Therefore, by using the nominal point as a reference, a range of z spaced by typically $1\ \mu\text{m}$ was taken which allowed the correct focal plane to be identified in post analysis whilst limiting the post-refocussing required to under $500\ \text{nm}$. In this way we are able to, for a stable vesicle, mitigate refocussing errors and reduce them for an unstable one. It was considered that the fluctuations we observed of a highly fluctuating vesicle may have been amplified through the defocus.

6.6 Spatio-temporal fluctuation frequency analysis

Analysis of fluctuations was undertaken either using the aforementioned approach including a trace analysis of each pixel with its corresponding distance from the centre. A more sophisticated approach was power spectral analysis. The spatio-temporal data (amplitude, phase, or complex field) was Fourier-transformed into the spatial and temporal frequency domain, using finite time-segments, weighted with a Hanning window. The subsequent segments were shifted by half the segment duration from each other.

The power at each point (k_x, k_y, ω) was averaged over a large number of segments to provide a statistical mean over the fluctuations. Assuming in-plane asymmetry, the power spectra were then expressed in polar coordinates k , θ and averaged over theta, to provide the power spectral density, $P(k, \omega)$.

A plot was then generated of the Fourier transformed ω value against k . Any direct relationship was characterised as a normal wave. The ω/k ie. the gradient was the wave velocity (speed) and gave us an indication of the waves passing across the surface of the membrane. Any uncorrelated data appeared as a background that could be discarded.

6.7 Original data

This section discusses the initial analysis of data acquired with the first iteration of the acquisition protocol with the larger aperture for the signal beam. As the data shown were stable vesicles we do not anticipate a large error introduced by the aforementioned local interference effects. Though these data sets aren't suitable for quantitative analysis due to later discussed hardware changes, there was proof of principle that the fluctuations could be seen at the top of the vesicle.

6.7.1 POPC:POPE (1:1)

The data shown in Fig. 6.12 demonstrates the ability to qualitatively analyse the deformations at the top of a vesicle associated with an increased fluctuation rate upon loss of internal solution.

By adding assessment of the fluctuations of specific pixels as shown, we started to quantify the movement associated with the membrane. The fluctuations were plotted as the difference in value of the pixel at the centre of the field of view. The

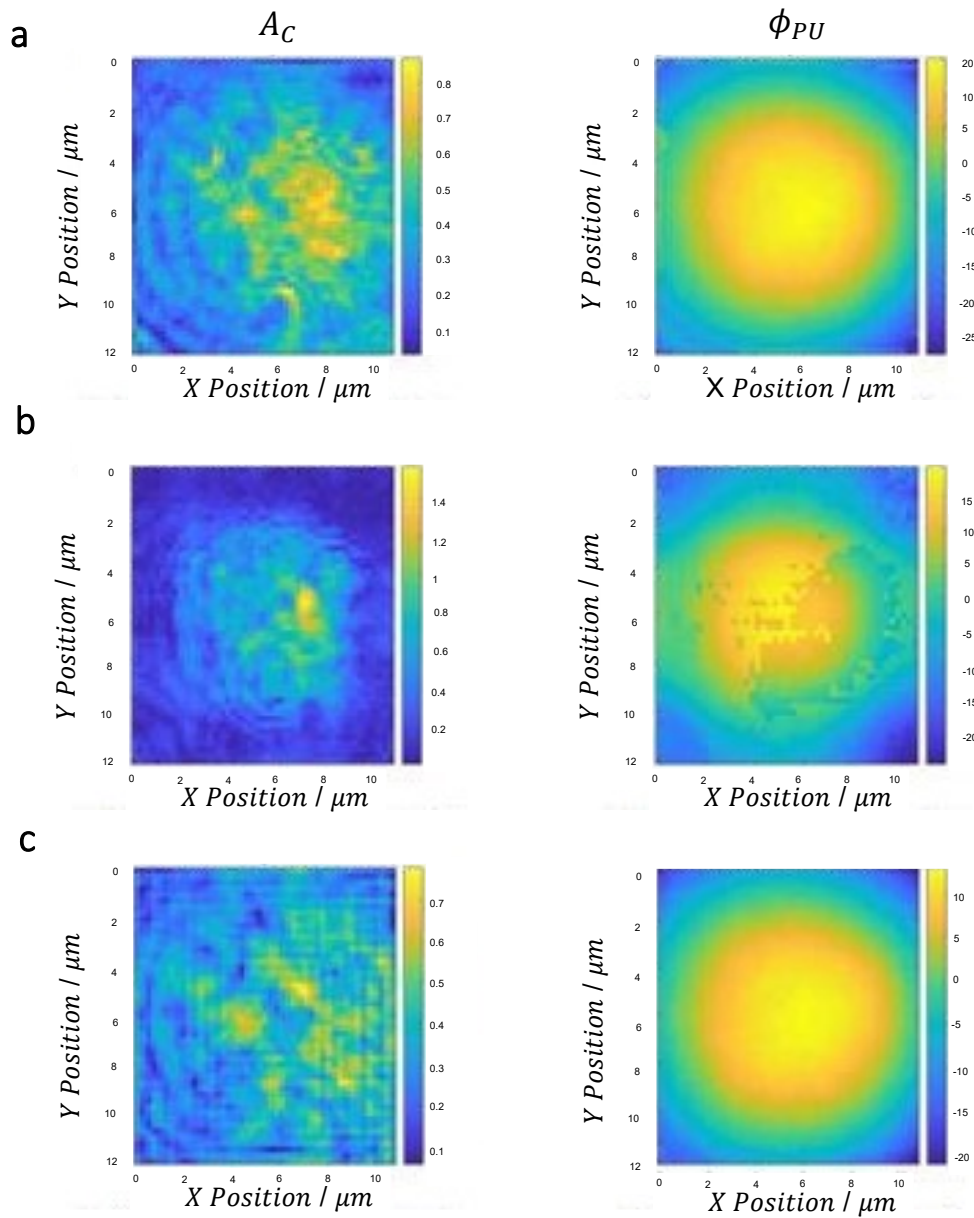


Figure 6.11: iGOR refocusing data An image sequence of iGOR images taken in copolarisation demonstrating the refocusing of the iGOR technique. **a)** Image taken at the nominal top of the vesicle, not refocused. **b)** The focal plane adjusted by $-3\mu\text{m}$, amplitude signal not filling field of view **c)** The focal plane adjusted by $3\mu\text{m}$ showing artefact generation.

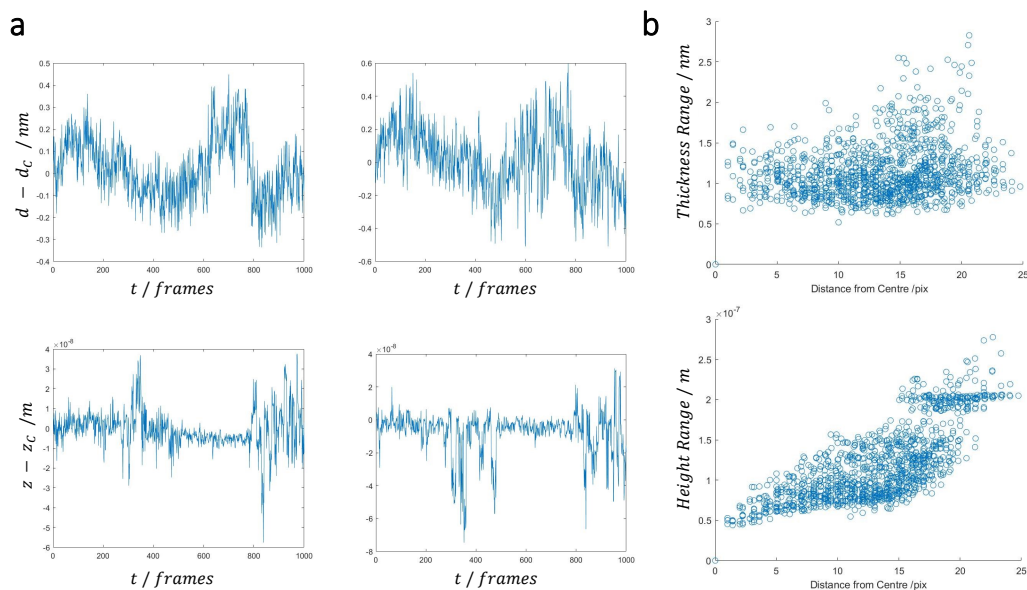


Figure 6.12: Original POPC:POPE iGOR analysis a) Time traces of centrally referenced height and thickness for 2 selected pixels. b) shows the temporal range for all pixels in the field of view for the batch measured. These were also plotted against the distance of the pixel from the central pixel.

thickness fluctuations observed were in the sub nanometer regime highlighting the sensitivity of our technique where the thickness changes could be quantified above the noise. To provide an overall measure of the thickness fluctuations present in the membrane, the range for each pixel was plotted relative to their distance from the central height. These results showed a fluctuation range of 1 to 1.5 nm for most of the pixels measured with no clear correlation with distance from centre. Height fluctuations showed a dependency on distance from the centre with the pixels further from the centre exhibiting a greater change of height.

6.7.2 DC₁₅PC membranes

Initial comparison can be seen in Fig. 6.13 where a and b show the cross-sections of the DC₁₅PC and POPC:POPE(1:1), respectively. The more non-circular undulating membrane observed for the DC₁₅PC vesicle was due to the lipids forming facets as they were in a gel phase at the 20°C they are measured at. In terms of analysis this made any further phase unwrapping challenging as the 2D polynomial fit struggled to fit the membrane shape to allow our further pi jump correction in this case. However, we saw increased thickness along these borders in the amplitude measurements in Fig. 6.13c as compared to that in Fig. 6.13d for POPC:POPE. Another noticeable difference was the much stronger signal in the cross-polarised channel, in amplitude it was a 60× increase in signal. Previous discussion would suggest birefringence as a cause for this difference in signal, however in this case it was likely to be the angled facets of the membrane having a larger angle to the imaging plane and therefore creating more signal in the cross-polarised channel.

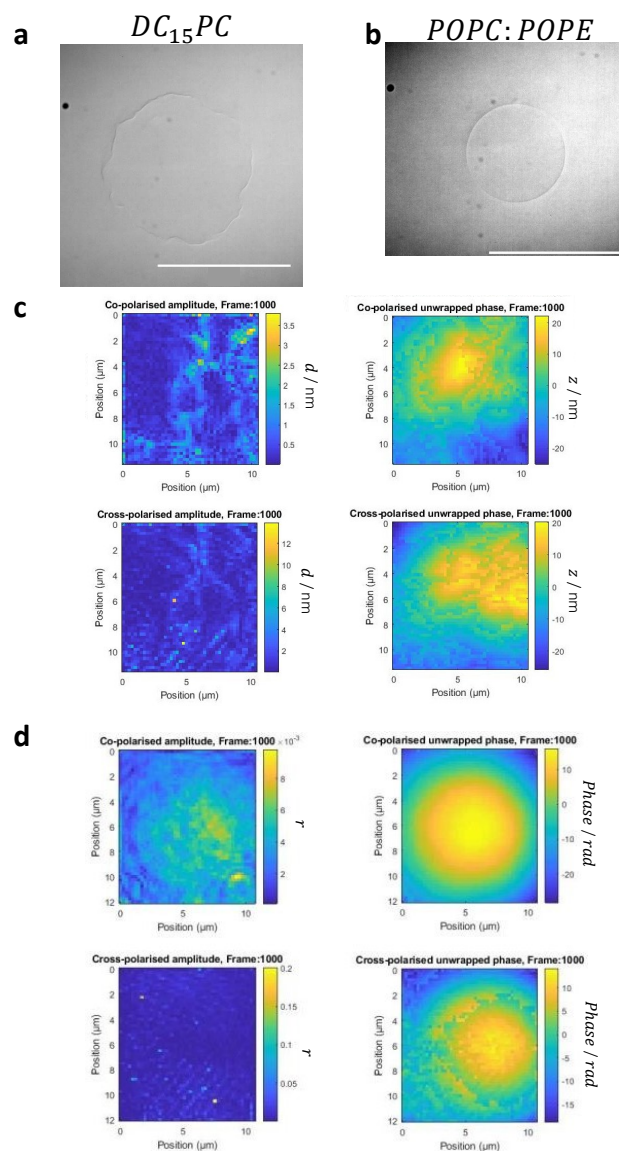


Figure 6.13: iGOR images with their corresponding DIC images a) DIC at the cross-section of the vesicle, scale bar $50\ \mu\text{m}$, corresponding to iGOR frames (Φ_{PU} and A_C , converted to thickness, d and height z) shown in c) The more crumpled membrane and irregular top surface were due to the DC_{15}PC lipid composition of the vesicle as they were imaged in the gel phase. The iGOR image was taken at the nominal top of $57\ \mu\text{m}$ whilst the cross-section shown in DIC was at $34\ \mu\text{m}$ from the surface. b) DIC at the cross-section of the vesicle, scale bar $50\ \mu\text{m}$, corresponding to iGOR frames (Φ_{PU} and A_C) shown in d). This smoother membrane and more regular top was due to the POPC:POPE lipid composition as the vesicle was in liquid disordered phase. This iGOR image was also taken at the nominal top of $40\ \mu\text{m}$ and the cross-section shown in the DIC image was taken at $22\ \mu\text{m}$ from the surface.

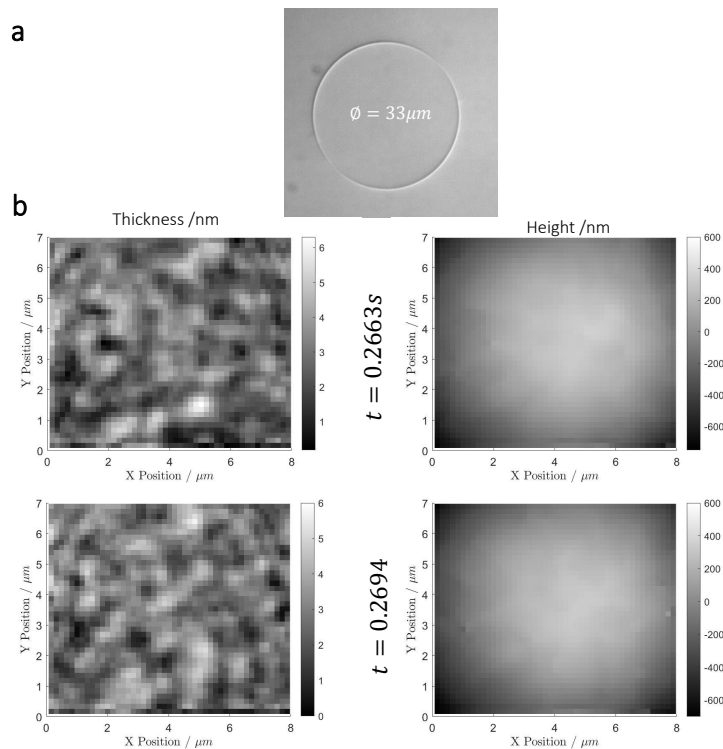


Figure 6.14: Unilamellar POPC:POPE vesicle as imaged in iGOR a) shows the central focal plane of the vesicle measured using DIC where from which the diameter was measured as $33\mu\text{m}$. b) shows consecutive frames measured at the top of the same vesicle showing the expected geometries in both thickness and height calculated as discussed. Images shown are the height and thickness calculated from Φ_{PU} and A_C .

6.8 POPC:POPE membrane properties

6.8.1 Unilamellar membrane fluctuations

This section discusses the inferences we made about the membrane of a unilamellar vesicle analysed to uncover the small-scale fluctuation of this surface. Fig. 6.14a shows the vesicle as imaged using DIC from which we determined a diameter of $33\mu\text{m}$ and a clean membrane. After the data had been cleaned as described above the absolute thickness of the membrane alongside the height could be seen as shown in Fig. 6.14b. From these results we could see the rapidly changing areas of additional membrane thickness with the appearance of random movement across the surface. Visually observable were thickness domains with areas in the order of nm. Determination of the randomness of these fluctuations is discussed further below during power spectral analysis. Fluctuations on this nanometre scale could also be measured in the phase however in the data shown in Fig. 6.14b this was dominated by the overall membrane curvature.

Once this curvature had been fitted and removed we used the fit to determine the radius of the vesicle at each frame, measured alongside any deformation causing asymmetry of the curvature of the vesicle top. In this case the ratio between the coefficients for the curvature in the x and y direction is shown in Fig. 6.15a, from which we expected symmetry and thus a ratio of 1. As this was the case, save for the few regions in which the ratio spiked, we used an average of the two where

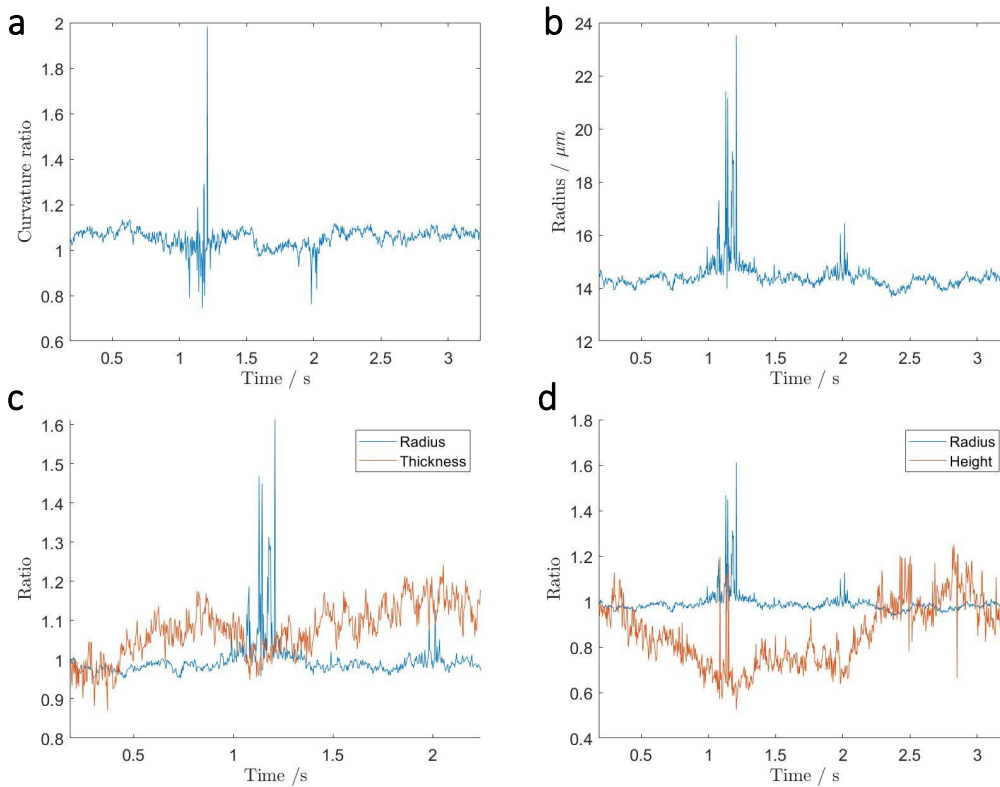


Figure 6.15: Correlation of radius with thickness and height a) Shows the ratio between the curvature coefficients in either axis demonstrating the expected symmetry for the majority of the frames. b) Shows calculated radii for each frame showing how the radius of the vesicle changed over time. b) and c) Show the ratio change calculated for both thickness and height, respectively, plotted against the ratio change to determine if any correlation is present.

$r = (1/a + 1/b)/2$. The frames for which the ratio deviated significantly from 1 we attributed to poor fitting of the phase unwrapping algorithm. The trace of this radius is shown in Fig. 6.15b, as this radius represented the elliptical deformation by thermal fluctuations we anticipated an altering of thickness and height correlating with this change. This is shown in Fig. 6.15c and d where the median thickness of the region of interest was plotted, as a ratio from the first frame and the height ratio as calculated from the peak of the fit, were plotted against the ratio change of the ratio. From these results we identified certain time regions for which counter correlation was observed, for example 0.8 to 1 s and 1.3 to 1.5 s, where membrane thickness and radii appeared to be inversely proportional. As radii increased so would the surface area and thus each of the lipids would have been under greater tension and therefore pulled thin. Height and radius did not appear to be correlated over this time scale. In terms of clear correlation, over this time scale no conclusions could be drawn however there was evidence of this behaviour with the thickness.

After removal of the fit the height fluctuations can be seen together with the thickness fluctuations in Fig. 6.16a. In this data a slight fringing pattern was observed at the edge of the frame, which, due to a separation comparable to the coherence length we attributed to an incomplete suppression of the surface reflection. However, we observed minimal effect in the centre therefore, further analysis was undertaken on data from this region. To analyse this data we started by looking

at time traces of randomly generated pixels to observe the fluctuations occurring in the membrane, as shown in Fig. 6.16b. When looking at the thickness traces we observed fluctuations above the noise to an angstrom sensitivity. Fluctuations were seen on various time scales for both thickness and height, in the height, the fluctuations were in the order of 5 - 10 nm allowing observation of thermal distortion of the surface as changes in height.

Power spectral analysis of the data showed a more sophisticated analysis of the fluctuations present in our membrane. By plotting fluctuation power versus spatial and temporal frequencies, we could observe any dispersal relationships. Fig. 6.17 shows such spectrum for both amplitude (thickness) and phase (height). As observed in Fig. 6.17a we identified a dominant spatial frequency that increased with temporal frequency providing evidence of dispersion relation. Fig. 6.17b shows the spectra for height from which no dispersion relation could be identified.

6.8.2 Bilamellar GV dynamics

To compare the dynamics of a POPC:POPE GV membrane we carried out the same analysis for a bilamellar vesicle of 47 μm diameter shown in Fig. 6.18a. The corrected data of the absolute membrane thickness and height is shown in Fig. 6.18b, the vesicle was identified as bilamellar with a membrane thickness fluctuating about a value of about 8 nm. The mean thickness for the first 10 frames was 7.2 nm. The ratio by which this changed with time is shown in Fig. 6.19a, the thickness trace is shifted up +0.5 to allow easier comparison. Anti correlation with the radius was observed in the zoomed regions of 2.2 to 3.4s and 12 to 14s demonstrating the behaviour of thickness decrease upon radius increase. Interestingly, the region of 0.2 to 1.2s did not demonstrate this relationship with an increase in radius occurring with an increase in thickness. However, as a whole we concluded that an increase of radius was correlated with a decrease in thickness. When assessing the correlation of radius and height as seen in Fig. 6.19b we observed a similar behaviour of counter correlation of the height decreasing with an increased radius. Our data suggested that as opposed to an expansion effect the vesicle was being squeezed to have a more elliptical cross section, however it was not statistically significant. As the trace shown is scaled by 0.3 to allow easier comparison it can be seen that the height was fluctuating far more than the radius. This suggested a vesicle with low internal pressure as the membrane could tolerate changes in height without an altered top surface curvature. The rate of change of the radius was greater than that of a unilamellar vesicle as seen in Fig. 6.20 suggesting that the vesicle was more unstable with a lower internal pressure. One would expect that an additional bilayer would have conferred stability and decreased the radius fluctuations. It could also be that the interpretation of the phase as curvature was problematic for a bilamellar vesicle due to the interference of the two bilayer signals. Generally the phase should still have given the average curvature, but destructive interference could have led to pi phase jumps which would have upset the analysis. The thickness of the unilamellar vesicle fluctuated in the order of 0.3 compared to the bilamellar vesicle fluctuating in the order of 0.4 of its original thickness. This suggested that the thickness fluctuations were independent of the lamellarity.

Time traces of the normalised thickness and phase are shown in Fig. 6.21. From these time traces we show thickness fluctuations in an order of 4 nm and height fluctuations in the order of 50 nm. When looking at the time frames shown and comparing them to those from the unilamellar vesicle it can be seen that the regions

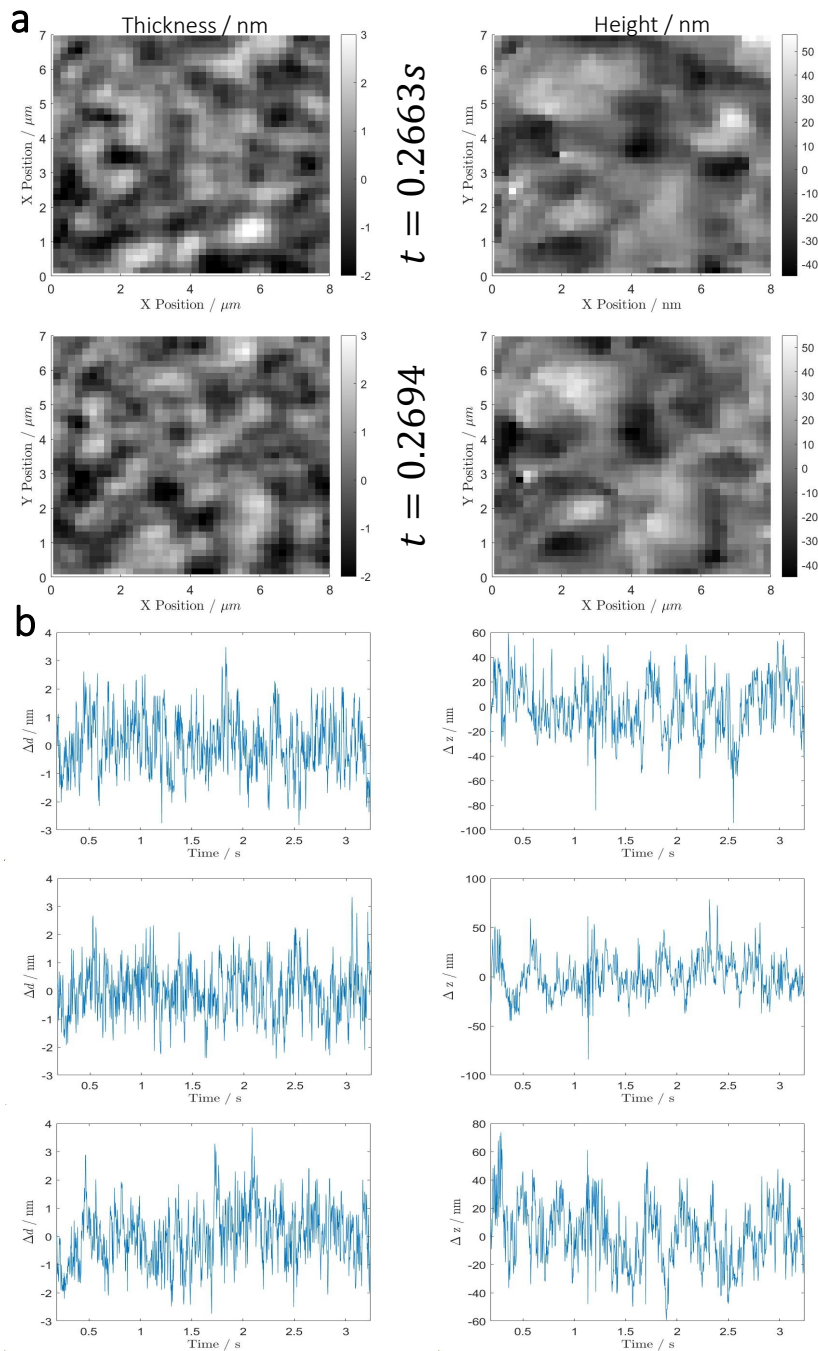


Figure 6.16: Time trace analysis of unilamellar POPC:POPE surface fluctuations a) Shows the same frames with their overall shape removed to uncover fluctuations (A_N , Φ_{DPU}). b) Shows traces of both thickness and height with time for 3 coordinates within the central region randomly generated. See supplementary media (M_5_1)

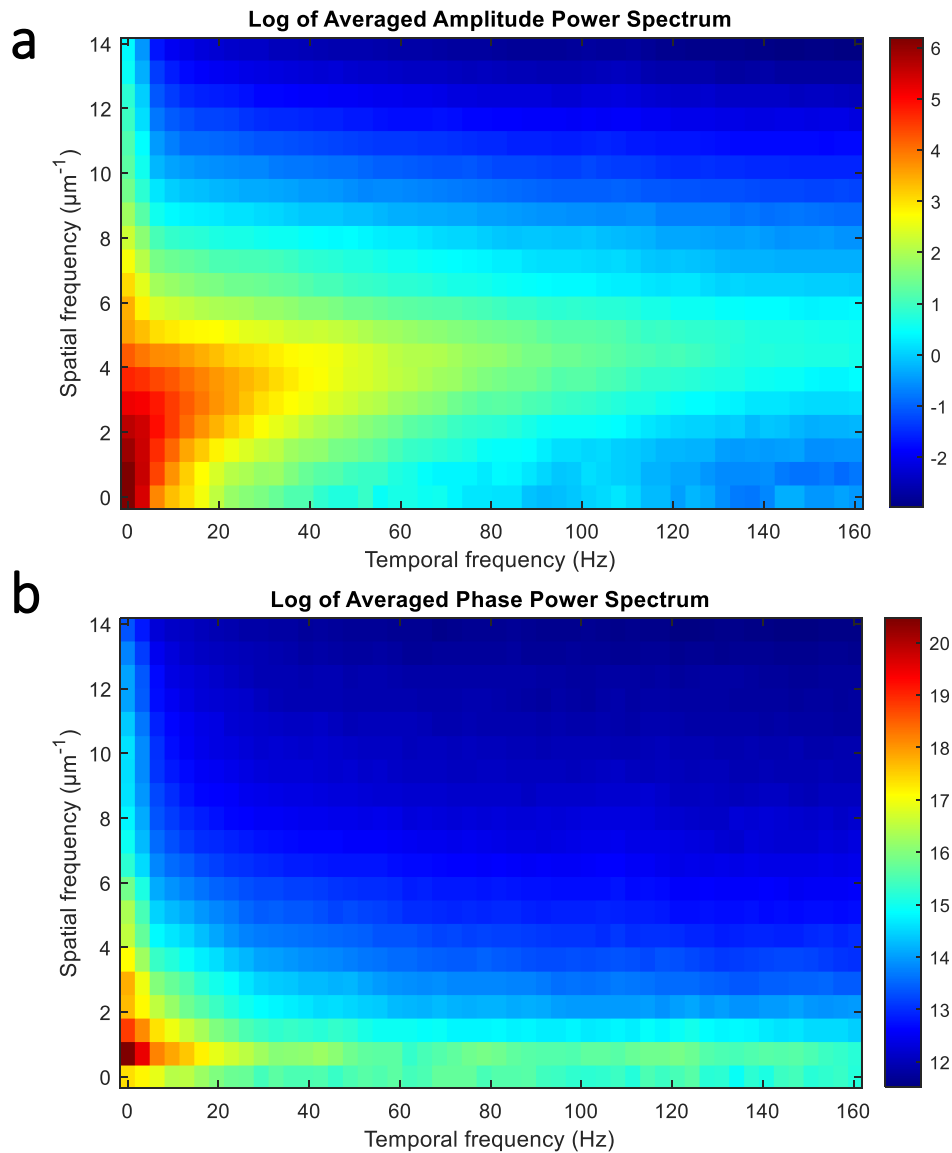


Figure 6.17: Power spectral analysis of unilamellar POPC:POPE surface fluctuations a) shows the power spectrum for the amplitude with that of the phase shown in b). A dispersion relation can be seen in a) characterised by a curve emerging from approximately 6 Hz appearing as a peak at $4 \mu\text{m}^{-1}$. No such relation can be seen in b).

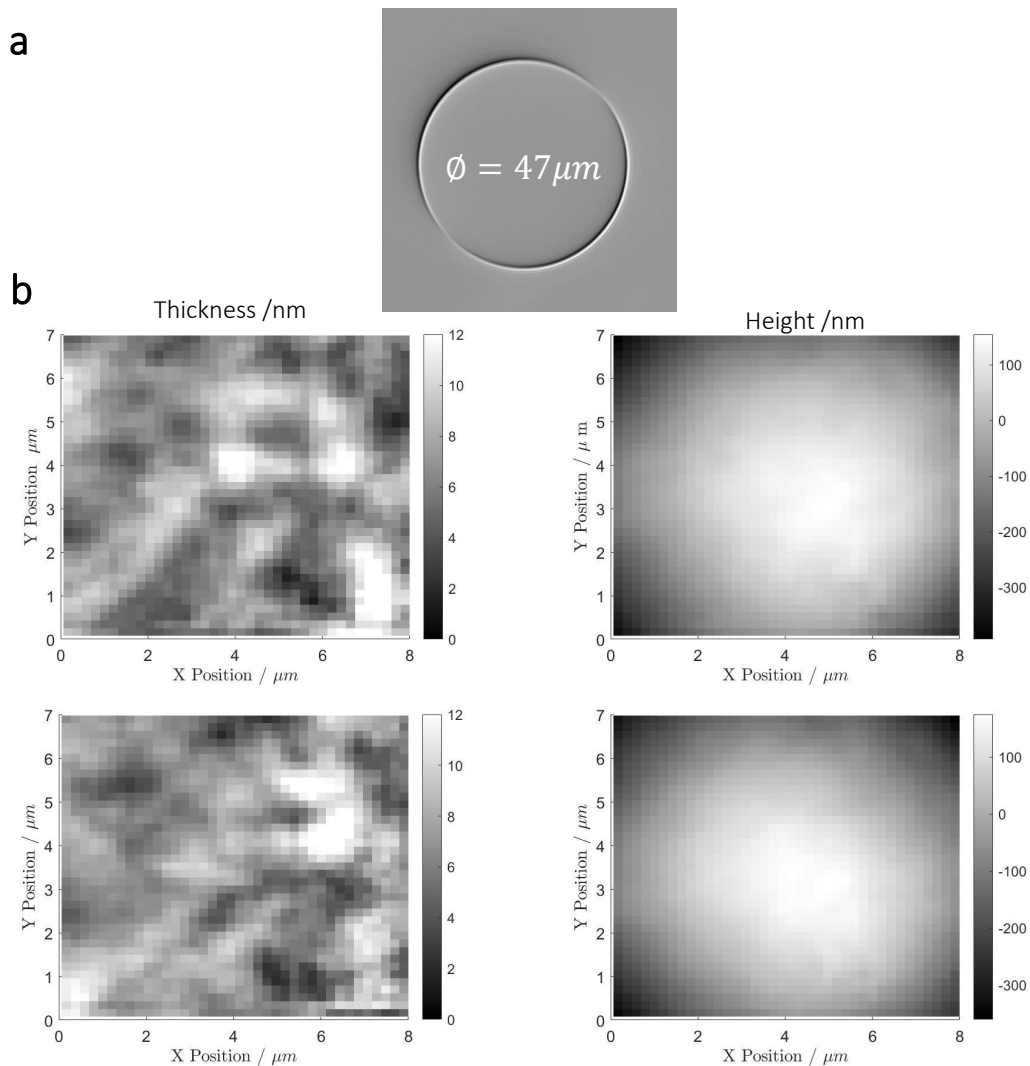


Figure 6.18: Bilamellar POPC:POPE vesicle as imaged in iGOR **a)** Shows the central focal plane of the vesicle measured using qDIC from which the diameter was measured as $47\mu\text{m}$. **b)** Shows consecutive frames measured at the top of the same vesicle where the thickness was double as expected for a single bilayer defining the vesicle as bilamellar. Images were taken from A_C and Φ_{PU} data.

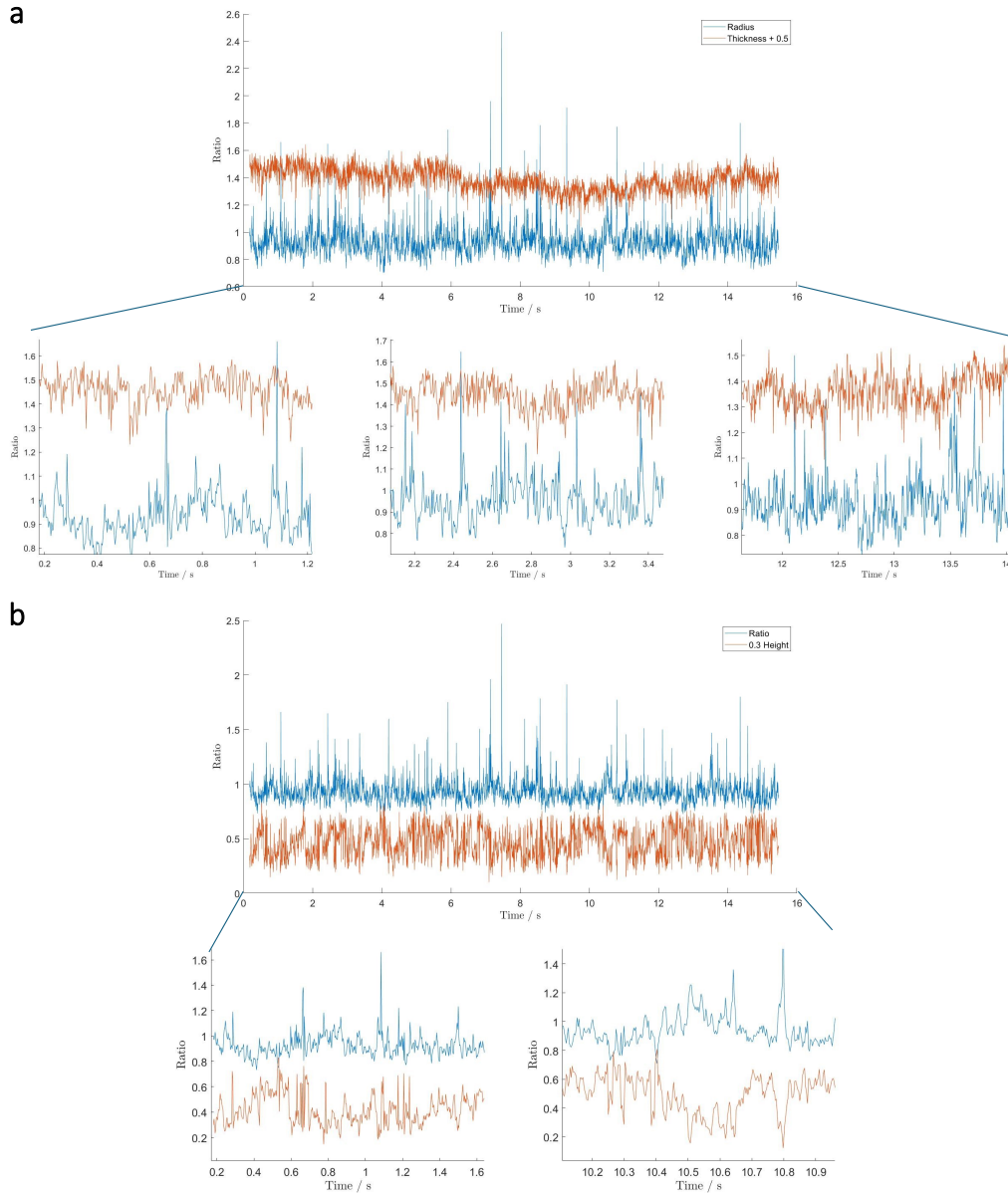


Figure 6.19: Correlation of radius with thickness and height a) Shows traces for both thickness and radius compared to their value in the first frame. The zoomed sections show regions representing the correlations described. b) Shows the traces for height and radius with the height scaled by 0.3 to allow comparison.

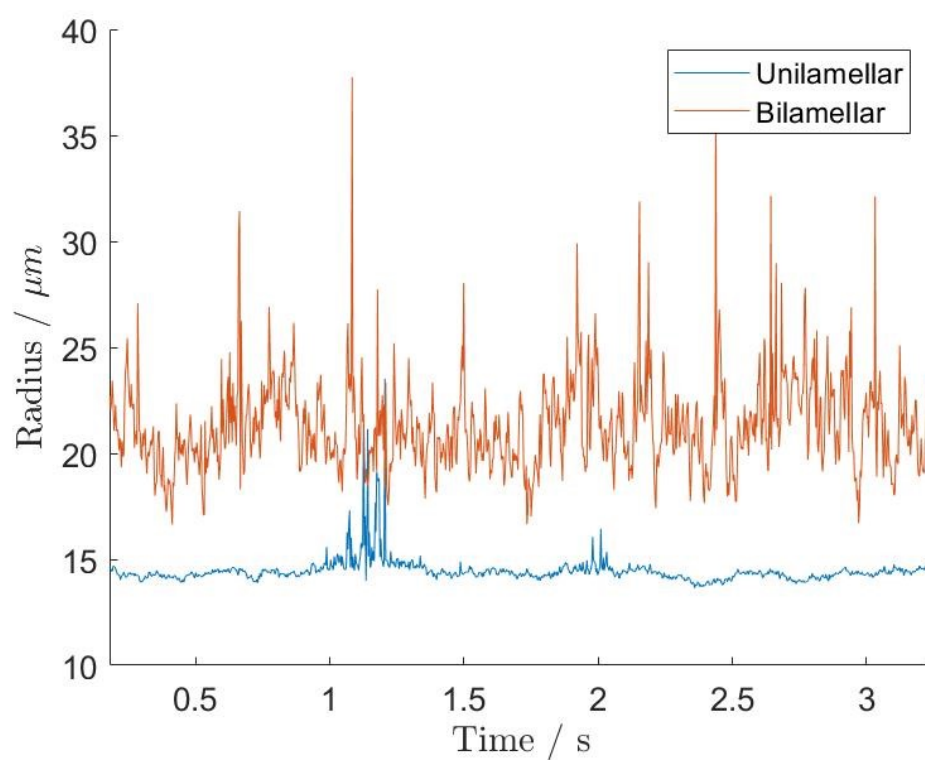


Figure 6.20: Radius fluctuation comparison between unilamellar and bilamellar vesicles Time traces of the radius showing greater fluctuation of the bilamellar vesicle. An increased fluctuation range was experienced by the bilamellar vesicle starting from a larger radius.

of differing thicknesses, termed domains, were different sizes. For the unilamellar surface the domains were in the order of 0.5 to 1 μm compared to the 1 to 1.5 μm observed on the bilamellar surface. The same effect was seen when observing the height. These findings suggest that the unilamellar vesicle fluctuated in regions within a small diameter in contrast to the larger domains for which the membrane thickness fluctuated. However, there was also interference between the two layers that had a variable distance to each other which could have been causing the difference in fluctuations observed.

Upon the completion of Fourier frequency analysis no dispersion relationship could be identified as shown in Fig. 6.22. The most likely reason for this was the lower internal pressure identified and discussed in prior analysis. Due to increased overall membrane fluctuation the frequencies of waves passing across the membrane surface were masked by larger deformations that didn't progress with well defined parameters and therefore were not identified by this analysis.

6.9 POPC:POPE loss of internal pressure

This section will discuss the analysis of a POPC:POPE (1:1) vesicle of 33 μm diameter. This vesicle was measured over the course of 90 min over which the internal pressure decreased and the fluctuations increased. No other environmental changes we encountered by the vesicle during this time.

6.9.1 Initial characterisation

When looking at the frames taken at the start, Fig. 6.23, we observed a fringing pattern that appeared artefactual as it was fluctuating less than the membrane enough to appear in the time averaged median, however, it was not sufficient to remove it. After tracking with the vesicle height observed in phase it moved with the slight drifting observed, making it a GUV dependent effect. Efforts were made to remove this via phase correction of the complex field to stabilise this pattern and allow its removal before correcting the phase back. Whilst this was successful in removing the pattern it was decided that it was also removing signal from the GUV and was therefore left as whatever was removed using the median average correction.

It can be seen that the fringing pattern was dominant on the left side of the frame with the right side showing the expected geometries and a thickness centred around 3.5 nm. For this reason further analysis was limited to this region.

When looking at the power spectral analysis of the initial data for which fringing artefacts had been identified, it appeared to have a set frequency we could look for in the power spectra. Fig. 6.24a shows the spectra for the full frame in comparison to the cropped frame in Fig. 6.24b. In the phase the spectra was very similar with the cropping not showing an identifiable change, save from the loss of 0 frequencies. However, in the amplitude, points corresponding to high spatial frequencies and low temporal frequencies were seen to be much less. For temporal frequencies below 10 this relationship of spatial frequency was much lower overall with minimal spatial frequencies over 8 μm^{-1} as compared to 12 μm^{-1} . When looking at the spectrum for the complex data the overall magnitude of fluctuations was decreased. These results showed that we were removing a reasonable amount of the interference caused by this fringing pattern and looking at the underlying dynamics.

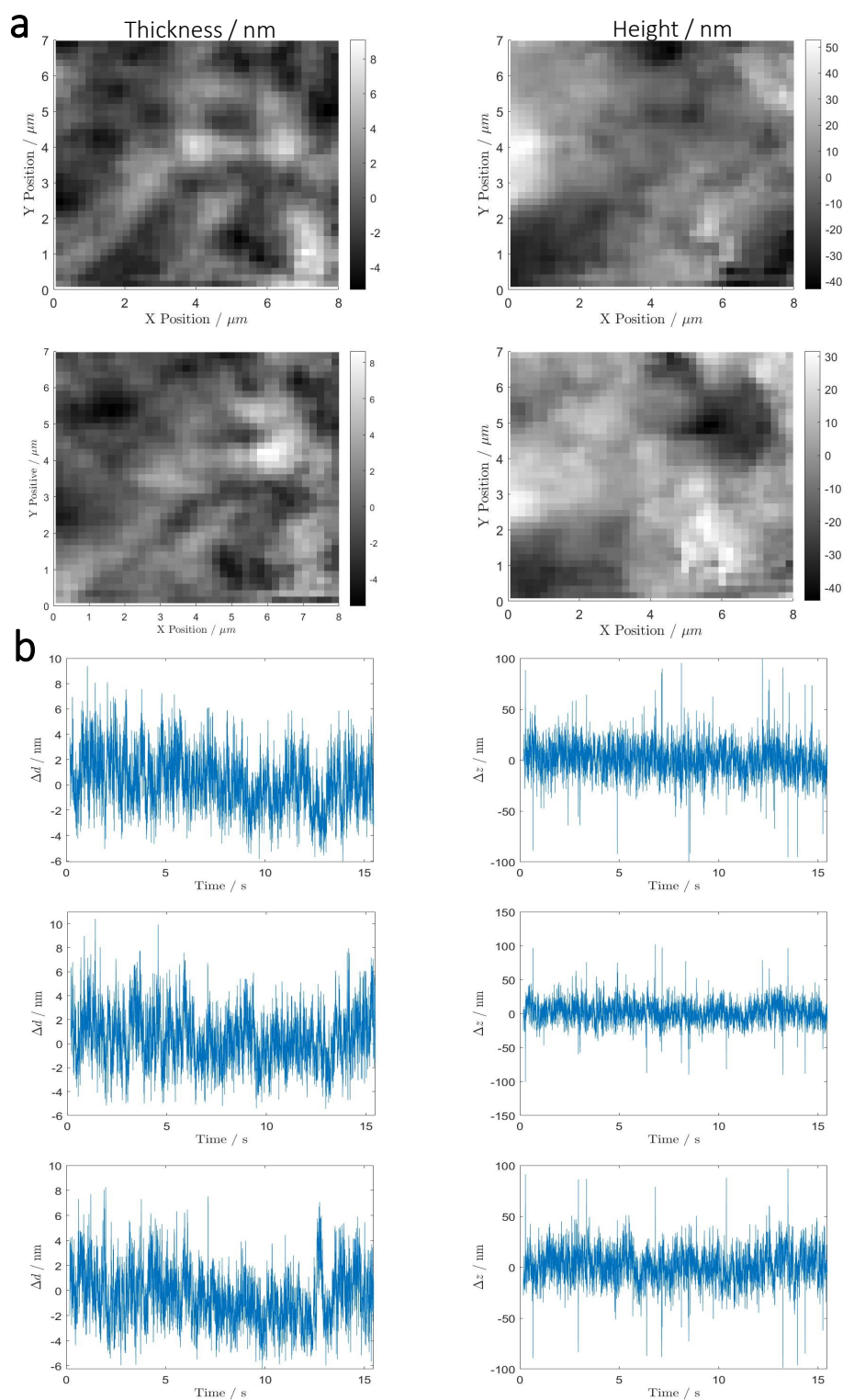


Figure 6.21: Time trace analysis of bilamellar POPC:POPE surface fluctuations
a) Shows the thickness and height with their overall shape removed to uncover fluctuations. Images were taken from A_N and Φ_{DPU} data. **b)** Shows traces of the changes of thickness and height with time for randomly selected coordinates of the central region demonstrating an increased fluctuation range. (see supplementary media M_5_2)

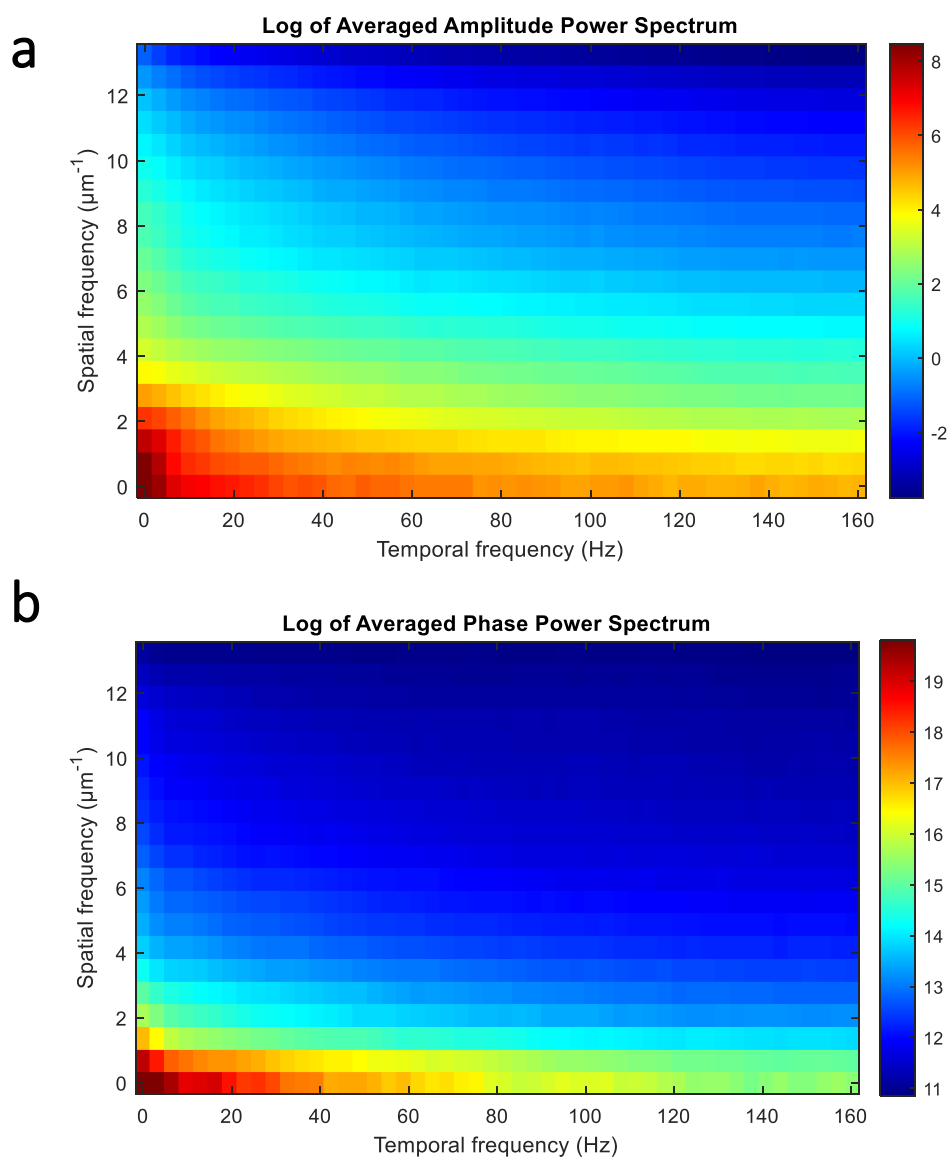


Figure 6.22: Power spectral analysis of bilamellar POPC:POPE surface fluctuations a) shows the power spectrum for the amplitude with that of the phase shown in b). No dispersion relation was identified.

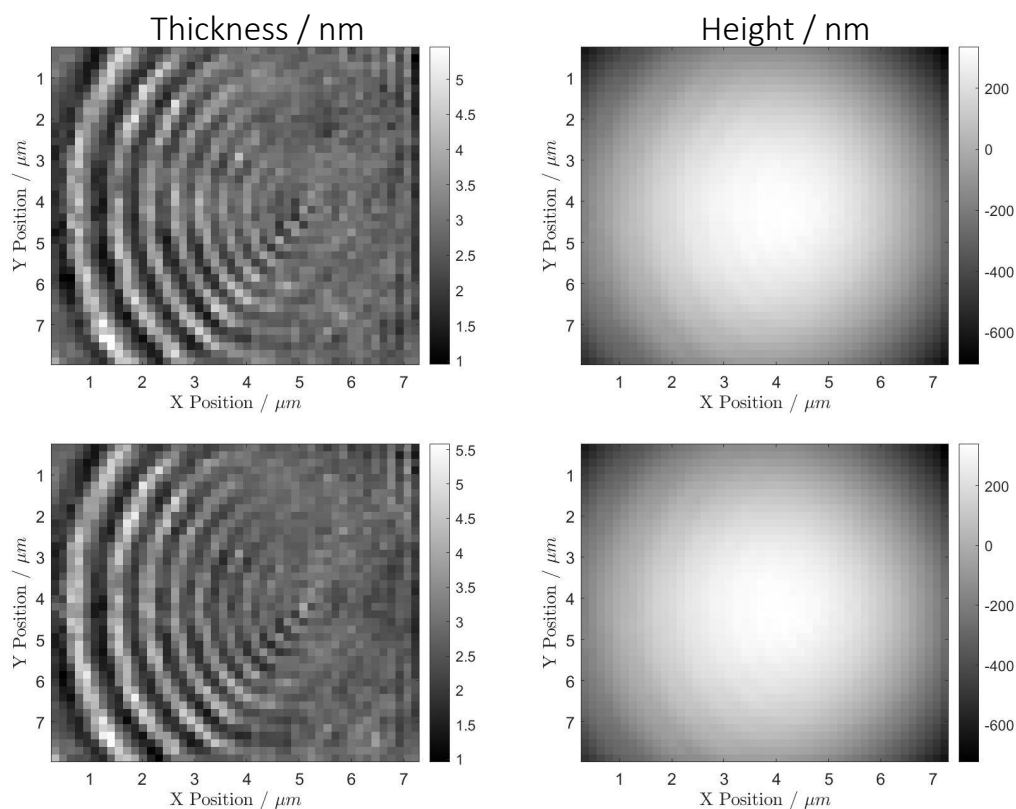


Figure 6.23: Initial unilamellar POPC:POPE vesicle as imaged in iGOR Consecutive frames measured at the top of the same vesicle where the thickness was as expected defining the vesicle as unilamellar prior to the loss of internal solution. The fringing pattern discussed above can be seen in the amplitude. Images were taken from A_C and Φ_{PU} data.

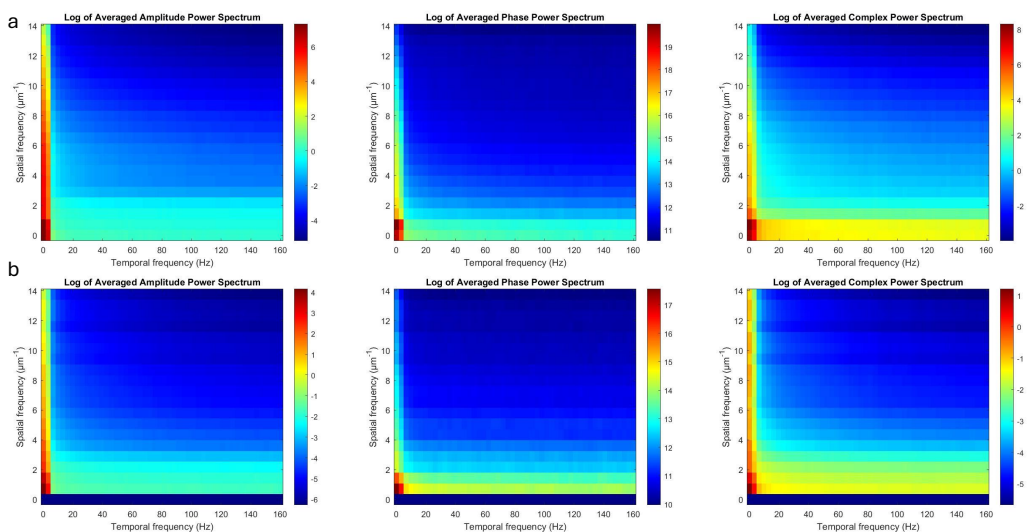


Figure 6.24: Comparison of the power spectra after fringe removal a) Power spectrum of the full frame of the POPC:POPE vesicle before loss of internal pressure containing the fringing pattern b) Power spectrum of the same vesicle over the same time frame but with the fringe pattern cropped out (Same frame cropping as in Fig. 6.23 and Fig. 6.25)

6.9.2 Time trace analysis

The time traces shown in Fig. 6.25b for the vesicle at the start showed fluctuations in the order of 2 nm in thickness and 20-30 nm in height, there were also frames for which the phase unwrapping still had trouble, causing spikes, these points are discarded.

Time traces were selected using a random coordinate selection restricted to the central region. The central region was defined as any coordinate within 0.5 μm of the top vesicle height. For the initial data this was further restricted by the cropping undertaken due to interference issues. A further measure of thickness was taken as the overall average for each frame for this central region. Fig. 6.26 shows the fluctuation prior to the loss of internal pressure for both radius and thickness where they have an anti-correlated relationship on the whole, however on a short time scale the thickness was fluctuating more than the radius suggesting we were also measuring dynamics within the membrane that were independent of the radius.

Once the vesicle had lost internal pressure after an hour and a half the vesicle fluctuated at a much higher rate with a greater magnitude as seen in Fig. 6.27. The top of the vesicle was deforming at a much higher rate as determined by the drastically different shapes observed in the thickness, Fig. 6.27a. This meant the top could no longer be fitted with a 2D 2nd order polynomial effectively to provide further phase unwrapping than the algorithm as can be seen in Fig. 6.27b. This made analysis of time traces hard as they were dominated by phase errors, for this reason the time traces shown in Fig. 6.27c, d and e were restricted in time to allow the non-artefactual time trace to be observed. The thickness traces shown in Fig. 6.27c demonstrated thickness changes in the order of 3 nm showing an increase from starting. To better compare temporal frequency the trace was compared to Fig. 6.27e, an extract from Fig. 6.26, which revealed that the membrane thickness was changing more rapidly across these 3 nm.

Fig. 6.27d demonstrates the height fluctuations observed over this time frame where, not considering spikes caused by phase errors, the fluctuations were in an order of 50 nm showing a marked increase from the initial dataset also shown in Fig. 6.27e. Fig. 6.28 demonstrates the change in fluctuation rate of the radius across this change of pressure. As this radius was calculated from the fit of the vesicle top, which was not well resolved in phase, it may be where some of the fluctuation arose. However, when considering the noise that was likely coming from this, there was still an underlying fluctuation that was clearly seen. In comparison to the radius prior to this change, a conservative estimate of a 5 fold increase in radius fluctuation was made. At this point, due to the phase unwrapping problems no further quantification of these values could be reliably made. There was an overlap between the traces at 15 μm suggesting that the vesicle did not change in size through any processes like deformation that would have caused a loss of surface area.

Combined these show we detected nanometer changes in the overall change of thickness fluctuations in a membrane's thickness upon the loss of internal pressure. It was also seen that the increasing fluctuations observed in the membrane upon internal pressure loss were dominated by changes in the height. This could have induced changes in membrane thickness as seen by the camera, as areas with an increased height generated a region of increased thickness perpendicular to the focal plane between it and the lower membrane areas. In this case the increase in membrane thickness would not have been a true thickness increase but rather an extended degree of bending.

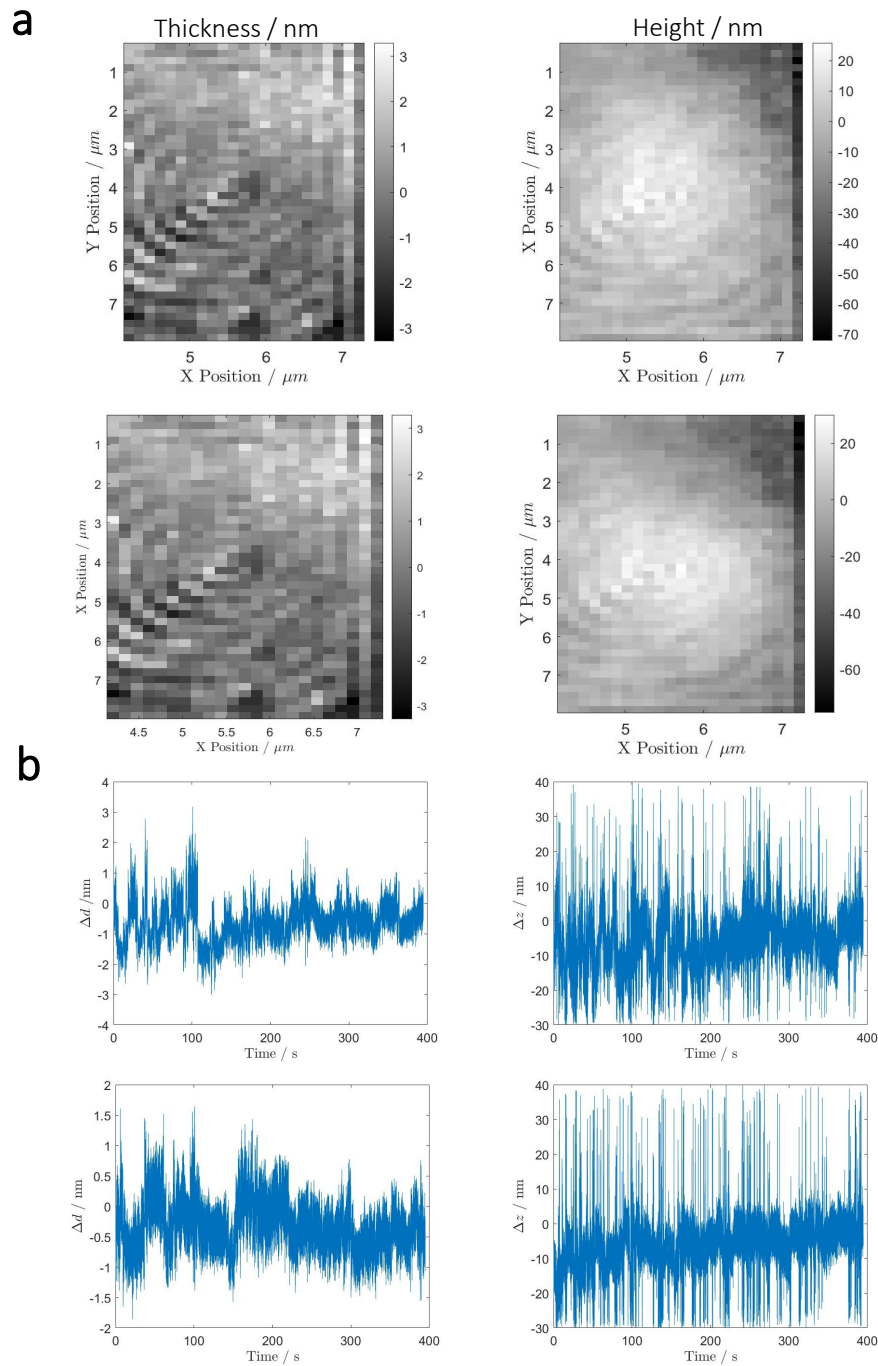


Figure 6.25: Initial unilamellar POPC:POPE vesicle time traces Consecutive cropped frames showing the fluctuations present in the membrane once the overall shape of the membrane had been removed shown in **a**). Images were taken from A_N and Φ_{DPU} data. **b**) contains the time traces of the thickness and height from randomly selected points within the shown frame.(See supplementary M_5_3)

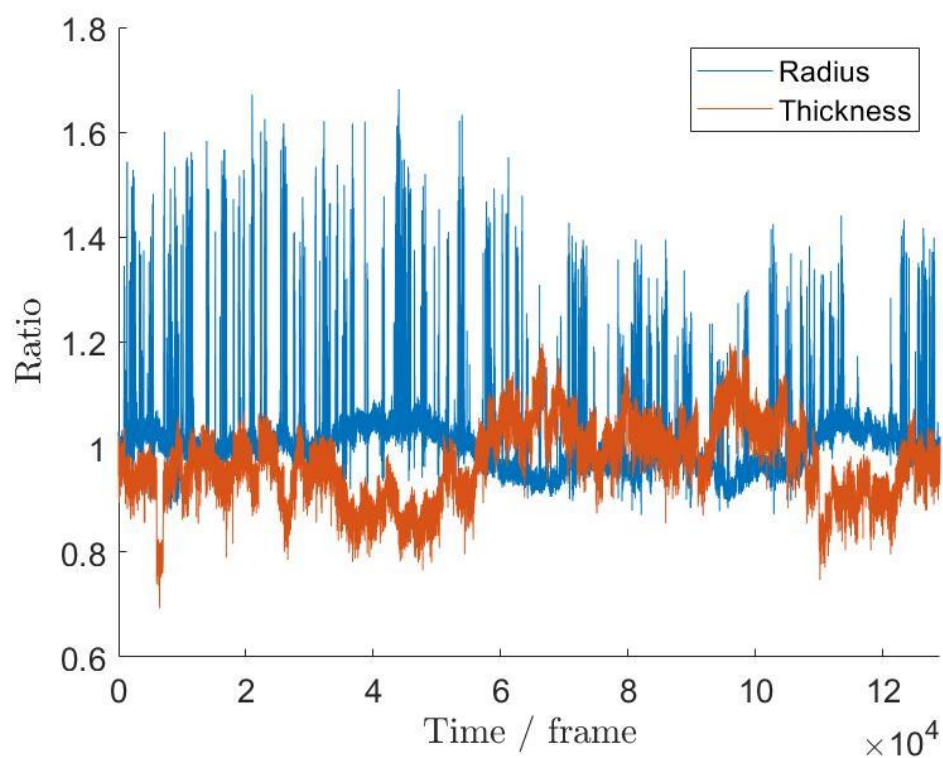


Figure 6.26: Unilamellar POPC:POPE ratio and thickness changes Ratio of the radius and thickness to their respective values from the first frame plotted against each other for the whole time trace showing the anti correlation present between these parameters.

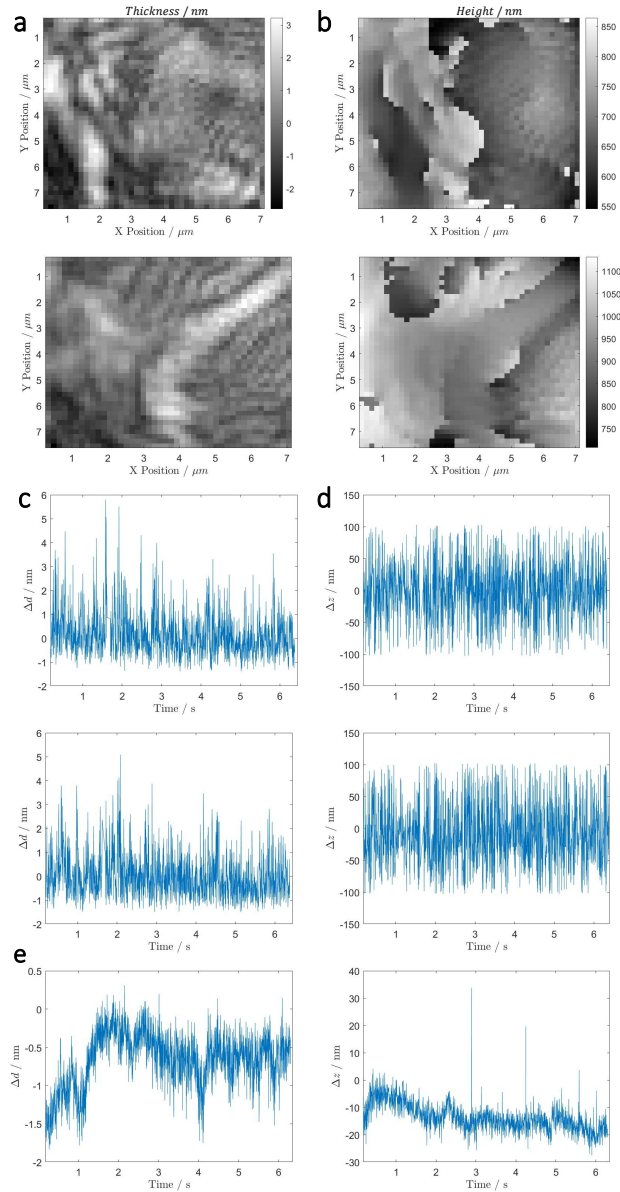


Figure 6.27: Time traces after the loss of internal pressure a) Thickness frames after loss of internal pressure. b) Height frames after loss of internal pressure. Images were taken from A_N and Φ_{DPV} data after 90 min. c) Shows the time traces of the thickness of a POPC:POPE (1:1) membrane after loss of internal pressure with the height traces seen in d). e) Shows the time traces from before the change, restricted to 2000 frames to allow comparison (see supplementary M_5_4).

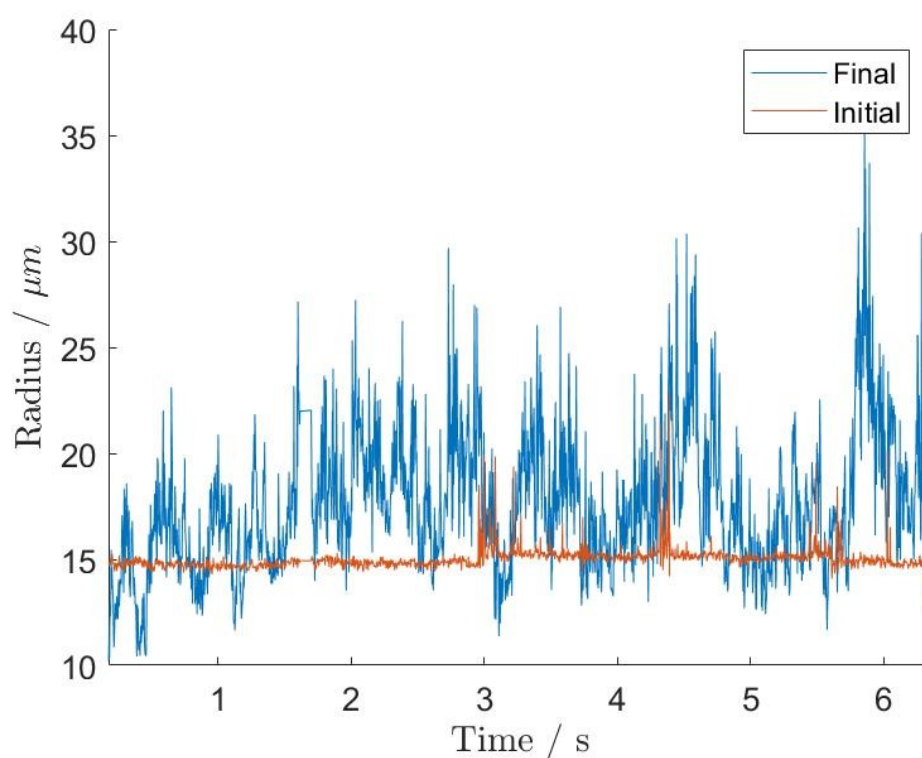


Figure 6.28: Comparison of radii fluctuations after loss of internal pressure The radius as calculated from the fit of the top surface of the vesicle for the same vesicle before (Initial) and after the loss of internal volume over the course of 90 min (Final) demonstrating much greater fluctuation range alongside a faster rate of fluctuations.

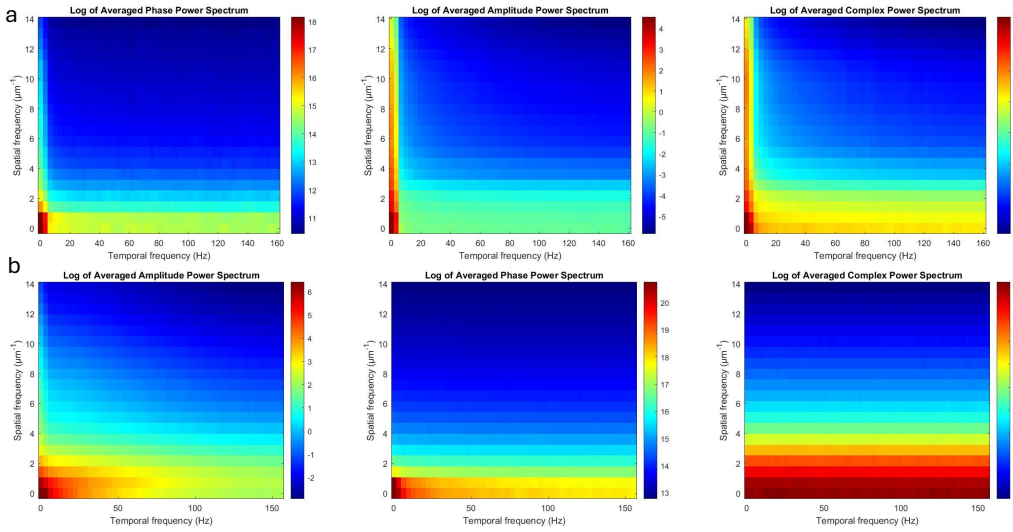


Figure 6.29: Power spectrum across the loss of internal pressure A comparison of power spectra of amplitude, phase and the complex compared from initial measurements, **a**), and after the loss of internal pressure, **b**). Of note was the overall increase in intensity between the spectra shown in **a**) and those in **b**).

The overall conclusions that can be made from this data are limited in terms of quantification of membrane properties, however, we can identify fluctuations above noise in the nanometre regime. We also show we can track a change across a loss of internal pressure in this same order of magnitude. We can see a change in both height and thickness traces and can make inferences over the vesicle shape deformations that may cause these, however these aren't quantifiable at this stage.

6.9.3 Power spectral analysis

When comparing the spectral analysis across this change what was clear in intensity scales was that the overall fluctuations were increased as shown in Fig. 6.29a, before, and Fig. 6.29b, after. In phase spectral power, between spatial frequencies 0 and $2\ \mu\text{m}^{-1}$ intensity was increased up to temporal frequencies of 150 Hz with a strong signal up to 75 Hz, and a slight dispersion relation starting at 70 Hz. This effect of increased temporal frequencies for spatial frequencies up to $2\ \mu\text{m}^{-1}$ was mirrored in both the amplitude and complex data showing that we detected this change in environment. It was the increase in overall fluctuations that indicated the vesicle had changed conformation.

6.10 DC₁₅PC phase transition

The DC₁₅PC vesicle measured across the liquid to gel phase transition was highly multilamellar which generated local interference affects, for that reason this analysis was difficult. A DC₁₅PC vesicle was imaged as it cooled from above its transition temperature (40°C) to below (20°C). In terms of absolute values associated with this transition we were unable to make any reasonable observations due to the multilamellarity, however, through power spectral analysis we are able to observe a change in frequency as shown in Fig. 6.30 where a) is in liquid disordered phase

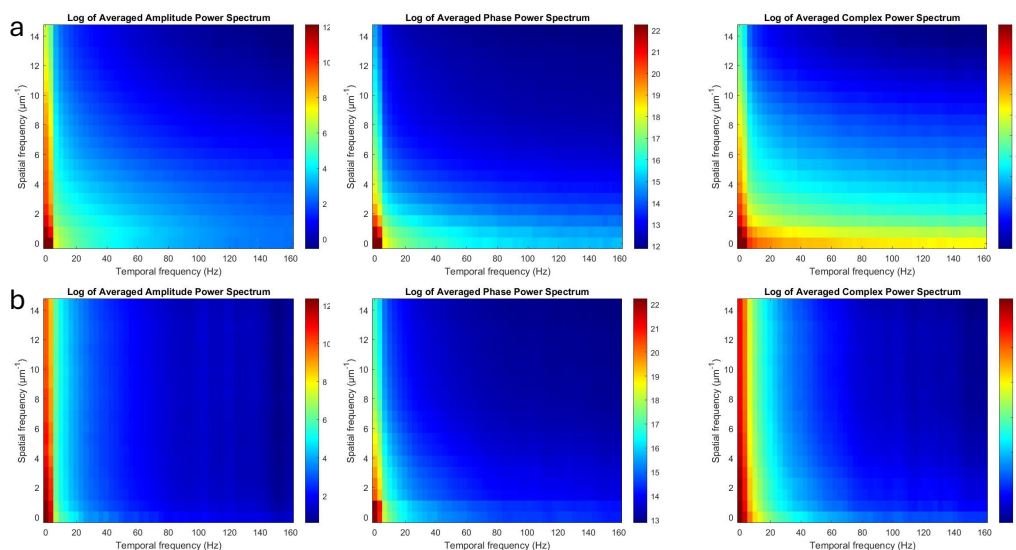


Figure 6.30: Power spectra across a liquid disordered to gel phase transition A comparison of power spectra from a vesicle in liquid disordered phase (a) and after the lipid has transitioned in the gel phase (b). The reduction of fluctuations is evidenced by the reduction of intensity present in the spectra. The reduction of intensity for the higher temporal frequencies indicated that the same spatial frequencies had been 'frozen in' to the membrane and were no longer fluctuating. (see supplementary M_5_5 for 40°C and M_5_6 for 20°C)

and b) in gel. In the amplitude spectrum the intensity of the fluctuations decreased significantly along the temporal axis. Once the membrane was in gel phase only temporal frequencies of any significance occurred under 20 Hz with the majority under 8 Hz but, for all spatial frequencies. This was altered from when the vesicle was in the liquid disordered phase where there were fluctuations of all frequencies up to 160 Hz for a range of spatial frequencies. To a lesser intensity an emergence of set temporal frequencies was observed in the amplitude, these temporal frequencies at 105 and 120 Hz alongside a wider less intense increase around 140 Hz occurred for all frequencies. It is not clear at this time whether these related to membrane features or were artefactual but, they did represent a change observed upon cooling beyond the phase transition temperature. These results demonstrate our ability to identify a phase change in a membrane thickness from the loss of fluctuations in the membrane.

6.11 Discussion

In summary, we have a working model membrane that can be imaged using iGOR to give quantitatively sensible results when qualitatively and quantitatively analysed. Whilst fluctuations could be analysed, analysis protocols for other biophysical properties are still to be developed. These properties include the bending modulus and the correlation between thickness and height changes to identify waveforms present across the membrane. Data retrieved in the cross-polarised channel is yet to be used to identify any in plane birefringence arising from tilted lipids.

It was optimal to take data at the correct focal height and the z dependency data set was taken with an aim to keep refocussing within 1 μm . This was additional to

the long acquisition taken at the optimal height to allow large averages to be taken. Long range fluctuations were also analysed as well as observation of any vesicle deformation.

For optimal imaging the intensity of the reference beam was kept to 100 counts and the signal approximately 45 counts out of a total of 255 maximum when they interfere. This was due to saturation occurring 255. Lambda half waveplates combined with polarisers were used in this setup to perform this attenuation. These were optimised and new reference images taken each time they were adjusted to ensure they reflected the correct relative intensity. When acquiring at the top surface of the vesicle the laser power of the excitation beam was increased to maximum which to maximise our sensitivity.

This high sensitivity is highlighted by our ability to observe thickness changes in the membrane to a sub-nanometer resolution with the mean thickness returning expected results. We have shown that we can track changes across environmental changes such as internal pressure loss and phase transition, however this analysis requires better data in order to fully quantitatively analyse these changes.

Challenges in this method included our ability to phase unwrap highly fluctuating data. Whilst we have improved our phase unwrapping in stable vesicles the additional polynomial fitting step implemented does not handle rapidly deforming top surfaces well, thereby leaving phase jumps in place making data interpretation challenging.

We have presented the improvements in both hardware and software we made to obtain more accurate results with fewer aberrations caused by interferences from the optical path or surrounding sample. Whilst our data still contained some interference as discussed we could, on the whole, remove them from our analysis for a stable vesicle. Work is being undertaken to improve the removal of these frequencies in Fourier space prior to power spectral analysis. We also aim to identify what was causing them within our image acquisition pipeline so they can be avoided in future imaging acquisitions. The source of these aberrations is as yet unclear, in the first datasets in which it was seen (data not shown) we were imaging at 30 μm above the glass-water interface which was on the limit of our coherence length and we therefore put it down to a delay that wasn't fully centred. This is no longer likely to be the case as we have seen it in datasets taken at various heights (30 - 40 μm) above the surface. As mentioned, we tried to remove the interference from the unilamellar vesicle, discussed in Section 6.9, by assuming it was a background signal fluctuating in line with the power. It appeared to be fluctuating less than the vesicle signal making it unlikely to be due to a small particle in the vesicle volume. This was further supported by the emergence of similar interference in different samples, by assuming it was a background signal we could correct the complex field to have a stable phase in the fringed regions. This was averaged and normalised to remove the fringes before being returned to its original value, however, in doing this we were removing vesicle signal alongside the fringes. It was therefore determined a vesicle interference as it has since been observed drifting in line with the peak of vesicles. More work needs to be undertaken to determine the cause of this interference alongside efforts to remove it from the data we have.

We demonstrated that we could correlate the behaviour changes in terms of radii and thickness in a way that described the movement occurring in our vesicles, as well as correlating changes to these parameters to environmental changes. This allowed us to make inferences about the lipid organisation and phase in the

membrane. Combined, these results showed a sensitivity that provides scope for membrane dynamic interpretation beyond the current understanding. Once more complex environmental changes are measured, such as more complex lipid compositions and protein insertion, more complex dynamics can be uncovered. Namely the identification of nano domain formation and the effect these have on membrane thickness, we can also probe formation after protein insertion. For the analysis of a membranes in gel phase such as the example in Fig. 6.13c we could analyse these facets in detail, looking at the light reflection polarisation state, and comparing with the plane orientation we see in the phase. In the analysis of our work we have shown that the identification of domains in the order of 500 nm is possible providing the basis for this work going forwards.

To further this work we plan to insert the App6Aa1 pore-forming toxin (described in Chapter 5) into our membranes to observe the membrane thickness changes and bending associated with insertion as well as the protein itself diffusing in the membrane. It was with these experiments in mind that preliminary membrane behaviour was quantified for POPC:POPE 1:1 membranes.

Chapter 7

Particle tracking

As iGOR is a form of digital holography it allows the refocusing of a particles signal and therefore particle tracking with nanometer precision in a large volume above a surface. The ability of the technique to track small particles down to 10 nm size through large a depth, makes iGOR an advancement over known nanoparticle tracking methods.[135] iGOR is compatible with both inorganic and organic samples, as my work focusses on organic systems this chapter will focus on these. However, it is important to note that both are possible and particle tracking has been achieved using metallic nanoparticles.

Using metallic nanoparticles, this tracking is as yet unpublished, but been shown to accurately measure the hydrodynamic radii of 10 nm gold nanoparticles. The findings from these experiments informed some of the analysis undertaken on lipid particles discussed in this chapter, centred around the noise correction of our set up. Therefore I will discuss these initially to contextualise some of the assumptions and corrections used in the subsequent analysis.

In terms of organic samples, particle tracking of liposomes could provide an insight into their diffusive behaviour, and if used in combination with cellular or membrane environments interactions could be quantified. Measurements of this manor, utilising a membrane environment and organic nanoparticles, would be interesting when investigating viral particles. Viruses are classified according to size and shape.[252] Immediately this indicates iGOR's particle tracking function as a potential diagnostic technique, and if completed in a cellular environment, docking and undocking events could be identified leading to the determination of residence times.

Lipid structures of many sizes are found within biological systems and are relevant within the medical field.[253, 254, 255, 256, 257] Many of the understudied but clinically relevant lipid structures are classed as nanoparticles. Of note, exosomes are biomarkers and can be used to monitor disease progression, viral load can be indicated in infectious disease control and the transport of drugs to target molecules and across membranes.[255, 256, 257, 258, 259, 260, 261] By showing we can track particles both organic and non organic in nature we provide a system that can start to answer some of these biological questions.

This chapter will detail the results we obtained when utilising the interferometric gated off-axis reflectometry (iGOR) technique to track both organic and inorganic particles. We show a sub-pixel positional resolution in both X and Y, due to intensity fitting, and Z, due to additional phase component correction. The sub-nanometer z resolution coupled with our temporal resolution of 3 ms allows us to accurately

identify a particle's position and in turn the mean square displacement (MSD) and hydrodynamic radii. I will commence discussing the measurement of inorganic controls, polystyrene beads of diameters 0.1 μm and 0.2 μm . These were imaged in 75% glycerol/water mixtures to control the viscosity, limiting motion during a frame exposure. This needs to be well below the light wavelength in the medium, λ/n to suppress destructive interference and gain an accurate hydrodynamic radii and particle track.

We can track particles across a large number of frames, with some tracks in an excess of 50,000 frames. This allowed us to average out the polarising effects of the particle due to positional and orientation factors. In a lipid context, the proportion of signal in both the co- and cross- polarised channel allows any anisotropic effects to be evaluated.[262, 263, 264] Due to the length of the tracks acquired, any effect on the light's polarisation state arising from the orientation of the nanoparticle will be averaged out, thereby leaving the chirality of the particle calculable from the difference between polarisations.[265, 266, 267]

For this work small unilamellar vesicles (SUVs) were utilised as a model membrane as they have radii within the nanoparticle range and can be made with biologically relevant lipid compositions. The lipid structures with the smallest radii (5 to 20 nm) were likely to be in a micelle conformation as this is the smallest hydrophobically stable conformation they can exist in.[268, 269] Increased sizes ranging from 20 nm to 1 μm are classified as SUVs and are made of a bilayer filled with water.[270]

7.1 Particle tracking analysis

Raw data was taken at a set field of view for a period of approximately 2 min. Data acquisition was started once a nanoparticle was in the field of view. A particle centred in field of view appeared as shown in Fig. 7.2a, where the maximum intensity was indicative of particle position. To follow the particle in the z axis the field of view was computationally refocussed to the z height of it's new position. Further description on this tracking process can be found in Section 7.1.2

Data was taken and saved as described above in Section 2.9.2. Our tracking method was, in the first place, intensity based and relied on the refocussing ability of iGOR to find the pixel in 3D planes with the highest intensity from frame to frame used to track movement. With the knowledge of medium viscosity, a hydrodynamic radii was calculated by fitting MSD to time for all dimensions. The agreement between the dimensions gave us confidence in our ability to accurately track particles in z.

7.1.1 Background Correction

The data was interpolated to smooth the image. In the Fourier domain the image was padded out with 0 to a size given by a power of 2 which was at least 2 times larger than the original size. Once inverse Fourier transformed, the pixel size in real space was reduced accordingly, the smoothing effect is demonstrated in Fig. 7.2a. Background correction for tracking analysis was a multi-step process that started with the average subtraction of the background. For our purposes we performed a 50 frame rolling average. Whilst this was effective in removing any secondary signals from the background, we also ran the risk of removing our primary signal of the particle, especially if it had a low diffusion coefficient. To avoid this, we

fitted the background with a 2D third order polynomial fit surrounding the last found particle position, this was carried out in three iterations. The fit was then subtracted excluding the particle position. It was the complex background field that was fitted.

7.1.2 Coarse intensity tracking

Initially the start coordinates were indicated by the user in all dimensions. A virtual 3D volume was formed around these coordinates, of which size was dependant on expected diffusive patterns. This provided the search area for the next frame and were input by the user. For these experiments the axes were ± 4 nm in x and y and ± 1.6 μ m in z. When locating the next particle position, to reduce the chance of picking up errant signals towards the edge of the volume the 3D volume was weighted with a 2D polynomial fit with a quadratic weighting. The polynomial used was again dependent on expected diffusive patterns. We used an iterative approach to tracking due to this weighting step as weighting could affect our particle localisation when looking at a high resolution. Each iteration used improved the fit as it reset the central position of the weighting and we could therefore be sure that we found the maximum intensity and in turn the correct position. The refocussing was carried out as described in [271] using fornell equations. Fig. 7.1 shows three examples of particle movement tracked using this coarse particle tracking where movement in all 3 axes from it's original position can be seen.

7.1.3 X, Y axis fine particle tracking

Once the highest intensity pixel had been identified, a second order polynomial fit was taken for the two neighbouring pixels alongside the nominal position from the coarse analysis. From this the fit peak was determined to provide sub-pixel resolution for the particle position. This was repeated for both x and y axes, an example of which is shown in Fig. 7.2b. Examples of particle tracks obtained with the coarse intensity tracking and x, y fine particle tracking are shown in Fig. 7.1, these examples encompass different track lengths to demonstrate the sensitivity and the ability to track over large time frames.

7.1.3.1 Z axis fine particle tracking

The phase of a particle's scattered light stays constant and therefore, once the contribution of the height change was removed the remaining phase was converted to sub pixel z axis precision. At any point, the phase of a particle can be described using Equation 7.1, where \mathbf{K}_{exe} is the excitation beam wavevector.

$$\phi = \phi_0 + \mathbf{K}_{\text{ex}} \cdot \mathbf{r} \quad (7.1)$$

Once the coarse intensity had identified the z position the phase offset was calculated and converted to a z offset with Equation 7.2. A penalty, referred to as α , was applied to limit the amount of phase correction that could occur. This acted to ensure we were not interpreting any background phase drift as particle phase offset. Once the phase offset had been calculated the axial position of the particle was corrected by the height corresponding to the phase offset.

$$\phi'(x_0, y_0, z) = \phi(x_0, y_0, z) + \mathbf{K}_{\text{ex}} \cdot \mathbf{r} \quad (7.2)$$

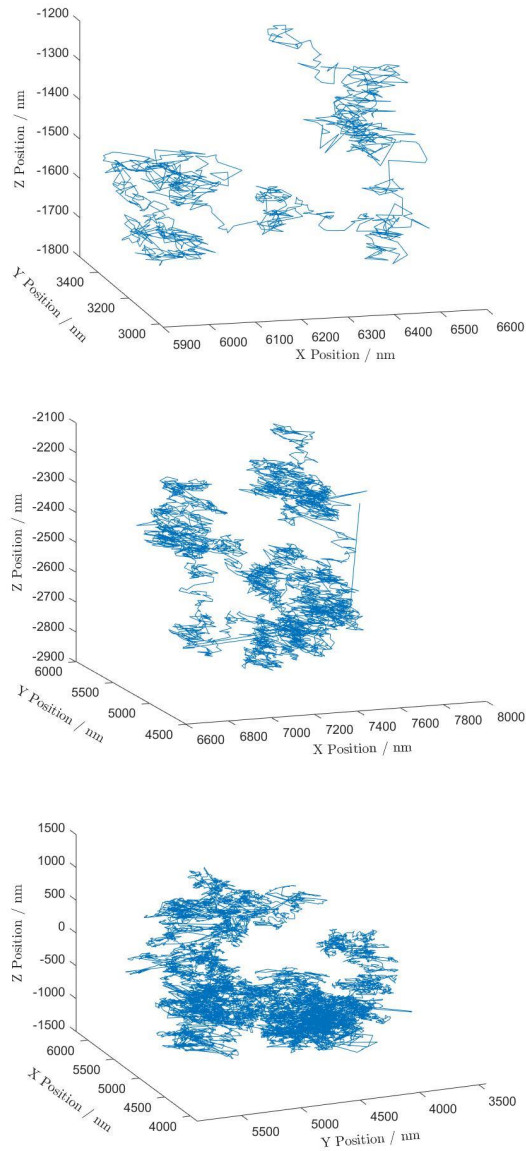


Figure 7.1: Coarse particle tracking Examples of particle tracks across the 3 measured axes obtained from the coarse particle tracking, plots were acquired with a 3 ms temporal resolution. These examples show tracks of different lengths demonstrating the sensitivity of the technique to positional changes in 3D alongside the ability to track across a large time range.

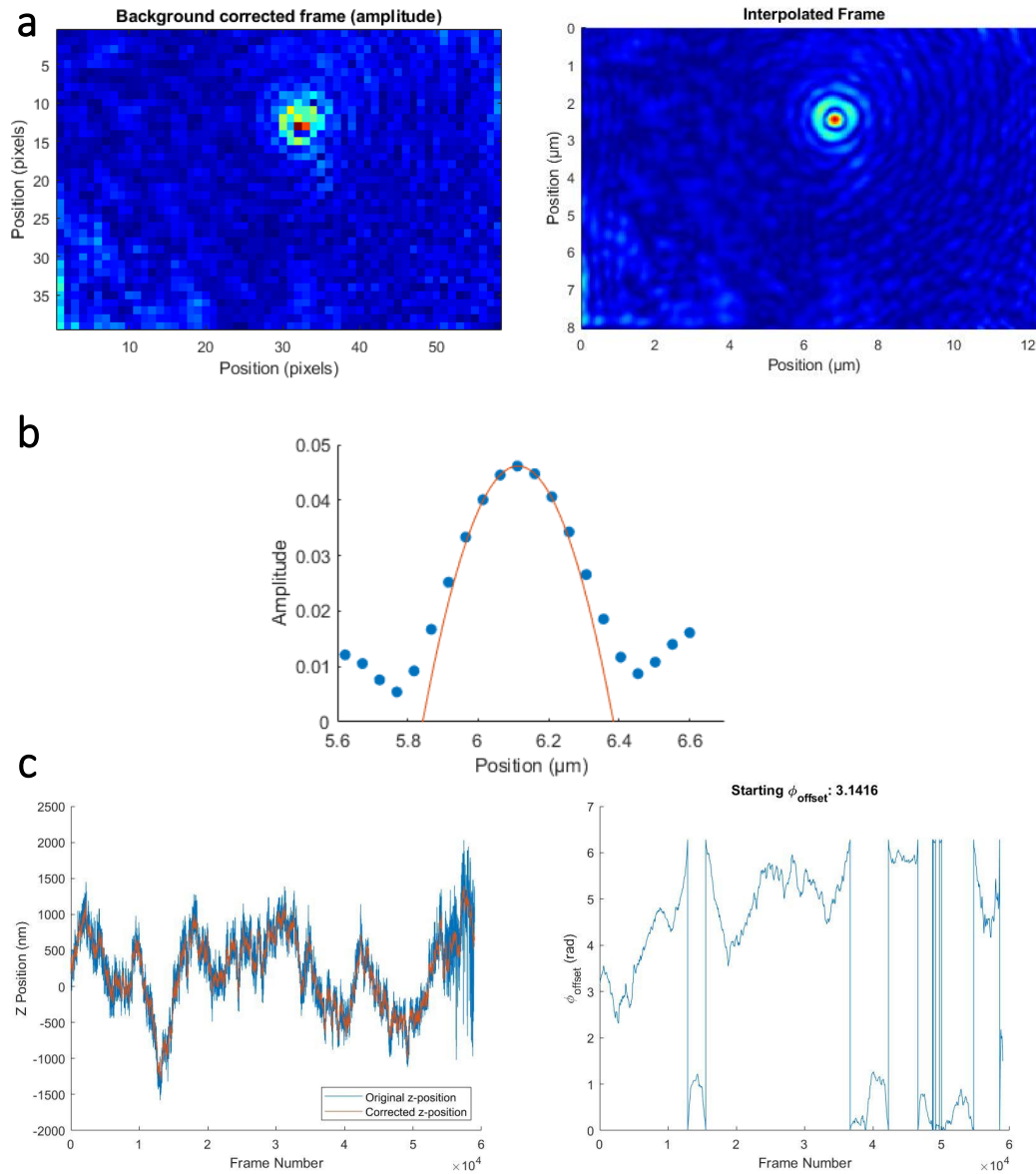


Figure 7.2: Steps used to improve particle tracking **a)** A before (background corrected frame) and after (Interpolated frame) of the interpolation step showing how we smoothed the data prior to tracking. **b)** shows an example of quadratic fitting to identify the peak position providing sub-pixel resolution. **c)** demonstrates the ability of the z correction step to provide additional z resolution using the phase.

A suitable α parameter was one that allowed the phase to be corrected, correcting any phase jumps and phase offset without being so sensitive that we were chasing the noise and over correcting the data. A calculated start point of 0.01 was used initially, with a smaller α factor generating a smaller correction of the particle track and a larger α factor facilitating a greater phase correction. To find the optimal factor we were looking for a maximal agreement of hydrodynamic radii calculated for z with that calculated for the x and y axis. When fitting the MSD we observed different behaviour in the region of the graph corresponding to short time intervals, where the curvature changed with alpha as demonstrated in Fig. 7.3. This behaviour was informed by the ability to follow reference phase drifts while not allowing the z -noise of the amplitude to create noise-related 2π phase jumps.

Fig. 7.3 shows the effect of changing alpha across 4 orders of magnitude, the higher alpha of 0.1 was generating a hydrodynamic radii adrift from those generated from the x and y axes. An α value of 0.001 was used. As we assumed natural diffusive behaviour, the MSD graph for each axis should show a linear dependency arising from the origin. An α too low would cause the initial region of the graph to have a negative curvature as at these small time intervals the Z track was over corrected reducing the displacement measured. Conversely, at a high α value, the displacement measured was higher than it's true value as the track was under-corrected causing noise to be analysed. We show data that had very good signal to noise and thus z -localisation, meaning a low alpha did not impact the z tracking too greatly. Therefore, we only had to avoid an alpha too small where external drift could not be followed. This can be seen in the graphs shown in Fig. 7.3.

This z correction step also acted as a phase unwrapping process to remove any remaining phase jumps. This step is demonstrated in Fig. 7.2c.

7.1.3.2 Displacement analysis of particles

To calculate a hydrodynamic radii from the displacement, MSD analysis was undertaken on the particle tracks. The mean displacement for increasing time intervals was calculated. For each time interval (τ) assessed an average displacement was calculated over all possible starting times within the track. From the MSD we found the diffusion coefficient (D) for these particles to convert into a hydrodynamic radii (r_H) using Equation 7.3. Plots showing this relationship are shown in Fig. 7.6.

$$r_H = \frac{k_B T_K}{6\pi\eta D} \quad (7.3)$$

We were interested in any motion caused by normal diffusion as this was solely affected by the particle size, medium viscosity (η) and temperature (T_K) which were factors controlled. We needed a τ much smaller than the track time to have sufficient statistical averaging. Drifts showed as a deviation from the linear scaling of the MSD, towards a quadratic scaling for a linear drift allowing identification of the τ where drift influenced results. This meant we could set our τ range to exclude these values.

The maximum time interval we included in our MSD analysis was 100 frames, equating to approximately 0.3s, as for these time intervals movement was solely impacted by normal diffusive movements and the x and y axes exhibited the same diffusive behaviour. We discarded time intervals where the x and y axes deviated as they were analysed in the same way and the noise terms associated with this analysis were the same. We can say that the regions for which they deviated are likely to

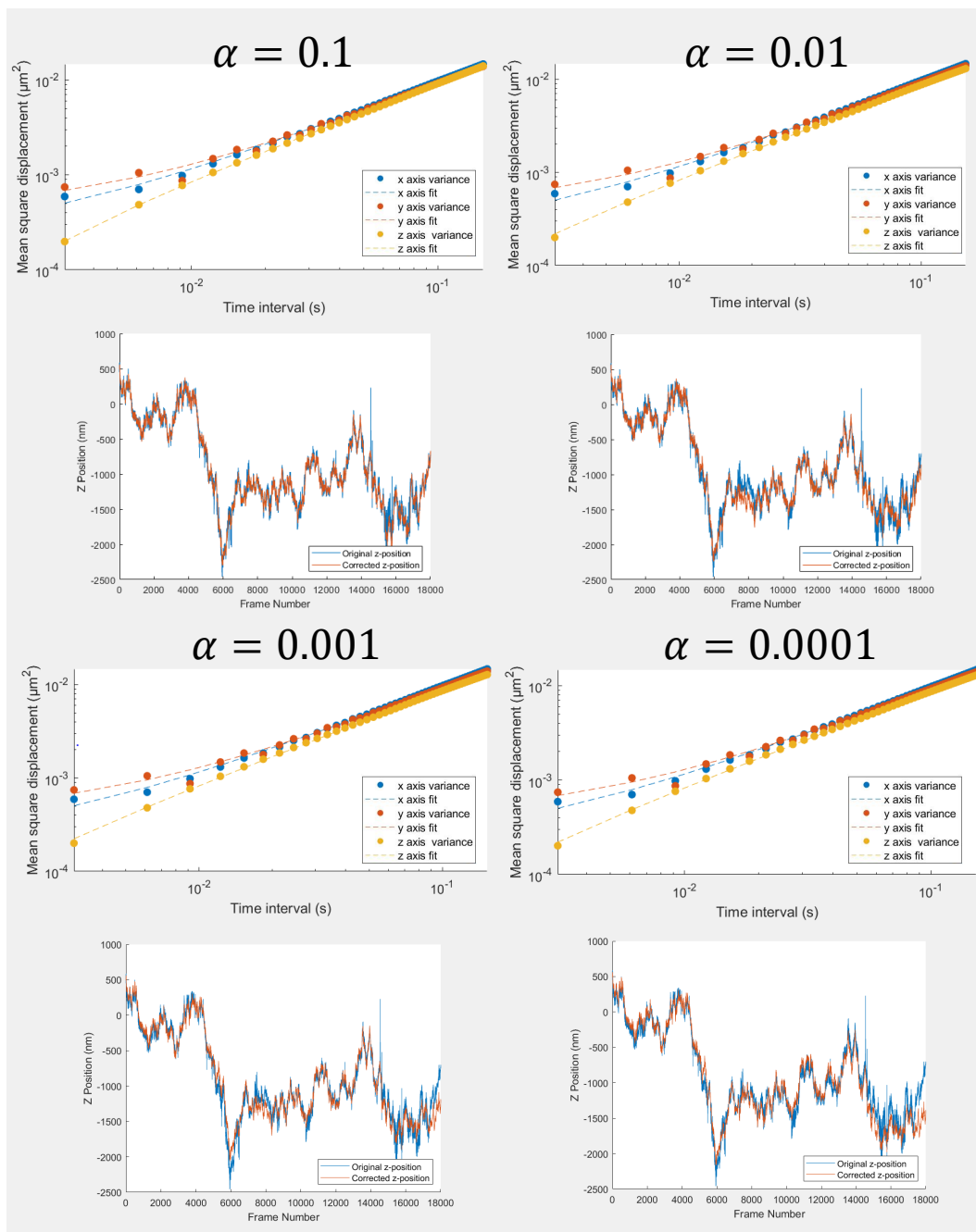


Figure 7.3: Comparing α factors for particle tracking z correction A series of MSD analysis of the same particle track to demonstrate the effect of a changing α , whilst this wasn't a very pronounced effect at low time intervals, a curved response was observed at an α of 0.1. Also shown are the original z axis tracks plotted with their corrected counterpart.

have been due to error. To ensure statistical significance the maximum time interval measured had to be less than 10% of the total track length which ensured for each time interval analysed we were calculating from 10 independent displacements.

Prior to the calculation of the diffusion coefficient from the MSD graphs a linear normalisation step was undertaken to remove the effect of sample drift if present in either the x or y axes. We subtracted a linear time dependence from beginning to end of the trace.

The following fitting of the MSD curves were weighted in favour of small time intervals due to the higher number of independent measurements, as shown in the right panels of Fig. 7.6. The weights scaled with the inverse square of the time interval according to Equation 7.4 where t is the time interval and t_0 is the smallest interval.

$$\left(\frac{1}{t - t_0}\right)^2 \quad (7.4)$$

To improve the fitting of the remaining MSD graph we took the initial equation (Equation 7.5) and added measurement and position noise terms based around our set up. One source of noise involved the piezoelectric stage which was actively regulated and had associated positioning noise and response times. These were added into the equation alongside a generalised noise term to encompass measurement noise in the determination of the position by iGOR, which is uncorrelated from frame to frame. These are detailed in Equation 7.6, where σ_r and σ_s are the position measurement and stage noise terms respectively, τ is the response time of the stage, D is the diffusion coefficient and t is the time interval.

$$\text{MSD} = \sigma_r^2 + 2Dt \quad (7.5)$$

$$\text{MSD} = \sigma_r^2 + \sigma_s^2 \left(1 - \exp\left(\frac{-t}{\tau}\right)\right) + 2Dt \quad (7.6)$$

As previously mentioned this methodology was initially developed for the analysis of metallic nanoparticles and therefore the stage specific noise and response times had been determined prior to these measurements. These were initially used in this analysis however, since this data was taken, our stage developed a problem and stopped responding completely in the x axis. For this reason we re-established these fitting parameters for our control sample of 0.2 μm polystyrene as these were the largest particles measured in this dataset and therefore the most reliable. The stage response time was set to 20 ms in all axes as this was constant for our system. The other noise terms were unrestrained and acted to minimise the goodness of fit through the root mean squared error. Our median average noise values were $15.2\text{e-}6$ nm, $6.03\text{e-}5$ nm and $1.57\text{e-}4$ nm for x,y and z, respectively and $7.8\text{e-}7$ nm, 10.2 nm and $5.8\text{e-}7$ for stage noise. An assessment of the fitting accuracy can be seen in Fig. 7.3 where the y intercepts of the fits were in agreement to that of the data for the $\alpha=0.001$ dataset. The Z axes was in exception of this trend as the additional phase correction removed this element of error and there was no stage movement when measuring the axial position, it was a purely algorithmic solution.

7.2 Expected results

The direct output of the MSD fitting was the diffusion coefficient of the measured particle. This in turn was used in the Equation 7.3 to calculate the hydrodynamic radius. The data was taken in a temperature controlled room and monitored, maintained at 20°C. The viscosity of the medium was depending on the concentration of glycerol in the medium surrounding the particles. During the aforementioned analysis of the gold nanoparticles this was found to be a ill-defined value, as the viscosity of 100% glycerol made it difficult to aliquot due to retention in pipettes. Even small inaccuracies in glycerol concentration caused significant error in the diffusion coefficient calculated, this was found during the previous metallic particle work. In an effort to reduce this source of error glycerol stocks were made in larger volumes and titrated to reduce retention, by washing the inside walls with the produced glycerol mixture. We anticipate the glycerol concentration error to be within 3%, due to the fact that for larger volumes of high percentage glycerol the water was added to the glycerol. The same glycerol stocks were used in all particle tracking measurements discussed in this chapter, meaning that we could evaluate the error in viscosity. We used the known hydrodynamic radii and the measured diffusion coefficient in Equation 7.3 from the controls to further determine the error.

Alongside the calculated radii, the peak amplitude of the particle measured was recorded, which, as it was calibrated in reflectivity could be quantified as proportional to the volume. This allowed a comparison to be made between particles of the same type. Simply, the hydrodynamic radii was expected to scale with the reflectivity as the scattering ability of the light is determined by it's scattering cross-section, and in turn volume.[272]

As we used a wavelength of 550 nm and measured particles smaller than this, we expected a reflectivity proportional to the third power of the radius, (r^3). A regime known as Rayleigh scattering states a proportionality to the scattering cross-section of the sixth power, which makes the proportionality to the volume the third power.[272] This regime is different in SUVs where the lipid volume is the only scattering portion. This thickness is constant and small compared to the size making the reflectivity proportional to the second power of the radius, (r^2). For differing nanoparticle types the exact nature of this scaling depends on the polarisability factor of the material which can be described using Equation 7.7 where ϵ_p and ϵ_m are the dielectric constant of the particle and medium, respectively and is the square of the refractive index.

$$\alpha = \frac{\epsilon_p - \epsilon_m}{\epsilon_p + 2\epsilon_m} \quad (7.7)$$

The intensity measurements of our particles could have also been dependent on axial height. As we used an incident beam at a slight angle, particles measured above the imaging focal plane may have seen a different intensity which would have altered their reflectivity. As our beam radius was about 10 μm and we limited our defocus to a z range of 4 μm , using a numerical aperture of 0.3 for 4 μm defocus, we had approximately 1 μm shift in our 10 μm beam size leading to an error in our intensity measurement. This effect was heightened for particles at the edge of our beam. The effect of this on controls is discussed below, but for this reason we took an average maximum particle intensity across the first batch of the track. We anticipated minimal displacement in z and therefore minimal augmentation of the particle intensity, making our noise minimal and intensity measurements reliable.

7.3 Controls

7.3.1 Polystyrene

Both 100 nm and 200 nm polystyrene beads were used to establish the fitting and analysis parameters for further SUV analysis. An example of this MSD analysis for a 100 nm particle track is shown in Fig. 7.6a. The fits shown reported a good agreement in diffusion coefficients of 0.119, 0.1, 0.101 $\mu\text{m}^2\text{s}^{-1}$ for x, y and z respectively. As previously mentioned, at high glycerol concentrations the viscosity is strongly dependent on glycerol concentration as can be seen in Fig. 7.5a, where this dependency was fitted using a 2 term exponential as shown. When looking at the diffusion coefficients measured for both the 200 nm and 100 nm we could see that they scaled suitably with the known hydrodynamic radii as seen in Fig. 7.7a. However, the mean hydrodynamic radii were slightly adrift of what we expected from manufacturers specifications. For the 200 nm beads we measured a mean radius of 86 nm, whilst our mean radius for 100 nm was 38 nm. Fig. 7.7b highlights the expected x^6 relationship of scattering cross section to hydrodynamic radius, which our data also followed. Our first idea for likely source of error was our glycerol concentration. These measurements were undertaken in a solution of 75% glycerol with a calculated viscosity of 0.05529 Pa/m². From our experimental data, by taking a mean diffusion coefficient for each dataset we calculated diffusion coefficients of 0.0433 $\mu\text{m}^2\text{s}^{-1}$ and 0.103 $\mu\text{m}^2\text{s}^{-1}$ for 200 μm and 100 μm , respectively. Combined with the known specified radii from manufacturers specifications we calculated viscosities of 0.0496 PaS and 0.0415 PaS, producing an average value of 0.0455 PaS for n=117, which, considering datasets were taken in different sessions was considered within reasonable error. This viscosity corresponded to a percentage glycerol of 72.7% which was within the estimated error of 3% of glycerol concentration. Alongside an increase in viscosity, an increase of refractive index also occurred as seen in Fig. 7.5, in which the refractive index was decreased from 1.44404 to 1.4415, considered insignificant. As previously mentioned, the z height and proximity to the centre of the beam could have caused an additional error in the peak intensity. Fig. 7.4a demonstrates the effect we observed for different levels of z defocus. The particle position of each axis was plotted against the scattering intensity measured for all positions measured for the 100 nm controls. This was repeated for the x and y positions. Whilst there was potentially a dependence of intensity on z position, as the scatter cloud was skewed with a positive proportionality, when fitted with a first order polynomial, the bulk of points were within the central mass showing a minimal effect on this intensity due to positioning of the laser in the focal plane. Fig. 7.4c and d show the same dependency for x and y where the effect was less pronounced. These results showed that whilst we observed the expected effect of laser position it was below the level for which we would need to correct for.

7.4 Small unilamellar vesicle analysis

To try and reduce sampling bias and gain a representative overview of the SUVs produced we took data at different glycerol concentrations. We took data at 90%, 50% and 0%. We don't show the data obtained in the 0% solution as most particles were moving too fast to obtain a full batch with the particle in frame, the only particles for which tracks were obtained were aggregates and therefore did not behave uniformly in all axes making it difficult to make inferences based on their diffusive

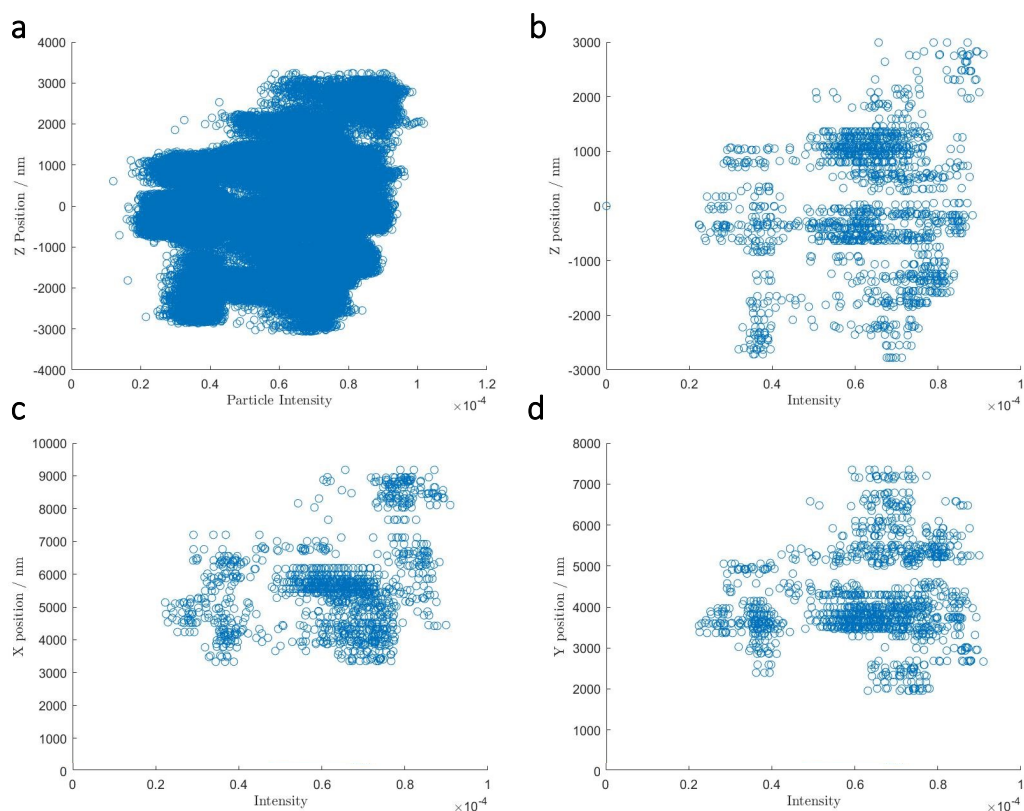


Figure 7.4: Effect of position in laser beam on scattering intensity Scatter plots showing the effect of the position in the laser beam in x,y and z axes on the scattering intensity of the particle at that position. **a)** shows all positions measured with no averaging in all tracks for 100 nm polystyrene controls, once the points had been averaged over 100 frames **b)** was produced. **c)** and **d)** show the averages positions and intensities for the x and y, respectively. A slight positive skew was observed in this data, however, the bulk of the points were within the central range. This indicated a minimal effect of laser beam positioning.

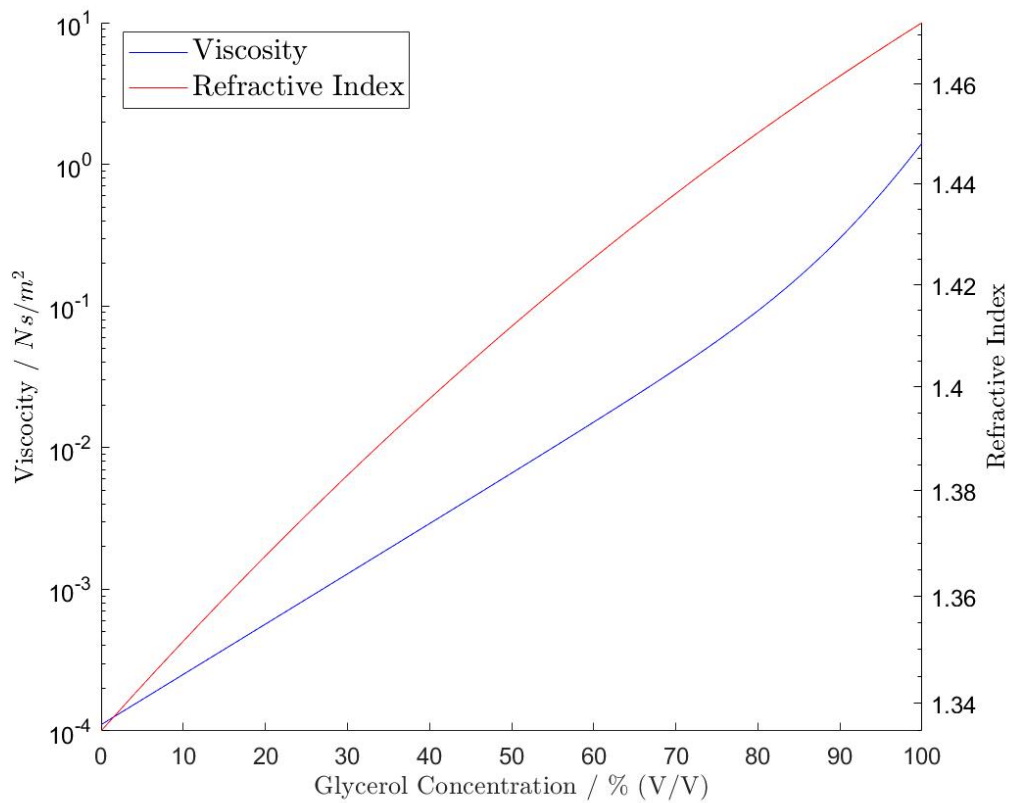


Figure 7.5: Properties of glycerol solutions A graph showing how the viscosity and refractive index changed with an increasing glycerol percentage in solution. The fits shown in both graphs were used in further analysis, for viscosity in Ns/m^2 , $\eta = 0.0001107 \exp^{0.08168G} + 1.058 \times 10^{-9} \exp^{00.2069G}$, where G was glycerol concentration in %, and for refractive index, $n_G = -3.255e^{-6}G^2 + 0.001702G + 1.335$. The calculations leading to these plots are shown in Appendix D.1.

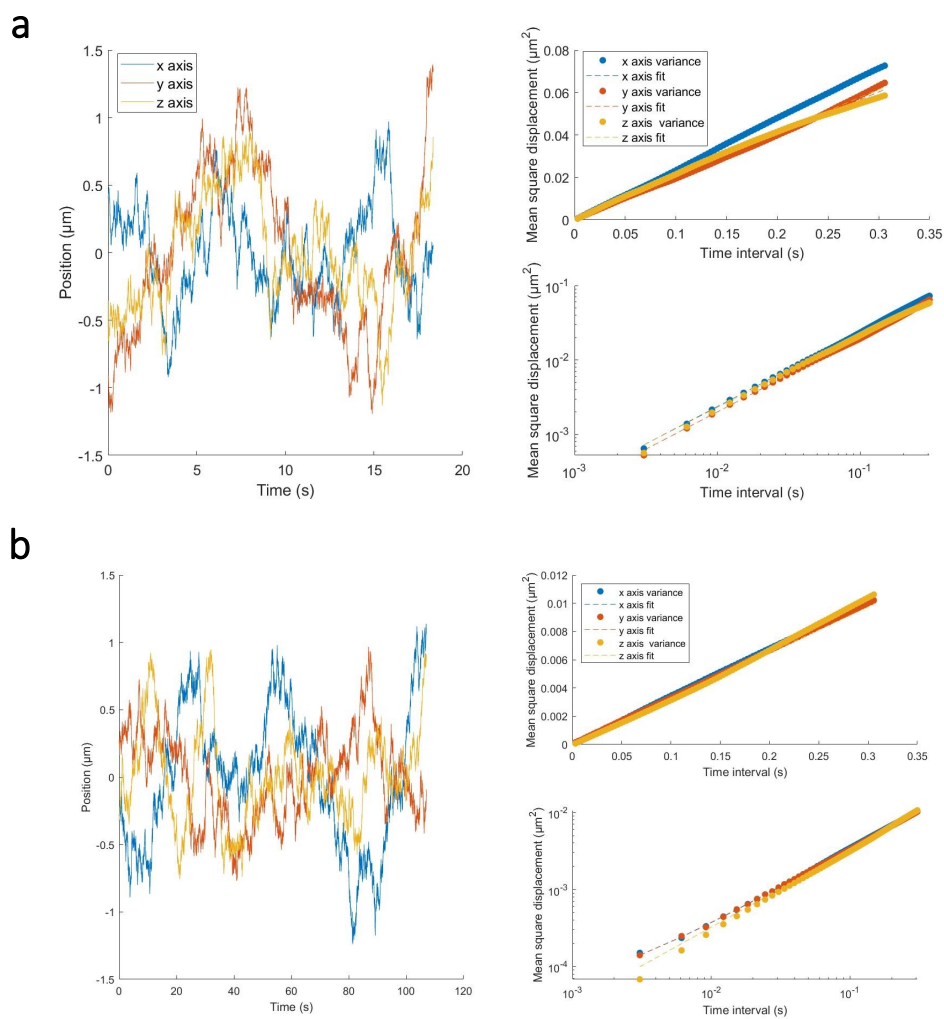


Figure 7.6: mean square displacement analysis example Examples of the fits produced during MSD analysis for a highly scattering material, polystyrene, shown in **a**), and an SUV (**b**). The tracks of the particle position as measured in the x,y and z are shown in the left panel with the mean square displacement shown against the time interval in the right. The fits used to calculate the diffusion coefficient from these plots are shown as the dashed lines.

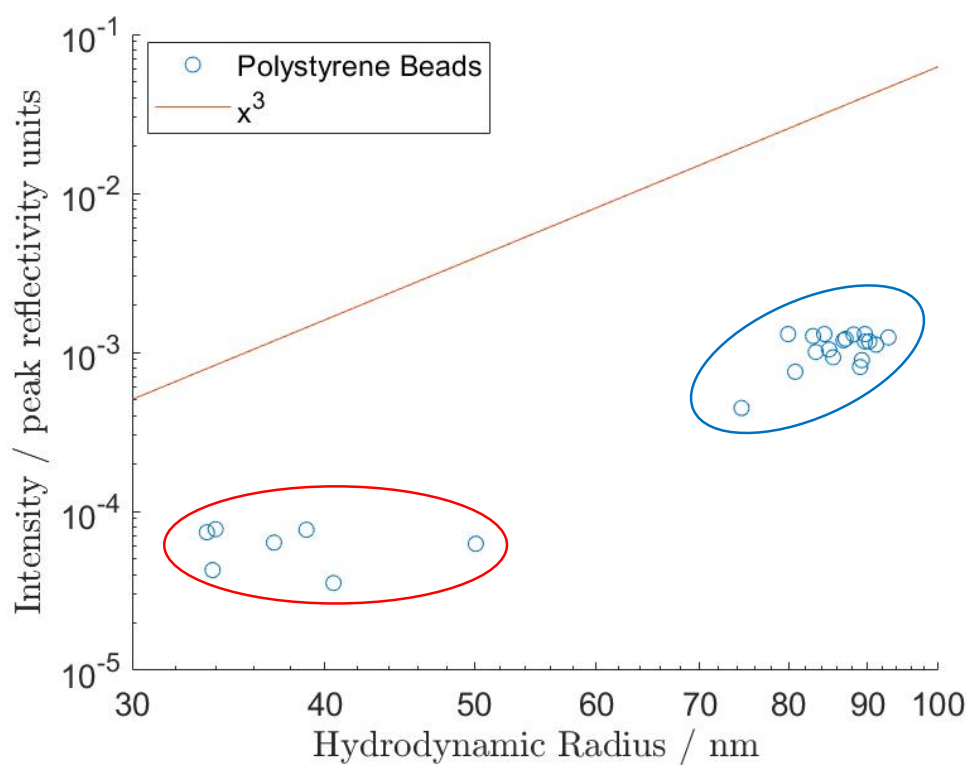


Figure 7.7: Measured hydrodynamic radii of controls The relationship between scattering intensity and hydrodynamic radius for 100 nm (Red) and 200 nm (Blue) of polystyrene beads as well as a plot displaying an $f(x) = x^3$ relationship demonstrating the expected gradient that we measured.

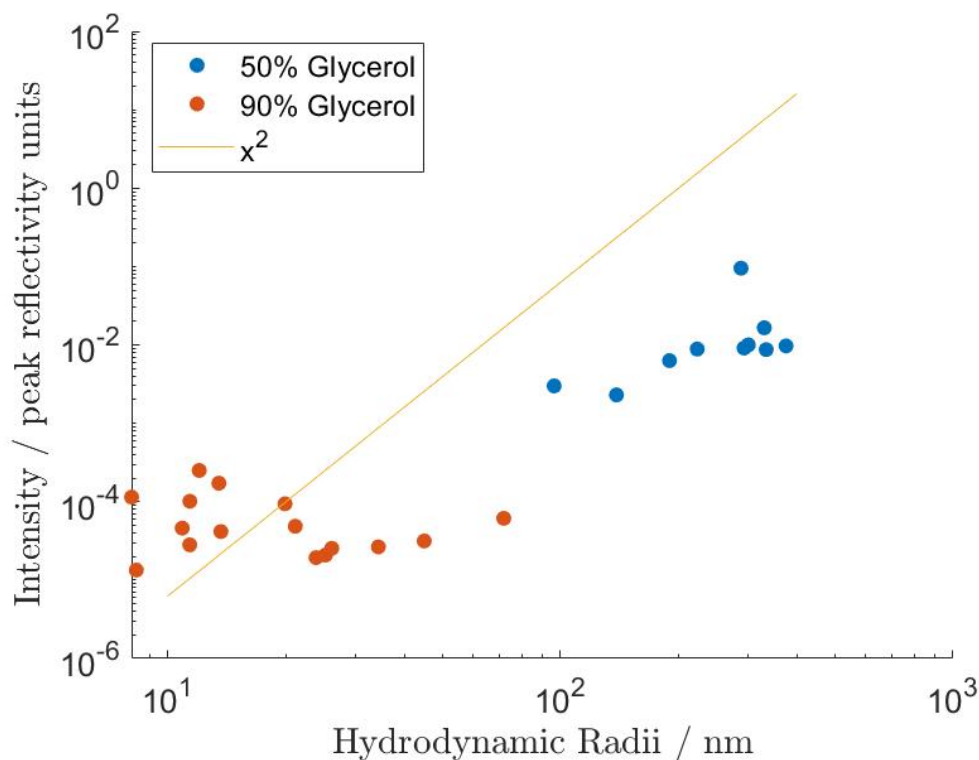


Figure 7.8: Measured hydrodynamic radii of SUVs A scatter plot showing the relationship between hydrodynamic radii and intensity for the tracked lipid nanoparticles. The plot contains data for particles measured in both 50% and 90% Glycerol allowing tracking of a wide range of hydrodynamic radii. The plot shows a gradient representing $f(x) \propto x^2$ to allow comparison to the expected relationship.

movement.

Off the back of the controls we evaluated the potential error arising from inaccuracies in viscosity, however as the 50% glycerol stock was generated by diluting the 90% stock down we could assume that the error in glycerol concentration was proportional and therefore we could compare between the two datasets. We analysed the SUVs with viscosity and refractive indices corresponding to a 90% glycerol stock and a 50% glycerol stock. The viscosity for 50% glycerol was 0.008368 Ns/m^2 . To account for viscosity a simple substitution of the viscosity term in the hydrodynamic radii calculation was required, however different media concentrations had different ϵ_m meaning the polarisability factor was altered.

The results shown in Fig. 7.8 demonstrate the particle radii we were able to measure with 50% and 90% glycerol solutions. A clear relationship between the intensity and the hydrodynamic radii was observed in line with the x^4 relationship expected, if we are to omit the particles for which the radii is low ($<12 \text{ nm}$). Therefore, classified these as small vesicles with an internal volume. The lipid particles with a radius smaller than 12 nm looked to have a different relationship between intensity and hydrodynamic radii. The most likely cause of this was a different ratio between internal volume and bilayers, for example micelles or multilamellar. They could have also been a contamination in the sample. Further work would need to be undertaken to determine the exact morphology of these particles, however we demonstrated the

ability to accurately track lipid nanoparticles in x, y and z showing a high agreement in diffusion coefficients for all three. We also demonstrated an intensity correlation as expected with hydrodynamic radii.

7.5 Discussion

The results discussed in this chapter demonstrate the capabilities of iGOR to track particles effectively for a changing axial position as well as lateral x and y motion. To demonstrate this tracking we showed agreement between the measured diffusion coefficients of all axes and for particles with different scattering cross-sections. iGOR had previously been used for the tracking of gold nanoparticles which are highly scattering particles. In this work, we demonstrated the ability to track organic nanoparticles in the form of SUVs. For these, we also demonstrated a high agreement for tracking in all axes, which gave us confidence in our ability to track nanoparticles despite the hydrodynamic radii not being as expected. During analysis we visually monitored the ability of the software to track and ascertain the correct particle position which provided additional confidence that our error was coming from factors external to our tracking software. For this, I have discussed the most likely sources of error leading to this; either inaccuracies in glycerol concentration or the selection of larger particles. In order to accurately determine the hydrodynamic radii for these particles repeats would be undertaken where the glycerol stocks were measured during preparation to minimise pipetting error associated with this step, alongside a larger number of particles measured to reduce the impact of sampling bias.

To better understand the results obtained from the SUV analysis in terms of the correlation with intensity, simulations could be undertaken to predict the intensity of specified morphologies of a set hydrodynamic radius. For this, additional morphologies to consider would be micelles, multilamellarity to differing degrees and vesicle in vesicle structures, predominately this would be to determine the ratio of different refractive indices within the vesicle. This simulation work combined with the pipeline discussed above provide a strong method for quantifying and classifying lipid nanoparticles and SUVs. This could prove useful in work understanding exosomes which are an important but poorly understood structure in biology.[258] The ability to track lipid nanoparticles in 3D is widely applicable within the biological field as some signalling requires a portion of the membrane as vesicles, for which tracking would be a useful tool especially with a temporal frequency of 3 ms.[268] We have also measured a thin section of an adhered HeLa cell using iGOR, the ability to measure both a thin section of a cell and pick up a secondary signal with a much smaller cross-section provides the potential for the identification of docking events and measurements of residence times.

In summary we have demonstrated the ability of iGOR to accurately track in 3D across an axial range of 4 μm , up to 70 μm away from a surface with a temporal resolution of 3 ms. This was demonstrated for particles with a refractive index close to the medium they were measured in. Combined this makes a powerful tool for nanoparticle tracking due to the increased sensitivity and tracking range when not using external labelling molecules. The ability to track small organic molecules, including micelles, away from a surface provides a step change from mass photometry and iSCAT methods and scope for biological studies.[135, 143]

Chapter 8

Conclusion and outlook

In this thesis I have discussed work to further the understanding of lipid membrane dynamics predominately using label free approaches. This included generating a model membrane suitable for the proposed imaging and characterising them using a range of techniques. Whilst this allowed us to have a well rounded view as to how our models were behaving it also highlighted the step change shown with each method.

For development of the preparation protocol we utilised epifluorescence to characterise the morphology of the lipid bilayer, this was primarily due to ease as we could easily incorporate fluorophore into the membrane at a low proportion meaning its impact on behaviour was negligible. The fluorescently labelled lipid was shown to be sufficiently photostable allowing for electroformation to be observed directly over the course of at least two hours. This was sufficient as the characterisation we were undertaking using epifluorescence was qualitative except for diameter measurements. Using this technique we were able to optimise our protocol to produce clean vesicles of sufficient size. We could also identify phase separation behaviour in our binary composition as the fluorophore was more likely to partition into the POPC lipid as the membrane separates.

We showed that we could reliably generate unilamellar vesicles with diameters in excess of $30\ \mu\text{m}$ with defect free membranes, in a clear solution. We showed comparability with non charged lipids and electroformation solutions, which in our case included DC₁₅PC, DOPC, POPC only and POPC:POPE lipid compositions and 5(6)-Carboxyfluorescein. These showed the versatility of our protocol making it applicable in a wide range of model systems for future experiments, to allow characterisation of different lipid compositions and protein additions into the membranes using iGOR. We developed a pipeline, through which characterisation of protein insertion is, in theory, possible. Once the interference source has been identified we will be in a position to carry out more complex lipid studies as well as starting to measure thickness changes in response to protein insertion, namely App6Aa1.

In this thesis I showed the work in the initial modification of the DIB system developed from the Castell lab. This was developed as a collaboration with an MPhil student, where we have recently produced a stable bilayer exhibiting a smooth surface in a device printed with specifications suitable for iGOR imaging. This provides an additional method for the measurement of bilayer systems in iGOR providing a larger flat surface and a greater control over the lipid bilayer whilst imaging.

We have shown two suitable model membrane systems that showed compatibility

with a range of lipid compositions making them versatile for the future membrane characterisation and insertion studies using iGOR.

Further characterisation was carried out using qDIC which allowed us to probe the optical thickness of both the bilayer and internal volume of vesicles. To improve the fitting of this data it was decided simulations would be carried out to ascertain a more accurate profile deconvolution.

After corrections and the calculation of the lamellarity and sucrose concentrations it could be determined that the majority of the vesicles were unilamellar proving that our preparation protocols are working as expected. They also contained sucrose concentrations up to 0.2 mM. There were still errors in this data as the lamellarities were not all integers and no vesicles were reported as having no sucrose concentration gradient which would both be expected results. However, when we calculated the ratio between the inner and outer ratio and compare the datasets containing different nominal concentration gradients we observed a difference, demonstrating the sensitivity of the technique to identify the difference between 0.2 and 0 mM sucrose.

To improve the simulations so they better represent the experimental system we plan to incorporate a birefringence effect. To do this, at each voxel the field propagation is related to both the in plane and out of plane refractive index. The calculated value can be used to simulate the effect birefringence has on the membrane. Once this has been simulated the profiles can be better quantified, which could provide additional information as to the composition of the membrane by the different lipid species causing birefringence to differing degrees. Here we provide a basis for the measurement of birefringence and lipid ordering in the method.

The bulk of the projected work involves the use of our iGOR technique. In this work we have shown that we have a sub-nanometer sensitivity when measuring both thickness and height of a suspended lipid bilayer. Coupled with the temporal resolution of 3 ms and a spatial resolution of 0.168 μm we demonstrate a sensitive method label-free able to quantify dynamics present in the membrane.

We have demonstrated a novel technique that can measure the amplitude and phase to the resolution described above in a wide-field conformation live in two polarisations, this allows the measurement of any chiral effects alongside the thickness and height of a suspended membrane. This allows us to access the dynamics of a suspended membrane not dampened by a surface as it would be in methods such as iSCAT. To improve the phase unwrapping, a polynomial fit was made of the underside of top surface of the vesicle allowing correction of π jumps back to the fitted plane of the membrane, in this way we have generated a method to correct phase jumps. This method provided additional information regarding the vesicle as we have demonstrated with the radius calculations at 327 Hz.

In this work we discuss our results measuring POPC:POPE and DC₁₅PC membranes, we showed that we were able to analyse vesicles with high internal pressure to determine the bilayer thickness and assign the lamellarity of the vesicles. Within these surfaces we identified regions of the membrane that were thicker, termed 'domains'. Through time trace and power spectral analysis we identified the fluctuations associated with the membrane thickness. A wave propagating across the surface altering thickness was identified using power spectral analysis. We also observed the changes across the loss of internal pressure with time where the fluctuations of both height and thickness increased in magnitude. In terms of the height, we accurately traced a stable vesicle with the bending of the top surface lining up with expected

values, however, we were not able to identify any propagating waves in the power spectral analysis and continued work needs to be undertaken to effectively unwrap the phase to allow accurate analysis of height fluctuations to be undertaken.

We also demonstrated our ability to identify a loss of membrane fluctuations of a DC₁₅PC vesicle upon cooling from 40 °C to 20 °C hence a phase transition from liquid disordered to gel phase. This can be expanded to other lipid species experiencing phase transitions. As identified in a DC₁₅PC vesicle measured in the gel phase, we could identify facets which we can analyse in detail looking at the light reflection polarisation state, and compare with plane orientation observed in the phase. By comparing the angle of the phase to the cross-polarised signal we can determine if in-plane birefringence is present.

By expanding this dataset and extending to more lipid compositions we can determine the membrane properties associated with the fluctuations measured, such as the bending modulus and the identification of waves propagating across the membrane surface. We have presented a pipeline for the measurement and analysis to uncover the thickness and height fluctuations associated with a suspended membrane. This can be applied to different lipid compositions, such as a binary composition likely to phase separate, alongside the addition of App6Aa1 protein to observe pore formation and the expected dynamics. This can either be done within a slide or a funnel to allow addition of protein during imaging.

iGOR also has been shown to have applications in particle tracking where, in this work, I presented our tracking of organic nanoparticles. The ability of this technique to track nanoparticles in three dimensions with a temporal resolution of 3 ms, showing high agreement of diffusion coefficients with each axes, at large axial distances (in excess of 40 µm) provides a step change in label-free tracking methods.

When using this to measure SUVs acting as our model membrane we observed the majority of the particles following the expected relationship between intensity and hydrodynamic radii, for a vesicle with an internal volume. However some particles did not follow this relationship. These particles had a small hydrodynamic radii, which could have been due to a micellar conformation, or containing multiple bilayers. Further investigation into this relationship including simulations could provide a basis for the determination of the morphology of small lipid nanoparticles. This has wider applications into exosome analysis which is an important area in signalling biology as well as viral diagnostics and membrane residence times.[256, 258, 259]

In conclusion, we have presented the pipelines developed for the production and measurement of model membranes using label free techniques to a high sensitivity and resolution with scope for a wide range of membrane studies.

Bibliography

- [1] Marc Eeman and Magali Deleu. From biological membranes to biomimetic model membranes. *Biotechnology, Agronomy, Society and Environment*, 14(4):720-736, 2010.
- [2] E. Gorter and F. Grendel. ON BIMOLECULAR LAYERS OF LIPOIDS ON THE CHROMOCYTES OF THE BLOOD. *Journal of Experimental Medicine*, 41(4):439-443, April 1925.
- [3] James Frederic Danielli and Hugh Davson. A contribution to the theory of permeability of thin films. *Journal of Cellular and Comparative Physiology*, 5(4):495-508, February 1935.
- [4] Ankita Roy. Membrane Preparation and Solubilization. In *Methods in Enzymology*, volume 557, pages 45-56. Elsevier, 2015.
- [5] Daniel Huster, Sudipta Maiti, and Andreas Herrmann. Phospholipid Membranes as Chemically and Functionally Tunable Materials. *Advanced Materials*, 36(23):2312898, June 2024.
- [6] Bruce Alberts, Alexander Johnson, Julian Lewis, and al et. Membrane Proteins. In *Molecular Biology of the Cell*. Garland Science, New York, 4 edition, 2002.
- [7] Zoe Cournia, Toby W. Allen, Ioan Andricioaei, Bruno Antonny, Daniel Baum, Grace Brannigan, Nicolae-Viorel Buchete, Jason T. Deckman, Lucie Delemotte, Coral Del Val, Ran Friedman, Paraskevi Gkeka, Hans-Christian Hege, Jérôme Hémin, Marina A. Kasimova, Antonios Kolocouris, Michael L. Klein, Syma Khalid, M. Joanne Lemieux, Norbert Lindow, Mahua Roy, Jana Selent, Mounir Tarek, Florentina Tofoleanu, Stefano Vanni, Sinisa Urban, David J. Wales, Jeremy C. Smith, and Ana-Nicoleta Bondar. Membrane Protein Structure, Function, and Dynamics: a Perspective from Experiments and Theory. *The Journal of Membrane Biology*, 248(4):611-640, August 2015.
- [8] Erick J. Dufourc. Sterols and membrane dynamics. *Journal of Chemical Biology*, 1(1-4):63-77, November 2008.
- [9] Lisa M. Kawakami, Bo Kyeong Yoon, Joshua A. Jackman, Wolfgang Knoll, Paul S. Weiss, and Nam-Joon Cho. Understanding How Sterols Regulate Membrane Remodeling in Supported Lipid Bilayers. *Langmuir*, 33(51):14756-14765, December 2017.
- [10] Overton E. Ueber die allgemeinen osmotischen Eigenschaften der Zelle. *Vierteljahrschr Naturf Ges Zurich*. 1899;44:88-135.

-
- [11] Carl-Henrik Heldin, Benson Lu, Ron Evans, and J. Silvio Gutkind. Signals and Receptors. *Cold Spring Harbor Perspectives in Biology*, 8(4):a005900, April 2016.
- [12] Patrick Müller and Alexander F. Schier. Extracellular Movement of Signaling Molecules. *Developmental Cell*, 21(1):145–158, July 2011.
- [13] Ken Jacobson, Ping Liu, and B. Christoffer Lagerholm. The Lateral Organization and Mobility of Plasma Membrane Components. *Cell*, 177(4):806–819, May 2019.
- [14] Masoud Jelokhani-Niaraki. Membrane Proteins: Structure, Function and Motion. *International Journal of Molecular Sciences*, 24(1):468, December 2022.
- [15] Gerrit van Meer and Anton I. P. M. de Kroon. Lipid map of the mammalian cell. *Journal of Cell Science*, 124(1):5–8, January 2011.
- [16] Gerrit van Meer and Quirine Lisman. Sphingolipid Transport: Rafts and Translocators. *Journal of Biological Chemistry*, 277(29):25855–25858, July 2002.
- [17] Alex H. De Vries, Alan E. Mark, and Siewert J. Marrink. The Binary Mixing Behavior of Phospholipids in a Bilayer: A Molecular Dynamics Study. *The Journal of Physical Chemistry B*, 108(7):2454–2463, February 2004.
- [18] W. Dowhan. MOLECULAR BASIS FOR MEMBRANE PHOSPHOLIPID DIVERSITY: Why Are There So Many Lipids? *Annual Review of Biochemistry*, 66(1):199–232, June 1997.
- [19] Philip L. Yeagle. Phospholipid headgroup behavior in biological assemblies. *Accounts of Chemical Research*, 11(9):321–327, September 1978.
- [20] Dowhan W, Bogdanov M. In: Biochemistry of Lipids, Lipoproteins and Membranes. Vance DE, Vance JE, editors. Vol. 36. Elsevier; Amsterdam: 2002. pp. 1-35.
- [21] Derek Marsh. Lateral Pressure Profile, Spontaneous Curvature Frustration, and the Incorporation and Conformation of Proteins in Membranes. *Biophysical Journal*, 93(11):3884–3899, December 2007.
- [22] Gerrit Van Meer, Dennis R. Voelker, and Gerald W. Feigenson. Membrane lipids: where they are and how they behave. *Nature Reviews Molecular Cell Biology*, 9(2):112–124, February 2008.
- [23] Félix M. Goñi and Alicia Alonso. Biophysics of sphingolipids I. Membrane properties of sphingosine, ceramides and other simple sphingolipids. *Biochimica et Biophysica Acta (BBA) - Biomembranes*, 1758(12):1902–1921, December 2006.
- [24] Félix M. Goñi and Alicia Alonso. Effects of ceramide and other simple sphingolipids on membrane lateral structure. *Biochimica et Biophysica Acta (BBA) - Biomembranes*, 1788(1):169–177, January 2009.
-

- [25] Helgi I. Ingólfsson, Manuel N. Melo, Floris J. van Eerden, Clément Arnarez, Cesar A. Lopez, Tsjerk A. Wassenaar, Xavier Periole, Alex H. de Vries, D. Peter Tieleman, and Siewert J. Marrink. Lipid Organization of the Plasma Membrane. *Journal of the American Chemical Society*, 136(41):14554–14559, October 2014.
- [26] Thomas Harder, Peter Scheiffele, Paul Verkade, and Kai Simons. Lipid Domain Structure of the Plasma Membrane Revealed by Patching of Membrane Components. *The Journal of Cell Biology*, 141(4):929–942, May 1998.
- [27] S. J. Singer and G. L. Nicolson. The Fluid Mosaic Model of the Structure of Cell Membranes. *Science*, 175(4023):720–731, February 1972.
- [28] Md Rejwan Ali, Kwan Hon Cheng, and Juyang Huang. Ceramide Drives Cholesterol Out of the Ordered Lipid Bilayer Phase into the Crystal Phase in 1-Palmitoyl-2-oleoyl- *sn* -glycero-3-phosphocholine/Cholesterol/Ceramide Ternary Mixtures. *Biochemistry*, 45(41):12629–12638, October 2006.
- [29] Jonas Henriksen, Amy C. Rowat, and John H. Ipsen. Vesicle fluctuation analysis of the effects of sterols on membrane bending rigidity. *European Biophysics Journal*, 33(8):732–741, December 2004.
- [30] Juyang Huang and Gerald W. Feigenson. A Microscopic Interaction Model of Maximum Solubility of Cholesterol in Lipid Bilayers. *Biophysical Journal*, 76(4):2142–2157, April 1999.
- [31] Ilya Levental and Ed Lyman. Regulation of membrane protein structure and function by their lipid nano-environment. *Nature Reviews Molecular Cell Biology*, 24(2):107–122, February 2023.
- [32] Yosuke Senju and Shiro Suetsugu. Membrane Proteins: Function, Structure, and Dynamics. *Membranes*, 13(12):904, December 2023.
- [33] *Alberts B, Johnson A, Lewis J, et al. Molecular Biology of the Cell. 4th edition. New York: Garland Science; 2002. Membrane Proteins. Available from: <https://www.ncbi.nlm.nih.gov/books/NBK26878/>.*
- [34] Aina W. Ravna, Georg Sager, Svein G. Dahl, and Ingebrigt Sylte. Membrane Transporters: Structure, Function and Targets for Drug Design. In Susan Napier and Matilda Bingham, editors, *Transporters as Targets for Drugs*, volume 4, pages 15–51. Springer Berlin Heidelberg, Berlin, Heidelberg, 2008.
- [35] Minttu T. De Marothy and Arne Elofsson. Marginally hydrophobic transmembrane α -helices shaping membrane protein folding. *Protein Science*, 24(7):1057–1074, July 2015.
- [36] Gerard Duart, Ricardo Graña-Montes, Noelia Pastor-Cantizano, and Ismael Mingarro. Experimental and computational approaches for membrane protein insertion and topology determination. *Methods*, 226:102–119, June 2024.
- [37] Andrei L Lomize, Irina D Pogozheva, Mikhail A Lomize, and Henry I Mosberg. The role of hydrophobic interactions in positioning of peripheral proteins in membranes. *BMC Structural Biology*, 7(1):44, 2007.

-
- [38] Abhinav Nath, William M. Atkins, and Stephen G. Sligar. Applications of Phospholipid Bilayer Nanodiscs in the Study of Membranes and Membrane Proteins. *Biochemistry*, 46(8):2059–2069, February 2007.
- [39] Kira L. F. Hilton, Chandni Manwani, Jessica E. Boles, Lisa J. White, Sena Ozturk, Michelle D. Garrett, and Jennifer R. Hiscock. The phospholipid membrane compositions of bacterial cells, cancer cell lines and biological samples from cancer patients. *Chemical Science*, 12(40):13273–13282, 2021.
- [40] Vitaly Kocherbitov. Driving Forces of Phase Transitions in Surfactant and Lipid Systems. *The Journal of Physical Chemistry B*, 109(13):6430–6435, April 2005.
- [41] Lubin Chen, Michael L. Johnson, and Rodney L. Biltonen. A Macroscopic Description of Lipid Bilayer Phase Transitions of Mixed-Chain Phosphatidylcholines: Chain-Length and Chain-Asymmetry Dependence. *Biophysical Journal*, 80(1):254–270, January 2001.
- [42] Andrea Alessandrini and Paolo Facci. Phase transitions in supported lipid bilayers studied by AFM. *Soft Matter*, 10(37):7145–7164, 2014.
- [43] Joost C.M. Holthuis and Anant K. Menon. Lipid landscapes and pipelines in membrane homeostasis. *Nature*, 510(7503):48–57, June 2014.
- [44] Rumiana Koynova and Martin Caffrey. Phases and phase transitions of the phosphatidylcholines. *Biochimica et Biophysica Acta (BBA) - Reviews on Biomembranes*, 1376(1):91–145, June 1998.
- [45] Yi Liu, Zhiying Yao, Guiwei Lian, and Peiguo Yang. Biomolecular phase separation in stress granule assembly and virus infection. *Acta Biochimica et Biophysica Sinica*, 55(7):1099–1118, July 2023.
- [46] Denis L. J. Lafontaine, Joshua A. Riback, RÅ¼meyza Bascetin, and Clifford P. Brangwynne. The nucleolus as a multiphase liquid condensate. *Nature Reviews Molecular Cell Biology*, 22(3):165–182, March 2021.
- [47] Qian Xiao, Ceara K. McAtee, and Xiaolei Su. Phase separation in immune signalling. *Nature Reviews Immunology*, 22(3):188–199, March 2022.
- [48] Yong-Hao Ma, Yan Zhu, Hui Wu, Yao He, Qiang Zhang, Qiuling Huang, Zhimin Wang, Hang Xing, Liping Qiu, and Weihong Tan. Domain-Targeted Membrane Partitioning of Specific Proteins with DNA Nanodevices. *Journal of the American Chemical Society*, 146(11):7640–7648, March 2024.
- [49] Xubo Lin, Alemayehu A. Gorfe, and Ilya Levental. Protein Partitioning into Ordered Membrane Domains: Insights from Simulations. *Biophysical Journal*, 114(8):1936–1944, April 2018.
- [50] Moritz Hoferer, Silvia Bonfanti, Alessandro Taloni, Caterina A. M. La Porta, and Stefano Zapperi. Protein-driven lipid domain nucleation in biological membranes. *Physical Review E*, 100(4):042410, October 2019.
- [51] Bernd Henning Stumpf, Piotr Nowakowski, Christian Eggeling, Anna Maciołek, and Ana-Sunčana Smith. Protein induced lipid demixing in homogeneous membranes. *Physical Review Research*, 3(4):L042013, October 2021.
-

- [52] Sylvio May, Daniel Harries, and Avinoam Ben-Shaul. Lipid Demixing and Protein-Protein Interactions in the Adsorption of Charged Proteins on Mixed Membranes. *Biophysical Journal*, 79(4):1747–1760, October 2000.
- [53] Benoit Sorre, Andrew Callan-Jones, Jean-Baptiste Manneville, Pierre Nassoy, Jean-François Joanny, Jacques Prost, Bruno Goud, and Patricia Bassereau. Curvature-driven lipid sorting needs proximity to a demixing point and is aided by proteins. *Proceedings of the National Academy of Sciences*, 106(14):5622–5626, April 2009.
- [54] A. Callan-Jones, B. Sorre, and P. Bassereau. Curvature-Driven Lipid Sorting in Biomembranes. *Cold Spring Harbor Perspectives in Biology*, 3(2):a004648–a004648, February 2011.
- [55] Christine Salaün, Declan J. James, and Luke H. Chamberlain. Lipid Rafts and the Regulation of Exocytosis. *Traffic*, 5(4):255–264, April 2004.
- [56] Hsueh-Cheng Chiang, Wonchul Shin, Wei-Dong Zhao, Edaeni Hamid, Jiansong Sheng, Maryna Baydyuk, Peter J. Wen, Albert Jin, Fanny Mombousse, and Ling-Gang Wu. Post-fusion structural changes and their roles in exocytosis and endocytosis of dense-core vesicles. *Nature Communications*, 5(1):3356, February 2014.
- [57] Yan G. Zhao and Hong Zhang. Phase Separation in Membrane Biology: The Interplay between Membrane-Bound Organelles and Membraneless Condensates. *Developmental Cell*, 55(1):30–44, October 2020.
- [58] John J. Williamson and Peter D. Olmsted. Effects of Passive Phospholipid Flip-Flop and Asymmetric External Fields on Bilayer Phase Equilibria. *Biophysical Journal*, 115(10):1956–1965, November 2018.
- [59] Philippe F. Devaux, Andreas Herrmann, Nina Ohlwein, and Michael M. Kozlov. How lipid flippases can modulate membrane structure. *Biochimica et Biophysica Acta (BBA) - Biomembranes*, 1778(7-8):1591–1600, July 2008.
- [60] Markus S. Miettinen and Reinhard Lipowsky. Bilayer Membranes with Frequent Flip-Flops Have Tensionless Leaflets. *Nano Letters*, 19(8):5011–5016, August 2019.
- [61] Diego Krapf. Compartmentalization of the plasma membrane. *Current Opinion in Cell Biology*, 53:15–21, August 2018.
- [62] Francesca Rizzelli, Maria Grazia Malabarba, Sara Sigismund, and Marina Mapelli. The crosstalk between microtubules, actin and membranes shapes cell division. *Open Biology*, 10(3):190314, March 2020.
- [63] Max Urbanczyk, Shannon L. Layland, and Katja Schenke-Layland. The role of extracellular matrix in biomechanics and its impact on bioengineering of cells and 3D tissues. *Matrix Biology*, 85-86:1–14, January 2020.
- [64] Dima Bolmatov, William T. McClintic, Graham Taylor, Christopher B. Stanley, Changwoo Do, C. Patrick Collier, Zoya Leonenko, Maxim O. Lavrentovich, and John Katsaras. Deciphering Melatonin-Stabilized Phase Separation in Phospholipid Bilayers. *Langmuir*, 35(37):12236–12245, September 2019.

-
- [65] M J Karnovsky, A M Kleinfeld, R L Hoover, and R D Klausner. The concept of lipid domains in membranes. *Journal of Cell Biology*, 94(1):1–6, July 1982.
- [66] Pamina M. Winkler, Raju Regmi, Valentin Flauraud, Jürgen Brugger, Hervé Rigneault, Jérôme Wenger, and María F. García-Parajo. Transient Nanoscopic Phase Separation in Biological Lipid Membranes Resolved by Planar Plasmonic Antennas. *ACS Nano*, 11(7):7241–7250, July 2017.
- [67] Ivan V. Polozov and Klaus Gawrisch. Domains in Binary SOPC/POPE Lipid Mixtures Studied by Pulsed Field Gradient 1H MAS NMR. *Biophysical Journal*, 87(3):1741–1751, September 2004.
- [68] F. A. Heberle and G. W. Feigenson. Phase Separation in Lipid Membranes. *Cold Spring Harbor Perspectives in Biology*, 3(4):a004630–a004630, April 2011.
- [69] P. J. Quinn. Principles of membrane stability and phase behavior under extreme conditions. *Journal of Bioenergetics and Biomembranes*, 21(1):3–19, February 1989.
- [70] Thomas Heimburg. Phase Transitions in Biological Membranes. In Costas Demetzos and Natassa Pippa, editors, *Thermodynamics and Biophysics of Biomedical Nanosystems*, pages 39–61. Springer Singapore, Singapore, 2019. Series Title: Series in BioEngineering.
- [71] Prabuddha Sengupta, Barbara Baird, and David Holowka. Lipid rafts, fluid/fluid phase separation, and their relevance to plasma membrane structure and function. *Seminars in Cell & Developmental Biology*, 18(5):583–590, October 2007.
- [72] Deborah A. Brown. Lipid Rafts, Detergent-Resistant Membranes, and Raft Targeting Signals. *Physiology*, 21(6):430–439, December 2006.
- [73] Hidehiko Shogomori, Adam T. Hammond, Anne G. Ostermeyer-Fay, Daniel J. Barr, Gerald W. Feigenson, Erwin London, and Deborah A. Brown. Palmitoylation and Intracellular Domain Interactions Both Contribute to Raft Targeting of Linker for Activation of T Cells. *Journal of Biological Chemistry*, 280(19):18931–18942, May 2005.
- [74] Richard M. Epanand. Cholesterol and the interaction of proteins with membrane domains. *Progress in Lipid Research*, 45(4):279–294, July 2006.
- [75] Erwin London and Gerald W. Feigenson. Fluorescence quenching in model membranes. 2. Determination of the local lipid environment of the calcium adenosinetriphosphatase from sarcoplasmic reticulum. *Biochemistry*, 20(7):1939–1948, March 1981.
- [76] Ken Jacobson, Ole G. Mouritsen, and Richard G. W. Anderson. Lipid rafts: at a crossroad between cell biology and physics. *Nature Cell Biology*, 9(1):7–14, January 2007.
- [77] Olaf S. Andersen and Roger E. Koeppe. Bilayer Thickness and Membrane Protein Function: An Energetic Perspective. *Annual Review of Biophysics and Biomolecular Structure*, 36(1):107–130, June 2007.
-

- [78] Frederick A. Heberle, Robin S. Petruzielo, Jianjun Pan, Paul Drazba, Norbert Kučerka, Robert F. Standaert, Gerald W. Feigenson, and John Katsaras. Bilayer Thickness Mismatch Controls Domain Size in Model Membranes. *Journal of the American Chemical Society*, 135(18):6853–6859, May 2013.
- [79] Dima Bolmatov, Mikhail Zhernenkov, Dmitry Zav’yalov, Stanislav Stoupin, Alessandro Cunsolo, and Yong Q. Cai. Thermally triggered phononic gaps in liquids at THz scale. *Scientific Reports*, 6(1):19469, May 2016.
- [80] Dima Bolmatov, Yong Q. Cai, Dmitry Zav’yalov, and Mikhail Zhernenkov. Crossover from picosecond collective to single particle dynamics defines the mechanism of lateral lipid diffusion. *Biochimica et Biophysica Acta (BBA) - Biomembranes*, 1860(11):2446–2455, November 2018.
- [81] Dima Bolmatov, Dmitry Zav’yalov, Mikhail Zhernenkov, Edvard T. Musaev, and Yong Q. Cai. Unified phonon-based approach to the thermodynamics of solid, liquid and gas states. *Annals of Physics*, 363:221–242, December 2015.
- [82] Mikhail Zhernenkov, Dima Bolmatov, Dmitry Soloviov, Kirill Zhernenkov, Boris P. Toperverg, Alessandro Cunsolo, Alexey Bosak, and Yong Q. Cai. Revealing the mechanism of passive transport in lipid bilayers via phonon-mediated nanometre-scale density fluctuations. *Nature Communications*, 7(1):11575, September 2016.
- [83] Arikta Biswas, Amal Alex, and Bidisha Sinha. Mapping Cell Membrane Fluctuations Reveals Their Active Regulation and Transient Heterogeneities. *Biophysical Journal*, 113(8):1768–1781, October 2017.
- [84] C. Monzel, D. Schmidt, C. Kleusch, D. Kirchenbühler, U. Seifert, A-S Smith, K. Sengupta, and R. Merkel. Measuring fast stochastic displacements of biomembranes with dynamic optical displacement spectroscopy. *Nature Communications*, 6(1):8162, October 2015.
- [85] Susanne F. Fenz, Timo Bihl, Daniel Schmidt, Rudolf Merkel, Udo Seifert, Kheya Sengupta, and Ana-Sunčana Smith. Membrane fluctuations mediate lateral interaction between cadherin bonds. *Nature Physics*, 13(9):906–913, September 2017.
- [86] Grégory Giannone, Benjamin J Dubin-Thaler, Hans-Günther Döbereiner, Nelly Kieffer, Anne R Bresnick, and Michael P Sheetz. Periodic Lamellipodial Contractions Correlate with Rearward Actin Waves. *Cell*, 116(3):431–443, February 2004.
- [87] Hans-Günther Döbereiner, Benjamin J. Dubin-Thaler, Jake M. Hofman, Harry S. Xenias, Tasha N. Sims, Grégory Giannone, Michael L. Dustin, Chris H. Wiggins, and Michael P. Sheetz. Lateral Membrane Waves Constitute a Universal Dynamic Pattern of Motile Cells. *Physical Review Letters*, 97(3):038102, July 2006.
- [88] Chien-Hong Chen, Feng-Ching Tsai, Chun-Chieh Wang, and Chau-Hwang Lee. Three-Dimensional Characterization of Active Membrane Waves on Living Cells. *Physical Review Letters*, 103(23):238101, November 2009.

-
- [89] Valeria Conti Nibali, Giovanna D'Angelo, and Mounir Tarek. Molecular dynamics simulation of short-wavelength collective dynamics of phospholipid membranes. *Physical Review E*, 89(5):050301, May 2014.
- [90] Andrey Filippov, Greger Orädd, and Göran Lindblom. The Effect of Cholesterol on the Lateral Diffusion of Phospholipids in Oriented Bilayers. *Biophysical Journal*, 84(5):3079–3086, May 2003.
- [91] Erhard Bieberich. Sphingolipids and lipid rafts: Novel concepts and methods of analysis. *Chemistry and Physics of Lipids*, 216:114–131, November 2018.
- [92] Dima Bolmatov, Dmytro Soloviov, Mikhail Zhernenkov, Dmitry Zav'yalov, Eugene Mamontov, Alexey Suvorov, Yong Q. Cai, and John Katsaras. Molecular Picture of the Transient Nature of Lipid Rafts. *Langmuir*, 36(18):4887–4896, May 2020.
- [93] Itay Budin, Tristan de Rond, Yan Chen, Leanne Jade G. Chan, Christopher J. Petzold, and Jay D. Keasling. Viscous control of cellular respiration by membrane lipid composition. *Science*, 362(6419):1186–1189, December 2018.
- [94] Alex J. B. Kreutzberger, Ming Ji, Jesse Aaron, Ljubica Mihaljević, and Siniša Urban. Rhomboid distorts lipids to break the viscosity-imposed speed limit of membrane diffusion. *Science*, 363(6426):eaao0076, February 2019.
- [95] Irving Langmuir. THE CONSTITUTION AND FUNDAMENTAL PROPERTIES OF SOLIDS AND LIQUIDS. II. LIQUIDS. ¹. *Journal of the American Chemical Society*, 39(9):1848–1906, September 1917.
- [96] Walter Stoeckenius. Structure of the Plasma Membrane: An Electron-Microscope Study. *Circulation*, 26(5):1066–1069, November 1962.
- [97] D. Chapman and S. A. Penkett. Nuclear Magnetic Resonance Spectroscopic Studies of the Interaction of Phospholipids with Cholesterol. *Nature*, 211(5055):1304–1305, September 1966.
- [98] Sagar Kamble, Snehal Patil, Mandar Kulkarni, and Appala Venkata Ramana Murthy. Spectroscopic Ellipsometry of fluid and gel phase lipid bilayers in hydrated conditions. *Colloids and Surfaces B: Biointerfaces*, 176:55–61, April 2019.
- [99] Ruthven N.A.H. Lewis, Yuan-Peng Zhang, and Ronald N. McElhaney. Calorimetric and spectroscopic studies of the phase behavior and organization of lipid bilayer model membranes composed of binary mixtures of dimyristoylphosphatidylcholine and dimyristoylphosphatidylglycerol. *Biochimica et Biophysica Acta (BBA) - Biomembranes*, 1668(2):203–214, March 2005.
- [100] A.C. Croce and G. Bottiroli. Autofluorescence spectroscopy and imaging: a tool for biomedical research and diagnosis. *European Journal of Histochemistry*, December 2014.
- [101] Monica Monici. Cell and tissue autofluorescence research and diagnostic applications. In *Biotechnology Annual Review*, volume 11, pages 227–256. Elsevier, 2005.
-

- [102] Alexandra Moreno-García, Alejandra Kun, Olga Calero, Miguel Medina, and Miguel Calero. An Overview of the Role of Lipofuscin in Age-Related Neurodegeneration. *Frontiers in Neuroscience*, 12:464, July 2018.
- [103] Jacob M. Stillman, Francisco Mendes Lopes, Jing-Ping Lin, Kevin Hu, Daniel S. Reich, and Dorothy P. Schafer. Lipofuscin-like autofluorescence within microglia and its impact on studying microglial engulfment. *Nature Communications*, 14(1):7060, November 2023.
- [104] Ulf T Brunk and Alexei Terman. Lipofuscin: mechanisms of age-related accumulation and influence on cell function. 12 Guest Editor: Rajindar S. Sohal 2 This article is part of a series of reviews on "Oxidative Stress and Aging." The full list of papers may be found on the homepage of the journal. *Free Radical Biology and Medicine*, 33(5):611–619, September 2002.
- [105] Daniel Riani Gotardelo, Lilia Coronato Courrol, Maria Helena Bellini, Flávia Rodrigues De Oliveira Silva, and Carlos Roberto Jorge Soares. Porphyrins are increased in the faeces of patients with prostate cancer: a case-control study. *BMC Cancer*, 18(1):1090, December 2018.
- [106] Robert Bissonnette, Haishan Zeng, David I. McLean, William E. Schreiber, and Harvey Lui. Psoriatic Plaques Exhibit Red Autofluorescence that is Due to Protoporphyrin IX. *Journal of Investigative Dermatology*, 111(4):586–591, October 1998.
- [107] C.I. McPhee, G. Zorinants, W. Langbein, and P. Borri. Measuring the Lamellarity of Giant Lipid Vesicles with Differential Interference Contrast Microscopy. *Biophysical Journal*, 105(6):1414–1420, September 2013.
- [108] Alexey S. Ladokhin, Sajith Jayasinghe, and Stephen H. White. How to Measure and Analyze Tryptophan Fluorescence in Membranes Properly, and Why Bother? *Analytical Biochemistry*, 285(2):235–245, October 2000.
- [109] Bhaskar Banerjee, Timothy Renkoski, Logan R. Graves, Nathaniel S. Rial, Vassiliki Liana Tsikitis, Valentine Nfonsom, Judith Pugh, Piyush Tiwari, Hemant Gavini, and Urs Utzinger. Tryptophan autofluorescence imaging of neoplasms of the human colon. *Journal of Biomedical Optics*, 17(1):016003, 2012.
- [110] Yu Chen and Mary D. Barkley. Toward Understanding Tryptophan Fluorescence in Proteins. *Biochemistry*, 37(28):9976–9982, July 1998.
- [111] Yangyundou Wang, Jian Lin, Qiming Zhang, Xi Chen, Haitao Luan, and Min Gu. Fluorescence Nanoscopy in Neuroscience. *Engineering*, 16:29–38, September 2022.
- [112] Philip Gribbon and Timothy E. Hardingham. Macromolecular Diffusion of Biological Polymers Measured by Confocal Fluorescence Recovery after Photobleaching. *Biophysical Journal*, 75(2):1032–1039, August 1998.
- [113] M. Edidin, Y. Zagyansky, and T. J. Lardner. Measurement of Membrane Protein Lateral Diffusion in Single Cells. *Science*, 191(4226):466–468, February 1976.

-
- [114] D. Axelrod, D.E. Koppel, J. Schlessinger, E. Elson, and W.W. Webb. Mobility measurement by analysis of fluorescence photobleaching recovery kinetics. *Biophysical Journal*, 16(9):1055–1069, September 1976.
- [115] Oleg Krichevsky and Grégoire Bonnet. Fluorescence correlation spectroscopy: the technique and its applications. *Reports on Progress in Physics*, 65(2):251–297, February 2002.
- [116] Elliot L. Elson and Douglas Magde. Fluorescence correlation spectroscopy. I. Conceptual basis and theory. *Biopolymers*, 13(1):1–27, January 1974.
- [117] Helen Farrants, Yichun Shuai, William C. Lemon, Christian Monroy Hernandez, Deng Zhang, Shang Yang, Ronak Patel, Guanda Qiao, Michelle S. Frei, Sarah E. Plutkis, Jonathan B. Grimm, Timothy L. Hanson, Filip Tomaska, Glenn C. Turner, Carsen Stringer, Philipp J. Keller, Abraham G. Beyene, Yao Chen, Yajie Liang, Luke D. Lavis, and Eric R. Schreiter. A modular chemi-genetic calcium indicator for multiplexed in vivo functional imaging. *Nature Methods*, 21(10):1916–1925, October 2024.
- [118] Yan Zhang and Loren L. Looger. Fast and sensitive GCaMP calcium indicators for neuronal imaging. *The Journal of Physiology*, 602(8):1595–1604, April 2024.
- [119] Colin P O’Banion and Ryohei Yasuda. Fluorescent sensors for neuronal signaling. *Current Opinion in Neurobiology*, 63:31–41, August 2020.
- [120] Dilip Shrestha, Attila Jenei, P  ter Nagy, Gy  rgy Vereb, and J  nos Sz  ll  si. Understanding FRET as a Research Tool for Cellular Studies. *International Journal of Molecular Sciences*, 16(4):6718–6756, March 2015.
- [121] Ana J. Garc  a-S  ez and Petra Schwille. Single molecule techniques for the study of membrane proteins. *Applied Microbiology and Biotechnology*, 76(2):257–266, August 2007.
- [122] Bo Huang, Hazen Babcock, and Xiaowei Zhuang. Breaking the Diffraction Barrier: Super-Resolution Imaging of Cells. *Cell*, 143(7):1047–1058, December 2010.
- [123] Micka  l Lelek, Melina T. Gyparaki, Gerti Beliu, Florian Schueder, Juliette Griffi  , Suliana Manley, Ralf Jungmann, Markus Sauer, Melike Lakadamyali, and Christophe Zimmer. Single-molecule localization microscopy. *Nature Reviews Methods Primers*, 1(1):39, June 2021.
- [124] Giuseppe Vicidomini, Paolo Bianchini, and Alberto Diaspro. STED super-resolved microscopy. *Nature Methods*, 15(3):173–182, March 2018.
- [125] Fei Chen, Paul W. Tillberg, and Edward S. Boyden. Expansion microscopy. *Science*, 347(6221):543–548, January 2015.
- [126] Simon Sehayek, Yasser Gidi, Viktorija Glembockyte, Hugo B. Brand  o, Paul Fran  ois, Gonzalo Cosa, and Paul W. Wiseman. A High-Throughput Image Correlation Method for Rapid Analysis of Fluorophore Photoblinking and Photobleaching Rates. *ACS Nano*, 13(10):11955–11966, October 2019.
-

- [127] Kalina L Tosheva, Yue Yuan, Pedro Matos Pereira, Siân Culley, and Ricardo Henriques. Between life and death: strategies to reduce phototoxicity in super-resolution microscopy. *Journal of Physics D: Applied Physics*, 53(16):163001, April 2020.
- [128] Hong Wang, Guangmei Han, Heseng Tang, Ruilong Zhang, Zhengjie Liu, Yingqiang Sun, Bianhua Liu, Junlong Geng, and Zhongping Zhang. Synchronous Photoactivation-Imaging Fluorophores Break Limitations of Photobleaching and Phototoxicity in Live-cell Microscopy. *Analytical Chemistry*, 95(44):16243–16250, November 2023.
- [129] Susann Spindler, Jens Ehrig, Katharina König, Tristan Nowak, Marek Piliarik, Hannah E Stein, Richard W Taylor, Elisabeth Garanger, S bastien Lecommandoux, Isabel D Alves, and Vahid Sandoghdar. Visualization of lipids and proteins at high spatial and temporal resolution via interferometric scattering (iSCAT) microscopy. *Journal of Physics D: Applied Physics*, 49(27):274002, July 2016.
- [130] Volker Jacobsen, Patrick Stoller, Christian Brunner, Viola Vogel, and Vahid Sandoghdar. Interferometric optical detection and tracking of very small gold nanoparticles at a water-glass interface. *Optics Express*, 14(1):405, 2006.
- [131] J. Andrecka, Y. Takagi, K.J. Mickolajczyk, L.G. Lippert, J.R. Sellers, W.O. Hancock, Y.E. Goldman, and P. Kukura. Interferometric Scattering Microscopy for the Study of Molecular Motors. In *Methods in Enzymology*, volume 581, pages 517–539. Elsevier, 2016.
- [132] Anna D. Kashkanova, Martin Blessing, Marie Reischke, Jan-Ole Baur, Andreas S. Baur, Vahid Sandoghdar, and Jan Van Deun. Label-free discrimination of extracellular vesicles from large lipoproteins. *Journal of Extracellular Vesicles*, 12(8):12348, August 2023.
- [133] Mahdi Mazaheri, Kiarash Kasaian, David Albrecht, Jan Renger, Tobias Utikal, Cornelia Holler, and Vahid Sandoghdar. iSCAT microscopy and particle tracking with tailored spatial coherence. *Optica*, 11(7):1030, July 2024.
- [134] Jaime Ortega Arroyo, Daniel Cole, and Philipp Kukura. Interferometric scattering microscopy and its combination with single-molecule fluorescence imaging. *Nature Protocols*, 11(4):617–633, April 2016.
- [135] Kiarash Kasaian, Mahdi Mazaheri, and Vahid Sandoghdar. Long-Range Three-Dimensional Tracking of Nanoparticles Using Interferometric Scattering Microscopy. *ACS Nano*, 18(44):30463–30472, November 2024.
- [136] Gavin Young, Nikolas Hundt, Daniel Cole, Adam Fineberg, Joanna Andrecka, Andrew Tyler, Anna Olerinyova, Ayla Ansari, Erik G. Marklund, Miranda P. Collier, Shane A. Chandler, Olga Tkachenko, Joel Allen, Max Crispin, Neil Billington, Yasuharu Takagi, James R. Sellers, C dric Eichmann, Philipp Selenko, Lukas Frey, Roland Riek, Martin R. Galpin, Weston B. Struwe, Justin L. P. Benesch, and Philipp Kukura. Quantitative mass imaging of single biological macromolecules. *Science*, 360(6387):423–427, April 2018.

-
- [137] K. Czamara, K. Majzner, M. Z. Pacia, K. Kochan, A. Kaczor, and M. Baranska. Raman spectroscopy of lipids: a review. *Journal of Raman Spectroscopy*, 46(1):4–20, January 2015.
- [138] Ji-Xin Cheng and X. Sunney Xie. Coherent Anti-Stokes Raman Scattering Microscopy: Instrumentation, Theory, and Applications. *The Journal of Physical Chemistry B*, 108(3):827–840, January 2004.
- [139] Eric O. Potma and X. S. Xie. Detection of single lipid bilayers with coherent anti-Stokes Raman scattering (CARS) microscopy. *Journal of Raman Spectroscopy*, 34(9):642–650, September 2003.
- [140] Michiel Müller and Juleon M. Schins. Imaging the Thermodynamic State of Lipid Membranes with Multiplex CARS Microscopy. *The Journal of Physical Chemistry B*, 106(14):3715–3723, April 2002.
- [141] Wolfgang Langbein, Dafydd S. Harlow, David Regan, Iestyn Pope, and Paola Borri. Heterodyne dual-polarization epi-detected CARS microscopy for chemical and topographic imaging of interfaces. In Natan T. Shaked and Oliver Hayden, editors, *Label-free Biomedical Imaging and Sensing (LBIS) 2019*, page 2, San Francisco, United States, March 2019. SPIE.
- [142] Zdzislaw Salamon, Savitha Devanathan, Isabel D. Alves, and Gordon Tollin. Plasmon-waveguide Resonance Studies of Lateral Segregation of Lipids and Proteins into Microdomains (Rafts) in Solid-supported Bilayers. *Journal of Biological Chemistry*, 280(12):11175–11184, March 2005.
- [143] Eric D. B. Foley, Manish S. Kushwah, Gavin Young, and Philipp Kukura. Mass photometry enables label-free tracking and mass measurement of single proteins on lipid bilayers. *Nature Methods*, 18(10):1247–1252, October 2021.
- [144] Andrea Alessandrini and Paolo Facci. Unraveling lipid/protein interaction in model lipid bilayers by Atomic Force Microscopy. *Journal of Molecular Recognition*, 24(3):387–396, May 2011.
- [145] Thang L. Nguyen, Soorya Pradeep, Robert L. Judson-Torres, Jason Reed, Michael A. Teitell, and Thomas A. Zangle. Quantitative Phase Imaging: Recent Advances and Expanding Potential in Biomedicine. *ACS Nano*, 16(8):11516–11544, August 2022.
- [146] Teresa Cacace, Vittorio Bianco, and Pietro Ferraro. Quantitative phase imaging trends in biomedical applications. *Optics and Lasers in Engineering*, 135:106188, December 2020.
- [147] YongKeun Park, Christian Depeursinge, and Gabriel Popescu. Quantitative phase imaging in biomedicine. *Nature Photonics*, 12(10):578–589, October 2018.
- [148] Andrei B. Vakhtin, Kristen A. Peterson, William R. Wood, and Daniel J. Kane. Differential spectral interferometry: an imaging technique for biomedical applications. *Optics Letters*, 28(15):1332, August 2003.
- [149] Christopher J. Mann, Lingfeng Yu, Chun-Min Lo, and Myung K. Kim. High-resolution quantitative phase-contrast microscopy by digital holography. *Optics Express*, 13(22):8693, 2005.
-

- [150] Gabriel Popescu, YoungKeun Park, Niyom Lue, Catherine Best-Popescu, Lauren Deflores, Ramachandra R. Dasari, Michael S. Feld, and Kamran Badizadegan. Optical imaging of cell mass and growth dynamics. *American Journal of Physiology-Cell Physiology*, 295(2):C538–C544, August 2008.
- [151] Pierre Marquet, Christian Depeursinge, and Pierre J. Magistretti. Review of quantitative phase-digital holographic microscopy: promising novel imaging technique to resolve neuronal network activity and identify cellular biomarkers of psychiatric disorders. *Neurophotonics*, 1(2):020901, September 2014.
- [152] Inkyu Moon, Faliu Yi, Yeon H. Lee, Bahram Javidi, Daniel Boss, and Pierre Marquet. Automated quantitative analysis of 3D morphology and mean corpuscular hemoglobin in human red blood cells stored in different periods. *Optics Express*, 21(25):30947, December 2013.
- [153] Ondřej Tolde, Aneta Gandalovičová, Aneta Křížová, Pavel Veselý, Radim Chmelík, Daniel Rosel, and Jan Brábek. Quantitative phase imaging unravels new insight into dynamics of mesenchymal and amoeboid cancer cell invasion. *Scientific Reports*, 8(1):12020, August 2018.
- [154] David Regan, Joseph Williams, Francesco Masia, Paola Borri, and Wolfgang Langbein. Measuring sub-nanometre thickness changes during phase transitions of supported lipid bilayers with quantitative differential interference contrast microscopy. In Gabriel Popescu and YongKeun Park, editors, *Quantitative Phase Imaging V*, page 44, San Francisco, United States, March 2019. SPIE.
- [155] David Regan. *Measurement of thickness and phase transitions in supported lipid bilayers using quantitative differential interference contrast microscopy*. PhD Thesis, Cardiff University, 2019.
- [156] Yair Rivenson, Yibo Zhang, Harun Günaydin, Da Teng, and Aydogan Ozcan. Phase recovery and holographic image reconstruction using deep learning in neural networks. *Light: Science & Applications*, 7(2):17141–17141, October 2017.
- [157] Junwei Min, Baoli Yao, Veselina Trendafilova, Steffi Ketelhut, Lena Kastl, Burkhard Greve, and Björn Kemper. Quantitative phase imaging of cells in a flow cytometry arrangement utilizing Michelson interferometer-based off-axis digital holographic microscopy. *Journal of Biophotonics*, 12(9):e201900085, September 2019.
- [158] Yichen Wu and Aydogan Ozcan. Lensless digital holographic microscopy and its applications in biomedicine and environmental monitoring. *Methods*, 136:4–16, March 2018.
- [159] Philipp Lenz, Dominik Bettenworth, Philipp Krausewitz, Markus Brückner, Steffi Ketelhut, Gert Von Bally, Dirk Domagk, and Björn Kemper. Digital holographic microscopy quantifies the degree of inflammation in experimental colitis. *Integrative Biology*, 5(3):624–630, March 2013.
- [160] Tomoyoshi Shimobaba, Yoshikuni Sato, Junya Miura, Mai Takenouchi, and Tomoyoshi Ito. Real-time digital holographic microscopy using the graphic processing unit. *Optics Express*, 16(16):11776, August 2008.

-
- [161] Kaiqiang Wang, Qian Kemao, Jianglei Di, and Jianlin Zhao. Deep learning spatial phase unwrapping: a comparative review. *Advanced Photonics Nexus*, 1(01), August 2022.
- [162] Howard Y. H. Huang, L. Tian, Z. Zhang, Y. Liu, Z. Chen, and G. Barbastathis. Path-independent phase unwrapping using phase gradient and total-variation (TV) denoising. *Optics Express*, 20(13):14075, June 2012.
- [163] M.D. Pritt. Comparison of path-following and least-squares phase unwrapping algorithms. In *IGARSS'97. 1997 IEEE International Geoscience and Remote Sensing Symposium Proceedings. Remote Sensing - A Scientific Vision for Sustainable Development*, volume 2, pages 872–874, Singapore, 1997. IEEE.
- [164] J. C. De Souza, M. E. Oliveira, and P. A. M. Dos Santos. Branch-cut algorithm for optical phase unwrapping. *Optics Letters*, 40(15):3456, August 2015.
- [165] Marvin A. Schofield and Yimei Zhu. Fast phase unwrapping algorithm for interferometric applications. *Optics Letters*, 28(14):1194, July 2003.
- [166] Jos M. Bioucas-Dias and Gonalo Valadao. Phase Unwrapping via Graph Cuts. *IEEE Transactions on Image Processing*, 16(3):698–709, March 2007.
- [167] G. Ferraioli, A. Shabou, F. Tupin, and V. Pascazio. Multichannel Phase Unwrapping With Graph Cuts. *IEEE Geoscience and Remote Sensing Letters*, 6(3):562–566, July 2009.
- [168] Xin-Cheng Yao, Amanda Foust, David M. Rector, Benjamin Barrowes, and John S. George. Cross-Polarized Reflected Light Measurement of Fast Optical Responses Associated with Neural Activation. *Biophysical Journal*, 88(6):4170–4177, June 2005.
- [169] Yee-Hung M Chan and Steven G Boxer. Model membrane systems and their applications. *Current Opinion in Chemical Biology*, 11(6):581–587, December 2007.
- [170] Kenichi Morigaki and Yasushi Tanimoto. Evolution and development of model membranes for physicochemical and functional studies of the membrane lateral heterogeneity. *Biochimica et Biophysica Acta (BBA) - Biomembranes*, 1860(10):2012–2017, October 2018.
- [171] Kandice R. Levental and Ilya Levental. Giant Plasma Membrane Vesicles: Models for Understanding Membrane Organization. In *Current Topics in Membranes*, volume 75, pages 25–57. Elsevier, 2015.
- [172] Gregory J. Hardy, Rahul Nayak, and Stefan Zauscher. Model cell membranes: Techniques to form complex biomimetic supported lipid bilayers via vesicle fusion. *Current Opinion in Colloid & Interface Science*, 18(5):448–458, October 2013.
- [173] Jakob Andersson, Ingo Köper, and Wolfgang Knoll. Tethered Membrane Architectures-Design and Applications. *Frontiers in Materials*, 5:55, September 2018.
-

- [174] Minsub Chung, Randall D. Lowe, Yee-Hung M. Chan, Prasad V. Ganesan, and Steven G. Boxer. DNA-tethered membranes formed by giant vesicle rupture. *Journal of Structural Biology*, 168(1):190–199, October 2009.
- [175] Charles Cranfield, Sonia Carne, Boris Martinac, and Bruce Cornell. The Assembly and Use of Tethered Bilayer Lipid Membranes (tBLMs). In Dylan M. Owen, editor, *Methods in Membrane Lipids*, volume 1232, pages 45–53. Springer New York, New York, NY, 2015. Series Title: Methods in Molecular Biology.
- [176] Oskar Staufer, Franziska Dietrich, Rahul Rimal, Martin Schröter, Sebastian Fabritz, Heike Boehm, Smriti Singh, Martin Möller, Ilia Platzman, and Joachim Pius Spatz. Bottom-up assembly of biomedical relevant fully synthetic extracellular vesicles. *Science Advances*, 7(36):eabg6666, September 2021.
- [177] Petra Schwille. Bottom-Up Synthetic Biology: Engineering in a Tinkerer’s World. *Science*, 333(6047):1252–1254, September 2011.
- [178] Martin Loose, Elisabeth Fischer-Friedrich, Christoph Herold, Karsten Kruse, and Petra Schwille. Min protein patterns emerge from rapid rebinding and membrane interaction of MinE. *Nature Structural & Molecular Biology*, 18(5):577–583, May 2011.
- [179] Mark A. Haidekker, Taotao Ling, Michael Anglo, Hazel Y. Stevens, John A. Frangos, and Emmanuel A. Theodorakis. New fluorescent probes for the measurement of cell membrane viscosity. *Chemistry & Biology*, 8(2):123–131, February 2001.
- [180] Anjul Khadria. Tools to measure membrane potential of neurons. *Biomedical Journal*, 45(5):749–762, October 2022.
- [181] Inc. AAT Bioquest. Spectrum [Atto 488], 2024.
- [182] Inc. AAT Bioquest. Spectrum [Atto 425], 2024.
- [183] Dafydd S. Harlow. *Sensing local biological environments using coherent optical nanoscopy*. PhD Thesis, Cardiff University, 2022.
- [184] David Regan, Joseph Williams, Paola Borri, and Wolfgang Langbein. Lipid Bilayer Thickness Measured by Quantitative DIC Reveals Phase Transitions and Effects of Substrate Hydrophilicity. *Langmuir*, 35(43):13805–13814, October 2019.
- [185] Samuel Hamilton, David Regan, Lukas Payne, Paola Borri, and Wolfgang Langbein. Quantitative measurement of graphitic sp² on single nanodiamonds with sub-monolayer sensitivity using differential interference contrast and photo-thermal microscopy. *Carbon*, 228:119371, September 2024.
- [186] Wolfgang W. Langbein, Freya Turley, David Regan, and Paola Borri. Interferometric Gated Off-Axis Reflectometry (iGOR): ultrasensitive label-free tracking of nanoparticles and suspended membranes in three dimensions. In Marc P. Georges, Nicolas Verrier, and Irene Georgakoudi, editors, *Unconventional Optical Imaging IV*, page 16, Strasbourg, France, June 2024. SPIE.

-
- [187] Ewelina Pijewska, Iwona Gorczynska, and Maciej Szkulmowski. Computationally effective 2D and 3D fast phase unwrapping algorithms and their applications to Doppler optical coherence tomography. *Biomedical Optics Express*, 10(3):1365, March 2019.
- [188] Alexander Nahmad-Rohen. *Optical imaging of lipid bilayers and its applications to neurology*. PhD thesis, Cardiff University, 2019.
- [189] Volker Kiessling, Sung-Tae Yang, and Lukas K. Tamm. Supported Lipid Bilayers as Models for Studying Membrane Domains. In *Current Topics in Membranes*, volume 75, pages 1–23. Elsevier, 2015.
- [190] Tania Kjellerup Lind, Maximilian W. A. Skoda, and Marit Årdenas. Formation and Characterization of Supported Lipid Bilayers Composed of Phosphatidylethanolamine and Phosphatidylglycerol by Vesicle Fusion, a Simple but Relevant Model for Bacterial Membranes. *ACS Omega*, 4(6):10687–10694, June 2019.
- [191] Mathias Winterhalter. Black lipid membranes. *Current Opinion in Colloid & Interface Science*, 5(3-4):250–255, July 2000.
- [192] Zahra Aminipour, Mehran Khorshid, Mariam Bayoumi, Patricia Losada-Pérez, Ronald Thoelen, Shahin Bonakdar, Hamid Keshvari, Giovanni Maglia, Patrick Wagner, and Bart Van Der Bruggen. Formation and electrical characterization of black lipid membranes in porous filter materials: Black lipid membranes in porous filter materials. *physica status solidi (a)*, 214(9):1700104, September 2017.
- [193] Elanna B. Stephenson, Jaime L. Korner, and Katherine S. Elvira. Challenges and opportunities in achieving the full potential of droplet interface bilayers. *Nature Chemistry*, 14(8):862–870, August 2022.
- [194] Hagan Bayley, Brid Cronin, Andrew Heron, Matthew A. Holden, William L. Hwang, Ruhma Syeda, James Thompson, and Mark Wallace. Droplet interface bilayers. *Molecular BioSystems*, 4(12):1191, 2008.
- [195] Oliver K. Castell, James Berridge, and Mark I. Wallace. Quantification of Membrane Protein Inhibition by Optical Ion Flux in a Droplet Interface Bilayer Array. *Angewandte Chemie International Edition*, 51(13):3134–3138, March 2012.
- [196] Matias A. Crosio, Raquel V. Vico, and Natalia Wilke. Giant unilamellar vesicles (GUVs): A key tool for the study of biophysical properties of membranes. In *Advances in Biomembranes and Lipid Self-Assembly*, volume 40, pages 55–65. Elsevier, 2024.
- [197] Susanne F. Fenz and Kheya Sengupta. Giant vesicles as cell models. *Integrative Biology*, 4(9):982, 2012.
- [198] Eva M. Schmid, David L. Richmond, and Daniel A. Fletcher. Reconstitution of proteins on electroformed giant unilamellar vesicles. In *Methods in Cell Biology*, volume 128, pages 319–338. Elsevier, 2015.
-

- [199] Lori Van De Cauter, Lennard Van Buren, Gijsje H. Koenderink, and Kristina A. Ganzinger. Exploring Giant Unilamellar Vesicle Production for Artificial Cells - Current Challenges and Future Directions. *Small Methods*, 7(12):2300416, December 2023.
- [200] Xiaoyan Liu, Joakim Stenhammar, Håkan Wennerström, and Emma Sparr. Vesicles Balance Osmotic Stress with Bending Energy That Can Be Released to Form Daughter Vesicles. *The Journal of Physical Chemistry Letters*, 13(2):498–507, January 2022.
- [201] Valeska Rathe, Daniel Kuckla, and Cornelia Monzel. Phase separation in biological membranes: An overview with focus on experimental effects of illumination and osmotic pressure changes. In *Advances in Biomembranes and Lipid Self-Assembly*, volume 34, pages 31–66. Elsevier, 2021.
- [202] Anne-Laure Bernard, Marie-Alice Guedeau-Boudeville, Ludovic Jullien, and Jean-Marc Di Meglio. Raspberry vesicles. *Biochimica et Biophysica Acta (BBA) - Biomembranes*, 1567:1–5, December 2002.
- [203] Andreas Weinberger, Feng-Ching Tsai, Gijsje H. Koenderink, Thais F. Schmidt, Rosângela Itri, Wolfgang Meier, Tatiana Schmatko, André Schröder, and Carlos Marques. Gel-Assisted Formation of Giant Unilamellar Vesicles. *Biophysical Journal*, 105(1):154–164, July 2013.
- [204] N. S. Averkiev and A. Shik. Capacitance properties of a system of coupled nanowires. *Physical Review B*, 59(4):3250–3254, January 1999.
- [205] Dominik Drabik, Joanna Doskocz, and Magda Przybyło. Effects of electroformation protocol parameters on quality of homogeneous GUV populations. *Chemistry and Physics of Lipids*, 212:88–95, May 2018.
- [206] Zvonimir Boban, Ivan Mardešić, Witold Karol Subczynski, and Marija Raguz. Giant Unilamellar Vesicle Electroformation: What to Use, What to Avoid, and How to Quantify the Results. *Membranes*, 11(11):860, November 2021.
- [207] Wenman Li, Qiong Wang, Zhong Yang, Wangang Wang, Yi Cao, Ning Hu, Hongyan Luo, Yanjian Liao, and Jun Yang. Impacts of electrical parameters on the electroformation of giant vesicles on ITO glass chips. *Colloids and Surfaces B: Biointerfaces*, 140:560–566, April 2016.
- [208] Miglena I. Angelova and Dimiter S. Dimitrov. Liposome electroformation. *Faraday Discussions of the Chemical Society*, 81:303, 1986.
- [209] Zvonimir Boban, Ivan Mardešić, Witold Karol Subczynski, Dražan Jozić, and Marija Raguz. Optimization of Giant Unilamellar Vesicle Electroformation for Phosphatidylcholine/Sphingomyelin/Cholesterol Ternary Mixtures. *Membranes*, 12(5):525, May 2022.
- [210] Thomas G. Barclay, Kristina Constantopoulos, and Janis Matison. Nanotubes Self-Assembled from Amphiphilic Molecules via Helical Intermediates. *Chemical Reviews*, 114(20):10217–10291, October 2014.

-
- [211] Niloy Kundu, Debasis Banik, and Nilmoni Sarkar. Self-Assembly of Amphiphiles into Vesicles and Fibrils: Investigation of Structure and Dynamics Using Spectroscopy and Microscopy Techniques. *Langmuir*, 34(39):11637–11654, October 2018.
- [212] Jan Steinkühler, Philippe De Tillieux, Roland L. Knorr, Reinhard Lipowsky, and Rumiana Dimova. Charged giant unilamellar vesicles prepared by electroformation exhibit nanotubes and transbilayer lipid asymmetry. *Scientific Reports*, 8(1):11838, August 2018.
- [213] Valerio Pereno, Dario Carugo, Luca Bau, Erdinc Sezgin, Jorge Bernardino De La Serna, Christian Eggeling, and Eleanor Stride. Electroformation of Giant Unilamellar Vesicles on Stainless Steel Electrodes. *ACS Omega*, 2(3):994–1002, March 2017.
- [214] Zhihua Liang, Miao Chen, Xin Yi, and Wenpeng Zhu. Membrane-tension-dominated growth mechanism and size modulation of giant unilamellar vesicles in electroformation. *Journal of the Mechanics and Physics of Solids*, 170:105120, January 2023.
- [215] Mohammad Maoyafikuddin and Rochish M. Thaokar. Effect of the Waveform of the Pulsed Electric Field on the Cylindrical Deformation of Uncharged Giant Unilamellar Vesicles. *Langmuir*, 39(28):9660–9670, July 2023.
- [216] Javier Alejandro Bellon, Marcelo Javier Pino, and Natalia Wilke. Low-cost equipment for electroformation of Giant Unilamellar Vesicles. *HardwareX*, 4:e00037, October 2018.
- [217] Tripta Bhatia, Simon Christ, Jan Steinkühler, Rumiana Dimova, and Reinhard Lipowsky. Simple sugars shape giant vesicles into multispheres with many membrane necks. *Soft Matter*, 16(5):1246–1258, 2020.
- [218] Hannah Stein, Susann Spindler, Navid Bonakdar, Chun Wang, and Vahid Sandoghdar. Production of Isolated Giant Unilamellar Vesicles under High Salt Concentrations. *Frontiers in Physiology*, 8, February 2017.
- [219] M.J. Sarmiento, M. Prieto, and Fábio Fernandes. Reorganization of lipid domain distribution in giant unilamellar vesicles upon immobilization with different membrane tethers. *Biochimica et Biophysica Acta (BBA) - Biomembranes*, 1818(11):2605–2615, November 2012.
- [220] Milka Doktorova, Michael V. LeVine, George Khelashvili, and Harel Weinstein. A New Computational Method for Membrane Compressibility: Bilayer Mechanical Thickness Revisited. *Biophysical Journal*, 116(3):487–502, February 2019.
- [221] Craig McPhee. *Development and characterisation of synthetic model lipid membranes under linear and non-linear microscopy*. PhD thesis, Cardiff University, 2016.
- [222] Vikramdeep Singh. *Single emitter cryo-micro-spectroscopy of pyramidal quantum dots, fluorescent proteins, and light-harvesting complexes*. PhD Thesis, Cardiff University, 2023.
-

- [223] Yixing Chen, Halil I. Okur, Cornelis Lütgebaucks, and Sylvie Roke. Zwitterionic and Charged Lipids Form Remarkably Different Structures on Nanoscale Oil Droplets in Aqueous Solution. *Langmuir*, 34(3):1042–1050, January 2018.
- [224] Joseph Williams. *Quantitative optical microscopy of bio-nanostructures*. PhD thesis.
- [225] BAUSCH & LOMB OPTICAL COMPANY. *Abbe-56 Refractometer Reference Manual*. New York: Bausch & Lomb Optical Company, 1936.
- [226] Ganesh Shahane, Wei Ding, Michail Palaiokostas, and Mario Orsi. Physical properties of model biological lipid bilayers: insights from all-atom molecular dynamics simulations. *Journal of Molecular Modeling*, 25(3):76, March 2019.
- [227] Norbert Kučerka, Mu-Ping Nieh, and John Katsaras. Fluid phase lipid areas and bilayer thicknesses of commonly used phosphatidylcholines as a function of temperature. *Biochimica et Biophysica Acta (BBA) - Biomembranes*, 1808(11):2761–2771, November 2011.
- [228] Petteri Parkkila, Mohamed Elderdfi, Alex Bunker, and Tapani Viitala. Biophysical Characterization of Supported Lipid Bilayers Using Parallel Dual-Wavelength Surface Plasmon Resonance and Quartz Crystal Microbalance Measurements. *Langmuir*, 34(27):8081–8091, July 2018.
- [229] Kiyoshi Mishima, Koichi Satoh, and Toshihiko Ogihara. Optical birefringence of phosphatidylcholine liposomes in gel phases. *Biochimica et Biophysica Acta (BBA) - Biomembranes*, 898(2):231–238, April 1987.
- [230] Lori Van De Cauter, Federico Fanalista, Lennard Van Buren, Nicola De Franceschi, Elisa Godino, Sharon Bouw, Christophe Danelon, Cees Dekker, Gijse H. Koenderink, and Kristina A. Ganzinger. Optimized cDICE for Efficient Reconstitution of Biological Systems in Giant Unilamellar Vesicles. *ACS Synthetic Biology*, 10(7):1690–1702, July 2021.
- [231] Stephan Benke, Daniel Roderer, Bengt Wunderlich, Daniel Nettels, Rudi Glockshuber, and Benjamin Schuler. The assembly dynamics of the cytolytic pore toxin ClyA. *Nature Communications*, 6(1):6198, February 2015.
- [232] Joe Carroll and David J. Ellar. An analysis of *Bacillus thuringiensis* delta-endotoxin action on insect-midgut-membrane permeability using a light-scattering assay. *European Journal of Biochemistry*, 214(3):771–778, June 1993.
- [233] M. Kirouac, V. Vachon, S. Rivest, J. L. Schwartz, and R. Laprade. Analysis of the Properties of *Bacillus thuringiensis* Insecticidal Toxins Using a Potential-sensitive Fluorescent Probe. *Journal of Membrane Biology*, 196(1):51–59, November 2003.
- [234] Barbara H. Knowles and David J. Ellar. Colloid-osmotic lysis is a general feature of the mechanism of action of *Bacillus thuringiensis* δ -endotoxins with different insect specificity. *Biochimica et Biophysica Acta (BBA) - General Subjects*, 924(3):509–518, June 1987.

-
- [235] Aaron J. Gassmann, Jennifer L. Petzold-Maxwell, Ryan S. Keweshan, and Mike W. Dunbar. Field-Evolved Resistance to Bt Maize by Western Corn Rootworm. *PLoS ONE*, 6(7):e22629, July 2011.
- [236] Jinbo Huang, Zeyuan Guan, Liting Wan, Tingting Zou, and Ming Sun. Crystal structure of Cry6Aa: A novel nematocidal ClyA-type α -pore-forming toxin from *Bacillus thuringiensis*. *Biochemical and Biophysical Research Communications*, 478(1):307–313, September 2016.
- [237] Alistair J. Wallace, Timothy J. Stillman, Angela Atkins, Stuart J. Jamieson, Per A. Bullough, Jeffrey Green, and Peter J. Artymiuk. *E. coli* Hemolysin E (HlyE, ClyA, SheA). *Cell*, 100(2):265–276, January 2000.
- [238] Eva Fortea, Vincent Lemieux, Léna Potvin, Vimbai Chikwana, Samantha Griffin, Timothy Hey, David McCaskill, Kenneth Narva, Sek Yee Tan, Xiaoping Xu, Vincent Vachon, and Jean-Louis Schwartz. Cry6Aa1, a *Bacillus thuringiensis* nematocidal and insecticidal toxin, forms pores in planar lipid bilayers at extremely low concentrations and without the need of proteolytic processing. *Journal of Biological Chemistry*, 292(32):13122–13132, August 2017.
- [239] Alexey Dementiev, Jason Board, Anand Sitaram, Timothy Hey, Matthew S. Kelker, Xiaoping Xu, Yan Hu, Cristian Vidal-Quist, Vimbai Chikwana, Samantha Griffin, David McCaskill, Nick X. Wang, Shao-Ching Hung, Michael K. Chan, Marianne M. Lee, Jessica Hughes, Alice Wegener, Raffi V. Aroian, Kenneth E. Narva, and Colin Berry. The pesticidal Cry6Aa toxin from *Bacillus thuringiensis* is structurally similar to HlyE-family alpha pore-forming toxins. *BMC Biology*, 14(1):71, December 2016.
- [240] Wei Peng, Marcela De Souza Santos, Yang Li, Diana R. Tomchick, and Kim Orth. High-resolution cryo-EM structures of the *E. coli* hemolysin ClyA oligomers. *PLOS ONE*, 14(5):e0213423, May 2019.
- [241] Daniel Roderer, Stephan Benke, Marcus Müller, Helene Fäh-Rechsteiner, Nenad Ban, Benjamin Schuler, and Rudi Glockshuber. Characterization of Variants of the Pore-Forming Toxin ClyA from *Escherichia coli* Controlled by a Redox Switch. *Biochemistry*, 53(40):6357–6369, October 2014.
- [242] Richard M. Epand and Remo Bottega. Determination of the phase behaviour of phosphatidylethanolamine admixed with other lipids and the effects of calcium chloride: implications for protein kinase C regulation. *Biochimica et Biophysica Acta (BBA) - Biomembranes*, 944(2):144–154, October 1988.
- [243] Gerald W Feigenson. Phase behavior of lipid mixtures. *Nature Chemical Biology*, 2(11):560–563, November 2006. Publisher: Springer Science and Business Media LLC.
- [244] Sophie E. Ayscough, Luke A. Clifton, Maximilian W.A. Skoda, and Simon Timmuss. Suspended phospholipid bilayers: A new biological membrane mimetic. *Journal of Colloid and Interface Science*, 633:1002–1011, March 2023.
- [245] Zhaoyu Li, Luis B. Agellon, Theresa M. Allen, Masato Umeda, Larry Jewell, Andrew Mason, and Dennis E. Vance. The ratio of phosphatidylcholine to
-

- phosphatidylethanolamine influences membrane integrity and steatohepatitis. *Cell Metabolism*, 3(5):321–331, May 2006.
- [246] M.B. Priestley. Power spectral analysis of non-stationary random processes. *Journal of Sound and Vibration*, 6(1):86–97, July 1967.
- [247] An introduction to anaesthesia and general considerations. In *Veterinary Anaesthesia*, pages 3–18. Elsevier, 2014.
- [248] Joel B. Harley and José M. F. Moura. Sparse recovery of the multimodal and dispersive characteristics of Lamb waves. *The Journal of the Acoustical Society of America*, 133(5):2732–2745, May 2013.
- [249] Angelo Aloisio, Ferdinando Totani, and Gianfranco Totani. Experimental dispersion curves of non-penetrable soils from direct dynamic measurements using the seismic dilatometer (SDMT). *Soil Dynamics and Earthquake Engineering*, 143:106616, April 2021.
- [250] K. Porsezian and Krishnan Senthilnathan. Solitons in a Fiber Bragg Grating. In *Guided Wave Optical Components and Devices*, pages 251–280. Elsevier, 2006.
- [251] David Thompson. Low Frequency Ground Vibration. In *Railway Noise and Vibration*, pages 399–435. Elsevier, 2009.
- [252] Jennifer Louten. Virus Structure and Classification. In *Essential Human Virology*, pages 19–29. Elsevier, 2016.
- [253] Eleonora Muro, G. Ekin Atilla-Gokcumen, and Ulrike S. Eggert. Lipids in cell biology: how can we understand them better? *Molecular Biology of the Cell*, 25(12):1819–1823, June 2014.
- [254] U. Seifert and R. Lipowsky. Morphology of Vesicles. In *Handbook of Biological Physics*, volume 1, pages 403–463. Elsevier, 1995.
- [255] Telma Bezerra Soares, LuÃs Loureiro, Ana Carvalho, Maria Elisabete C.D. Real Oliveira, Alberto Dias, Bruno Sarmiento, and Marlene LÃcio. Lipid nanocarriers loaded with natural compounds: Potential new therapies for age related neurodegenerative diseases? *Progress in Neurobiology*, 168:21–41, September 2018.
- [256] Najma Bibi, Naveed Ahmed, and Gul Majid Khan. Nanostructures in transdermal drug delivery systems. In *Nanostructures for Drug Delivery*, pages 639–668. Elsevier, 2017.
- [257] Islam M. Saadeldin, Seif Ehab, and Jongki Cho. Relevance of multilamellar and multicompartmental vesicles in biological fluids: understanding the significance of proportional variations and disease correlation. *Biomarker Research*, 11(1):77, August 2023.
- [258] Yangyang Zhou, Hezhen Liu, and Hongxia Chen. Advancement in exosome isolation and label-free detection towards clinical diagnosis. *TrAC Trends in Analytical Chemistry*, 179:117874, October 2024.

-
- [259] Shufa Zheng, Jian Fan, Fei Yu, Baihuan Feng, Bin Lou, Qianda Zou, Guoliang Xie, Sha Lin, Ruonan Wang, Xianzhi Yang, Weizhen Chen, Qi Wang, Dan Zhang, Yanchao Liu, Renjie Gong, Zhaohui Ma, Siming Lu, Yanyan Xiao, Yaxi Gu, Jinming Zhang, Hangping Yao, Kaijin Xu, Xiaoyang Lu, Guoqing Wei, Jianying Zhou, Qiang Fang, Hongliu Cai, Yunqing Qiu, Jifang Sheng, Yu Chen, and Tingbo Liang. Viral load dynamics and disease severity in patients infected with SARS-CoV-2 in Zhejiang province, China, January–March 2020: retrospective cohort study. *BMJ*, page m1443, April 2020.
- [260] Chih-Kai Chang, Chi-Sheng Chen, Ming-Jr Jian, Hsing-Yi Chung, Feng-Yee Chang, Jung-Chung Lin, Shan-Shan Hsieh, Sheng-Hui Tang, Cherng-Lih Perng, Chien-Wen Chen, Chun-Hsiang Chiu, and Hung-Sheng Shang. Monitoring coronavirus disease progression and clinical impact through quantitative viral load testing. *Clinica Chimica Acta*, 560:119731, June 2024.
- [261] Shivani Singh, Simon Boyd, William H K Schilling, James A Watson, Mavuto Mukaka, and Nicholas J White. The relationship between viral clearance rates and disease progression in early symptomatic COVID-19: a systematic review and meta-regression analysis. *Journal of Antimicrobial Chemotherapy*, 79(5):935–945, May 2024.
- [262] X.J. Liu, X.W. Chen, C.Y. Zhao, and B.X. Wang. Polarized light transport in anisotropic media composed of ellipsoids: Influence of structural anisotropy. *Journal of Quantitative Spectroscopy and Radiative Transfer*, 245:106854, April 2020.
- [263] Steven L. Jacques, Stéphane Roussel, and Ravikant Samatham. Polarized light imaging specifies the anisotropy of light scattering in the superficial layer of a tissue. *Journal of Biomedical Optics*, 21(7):071115, May 2016.
- [264] Wanrong Gao. Coupling effects between dichroism and birefringence of anisotropic media. *Physics Letters A*, 384(27):126699, September 2020.
- [265] Xavier Vidal, Ivan Fernandez-Corbaton, Alex F. Barbara, and Gabriel Molina-Terriza. Polarization properties of light scattered off solutions of chiral molecules in non-forward direction. *Applied Physics Letters*, 107(21):211107, November 2015.
- [266] Cyriaque Genet. Chiral Light-Chiral Matter Interactions: an Optical Force Perspective. *ACS Photonics*, 9(2):319–332, February 2022.
- [267] Jungho Mun, Minkyung Kim, Younghwan Yang, Trevon Badloe, Jincheng Ni, Yang Chen, Cheng-Wei Qiu, and Junsuk Rho. Electromagnetic chirality: from fundamentals to nontraditional chiroptical phenomena. *Light: Science & Applications*, 9(1):139, September 2020.
- [268] Demi L. Pink, Fabrizia Foglia, David J. Barlow, M. Jayne Lawrence, and Christian D. Lorenz. The Impact of Lipid Digestion on the Dynamic and Structural Properties of Micelles. *Small*, 17(6):2004761, February 2021.
- [269] Vahid Forooqi Motlaq, Lars Gedda, Katarina Edwards, James Douth, and L. Magnus Bergström. Spontaneous Formation of Ultrasmall Unilamellar Vesicles in Mixtures of an Amphiphilic Drug and a Phospholipid. *Langmuir*, 39(32):11337–11344, August 2023.
-

- [270] Aldo Jesorka and Owe Orwar. Liposomes: Technologies and Analytical Applications. *Annual Review of Analytical Chemistry*, 1(1):801–832, July 2008.
- [271] Matěj Týč, Lukáš Kvasnica, Michala Slabá, and Radim Chmelík. Numerical refocusing in digital holographic microscopy with extended-sources illumination. *Optics Express*, 21(23):28258, November 2013.
- [272] Y.A. Eremin. SCATTERING | Scattering Theory. In *Encyclopedia of Modern Optics*, pages 326–330. Elsevier, 2005.

Appendix A

3D printed components

A.1 Tantalum wire holder

To better control the electroformation and improve reproducibly we designed a holder to ensure the same wire geometries. The print design is shown in Fig. A.1. This was printed using PLA and an Ultimaker, 3 Extended, fused filament printer.

A.2 Wire clip

To allow the wire holder to be placed in different environments without disturbing the wires and ensure they don't unintentionally touch surfaces a clip was designed as shown in Fig. A.2 and printed using PLA and an Ultimaker, 3 Extended, fused filament printer.

A.3 Imaging funnels

Iterations of funnels used to image samples as an open volume once adhered to a glass dish designed as shown in Fig. A.3, Fig. A.4 and Fig. A.5 printed as described in caption

A.4 ITO mount

A chamber designed to facilitate ITO electroformation by maintaining contact throughout. Chamber consists of a base (Fig. A.6) and screw (Fig. A.7) both printed using PLA and an Ultimaker, 3 Extended, fused filament printer.

A.5 Modified DIB device design

A drawing of the device planned for iGOR experiments using the DIB system.

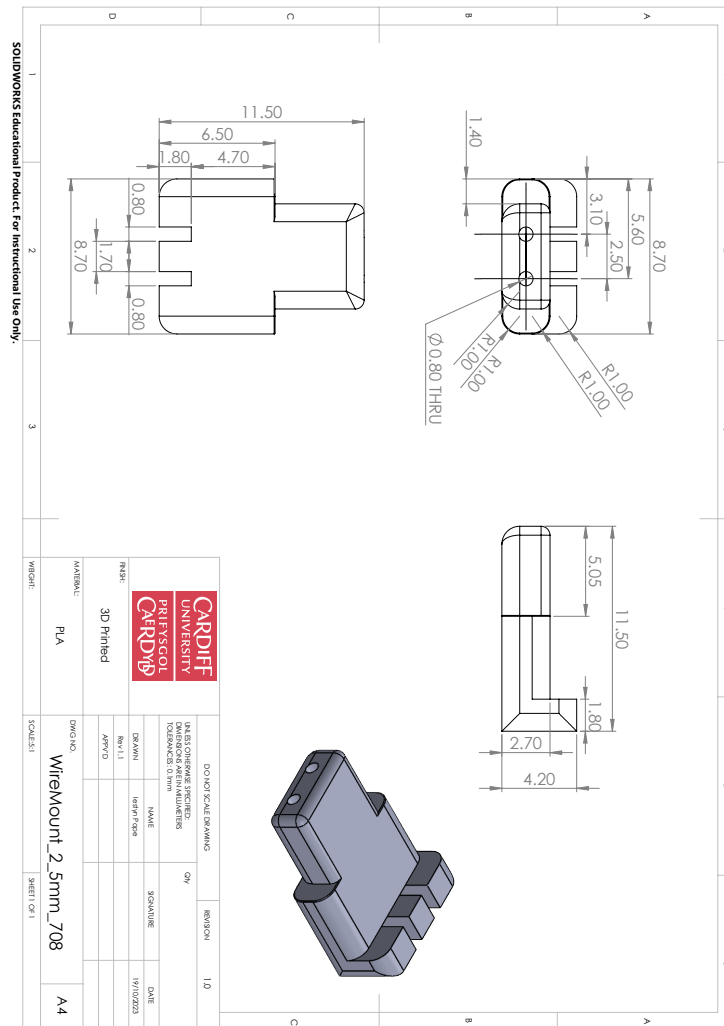


Figure A.1: Tantalum wire holder print design The print file used to print the tantalum wire holder, printed using PLA.

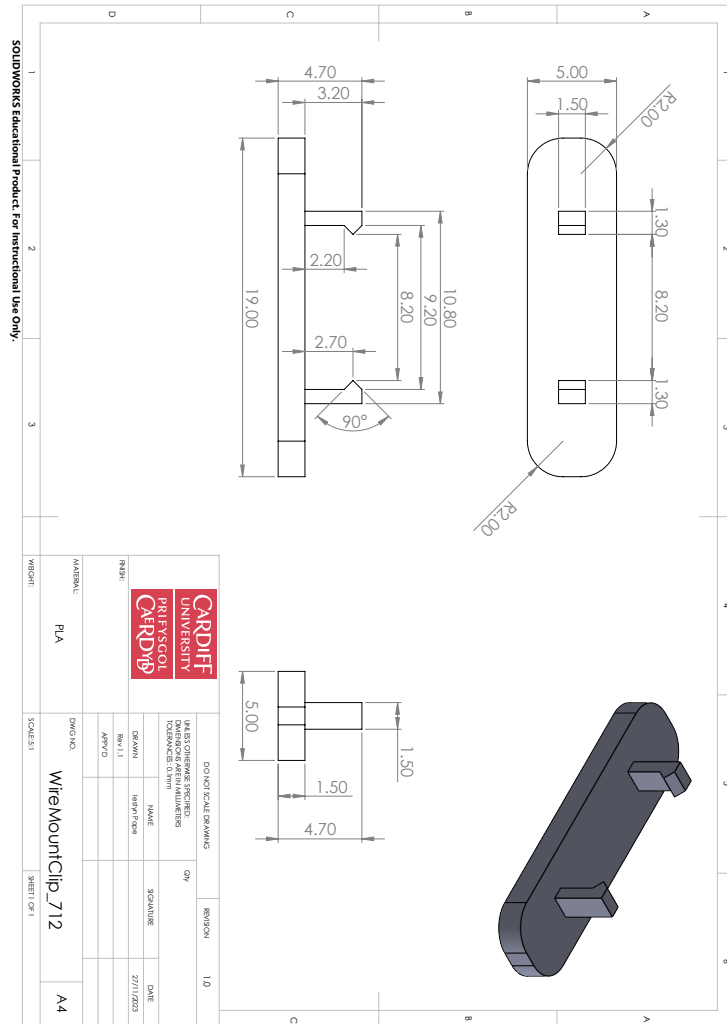


Figure A.2: Wire clip print design The print file used to print the clip used for the wire holder, printed using PLA.

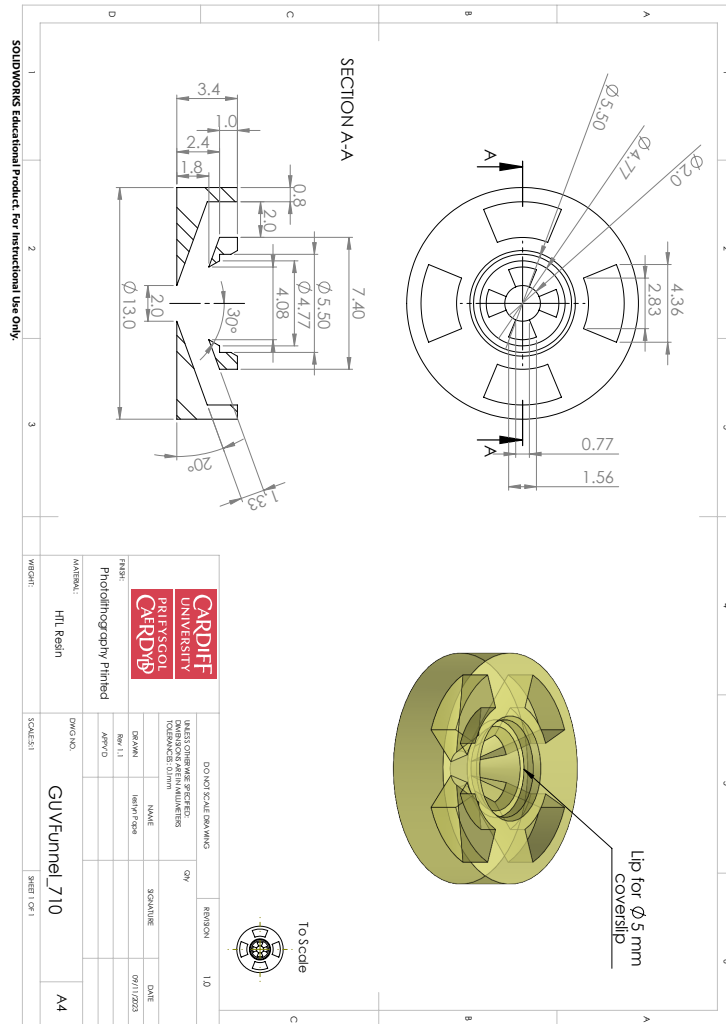


Figure A.4: Funnel design 2 The print file used to print the 2nd funnel, printed using a BMF, S230 photo lithography printer and HTL Resin

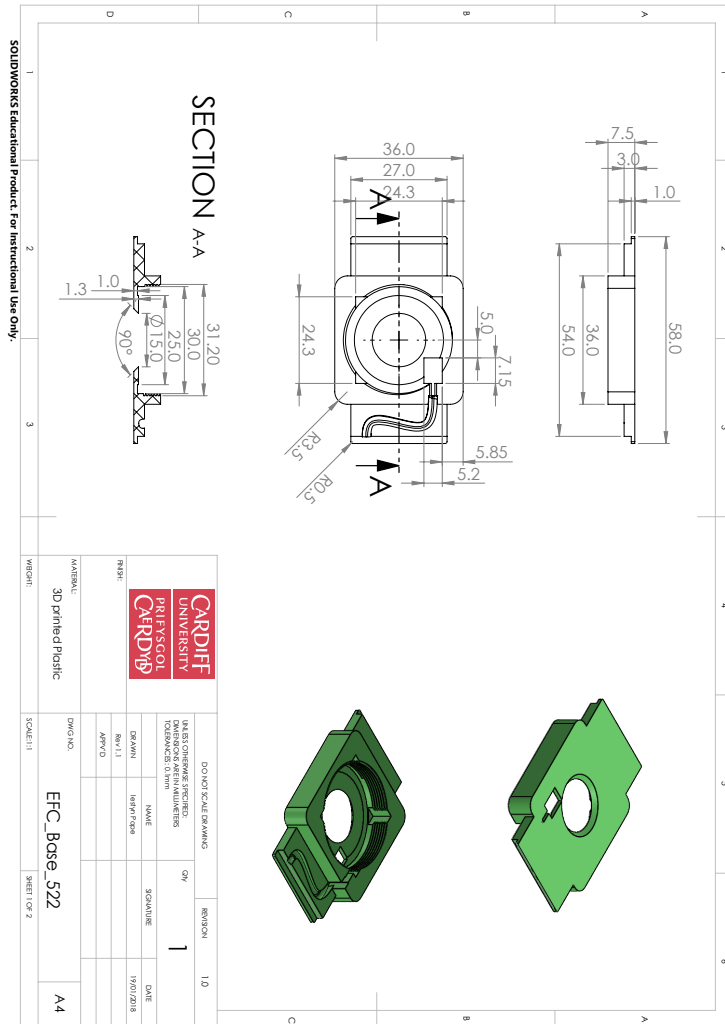


Figure A.6: ITO base design The print file used to print the base of the ITO chamber, printed using PLA and an Ultimaker, 3 Extended, fused filament printer.

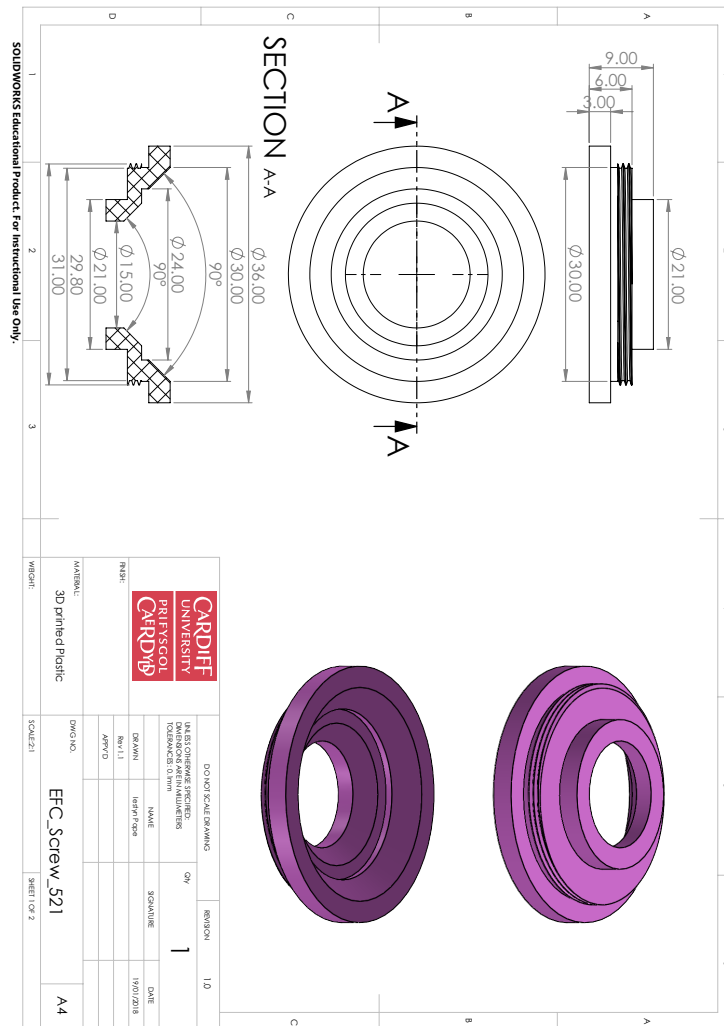


Figure A.7: ITO screw design The print file used to print the screw of the ITO chamber, printed using PLA and an Ultimaker, 3 Extended, fused filament printer.

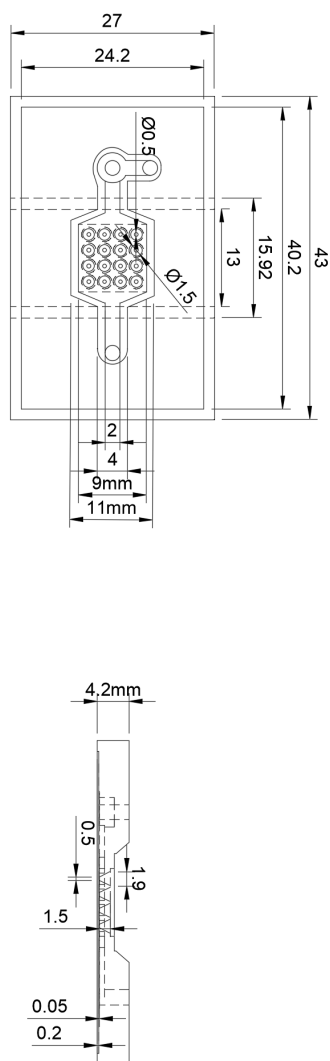


Figure A.8: ITO screw design The print file used to print the screw of the ITO chamber, printed using PLA and an Ultimaker, 3 Extended, fused filament printer.

Appendix B

Imaging supplementary

B.1 qDIC analysis software

An example of a GUV being analysed in home written qDIC software with all parameters input.

B.2 Detailed iGOR optical set up

A detailed schematic of the iGOR set up shown in Fig. B.2.

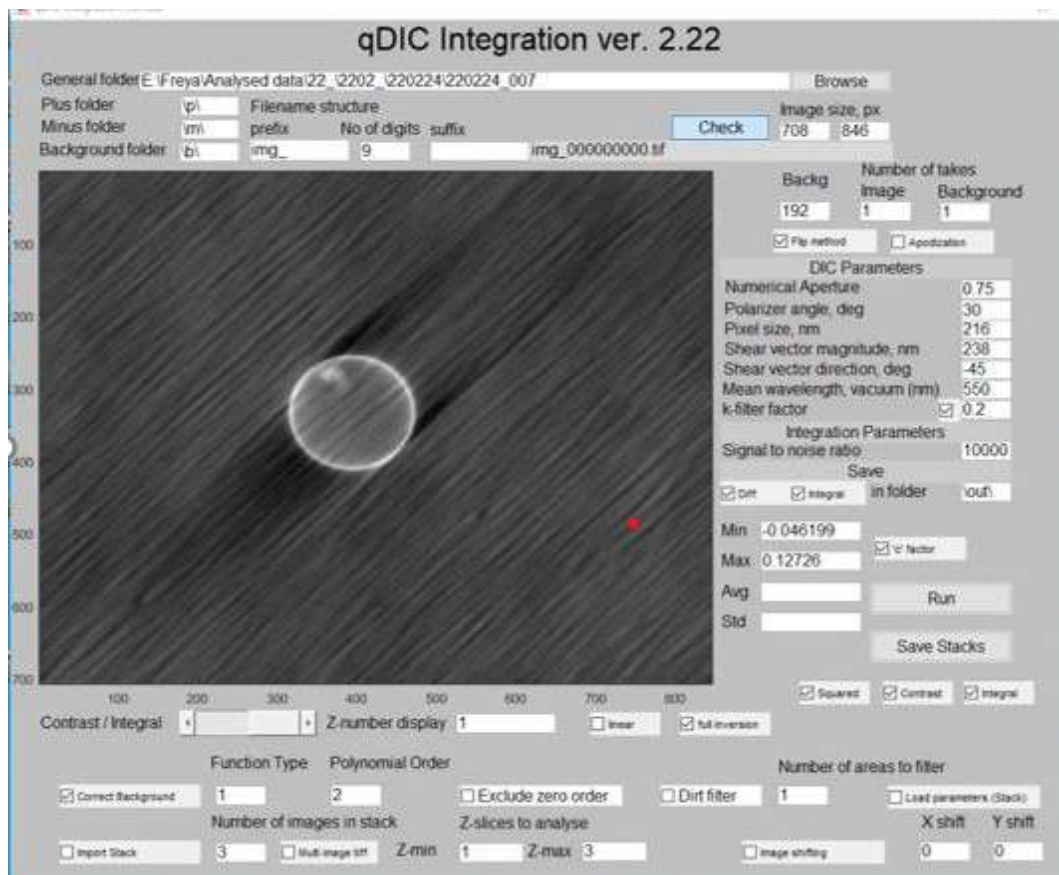


Figure B.1: qDIC software A screenshot of the qDIC software with parameters shown

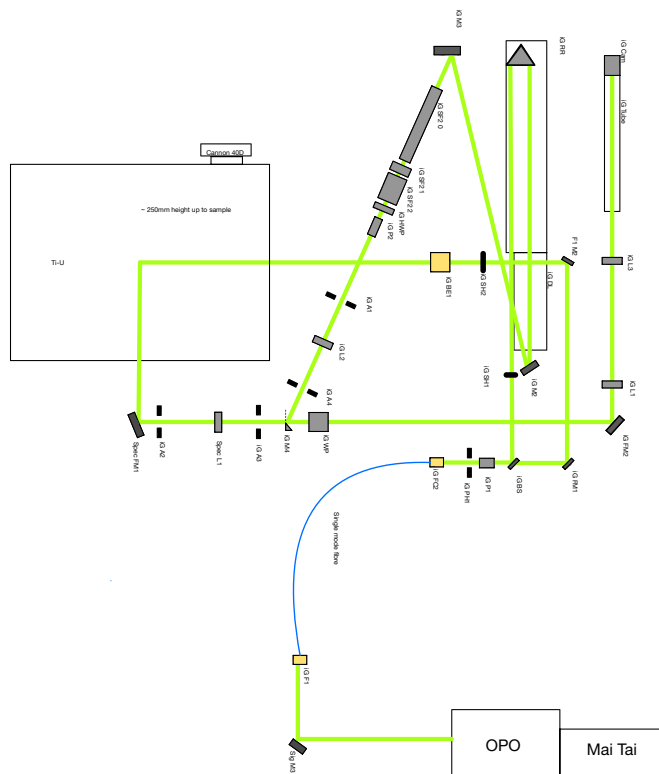


Figure B.2: iGOR optical diagram A diagram detailing the optical path for iGOR, The OPO and Mai Tai generate the lasing beam which is then transported to the iGOR components through the single mode fiber. PH denotes a pin hole, FM and M are flip mirrors and mirrors respectively, L represent lenses, BS is the beam splitter, A denotes apertures, WP the Wollaston prism, RR represents the retroreflector, DL the delay stage, HWP is the half-wave plate, BE the beam splitter and SH the shutters.

Appendix C

qDIC supplementary

C.1 Robust Fitting

The Matlab code used in the robust fitting to Page 1 Fig. C.1 and Page 2 Fig. C.2

```

for i = 1

x1 = XN(:,i);
Y1 = SY(:,i);

x = x1;
Y = Y1;

% load('Data_FM.mat')
r=[X(1) X(end)];%range

%Fit function parameters
n=2; %%harmonics or polynomial order
w=1; %%minimum width of background to fit; use same unit as x
N=n-(r(2)-r(1))/(2*w);%# period extension
if N<0
    N=0;
    w=(r(2)-r(1))/(2*n);
end
offset=0;%offset in the penalty function
sigma=0.1;%std of Gaussian penalty function or use min of local std
% locstd=zeros(length(X)-4,1);%local std of data
% for j=3:length(X)-2
%     locstd(j-2)=std(Y(j-2:j+2));
% end
% sigma=min(locstd);
sigma=10;%#steps to reach final sigma

mask=1;%1: mask points between w1 and wR; 0: no mask
M=true(size(X));
if mask
    P1 = P1(i);
    P2 = P2(i);
    P2P = P2W(i) - P1W(i);
    C = C(i);
    E = E(i);
    WL = WL(i);
    WR = floor(0.5*(P2P*1.19));
    M(1:WR)=false;
end

[maxValue, linearIndex(i)] = max(Y1(i,:));
NP(i) = linearIndex(i);

Inner_H_width = floor(0.35*P2P);
E = floor(0.5*(P2P*1.19));

% M = logical(M);

%%Fourier series
% sinf=zeros(length(X),n);
% cosf=sinf;
% dx=X(2)-X(1);
% for i=1:n %Fourier components
%     sinf(:,i)=sin(2*i*pi*(X-r(1)+N*w)/((2*n*w)));

```

Figure C.1: Robust fitting code 1 Page one of code for robust fitting

```

%   cosf(:,i)=cos(2*i*pi*(x-r(1)+N*w)/(2*n*w));
% end
% fitfun = @(a,x) fourierseries(x,a,n,sinf,cosf,M);%Fit function
% coeff0=calc_FourierCoeff(dx,r,n,N,w,Y(M),sinf(M,:),cosf(M,:));
% coeff0=nlinfit(X(M,:),Y(M,:),fitfun,coeff0);

% or use polynomial fitting
fitfun = @(a,x) polyn(x,a,n);%Fit function
coeff0=nlinfit(X(M,:),Y(M,:),fitfun,ones(1,n));

sigmast=1;%starting sigma or use the formula below
% sigmast=rms(Y(M,:)-fitfun(coeff0,X(M,:)));

%Fit settings
opts=statset('nlinfit');
opts.MaxIter=1e6;
opts.Robust='on';
opts.Tune=1;

for kk=0:sigmas-1
    sigma0=sigma*exp(log(sigmast/sigma)*(sigmas-1-kk)/(sigmas-1));
    opts.RobustwgtFun = @(y) 1orpenalty(y,sigma0,offset);
    coeff0=nlinfit(X(M,:),Y(M,:),fitfun,coeff0,opts);
end
% figure;plot(X,Y,X,fitfun(coeff0,X))
% figure;plot(X,Y-fitfun(coeff0,X))

Fit = fitfun(coeff0,X);
% RMSE = rmse(X(WR:end), Fit(WR:end));
% RMSEE = (sum((X(WR:end)-Fit(WR:end)).^2))* 1/size(X(WR:end),1);
RMSE = sqrt(immse(Y(WR:end), Fit(WR:end)));
RMSEE = sqrt(mean((Y(WR:end) - Fit(WR:end)).^2));

FPP = Y - Fit;

NAF(i,:) = FPP;

end

```

Figure C.2: Robust fitting code 2 Page two of code for robust fitting

Appendix D

Particle tracking software

D.1 Glycerol calculations

The Matlab code used to determine the viscosity (Fig.D.1) and refractive index (Fig.D.2) of glycerol.

```

function [eta, rho]=GetGlycerolViscosity(fraction_glyc,T)

volume_glycerol=fraction_glyc;
volume_water=1-fraction_glyc;

% Calculations:
% total_volume=volume_glycerol+volume_water;
% volume_fraction=volume_glycerol/total_volume;

%density_glycerol=1277-0.654*T; % kg/m^3, equation 24
density_glycerol=1273.3-0.6121*T; % UPDATED following Andreas Volk's suggestion

density_water=1000*(1-((abs(T-3.98))/615)^1.71); % UPDATED following A.V.'s suggestion

mass_glycerol=density_glycerol*volume_glycerol; % kg
mass_water=density_water*volume_water; % kg
total_mass=mass_glycerol+mass_water; % kg
mass_fraction=mass_glycerol/total_mass;

viscosity_glycerol=0.001*12100*exp((-1233+T)*T/(9900+70*T)); % equation 22. Note factor of
0.001 -> converts to Ns/m^2
viscosity_water=0.001*1.790*exp((-1230-T)*T/(36100+360*T)); % equation 21. Again, note
conversion to Ns/m^2

a=0.705-0.0017*T;
b=(4.9+0.036*T)*a^2.5;
alpha=1-mass_fraction+(a*b*mass_fraction*(1-mass_fraction))/(a*mass_fraction+b*(1-
mass_fraction));
A=log(viscosity_water/viscosity_glycerol); % Note this is NATURAL LOG (ln), not base 10.
viscosity_mix=viscosity_glycerol*exp(A*alpha); % Ns/m^2, equation 6

% Andreas Volk polynomial:
c=1.78E-6*T.^2-1.82E-4*T+1.41E-2;
contraction=1+(c.*sin((mass_fraction).^1.31.*pi).^0.81);

density_mix=(density_glycerol*fraction_glyc+density_water*(1-fraction_glyc))*contraction; %
equation 25

eta=viscosity_mix;
rho=density_mix;

```

Figure D.1: Glycerol viscosity code The code used to calculate the viscosity of % Glycerol

```
% Refractive index scales linearly with the volume fraction of glycerol
% Refractive indices are calculated at 20 deg C

function [n_mix] = GetGlycerolIndex(fraction_glyc,lambda)

lambda = lambda/1000; % Conversion to microns

% Pure glycerol refractive index
n_glyc = 1.46004 + (3.94934611e-3)/(lambda^2) - (1.77343e-5)/(lambda^4);

% Pure water refractive index
B = [5.684027565e-1,1.726177391e-1,2.086189578e-2,1.130748688e-1];
C = [5.101829712e-3,1.821153936e-2,2.620722293e-2,1.069792721e1];

n_h2o = 1;
for termNo = 1:4
    n_h2o = n_h2o + (B(termNo)*(lambda^2))/((lambda^2) - C(termNo));
end
n_h2o = sqrt(n_h2o);

% Calculates the weight fraction
weight_glyc = fraction_glyc*1260.8;
weight_h2o = (1-fraction_glyc)*998.29;

wFrac_glyc = weight_glyc/(weight_glyc+weight_h2o);
wFrac_h2o = weight_h2o/(weight_glyc+weight_h2o);

% disp(wFrac_glyc)
% disp(wFrac_h2o)

n_mix = n_glyc*wFrac_glyc + n_h2o*wFrac_h2o;
```

Figure D.2: Glycerol viscosity code The code used to calculate the refractive index of % Glycerol